UNIVERSITY OF LIEGE
Faculty of Applied Sciences

Mass Spectrometry Laboratory
Professor E. DE PAUW

Development and Characterization of Fullerene Based Molecular Systems using Mass Spectrometry and Related Techniques

by

Jean-François Greisch

Civil Engineer

Dissertation submitted to obtain the degree

of

Doctor of Philosophy

in

Applied Sciences

July 2008

Abstract

The investigation and control of the properties of carbon based materials such as fullerenes and nanotubes is a highly dynamic research field. Due to its unique properties, *e.g.* an almost nano-dimensional size, three-dimensional cage topology, hydrophobicity, rich redox- and photochemistry, large absorption cross section, … C_{60} has a high potential as building block for molecular devices and biological applications. It can be functionalized, anchored to a surface and self-assembled into larger supramolecular entities, such as monolayers. Mass spectrometry and related techniques such as ion-molecule reactions, action spectroscopy and ion mobility have been used throughout this work to study fullerene based systems, ranging from hydrides, derivatives, non-covalent complexes and coordinated metal complexes. Simulations predicting structural, electronic and mechanical properties have been combined with the experimental results to assist in their analysis and interpretation. Using ion molecule reactions, the reactivity of gas phase C_{60} anions with methanol has been studied. Hydride formation by simple collisions in the gas phase with methanol as well as reversible dehydrogenation by infrared multiphoton activation has been demonstrated. C_{60} functionalization by 3'-azido-3'-deoxythymidine (AZT) has been performed and the charged product characterized both by collisional activation and action spectroscopy. Deprotonation has been shown to lead to rearrangements of the nucleoside analogue and to a subsequent charge transfer to the fullerene. To prevent unwanted rearrangements and side reactions, encapsulation of C_{60} is suggested, the host molecule acting as a steric barrier. C_{60} complexation by γ-cyclodextrins has been performed and the ions of the complexes characterized both by collisional activation and ion mobility. It has been demonstrated that, compared to deprotonated species, the sodiated C_{60}:(γ-cyclodextrin)$_2$ ions were highly compact structures. With only two small polar caps accessible to reagents, sodiated C_{60}:(γ-cyclodextrin)$_2$ complexes sterically protect the C_{60} core from unwanted side reactions. Finally, explorative work on C_{60} immobilization on silver colloids using surface enhanced Raman spectroscopy and on the characterization of C_{60} complexes with iron and manganese porphyrin is presented.

If you hit a wall and find no way out,
Look afar, dream larger, you'll find a way.

Acknowledgements

I would like to express my deepest gratitude to my supervisor Professor Edwin De Pauw for his support and advice, for the latitude allowed to experiment and develop personal approaches and for giving access to wonderful top equipment. His guidance has prepared me well for the challenges that lie ahead.

I am ever so grateful to FNRS Director of Research Françoise Remacle for the time spent reading and discussing my work, and for giving me fruitful input. Enlightening discussions with Professor Bernard Leyh are also deeply acknowledged.

Furthermore I would like to thank Professor Michael T. Bowers and Dr. Thomas Wyttenbach (University of California Santa-Barbara) for allowing me to perform ion mobility measurements on their equipment. Professor Rainer Weinkauf (Heinrich Heine University Düsseldorf) is also deeply acknowledged for letting me use his equipment for electron detachment measurements and for enlightening discussions.

The members of the De Pauw group, both past and present, are also given thanks for their insights on various issues as well as for their friendship. To the “Lab 4” cluster, Gabriel and Dominique, thanks for never letting there be a dull moment!

Finally, I wish to express my affectionate thankfulness to my parents for their love, understanding and constant support.

Publications

J. F. Greisch, B. Leyh, F. Remacle, E. De Pauw, Reversible $C_{60}^{\bullet -}$ hydrogenation by methanol: a gas phase study. *Submitted.*

J. F. Greisch, B. Leyh, E. De Pauw, Collision induced dissociation of deuterium enriched protonated 2'-deoxyguanosine. *European Physical Journal D.* (2008) *Accepted*.

J. F. Greisch, S. Kyritsoglou, B. Leyh, E. De Pauw. Mass spectrometric study of the ionized C_{60}: (γ-cyclodextrin)$_2$ inclusion complex by collision induced dissociation. *Journal of Mass Spectrometry*. **43**, 242 (2008).

J. F. Greisch, R. Weinkauf, E. De Pauw, E. S. Kryachko, F. Remacle. Charge distribution in 3'-deoxythymidine-fullerene: Mass spectrometry, laser excitation, and computational studies. *Israel Journal of Chemistry*. **47**, 25 (2007).

J. F. Greisch, E. De Pauw. Mass spectrometric characterization of 3 -imino[60]fulleryl-3 deoxythymidine by collision induced dissociation. *Journal of Mass Spectrometry*. **42**, 304 (2007).

J. F. Greisch, V. Gabelica, F. Remacle, E. De Pauw. Thermometer ions for matrix-enhanced laser desorption/ionization internal energy calibration. *Rapid Communications in Mass Spectrometry*. **17**, 1847 (2003).

Table of Contents

List of Figures

List of Tables

Chapter 1. General Introduction

Scaling down the size of devices allows engineering smarter, faster and cheaper systems for applications ranging from mechanics, electronics, photonics, to medicine. As a consequence, micro- and nano-systems are two fields of research currently experiencing a huge investment policy. Even though such a classification retains an arbitrary character, nano-systems can be defined as those with at least one dimension falling within the nanometer scale. They include nanoparticles, nanorods, nanowires, thin films and bulk materials made of nanoscale building blocks or consisting of nanoscale structures, as well as a profusion of molecular systems. These systems can gain additional functionality either by covalent or non-covalent assembly. Supramolecular assembly that involves delicate balances of forces between the nano objects can also be used to precisely position the nano objects in order to form new architectures without having to precisely place each one-by-one [1, 2, 3, 4, 5, 6, 7, 8].

At the nanoscale, the spatial confinement of an electron or an exciton within a metallic or a semi-conductor isolated structure induces the quantification of the wavefunction in the direction of confinement and the quantification of the energy of the bound levels [9, 10, 11, 12], in other words the possible values form a discrete ensemble. It allows producing nanostructures from bulk material with properties mimicking those of atoms and molecules. The quantum confinement effect of nanocrystals can be classified into two categories: a strong confinement regime where electrons and holes are individually quantum confined and a weak confinement regime where excitons are quantum confined. For semiconductor nanocrystals the boundary criteria between these two regimes were theoretically determined [13] to be $R/a_B \geq 4$ for the regime of exciton confinement, $R/a_B \leq 2$ for the regime of

individual electron hole confinement, and $2 \leq R/a_B \leq 4$ for the intermediate regime where both electron and hole confinement and their Coulomb interaction have to be considered. R and a_B respectively stand for the radius of the semiconductor nanocrystal and the exciton Bohr radius (of the order of 10nm) of the semiconductor bulk crystal. For metallic nanocrystals, the weak and strong confinement regimes are respectively observed when the nanocluster size approaches the electron mean free path (~50nm) and the Fermi wavelength (i.e., de Broglie's wavelength of an electron at the Fermi energy; or ~0.5 nm for gold and silver), where the continuous-band structure of metals breaks up into discrete energy levels [14, 15, 16, 17, 18, 19]. In addition to electron/hole confinement and exciton confinement effects, metal nanocrystals exhibit quantized collective oscillations of the free electron gas density or plasmons down to dimensions smaller than the electron mean free path [14, 15, 16, 17, 18, 19]. The Au_{55} nanocluster (~1.4 nm without ligands) presents rather structureless optical spectra, neither showing a collective excitation resonance nor exhibiting distinct absorption bands known from few-atom clusters [19, 20], and possibly bridges the transition from discrete energy levels to collective oscillations[19], which become apparent in ~2-nm-diameter Au nanoparticles [20, 14, 15, 16, 17, 18, 19].

1.1 Molecular Devices and C_{60} Based Sensors

Currently, molecular devices are often more attractive than e.g. nano-size silicon based systems due to the capacity to chemically produce large numbers of identical units. In this context, molecular devices are expected to provide an attractive low-cost alternative to silicon circuitry for carrying out logical operations. Since the 1974 Aviram and Ratner [21] proposal that an electron donor–σ–electron acceptor

molecule, where σ is some saturated covalent sigma bridge, could be used as one-molecule rectifier, some circuit elements e.g. based on fullerenes [22] and nanotubes [23, 24, 25], ranging from molecular wires [26], diodes [27], rectifiers [28, 29], and transistors [30, 31] have been produced. However practical implementation of complex molecular electronic devices currently requires better manipulation, control, interfacing and understanding of the transport of electrons through molecules and molecular assemblies on a nanometre scale. Sensing (screening) applications, on the other hand, often involves only the simplest logical operations and two state systems suffice to perform these with numerous techniques available to detect an on/off answer.

Molecular sensors can be divided into tracers/reporters and transducers depending on their mode of operation, respectively static and dynamic. Both types of sensors involve a recognition site. For tracers, the role of the recognition site is to bind its target and it requires a high affinity. Transducers, on the other hand, convert the response of the recognition site to the presence of its target into a different kind of energy that can be amplified, processed or converted [32, 33]. Most sensors produce electrical or optical readouts [34, 35, 36, 37].

Electrical sensors typically rely either on a change in the electrical conductance of a wire or in a change of the capacitance of a surface system. Optical sensors on the other hand typically involve luminescence (fluorescence or phosphorescence), quenching and change in absorption. Compared to optical events, monitoring electrical events is often simpler and less expensive. The physico-chemical mechanisms of the readout generation typically involve electron transfer e.g. photo-

induced electron transfer (PET) [38, 39], intramolecular charge transfer (ICT) [40], metal-to-ligand charge transfer (MLCT) [41], proton/hydrogen transfer, energy transfer e.g. Förster resonant energy transfer (FRET) [42], excited state reactions e.g. excited state proton transfer (ESPT) across inter- or intramolecular hydrogen-bonded systems, etc. All in all, the physico-chemical mechanisms responsible for the signal generation are directly responsible for the sensor sensitivity.

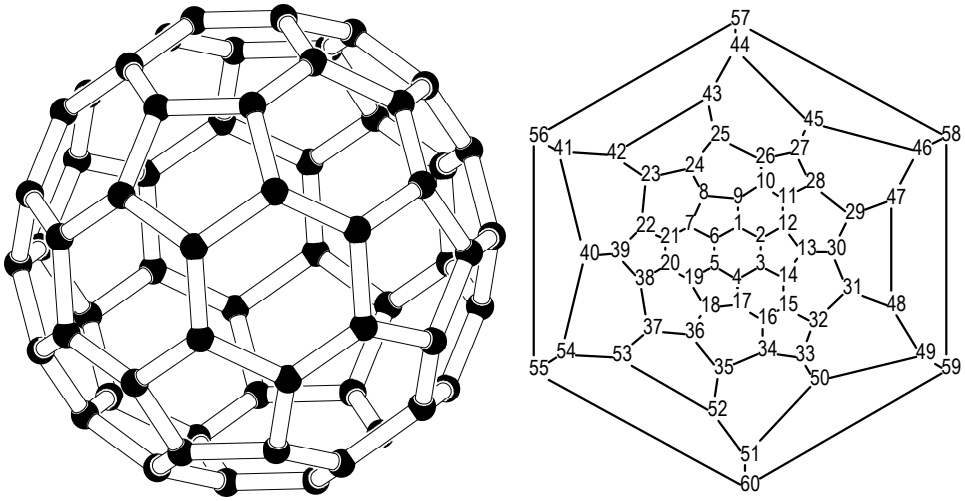

Fig. 1.1.1. C_{60} structure and Schlegel diagram.

The developments reported in the present work aim at producing a sensor relying on the physico-chemical C_{60} fullerenes for the sensitivity. Fullerenes and nanotubes occupy an important place in the science of low-dimensional systems and nanomaterials due to the fact that they can be produced in large quantities with high control over size and morphology [43, 44, 45, 46], and due to their many unique physical, chemical and electronic properties. C_{60}, the most prominent member of the family of fullerenes is a hydrophobic molecule made of 60 equivalent carbon atoms involved in 12 pentagons and 20 hexagons arranged in a soccer ball shape. The presence of pentagons in a curved π-system makes the 6-6 bonds (between hexagons, see Fig. 1.1.1) electron density higher than for 6-5 bonds (between pentagons, see Fig. 1.1.1) and explains why fullerenes react more easily on 6-6 bonds. C_{60} is a brown

black solid, mustard yellow when present in very thin films, and magenta in the dissolved state. Its UV-visible absorption almost extends over the whole visible region. The ^{13}C-NMR of C_{60} displays, as expected from the chemical equivalence of each carbon atom, only one line while the IR spectrum shows four lines. The electrochemical reduction of C_{60} occurs in six successive waves [47] in agreement with the theoretically predicted three-fold degenerate LUMO. The facile reduction of the fullerene C_{60}, together with its UV-visible absorption which extends over almost the whole visible region, makes [60]fullerene a good candidate as photoexcitable electron acceptor for use in photoinduced electron transfer systems. C_{60} properties furthermore can be modified via chemical functionalization of its surface (see Fig. 1.1.2), complexation, and endohedral compounds formation [48, 49, 50, 51, 52].

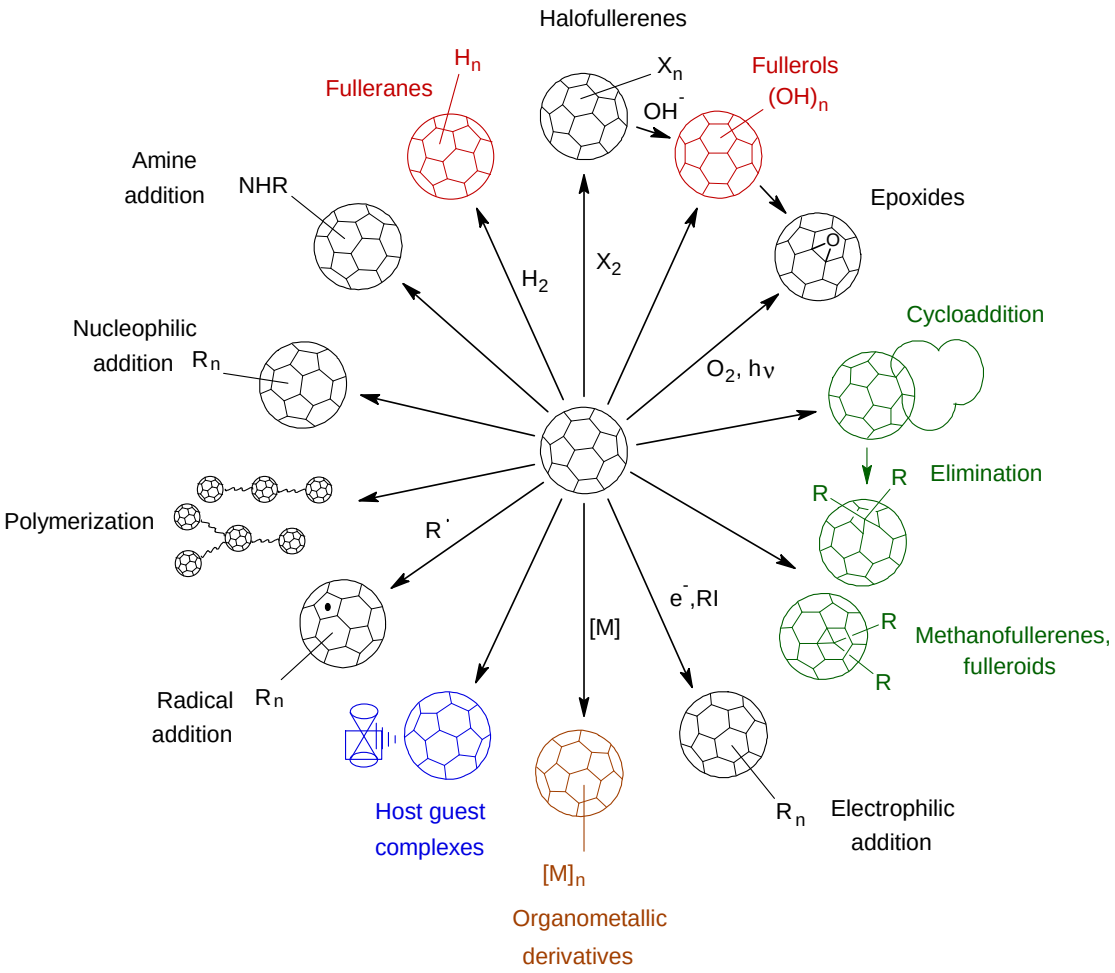

Fig. 1.1.2. Examples of reactions involving C_{60} [48].

Besides sensitivity the main quality criterion of a sensor is its selectivity. Selectivity refers to the extent to which a method can be used to determine particular analytes in mixtures or matrices without interferences from other components of similar behaviour [53]. A high degree of selectivity for the target analyte and an appropriate sensitivity to monitor it in the concentration range at which it is found in the sample is usually only displayed by biological molecules and related systems. Biological systems usually cooperate on a time span less than a few hours while demonstrating high affinity and selectivity. To do so, they bypass the problem of slow dissociation by the participative interaction of several anchor groups on one binding partner with a set of corresponding substructures on the other. Contrary to single-site binding, cooperative adhesion of host and guest can be destroyed in steps leading to greatly improved dissociation kinetics. In addition, the overall affinity can be modulated by the mutual influence of the anchor groups on one another. The contribution of each additional site can either go decreasing or the binding of the first anchor group can trigger all subsequent steps and an increasing contribution of each binding step to the overall affinity is observed. The last case is most interesting in sensing applications since the overall free energy provided by the binding steps can, when exceeding a threshold, more easily trigger a response. As a consequence most biological sensors rely on peptides, proteins, DNA, RNA and their synthetic analogues for the recognition site. The present work will be no exception, even though we will exclusively focus on single nucleosides.

1.2 Thesis Scope

This thesis presents developments towards the potential use of C_{60} fullerenes within biological sensors, using mass spectrometry (MS) and related approaches as the main

characterization tools. Simulations were used throughout this work to predict structural, electronic and mechanical properties and in support of the analysis and interpretation of the experimental results. This thesis is divided into the following chapters.

Chapter 1 is the present introduction on molecular and nanoscale systems. It briefly discusses their properties and introduces fullerenes while focusing on C_{60}.

Chapter 2 provides an overview of mass spectrometry. It describes the different mass to charge analysers used, gives a brief summary of the gas phase techniques related to mass spectrometry and discusses some practical limitations.

Chapter 3 provides an overview of the Quantum chemical modelling of molecular properties. It describes the approaches used and how some spectroscopic information is obtained.

Chapter 4 discusses ion-molecule reactions. Hydrogen-deuterium exchange is used to study the fragmentation mechanism of 2'-deoxyguanosine, a nucleoside entering in the composition of telomeric sequence. The hydrogen transferred upon fragmentation from one subunit to the other is identified. In the second section of chapter 4, C_{60} hydrides formation by reactive collisions of C_{60} anions with methanol in the gas phase is described. The reformation of C_{60} anions upon infrared multiphoton activation of C_{60} hydride anions is also demonstrated.

Chapter 5 discusses C_{60} functionalization by 3'-azido-3'-deoxythymidine. The product ions are characterized using collision induced dissociation and action spectroscopy. Deprotonation in opposition to reduction and cationization of 3'-imino[60]fulleryl-3'-deoxythymidine molecules is shown to induce rearrangements and a charge transfer to C_{60}. The present work suggests protection of C_{60} from rearrangements and side reaction *via* its encapsulation in a molecular host.

Chapter 6 focuses on C_{60} complexation by γ-cyclodextrins. The complexes are characterized using collision induced dissociation and ion mobility measurements. A highly compact structure with C_{60} only accessible to reagents at the two small polar caps is demonstrated for the sodiated complexes. The present work suggests C_{60} encapsulation prior to its functionalization.

Chapter 7 describes explorative work on the interaction of fullerenes and fullerene derivatives with transition metals. The adsorption of 3'-imino[60]fulleryl-3'-deoxythymidine on silver colloids is studied using surface enhanced Raman spectroscopy while C_{60} : metallo-porphyrins complexes are characterized using mass spectrometry and collision induced dissociation.

Chapter 8 presents a general conclusion.

References

[1] J. M. Lehn, *Angewandte Chemie International Edition in English* **35**, 1838 (1996).

[2] A. I. Day, *et al.*, *Angewandte Chemie International Edition* **275**, 41 (2002).

[3] S. Saha, *et al.*, *Small* **1**, 87 (2005).

[4] S. Saha, *et al.*, *Chemistry - a European Journal* **11**, 6846 (2005).

[5] D. S. Hecht, R. J. A. Ramirez, E. C. K. S. Briman, M. Artukovic, J. F. Stoddart, G. Gruner, *Nano Letters* **6**, 2031 (2006).

[6] J. E. Green, *et al.*, *Nature* **445**, 414 (2007).

[7] S. Saha, *et al.*, *Journal of the American Chemical Society* **129**, 12159 (2007).

[8] S. Anderson, H. L. Anderson, A. Bashall, M. McPartlin, J. K. M. Sanders, *Angewandte Chemie International Edition in English* **34**, 1096 (1995).

[9] M. A. Reed, *et al.*, *Physical Review Letters* **60**, 535 (1988).

[10] S. Furukawa, T. Miyasato, *Japanese Journal of Applied Physics* **27**, L2207 (1988).

[11] R. G. Wheeler, K. K. Choi, A. Goel, R. Wisnieff, D. E. Prober, *Physical Review Letters* **49**, 1674 (1982).

[12] R. Venkatasubramanian, M. L. Malta, D. P.and Timmons, J. A. Hutchby, *Applied Physics Letters* **59**, 1603 (1991).

[13] Y. Kayanuma, *Physical Review B* **38**, 9797 (1988).

[14] C. B. Murray, D. J. Norris, M. G. Bawendi, *Journal of the American Chemical Society* **115**, 8706 (1993).

[15] A. P. Alivisatos, *Science* **271**, 933 (1996).

[16] R. C. Ashoori, *Nature* **379**, 413 (1996).

[17] R. L. Whetten, *et al.*, *Advanced Materials* **8**, 428 (1996).

[18] M. M. Alvarez, *et al.*, *Journal of Physical Chemistry B* **101**, 3706 (1997).

[19] J. Zheng, P. R. Nicovich, R. M. Dickson, *Annual Review of Physical Chemistry* **58**, 409 (2007).

[20] Y. G. Kim, S. K. Oh, R. M. Crooks, *Chemistry of Materials* **16**, 167 (2004).

[21] A. Aviram, R. M. A., *Chemical Physics Letters* **29**, 277 (1974).

[22] H. W. Kroto, J. R. Heath, S. C. O'Brien, R. F. Curl, R. E. Smalley, *Nature* **318**, 162 (1985).

[23] S. Iijima, *Nature* **354**, 56 (1991).

[24] S. Iijama, *Nature* **363**, 603 (1993).

[25] D. S. Bethune, *et al.*, *Nature* **363**, 605 (1993).

[26] M. J. Frampton, H. L. Anderson, *Angewandte Chemie-International Edition* **46**, 1028 (2007).

[27] R. E. Martin, F. Diederich, *Angewandte Chemie International Edition* **38**, 1350 (1999).

[28] A. Honciuc, *et al.*, *Journal of Physical Chemistry B* **109**, 857 (2005).

[29] R. M. Metzger, *et al.*, *Journal of Physical Chemistry B* **107**, 1021 (2003).

[30] H. Park, *et al.*, *Nature* **407**, 57 (2000).

[31] A. Bachtold, P. Hadley, C. Dekker, *Science* **294**, 1317 (2001).

[32] R. Martinez-Manez, F. Sancenon, *Chemical Reviews* **103**, 4419 (2003).

[33] C. Suksai, T. Tuntulani, *Chemical Society Reviews* **32**, 192 (2003).

[34] F. Patolsky, G. L. Tao, E. Katz, I. Willner, *Journal of Electroanalytical Chemistry* **454**, 9 (1998).

[35] E. Katz, I. . Willner, *ChemPhysChem* **4**, 1085 (2004).

[36] L. Sheeney-Haj-Khia, B. Basnar, I. Willner, *Angewandte Chemie International Edition* **44**, 78 (2005).

[37] Y. M. Yan, O. Yehezkeli, I. Willner, *Chemistry - a European Journal* **13**, 10168 (2007).

[38] T. Gunnlaugsson, A. P. Davis, M. Glynn, *Chemical Communications* p. 2556 (2001).

[39] S. K. Kim, J. Yoon, *Journal of the Chemical Society, Chemical Communications* p. 770 (2002).

[40] E. W. Schlag, S. Y. Sheu, D. Y. Yang, H. L. Selzle, S. H. Lin, *Angewandte Chemie International Edition* **46**, 3196 (2007).

[41] C. Chow, B. K. W. Chiu, M. H. W. Lam, W. Wong, *Journal of the American Chemical Society* **125**, 7802 (2003).

[42] K. Choi, A. D. Hamilton, *Angewandte Chemie, International Edition* **40**, 3912 (2001).

[43] A. G. Nasibulin, A. Moisala, D. P. Brown, H. Jiang, E. I. Kauppinen, *Chemical Physics Letters* **402**, 227 (2005).

[44] S. Friedrichs, A. H. Windle, K. Koziol, C. Ducati, P. A. Midgley, *Microscopy and microanalysis* **11**, 1536 (2005).

[45] C. Ducati, *et al.*, *Small* **2**, 774 (2006).

[46] K. Koziol, *et al.*, *Science* **318**, 1892 (2007).

[47] Q. Xie, E. Perez-Cordero, L. Echegoyen, *Journal of the American Chemical Society* **114**, 3978 (1992).

[48] R. Taylor, D. R. M. Walton, *Nature* **363**, 685 (1993).

[49] A. Hirsch, *Synthesis-Stuttgart* p. 895 (1995).

[50] F. Diederich, C. Thilgen, *Science* **271**, 317 (1996).

[51] F. Diederich, R. Kessinger, *Accounts of Chemical Research* **32**, 537 (1999).

[52] C. Thilgen, F. Diederich, *Chemical Reviews* **106**, 5049 (2006).

[53] J. Vessman, *et al.*, *Pure and Applied Chemistry* **73**, 1381 (2001).

Chapter 2. Mass Spectrometry

"The basic principle of *mass spectrometry* (MS) is to generate ions from either inorganic or organic compounds by any suitable method, to separate these ions by their *mass-to-charge ratio* (m/z) and to detect them qualitatively and quantitatively by their respective m/z and abundances." [1]. The basic setup of all mass spectrometers consists of an ion source, a mass analyser and a detector operated under high vacuum conditions. Most ion sources involve evaporation/ionization or desorption/ionization steps, not always clearly separated from each other. The term ionization is used to describe the ion production. It does not refer exclusively to ionization by electron detachment. The analyte may be ionized thermally, by electric fields, by impacting energetic electrons, energetic neutral atoms, (atomic) ions, heavy cluster ions or photons, or by chemical reactions. The ions can be single ionized atoms, clusters, molecules, non-covalent complexes, their fragments or associates. Ion separation is effected by static or dynamic electric or magnetic fields, as well as in field free regions provided the ions possess a well-defined kinetic energy at the entrance of the flight path. The primary result of an analysis is a mass spectrum: a two-dimensional representation of signal intensity (ordinate) versus m/z (abscissa) [2]. In the course of this work four different types of mass analysers have been used, i.e. Time-of-Flight (ToF), Linear Quadrupole (Q), Quadrupole Ion Trap (QIT) and Fourier Transform - Ion Cyclotron Resonance (FT-ICR) analysers. The following section briefly describes their mode of operation. The discussion is based on [2, 3, 4].

2.1 Time-of-Flight (ToF)

The first construction of a Time-of-Flight has been published in 1946 by Stephens [5]. A localized bunch of ions of different m/z but close to identical kinetic energy is

dispersed in time during the ions flight along a field-free drift path of known length. Assuming the ions were at rest, which is correct in a first approximation, their kinetic energy can be inferred from the electric potential difference applied prior to their entrance in the field-free region. For a linear ToF, the time spent inside the analyser by an ion of mass m_i and charge z.e is given by $t = \frac{L}{\sqrt{2eU}}\sqrt{\frac{m_i}{z}}$, where U is the applied electric potential difference, L the travel distance and *e* the electric charge of an electron. In practice, resolution is degraded due to spatial and initial-energy distributions, metastable ion formation, etc. In 1966, Mamyrin proposed a way to compensate the temporal spread due to the ions initial velocity, the reflectron [6], later improved by Schlag and coworkers [7]. A reflectron consisting of a decelerating and reflecting field is placed within the field-free region. For a given m/z, ions with higher kinetic energy will penetrate the decelerating field further than ions with lower kinetic energy. Therefore the faster ions will spend more time within the reflecting field, and 'catch up' with lower energy ions further down the flight path. By adjusting the reflectron voltages it is possible to achieve a time-focusing plane at the detector [6]. The presence of a reflectron adds a time delay to the expression above.

The combination of continuous ion sources with ToF further led to the use of a separate direction for the ToF analysis, orthogonal to the continuous ion-beam axis of the ion source. A 10-100 ns electrostatic field accelerates the ions orthogonally to the direction of the beam axis and imparts to the sampled ions a component velocity vectorially independent of the axial velocity of the ion beam [8]. The ions are further accelerated to a final energy of several keV per charge prior entering the field-free drift space, where ToF mass separation occurs. The ratio of velocities (or energies) in

the two orthogonal directions is selected so that ions reach the ion mirror and then the ToF detector without requiring additional deflection in the drift region. A single-stage ion mirror provides effective compensation for the initial energy and spatial spread of the ions.

2.2 Linear quadrupole and quadrupole ion trap

The discovery of the mass-analysing, ion-trapping properties of two- and three-dimensional electric quadrupole fields and the concomitant construction of a quadrupole (Q) mass spectrometer were made by Paul in 1953 [9, 10].

A quadrupole field is expressed by its linear dependence on the coordinate position, $\mathbf{E} = E_0(\lambda x, \sigma y, \gamma z)$. The field is subject to the restraints imposed by the Laplace's equation (assuming no space charge within the electrode structure), $\nabla \cdot \mathbf{E} = 0$ so that $\lambda + \sigma + \gamma = 0$. The simplest ways of satisfying this equation are $\lambda = -\sigma$; $\gamma = 0$ and $\lambda = \sigma$; $\gamma = -2\sigma$.

The first set of relations corresponds to the potential $\phi = -\frac{1}{2} E_0 \lambda\left(x^2 - y^2\right)$ associated with a set of four hyperbolic cylinders with adjacent electrodes oppositely charged (linear quadrupole). If the minimum distance between opposite electrodes is $2r_0$ and the potential between opposite electrodes is ϕ_0, then $\phi = \frac{\phi_0\left(x^2 - y^2\right)}{2r_0^2}$. In practice, round rods closely approximating the correct hyperbolic rods are generally used (see Fig. 2.2.1).

The second set of relations corresponds to the potential $\phi = -\frac{1}{2} E_0 \lambda\left(x^2 + y^2 - 2z^2\right) = -\frac{1}{2} E_0 \lambda\left(r^2 - 2z^2\right)$ associated with a three-dimensional

rotationally symmetric quadrupole ion trap. The two “end-caps” and the ring electrode have cross-sections in the rz-plane which are complementary hyperbolae with a ratio of $\sqrt{2}$ in the semi-axes (r_0/z_0) (Fig. 2.2.2). Again, if ϕ_0 is the potential applied between the ring and the end caps, then $\phi = \frac{\phi_0\left(r^2 - 2z^2\right)}{2r_0^2}$. The equations of motion for an ion in an electric field are given by $m\frac{d^2\mathbf{r}}{dt^2} = q\mathbf{E} - m\Gamma\left(\frac{d\mathbf{r}}{dt}\right)$ where *m* and *q* are the ion mass and charge, **r** is the ion position, $\mathbf{E} = -\nabla\phi$ is the electric field inside the ion trap and the $\Gamma\left(\frac{d\mathbf{r}}{dt}\right)$ term takes into account collisional damping. In the following discussion the damping term will be dropped.

If ϕ_0 were merely time constant, the ion motion in the xz-plane of the linear quadrupole (Q) and in the xy-plane of the quadrupole ion trap (QIT) would be harmonic and all ion trajectories in these planes would be “stable”, i.e. remain finite in amplitude. In the yz-plane of the Q and z-direction of the QIT, however, the ions would not stay confined (defocusing). If, on the other hand, ϕ_0 is a periodic function of time, the ion trajectories in the xz- and yz-planes of the Q and in the ion trajectories in the xy-plane and z direction of the QIT will alternatively be focused and deflected. In this case, global stability can be achieved provided the periodicity is short enough and the ion inertia sufficient to prevent escaping the device during defocusing. Finally, the combination of a time constant (d.c) and periodic alternating (r.f.) component, typically $\phi_0 = (U - V\cos(\omega t))$, can be used to selectively stabilize ions of given m/z, as will be further discussed in the next sections [3].

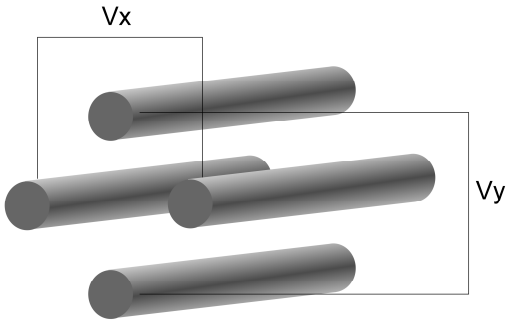

Fig. 2.2.1. Scheme of a linear quadrupole analyser. The rods are paired and their voltages respectively equal to $Vx = -(U + V\cos(\omega t))$ and $Vy = +(U + V\cos(\omega t))$. The rods are typically 10-20 mm in diameter and 15-25 cm in length. The radiofrequency is in the order of 1-4 MHz, and the d.c. (U) and r.f. (V) voltages are in the range of some 10^2-10^3 V. Ions of about 10 eV kinetic energy undergo approximatively 100 oscillations during their passage. r_0 is the distance between the principal axis of symmetry and one of the rods.

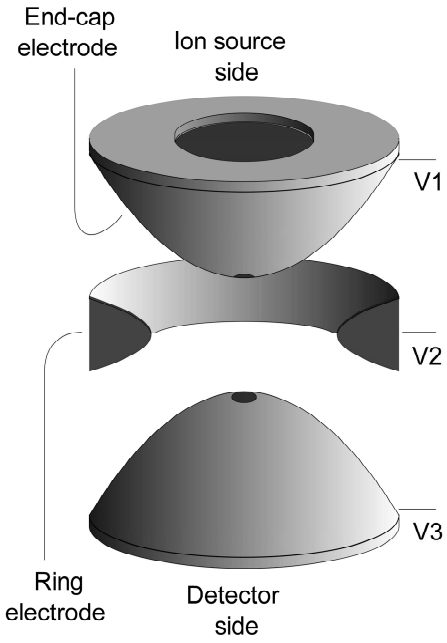

Fig. 2.2.2. Scheme of a quadrupole ion trap. The end-cap electrode voltages are respectively equal to the resonance a.c. voltages $V1 = +V_{res}\cos(\omega_{res}t + \phi_{res})$ and $V3 = -V_{res}\cos(\omega_{res}t + \phi_{res})$ while the voltage on the ring electrode is equal to the r.f. voltage $V2 = V\cos(\Omega t + \phi)$. All voltages are referenced to the ground potential. Figure adapted from reference [11] with the z axis corresponding to the principal symmetry axis.

2.2.1 Linear quadrupole (Q)

Linear quadrupoles can be operated in the r.f.-only or mass filter modes.

In the r.f.-only mode, a r.f.-field creates a potential well that provides radial confinement of the precursor and/or fragment ions. Since the r.f. quadrupoles are normally operated at pressures of several millitorr, the ions are thermalized in collisions with neutral gas molecules. The radial and axial collisional damping of the ion motion reduces both the energy spread and the beam diameter and results in better transmission into and through the quadrupole analyser [12]. Multipoles such as quadrupoles, hexapoles, octopoles … are often used as ion guides and in collision cells to transfer ions of low kinetic energy from one region to another without substantial losses. While a quadrupole in the r.f.-only mode acting as an ion guide provides a better ion focusing to the axis of the ion guide, higher multipoles (such as e.g. hexapoles and octapoles) have a steeper potential well close to the rods and are better at keeping the beam off the rods [13].

In the mass filter mode the quadrupole operates on the principle that ion trajectories in a two-dimensional quadrupole field are stable if the field has an r.f. component superimposed on a d.c. component with appropriate amplitudes and frequencies [14]. The time-dependent potential $\phi_0 = U - V\cos(\omega t)$ is applied to one pair of rods and $-\phi_0 = -[U - V\cos(\omega t)]$ to the other one (see Fig. 2.2.1).

The dimensionless equations of motion for an ion in a linear quadrupole with both r.f. and d.c. voltage components applied to the rods are the Mathieu equations:

$$\frac{d^2x}{d\tau^2} + (a_x - 2q_x\cos 2\tau)x = 0$$
$$\frac{d^2y}{d\tau^2} + (a_y - 2q_y\cos 2\tau)y = 0 \qquad (2.1)$$

where $\tau = \frac{\omega t}{2}$, and the reduced Mathieu parameters, $a_M = a_x = -a_y = \frac{4eU}{(m/z)\omega^2 r_0^2}$ and $q_M = q_x = -q_y = \frac{2eV}{(m/z)\omega^2 r_0^2}$, are used to characterize the amplitudes of both components; e is the charge of an electron, V and ω are the amplitude and the angular frequency of the r.f. voltage, respectively, U is the value of the d.c. voltage and r_0 is the inscribed radius of the quadrupole.

2.2.2 Quadrupole ion trap (QIT)

Three-dimensional quadrupole ion traps (QIT) create a three-dimensional RF quadrupole field to store ions within defined boundaries. The QIT consists of two hyperbolic electrodes serving as end caps and a ring electrode that replaces two of the linear quadrupole rods. The end caps are electrically connected and the d.c. and r.f. potentials are applied between them and the ring electrode (see Fig. 2.2.2). The working principle of the QIT is based on creating stable trajectories for ions of a certain m/z or m/z range while removing unwanted ions by colliding them with the walls or by axial ejection from the trap due to their unstable trajectories. The use of a light buffer gas (0.1 Pa He) to dampen the ion motion towards the centre of the trap significantly enhances resolution and sensitivity of the QIT (the damping term is omitted within the equations of motion hereafter).

The dimensionless equations of motion for an ion in a quadrupole ion trap with the potentials $\phi_0 = U - V\cos(\omega t)$ and $-\phi_0 = -[U - V\cos(\omega t)]$ respectively applied to the ring electrode and the hyperbolic end caps (see Fig 2.2.2), are the Mathieu equations:

$$\frac{d^2z}{d\tau^2} + (a_z - 2q_z \cos 2\tau)z = 0$$
$$\frac{d^2r}{d\tau^2} + (a_r - 2q_r \cos 2\tau)r = 0 \qquad (2.2)$$

where $\tau = \frac{\omega t}{2} = \pi f$ with *f* the fundamental r.f. frequency of the trap, and the reduced Mathieu parameters

$$a_M = a_z = -2a_r = -\frac{8eU}{(m/z)\omega^2 r_0^2} = -\frac{4eU}{(m/z)\omega^2 z_0^2}$$
$$q_M = q_z = -2q_r = -\frac{4eV}{(m/z)\omega^2 r_0^2} = -\frac{2eV}{(m/z)\omega^2 z_0^2} \qquad (2.3)$$

are used to characterize the amplitudes of both components; *e* is the charge of an electron, V and ω are the amplitude and the angular frequency of the r.f. voltage, respectively, *U* is the value of the d.c. voltage and r_0 and z_0 are the semi-axis of the hyperbolae shaping the quadrupole [3].

2.2.3 The ion trajectories

The linear quadrupole and the quadrupole ion trap have in common that the single equation $\frac{d^2u}{d\tau^2} + [a_u - 2q_u \cos 2(\tau - \tau_0)]u = 0$, with $2\tau_0$ the initial r.f. phase, describes the motion in both coordinate directions of importance. The motion in these two directions is independent except for the constraints:

$a_M = a_x = -a_y$ and $q_M = q_x = -q_y$ for the linear quadrupole, and

$a_M = a_z = -2a_r$ and $q_M = q_z = -2q_r$ for the quadrupole ion trap.

The solutions to this equation can be expressed by

$$u = \alpha' e^{\mu\tau} \sum_{n=-\infty}^{\infty} C_{2n} e^{2in\tau} + \alpha'' e^{-\mu\tau} \sum_{n=-\infty}^{\infty} C_{2n} e^{-2in\tau} \qquad (2.4)$$

where α' and α'' are integration constants depending on the initial conditions, u_0, $\dot{u}_0$, and $2\tau_0$. The constants C_{2n} and μ depend on the values of a_M and q_M, and not on the initial conditions. The solutions of the form 2.4 are either stable or unstable depending on μ. Stable solutions are those where *u* remains finite as $\tau \to \infty$, and such solutions may be useful providing that the value of u_{max} does not exceed r_0, the physical limit of the field. Unstable solutions are those where *u* increases without limit as $\tau \to \infty$. Four possibilities for μ exist [3].

1) μ is real and non-zero. Instability arises from the $e^{\mu\tau}$ or $e^{-\mu\tau}$ factor.

2) $\mu = i\beta$ is purely imaginary and β is not an integer. These solutions are the periodic stable ones.

3) μ is a complex number. The solutions are unstable (except for the trivial case $u_0 = \dot{u}_0 = 0$).

4) $\mu = im$ is purely imaginary and *m* is an integer. The solutions are periodic but unstable. For *m=2n* the periodicity is π in τ and for *m=(2n+1)* the periodicity is 2π. These solutions, called Mathieu functions of integral order, form the boundaries in (a_M, q_M) space between stable and unstable regions.

For a given set of *U*, *V* and ω, ions of a certain m/z value or m/z range oscillating within the region between the electrodes will have stable trajectories. By plotting a_M (ordinate, time invariant field) versus q_M (abscissa, time variant field) one obtains the stability diagram of the quadrupole field (Fig. 2.2.3). The stability diagram for a linear quadrupole and for a quadrupole ion trap are respectively obtained by superimposing two stability diagrams which differ by the factors -1 and -2. The y direction is conventionally taken as that for which a_M is negative.

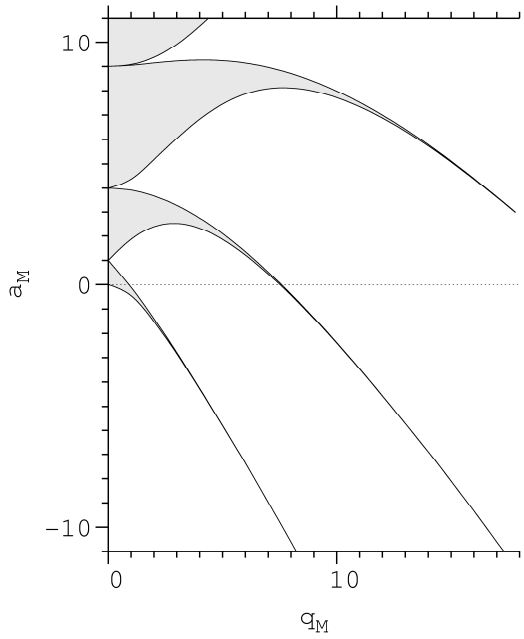

Fig. 2.2.3. The $a_M - q_M$ stability diagram for the Mathieu equation considering a single coordinate direction. The shaded areas result in "stable" ion trajectories where the ion displacement always remains finite.

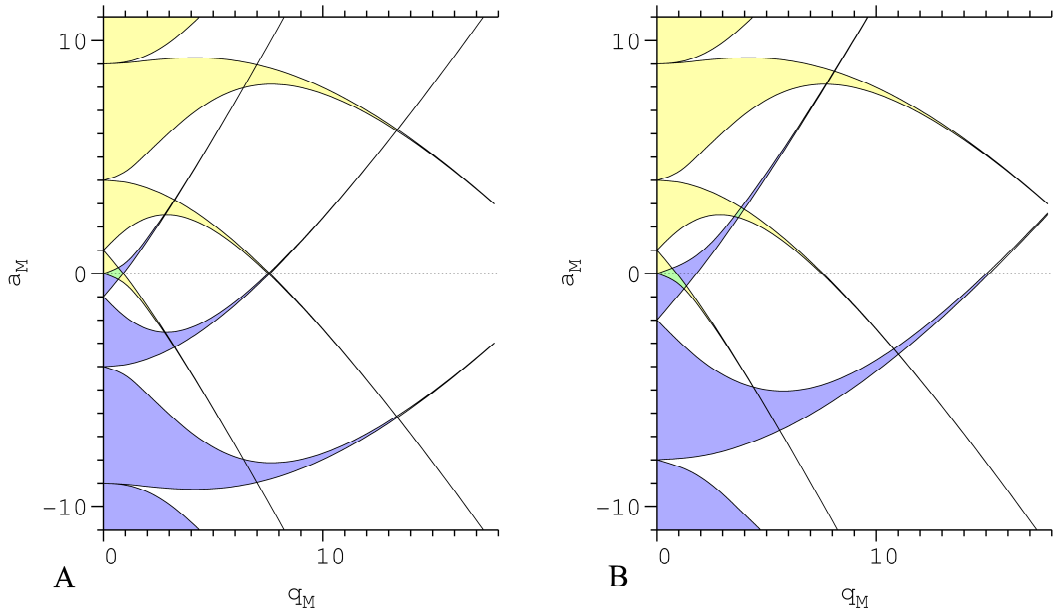

Fig. 2.2.4. Stability diagrams for a linear quadrupole (A) and for a quadrupole ion trap (B). The x-stable (A) and z-stable (B) regions are in yellow while the y-stable (A) and r-stable (B) regions are in blue. The regions of simultaneous stability are in green. The axes are labelled a_M and q_M but the scales are in units of a_x (or a_z) and q_x (or q_z).

In the r.f.-only operational mode, a_M=0, linear quadrupoles serve as high-mass filters: ions with m/z values below a certain cut-off value corresponding to q_M=0.908 diverge. Although there is no such sharp cut-off on the other end of the spectrum, transmission of ions with high m/z values suffer because of poorer focusing: the depth of the effective potential well is inversely proportional to m/z [15]. In the r.f.-only mode, ions covering approximately an order of magnitude in m/z range are transmitted simultaneously. If a wider m/z range is required, the r.f.-voltage is modulated (stepped or ramped between two or more r.f. levels) during the spectrum acquisition, providing a larger transmission window averaged over time. However it should be noted that the wider m/z range is obtained at the expense of the duty cycle: all light ions are lost when the r.f. is “high”, and the heavy ions are poorly focused in a shallow potential well when the r.f. is “low”.

In the mass filter mode, only ions within a narrow m/z window corresponding to q_M=0.706 and a_M=0.237 are transmitted. This point corresponds to the apex of the xy-stability region (see Fig. 2.2.4). A typical scan is obtained by increasing U and V while keeping the ratio constant, $\frac{a_M}{q_M} = 2\frac{U}{V} = cst$. This allows ions of increasingly higher m/z values to travel through the quadrupole.

The stability diagram for a quadrupole ion trap is obtained by superimposing two stability diagrams which differ by a factor -2. The z direction is conventionally taken as that for which a_M is negative.

The operation of the quadrupole ion trap is largely analogous to the operation of the linear quadrupole and will not be further discussed.

2.3 Fourier transform – ion cyclotron resonance (FT-ICR)

The first ICR mass spectrometers were reported by Smith [16] and Sommer *et al.* [17] in 1951 while FT-ICR was introduced in 1974 by Comisarow and Marshall [18, 19].

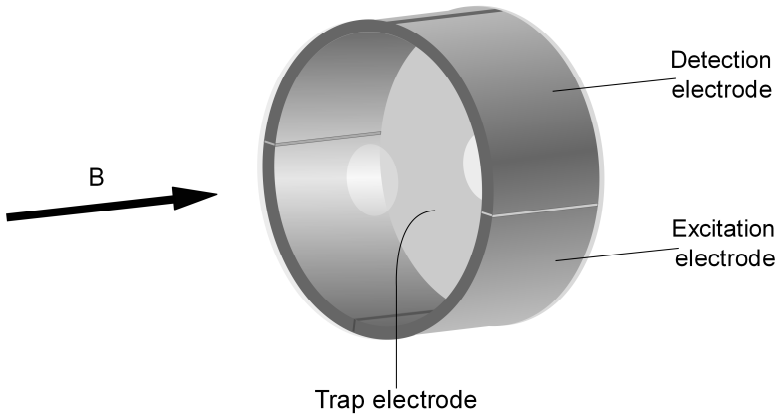

Fig. 2.3.1. Scheme of the FT-ICR Infinity™ Cell [20]. The cell is positioned inside the bore of a 9.4 T superconducting magnet. Indicated are the three sets of electrodes.

The motion of an ion in an ICR ion trap is described by the Lorentz equation [21]

$$m\frac{d^2\mathbf{r}}{dt^2} = q(\mathbf{v}\times\mathbf{B}+\mathbf{E}) - m\Gamma\left(\frac{d\mathbf{r}}{dt}\right) \qquad (2.5)$$

where m and q are the ion mass and charge, $\mathbf{r}$ is the ion position, $\mathbf{E}$ and $\mathbf{B}$ respectively are the electric and magnetic fields inside the ion trap and the $\Gamma\left(\frac{d\mathbf{r}}{dt}\right)$ term takes into account collisional damping. In the following discussion the damping term will be dropped.

The ions in an ion cyclotron resonance (ICR) cell (see Fig. 2.3.1) are trapped in the xy-direction by their cyclotron motion due to the static axial (z-axis) magnetic field, $\mathbf{B}$, and axially by two equally charged capping electrodes producing a convex approximately quadratic electrostatic potential.

The confinement in the z-direction results from the application of an electrostatic potential V_T to each of the two trapping electrodes, with the remaining electrodes electrically grounded. Solving the Laplace equation (assuming no space charge within the electrode structure), $\Delta\phi = 0$, yields an approximately quadrupolar electric potential near the centre of the trap, which can be written in the form

$$\phi(r,z) = V_T\left(\gamma + \frac{\alpha}{2a^2}\left(2z^2 - r^2\right)\right) \tag{2.6}$$

where *r* is the radial position of the ion in the x-y plane, *a* is a measure of the trap size, and γ and α are constants that depend on the trap shape [22].

The resultant electric field, $\mathbf{E} = -\nabla\phi$, has an axial component, $E_z = -\frac{d\phi}{dz} = -2\frac{V_T\alpha}{a^2}z$, and a repulsive radial component, $E_r = -\frac{d\phi}{dr} = \frac{V_T\alpha}{a^2}r$.

Replacement into the Lorentz force equation 2.5 yields for the motion in the z direction, $m\frac{d^2z}{dt^2} = -2\frac{qV_T\alpha}{a^2}z$, that describes a harmonic oscillator with a trapping frequency equal to $\omega_z = \sqrt{\frac{2qV_T\alpha}{ma^2}}$. The total radial force on the ion is obtained from the radial component of the Lorentz force equation. The analytical solution is, however, more easily obtained in the Cartesian form:

$$\begin{aligned} m\frac{d^2x}{dt^2} &= qB\frac{dy}{dt} + \frac{qV_T\alpha}{a^2}x \\ m\frac{d^2y}{dt^2} &= -qB\frac{dx}{dt} + \frac{qV_T\alpha}{a^2}y \end{aligned} \tag{2.7}$$

Posing $\omega_c = \frac{qB}{m} = \omega_+ + \omega_-$ and $\frac{\omega_z^2}{2} = \frac{qV_T\alpha}{a^2} = \omega_+\omega_-$, the frequencies ω_+ and ω_- are defined as $\omega_\pm = \frac{\omega_c}{2} \pm \sqrt{\frac{\omega_c^2}{4} - \frac{\omega_z^2}{2}}$, and the equations may be further rewritten as

$$\frac{d^2x}{dt^2} - (\omega_+ + \omega_-)\frac{dy}{dt} - \omega_+\omega_- x = 0$$
$$\frac{d^2y}{dt^2} + (\omega_+ + \omega_-)\frac{dx}{dt} - \omega_+\omega_- y = 0 \qquad (2.8)$$

A solution of the equations 2.8 is the radial ion trajectory (a special case of the solution obtained for the Mathieu equation, see equation 2.2) given by

$$x = \rho_+ \sin(\omega_+ t + \varphi_+) + \rho_- \sin(\omega_- t + \varphi_-)$$
$$y = \rho_+ \cos(\omega_+ t + \varphi_+) + \rho_- \cos(\omega_- t + \varphi_-) \qquad (2.9)$$

According to these equations the ions move in epicycles, where the (angular) eigenfrequencies ω_+ and ω_- are given by the trap parameters (B,V_T,a), and the radii ρ_+ and ρ_- and phases φ_+ and φ_- are given by the initial conditions. The ion motion is a superposition of the axial harmonic trapping motion with the trapping frequency, ω_z, and two radial (i.e. xy-plane) circular motions with the reduced cyclotron frequency, ω_+,and the magnetron frequency, ω_-. The cyclotron and magnetron modes of the ion motion are decoupled and their amplitudes are independent of each other [23].

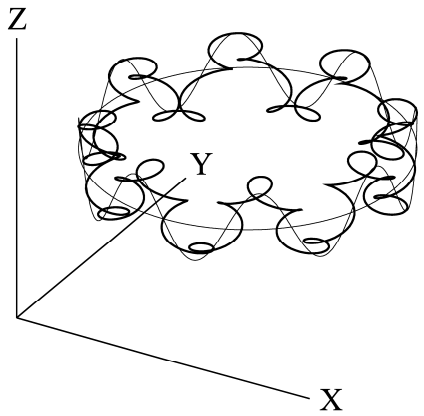

Fig. 2.3.2. Ion motion for $\omega_+ = 4\omega_z$, $\omega_z = 8\omega_-$, and $\rho_- = 4z_{amp} = 8\rho_+$; flat circle magnetron motion only; sigmoids combined magnetron and trapping motion; solid curve combined magnetron, cyclotron, and trapping motion [23].

Trapped ions with the same mass-to-charge ratio will have the same cyclotron frequency. If a rapid frequency sweep (chirp) is introduced into the measuring chamber, these ions will absorb energy at their specific cyclotron frequency and the added energy will cause the size of their orbit to increase as the cyclotron motion is resonantly amplified. The cyclotron motion establishes discrete coherent packets of ions with identical m/z and thereby provides a means to selectively separate one m/z from another. The time-varying electric field of the cyclotron rotating ion packets repeatedly passing the detector plates at their individual cyclotron frequency generates an induced image current proportional to the total number of ions. The transient signal is recorded and converted from the time domain to the frequency domain by means of Fourier transformation. The frequencies are converted to m/z values and the respective amplitudes represent the abundances of the corresponding ions [24, 18, 25, 24, 26].

One of the biggest advantages of FT-ICR-MS is its unparalleled mass resolution. Another unique feature of FT-ICR-MS is the control of stored ions within the ion trap

2.4 Electrospray ionization

Most experiments discussed in this thesis rely on electrospray ionization to generate ions in the gas phase. During the process of electrospray ionization, the analyte is gradually completely desolvated and the ions detected are usually expected to mirror the molecular species present in solution. According to Fenn [27] “electrospray ionization” refers to a complex combination of independent component processes, the two most important of which are electrospray dispersion, the electrostatic dispersion of sample liquid into charged droplets, and ionization, i.e., the transformation of

solute species in those droplets to free ions in the gas phase. Electrospray dispersion involves the high electric field applied between the metal capillary and the counter-electrode which causes the accumulation, at the solution-air interface, of ions of the same polarity as the voltage applied to the capillary [28, 27, 29, 30, 31]. The accumulation of charged species destabilizes the liquid at the capillary tip and causes the emission of charged droplets in the gas phase [28, 27, 29, 30, 31]. The rate of the charge separation process which determines the average current that flows between the electrodes is determined by the flow rate, applied voltage, conductivity, and liquid surface tension [28, 32, 27]. The involvement of electrochemical processes in the operation of electrospray sources was emphasized by Kebarle and coworkers [30]as well as by many others [27, 30, 31, 33]. As summarized by Van Berkel [27, 31], reduction /oxidation reactions involving solvents or analytes, and/or the elimination of cations /anions from solution, must occur during the negative/positive ion mode of operation to supply the necessary excess negative /positive charge. However the details of the ionization step and the different agents involved are often not controlled. In some electrospray source designs, additional control parameters such as heating part of the capillary or a sheath flow of nebulizer gas coaxial to the capillary are available in order to facilitate droplet emission and evaporation.

It has been theoretically described and experimentally demonstrated that narrower spray capillaries result in smaller droplets, and much reduced flow rates [34]. A 0.7 mm diameter borosilicate glass capillary with its extremity pulled to a 1-4 µm diameter aperture, sputtered gold film on the outer surface, and a spray voltage of 0.7-1.1 kV make flow rates of 20-50 nl min^{-1} sufficient to provide a stable ion current (sometimes with a small back pressure) [35]. Besides its low sample consumption,

NanoESI is well suited for solvents ranging from the highly polar pure water to the apolar toluene, both in positive- and negative-ion mode, and is free of memory effects since each sample is supplied in a fresh capillary.

Two models are typically considered to explain the formation of solute ions from charged droplets, the ‘charge residue model’ (CRM) proposed by Dole and co-workers and the ion desorption model (IDM) based on the work of Iribarne and Thomson. In the CRM model, ions originate from small droplets containing one molecule of the analyte. Evaporation of the solvent from the initially formed droplet as it traverses a pressure gradient towards the analyser leads to a reduction in diameter, and an increase in surface field, until the Rayleigh limit is reached. A Coulomb explosion occurs, as the magnitude of the charge is sufficient to overcome the surface tension holding the droplet together. The resulting instability disperses the droplet into a collection of smaller droplets that continue to evaporate until they too reach the Rayleigh limit and disintegrate. A continuation of this process might result in the formation of an ion containing a single analyte molecule. The molecule retains some of its droplet charge to become a free ion as the last of the solvent vaporises. The IDM model, on the other hand, assumes that before a droplet reaches the ultimate stage its surface electric field becomes sufficiently large to lift an analyte ion at the surface of the droplet over the energy barrier that prevents its escape [36, 28, 37, 38, 39, 40]. Although it is likely that both models occur to some extent, it is worth noting that while conventional ESI produces initial droplets of 1-2 µm in diameter, the droplet size for nanoESI is less than 200 nm, i.e., their volume is about 100-1000 times smaller.

2.5 Gas phase techniques related to mass spectrometry

In order to probe their structure, properties, mechanisms,… ions in the gas phase can be activated. For example, a straightforward strategy for measuring bond strength is to progressively increase the ion internal energy and observe the threshold at which bond cleavage begins or the value of the collision energy at which the parent ion survival yield amounts to 50% of the total ion current [41, 42, 43]. Collision-induced dissociation (CID), surface-induced dissociation (SID), heated capillary dissociation (HCD), blackbody infrared radiation dissociation (BIRD) [44, 45, 46] are commonly used in mass spectrometry to probe the strength of interactions in gas phase, while infrared multiphoton dissociation (IRMPD), electron-capture dissociation (ECD) [47, 48, 49, 50] and electron-detachment dissociation (EDD) are merely used to promote ergodic or in the last two cases non ergodic dissociation. Ion-molecule reactions (IMR) with neutral reagents can be used to study the reactivity of ions and infer structural information (see chapter 4). Electron photo-detachment can be used to detect or promote charge transfer within ions (see chapter 5). Ion mobility also called arrival time distributions (ATD) can be used to infer structural information (see chapter 6).

2.5.1 Collisional activation (CA)

Collisional activation, also known as collision activation dissociation (CAD) or collision induced dissociation (CID), involves the activation of the ions by few high-energy collisions or multiple low-energy gas-phase collisions (characteristic for the experimental conditions used in the present work), and, usually, the monitoring of the subsequent dissociation pathways.

The multiple collisions of neutral gas-phase molecules with an ion can be described using diffuse or specular scattering models [51]. Diffuse scattering is characterized by a complete memory loss of the incident momentum and the particle leaves the ion surface with a cosine distribution of angles perpendicular to the ion surface [52]. In contrast, specular scattering is equivalent to the hard-sphere scattering and results in conservation of the component of the momentum parallel to the surface and reversal of the normal component [52]. Interaction of large ions and particles with collision gas is better described by the diffuse scattering model [53, 54, 55]. The internal energy, E_{int}, acquired by the ions of mass m_i, passing through a collision cell containing a buffer gas of mass m_b and gas number density n, is calculated using the following equation:

$$E_{\text{int}} = \frac{m_i}{m_i + m_b} \frac{\phi E_0}{D} \left\{ 1 - e^{-\frac{Dnm_b \sigma L}{m_i}} \right\}$$ where ϕ is the average fraction of the centre-of-mass energy transferred to internal energy of the ion in a collision, E_0 is the initial laboratory frame kinetic energy of the ion injected in the collision cell, D a drag coefficient, σ the collision cross-section, and L is the length of the collision cell [52]. The only unknown parameter is the conversion efficiency of the centre-of-mass collision energy into the internal energy, ϕ. However, there is increasing evidence suggesting that the energy transfer efficiency increases with the size of the ion, reaching 90% for a nonapeptide [56, 57]. It is reasonable to assume that even higher energy transfer efficiency reaching 100% would be characteristic of larger ions with light collision gas [58]. For a small exponent and $\phi = 1$, the equation reduces to

$$E_{\text{int}} = \frac{m_b}{m_i + m_b} E_0 n \sigma L .$$

This energy transfer is thus influenced by the molecular weight of the collision gas, the initial kinetic energy of the ions (also called the injection energy of the ions), the collision gas pressure, the cross-section of the ions, and the collision cell length.

2.5.2 Infrared multiphoton activation (IRMPA)

Infrared multiphoton activation (IRMPA) involves multiple photon absorption. It is used to activate and often dissociate otherwise stable gaseous ions. Infrared multiphoton dissociation (IRMPD) is a technique that can be conveniently applied to trapped ions in Fourier transform ion cyclotron resonance (FT-ICR) analysers. The laser beam of a continuous wave carbon dioxide laser of 10.6µm wavelength having a power of 25-40W overlaps the ions stored within the ICR cell and the amount of energy transferred to the ions is typically varied via the duration of laser irradiation [59, 60].

2.6 Practical limitations

In mass spectrometry, the measured signal typically corresponds to the incoherent sum of the uncorrelated contributions of each molecule in the ion population considered. As such, the signal represents both a time and an ensemble average of the changes undergone by all molecules. Since very few (if any) of the ions in the ensemble actually behave as the average, interpreting the smooth, continuous changes characteristic of macroscopic observables in terms of equally smooth transformations at the molecular level can be both misleading and incorrect. In order to interpret the distribution of the experimental results, a unimodal assumption is typically made. If that is not the case, and the molecular properties are distributed in a multimodal fashion, the macroscopic average will lead to gross misinterpretations. This is the

main limitation, shared with many experimental techniques, of the physico-chemical interpretation of the results obtained from ions in gas-phase using mass spectrometry.

Finally, two important largely open questions are the extent of the results transferability between the gas phase (solvent free conditions) and condensed phases and between ions and neutrals. For example, in solution where noncovalent complexes are formed several attractive terms contribute to the overall stabilization of noncovalent assemblies [61]. In the gas phase, where the noncovalent complexes can be transferred using e.g. electrospray (ESI) to determine their stoechiometry, energy of interaction, etc., mass spectrometry (MS) and derived techniques suggest that the important structural features of large molecular assemblies are retained. However, some of the information obtained in gas phase may not be directly transferable to solution. Indeed, the strength of the electrostatic, induction and dispersion interactions (discussed in chapter 6) is expected to increase when going from solution to the gas phase due to the influence of the dielectric constant term, $\frac{1}{\varepsilon_r}$, whereas the hydrophobic interaction is expected to vanish [62]. However, even though solvent effects affect the chemical reactivity and the conformation of molecules, they also mask their intrinsic properties. Gas-phase ion-molecule reactions, free from the complication of solvent and counter-ion effects, can be used to obtain information on the intrinsic reactivity, including reaction kinetics, product ions, reaction mechanisms and thermodynamic properties of ionized molecules. Gas phase experiments can thus act as benchmarks for theoretical studies.

References

[1] H. Kienitz, *Einführung, in Massenspektrometrie* (Verlag Chemie: Weinheim, 1968).

[2] J. H. Gross, *Mass Spectrometry* (Springer-Verlag: Berlin Heidelberg, 2004).

[3] P. H. Dawson, *Quadrupole Mass Spectrometry and its Applications* (American Institute of Physics. Woodbury, New York, 1995).

[4] J. Kauppinen, J. Partanen, *Fourier Transforms in Spectroscopy* (Wiley-VCH Verlag: Berlin, 2001).

[5] W. E. Stephens, *Physical Review* **69**, 691 (1946).

[6] B. A. Mamyrin, V. I. Karataev, D. V. Shmikk, V. A. Zagulin, *Journal of Experimental and Theoretical Physics* **37**, 45 (1973).

[7] R. Frey, G. Weiss, H. Kaminski, E. W. Schlag, *Zeitschrift für Naturforschung A* **40**, 1349 (1985).

[8] M. Guilhaus, D. Selby, V. Mlynski, *Mass Spectrometry Reviews* **19**, 65 (2000).

[9] W. Paul, H. Steinwedel, *Zeitschrift für Naturforschung A* **8**, 448 (1953).

[10] W. Paul, *Angwandte Chemie* **102**, 780 (1990).

[11] K. Yoshinari, *Rapid Communications in Mass Spectrometry* **14**, 215 (2000).

[12] D. J. Douglas, J. B. French, *Journal of the American Society of Mass Spectrometry* **3**, 398 (1992).

[13] I. V. Chernushevich, A. Loboda, B. A. Thomson, *Journal of Mass Spectrometry* **36**, 849 (2001).

[14] W. Paul, H. P. Reinhard, U. von Zahn, *Zeitschrift für Physik* **152**, 143 (1958).

[15] D. Gerlich, *Advanced Chemical Physics* **82**, 1 (1992).

[16] L. G. Smith, *Review of Scientific Instruments* **22**, 114 (1951).

[17] H. Sommer, H. A. Thomas, J. A. Hipple, *Physcal Review* **82**, 697 (1951).

[18] M. B. Comisarow, A. G. Marshall, *Chemical Physics Letters* **25**, 282 (1974).

[19] M. B. Comisarow, A. G. Marshall, *Chemical Physics Letters* **26**, 489 (1974).

[20] P. Caravatti, M. Allemann, *Organic Mass Spectrometry* **26**, 514 (1991).

[21] S. Guan, *et al.*, *Chemical Reviews* **8**, 2161 (1994).

[22] H. Dehmelt, *Review of Modern Physics* **62**, 525 (1990).

[23] L. Schweikhard, H. Ziegler, J.and Bopp, K. Lützenkirchen, *International Journal of Mass Spectrometry and Ion Processes* **141**, 77 (1995).

[24] M. B. Comisarow, A. G. Marshall, *Journal of Chemical Physics* **64**, 110 (1976).

[25] A. G. Marshall, P. B. Gosshans, *Analytical Chemistry* **63**, 215A (1991).

[26] M. B. Comisarow, *Journal of Chemical Physics* **69**, 4097 (1978).

[27] J. F. de la Mora, *et al.*, *Journal of Mass Spectrometry* **35**, 939 (2000).

[28] R. B. Cole, *Journal of Mass Spectrometry* **35**, 763 (2000).

[29] M. G. Ikonomou, A. T. Blades, P. Kebarle, *Analytical Chemistry* **63**, 1989 (1991).

[30] A. T. Blades, M. G. Ikonomou, P. Kebarle, *Analytical Chemistry* **63**, 2109 (1991).

[31] G. J. Van Berkel, F. Zhou, *Analytical Chemistry* **67**, 2916 (1995).

[32] N. B. Cech, *Mass Spectrometry Reviews* **20**, 362 (2001).

[33] G. S. Jackson, C. G. Enke, *Analytical Chemistry* **71**, 3777 (1999).

[34] M. S. Wilm, M. Mann, *International Journal of Mass Spectrometry and Ion Processes* **136**, 167 (1994).

[35] M. Wilm, M. Mann, *Analytical Chemistry* **68**, 1 (1996).

[36] P. Kebarle, L. Tang, *Analytical Chemistry* **65**, 972A (1993).

[37] A. Gomez, K. Tang, *Physics of Fluids* **6**, 404 (1994).

[38] D. Duft, T. Achtzehn, R. Müller, B. A. Huber, T. Leisner, *Nature* **421**, 128 (2003).

[39] J. V. Iribarne, B. A. Thomson, *Journal of Chemical Physics* **64**, 2287 (1976).

[40] B. A. Thomson, J. V. Iribarne, *Journal of Chemical Physics* **71**, 4451 (1979).

[41] L. A. Marky, K. J. Breslauer, *Biopolymers* **26**, 1601 (1987).

[42] M. Moet-Ner, *Journal of the American Chemical Society* **110**, 3071 (1988).

[43] M. Moet-Ner, *Journal of the American Chemical Society* **110**, 3075 (1988).

[44] W. D. Price, P. D. Schnier, R. A. Jockusch, E. R. Strittmatter, E. F.and Williams, *Journal of the American Chemical Society* **118**, 10640 (1996).

[45] R. C. Dunbar, *Advances in Gas Phase Ion Chemistry* **2**, 87 (1996).

[46] R. C. Dunbar, T. B. McMahon, *Science* **279**, 194 (1998).

[47] R. A. Zubarev, N. L. Kelleher, F. W. McLafferty, *Journal of the American Chemical Society* **120**, 3265 (1998).

[48] N. Leymarie, C. E. Costello, P. B. O'Connor, *Journal of the American Chemical Society* **125**, 8949 (2003).

[49] E. A. Syrstad, F. Turecek, *Journal of the American Society of Mass Spectrometry* **16**, 208 (2005).

[50] M. M. Savitski, F. Kjeldsen, M. L. Nielsen, R. A. Zubarev, *Angewandte Chemie International Edition in English* **45**, 5301 (2006).

[51] P. S. Epstein, *Physical Review* **23**, 710 (1924).

[52] D. J. Douglas, *Journal of the American Society of Mass Spectrometry* **9**, 101 (1998).

[53] B. A. Chen, Y. L.and Collings, D. J. Douglas, *Journal of the American Society of Mass Spectrometry* **8**, 681 (1997).

[54] V. Nesatiy, Y. L. Chen, B. A. Collings, D. J. Douglas, *Rapid Communications in Mass Spectrometry* **12**, 1003 (1998).

[55] Y. L. Chen, J. M. Campbell, B. A. Collings, L. Konermann, D. J. Douglas, *Rapid Communications in Mass Spectrometry* **12**, 1003 (1998).

[56] M. Meroueh, W. L. Hase, *International Journal of Mass Spectrometry* **201**, 233 (2000).

[57] E. M. Marzuff, S. A. Campbell, M. T. Rodgers, J. L. Beauchamp, *Journal of the American Chemical Society* **116**, 6947 (1994).

[58] M. R. Mauk, A. G. Mauk, Y. L. Chen, D. J. Douglas, *Journal of the American Society of Mass Spectrometry* **13**, 59 (2002).

[59] D. P. Little, J. P. Speir, M. W. Senko, P. B. O'Connor, F. W. McLafferty, *Analytical. Chemistry* **66**, 2809 (1994).

[60] J. Laskin, J. H. Futrell, *Mass spectrometry reviews* **24**, 135 (2005).

[61] A. D. Buckingham, P. W. Fowler, J. M. Hutson, *Chemical Reviews* **88**, 963 (1988).

[62] J. M. Daniel, S. D. Friess, S. Rajagopalan, S. Wendt, R. Zenobi, *International Journal of Mass Spectrometry* **216**, 1 (2002).

Chapter 3. Quantum Chemical Modelling of Molecular Properties

In quantum mechanics the state of a system such as a molecule is defined by its wavefunction $|\psi\rangle$ and its evolution in time is governed by the Schrödinger equation, $i\hbar \frac{d}{dt}|\psi(t)\rangle = \hat{H}\psi(t)$ where $\hat{H}$ is the Hamiltonian operator associated with the total energy $E(t)$ of the system. When describing stationary states, one uses to the time-independent Schrödinger equation, $\hat{H}|\psi\rangle = E|\psi\rangle$.

The typical non-relativistic molecular Hamiltonian operator, in atomic units, can be divided into five terms,

$$\hat{H} = -\sum_i^N \frac{1}{2}\nabla_i^2 - \sum_k^M \frac{1}{2M_k}\nabla_k^2 - \sum_i^N \sum_k^M \frac{Z_k}{|\mathbf{r}_i - \mathbf{R}_k|} + \sum_i^N \sum_{j>i}^N \frac{1}{|\mathbf{r}_i - \mathbf{r}_j|} + \sum_k^M \sum_{l>k}^M \frac{Z_k Z_l}{|\mathbf{R}_k - \mathbf{R}_l|} \qquad (1)$$

where $\{i, j\}$ and $\{k, l\}$ respectively run over electrons and nuclei, and M_k is the ratio of the mass of nucleus k to the mass of an electron. In the presence of an external field, or in the event of significant relativistic effects, etc., other terms are added to the Hamiltonian; e.g. in the case of an external electric field $\mathbf{E}(t)$, one adds the term $(-\boldsymbol{\mu}.\mathbf{E}(t))$ where $\boldsymbol{\mu}$ is the dipole moment of the molecule. The discussion is based on [1, 2, 3, 4].

3.1 The Born-Oppenheimer approximation

In order to simplify the solution of the Schrödinger equation, the Born-Oppenheimer approximation is used. Due to the nuclei being about four orders of magnitude heavier than the electrons, the electronic relaxation can be considered as instantaneous with respect to the nuclear motion. Hence, in good approximation, the nuclei move in the

average field due to the electrons and to the other nuclei. This approximation allows to decouple the electronic motion from the nuclear one. One first solves the electronic Schrödinger equation ("el") for fixed nuclear positions $\{\mathbf{R}_k\}$:

$$\left(-\sum_i^N \frac{1}{2}\nabla_i^2 - \sum_i^N \sum_k^M \frac{Z_k}{|\mathbf{r}_i - \mathbf{R}_k|} + \sum_i^N \sum_{j>i}^N \frac{1}{|\mathbf{r}_i - \mathbf{r}_j|} \right) |\psi_{el}(\mathbf{r}_i;\mathbf{R}_k)\rangle = E_{el}(\mathbf{R}_k)|\psi_{el}(\mathbf{r}_i;\mathbf{R}_k)\rangle \quad (3.1)$$

while the total energy, in absence of nuclear motions, is :

$$E_{tot} = E_{el}(\mathbf{R}_k) + \sum_k^M \sum_{l>k}^M \frac{Z_k Z_l}{|\mathbf{R}_k - \mathbf{R}_l|} \quad (3.2)$$

Then, one can solve the equation for the nuclei, which moves in the potential generated by the electrons and in the potential due to the other nuclei.

The Born-Oppenheimer approximation considerably reduces the complexity of the Schrödinger equation. However, in many electron systems, the resulting equation for the electrons is still impossible to solve exactly, due to the electron-electron interactions. One of the most common ways of dealing with the many-electron problem is to separate the many-electron Schrödinger equation into independent/effectively non-interacting one-electron equations $\hat{h}_i|\psi_i\rangle = \varepsilon_i|\psi_i\rangle$. In the present work calculations were performed at three different levels of approximation, i.e. Hartree-Fock Theory, Semi-empirical PM3/PM6 methods, and Density Functional Theory.

3.2 The Hartree-Fock method

The Hartree-Fock (HF) theory is a deliberately approximate theory, whose development was partly motivated by an ability to solve the relevant equations exactly.

In the HF Molecular Orbital Theory, each electron is described by a spin-orbital $\chi_i(\mathbf{x}) = \psi_i(\mathbf{r})\varsigma(\omega)$ where $\psi_i(\mathbf{r})$ is its spatial orbital, $\varsigma(\omega)$ is its spin ($\alpha(\omega)$ or $\beta(\omega)$) and $\mathbf{x} = (\mathbf{r}, \omega)$ indicates both space and spin coordinates. The total antisymmetric wavefunction of the N-electron system in its ground-state is then approximated by a single Slater determinant of spin-orbitals, $\psi_{el}^{tot} = \frac{1}{\sqrt{N!}} \sum_{P \in S_N} \mathrm{sgn}(P) \prod_{i=1}^{N} \left| \chi_{P(i)}(\mathbf{x}_i) \right\rangle$ where P is a permutation of the N first integers. The determination of spin-orbitals relies on a variational principle. The expectation value of the electronic Hamiltonian, $\langle \psi_{el}(\mathbf{r}_i; \mathbf{R}_k) | \hat{H}_{el} | \psi_{el}(\mathbf{r}_i; \mathbf{R}_k) \rangle$, is made stationary with respect to the spin-orbitals, $\chi_i(\mathbf{x})$, subject to the condition of their orthogonalization and normalization by means of Lagrange multipliers ε_i:

$$\frac{\delta}{\delta \chi_i^*(\mathbf{x})} \left[\left\langle \psi_{el}^{tot} \middle| \hat{H}_{el} \middle| \psi_{el}^{tot} \right\rangle - \varepsilon_i \langle \chi_i(\mathbf{x}) | \chi_i(\mathbf{x}) \rangle \right] = 0 \qquad (3.3)$$

The variation leads to a set of coupled integro-differential equations of Schrödinger form, the so-called HF equations. The one-electron molecular spin-orbitals $|\chi_i(\mathbf{x})\rangle$ are individually determined as eigenfunctions of a set of one-electron Fock operators,

$$\left(-\frac{1}{2}\nabla^2 - \sum_{k=1}^{M} \frac{Z_k}{|\mathbf{r}_i - \mathbf{R}_k|} + \sum_{j}^{N} \int d\mathbf{r}' \frac{|\chi_j(\mathbf{x}')|}{|\mathbf{r} - \mathbf{r}'|} \right) |\chi_i(\mathbf{x})\rangle$$

$$- \sum_{j}^{N} \delta_{s_i s_j} \int d\mathbf{r}' \frac{\chi_j^*(\mathbf{x}')\chi_i(\mathbf{x}')}{|\mathbf{r} - \mathbf{r}'|} |\chi_j(\mathbf{x})\rangle = \varepsilon_i |\chi_i(\mathbf{x})\rangle \qquad (3.4)$$

where s_i labels the spin of particle *i*. The last two terms on the l.h.s. represent the interaction of each electron with the static field of all the other electrons and are respectively the Coulomb and exchange term. The exchange term, which arises because of the antisymmetric character of the determinantal wavefunction, is only

non-zero when considering electrons of the same spin and cancels out the unphysical self-interaction present in the Coulomb term. The effect of exchange on the many-body system is that electrons of like spin tend to avoid each other. Each electron of a given spin is consequently surrounded by an "exchange hole", a small volume around the electron which like-spin electrons avoid. Unlike all the other terms acting on $|\chi_i(\mathbf{x})\rangle$, the exchange term is a non-local integral operator and this makes the Hartree-Fock equations nonlinear and implies an iterative solution.

The procedure for solving the Hartree-Fock equation is called the self-consistent-field (SCF) method. The spatial part of each unknown one-electron molecular spin-orbitals is approximated by a linear combination, $|\psi_i^{trial}\rangle = \sum_{\mu}^{K} C_{\mu i} |\phi_\mu\rangle$, of a finite set of spatial basis functions $\{|\phi_\mu(r)\rangle, \mu = 1,\ldots,K\}$, typically atomic orbitals (LCAO approximation). Starting from a guess, the Hartree-Fock system of equations is expressed as a set of matrix equations known as Hall-Roothaan's equations: $\mathbf{FC} = \mathbf{SC\varepsilon}$ where **F** is the Fock matrix, **C** is the expansion coefficient matrix, $S_{\mu\nu} = \langle \phi_\mu | \phi_\nu \rangle$ is the overlap matrix, and $\boldsymbol{\varepsilon}$ is the diagonal matrix of the orbital energies. Hall-Roothaan's equations are then solved iteratively until self-consistency is reached and, according to the variation principle, the best set $\{\chi_k\}$ of orthogonal Hartree-Fock spin-orbitals and corresponding orbital energies $\{\varepsilon_k\}$ that yields the lowest E_{el} is found. The N spin-orbitals with the lowest energies are called the occupied spin-orbitals. The Slater determinant formed from these orbitals is the Hartree-Fock ground state wavefunction and is the best approximation to the ground state of the system of the single determinant form.

In many cases it is advantageous to apply the restriction that electrons with opposite spin pairwise occupy the same spatial orbital. This is the case for closed-shell systems and leads to the Restricted Hartree Fock method (RHF). When the system has open shells (MO occupied by a single electron), two formalisms can be used: in the open-shell variant (ROHF) of the restricted HF methods, all doubly occupied orbitals are constrained to have the same spatial part whereas in the Unrestricted version (UHF), two different sets of spatial parts are used, a set of spatial parts for spin α and a set of spatial parts for spin β. An important advantage of the restricted methods is that the magnetic moments associated with the electron spin cancel out exactly for the pair of electrons in the same spatial orbital, so that the SCF wavefunction is an eigenfunction of the spin operators $\hat{S}^2$ and $\hat{S}_z$. Although UHF generally predicts the energy better, due to greater variational freedom since one allows different spatial parts for spin orbitals of spin α and β, UHF sometimes has problems when predicting molecular properties such as bond lengths.

In short, the Hartree-Fock theory generates a well-controlled approximation to the many-electron wavefunction that is antisymmetric with respect to the exchange of two electron coordinates. It includes exchange between like-spin electrons but all the instantaneous electron-electron interactions are approximated with the mean-field interaction. In other words, it neglects dynamic or instantaneous electron correlation. Even though exchange corrections to the classical interelectronic repulsion are significantly larger than the neglected correlation corrections (typically between one and two orders of magnitude), neglect of electron correlation can have profound chemical consequences when it comes to determining accurate wavefunctions and derived properties. Another limitation of the HF theory is the finite atomic basis set

used in the SCF calculation. Indeed, the larger and more complete the set of basis functions $\{\phi_\mu\}$, the greater the degree of flexibility in the expansion of the spin orbitals.

3.3 Post Hartree-Fock methods

In order to introduce correlation corrections, the wavefunction can be written as a sum of Slater determinants with both the coefficients in front of each determinant and the spin-orbitals in each determinant optimized variationally. The equations for the orbitals are similar to the Hartree-Fock equations. They must be solved self-consistently but with two-electron repulsion and exchange terms that reflect the multi-determinantal nature of the wavefunction. Usually, the basis of Slater determinants is truncated. If the determinants summed are those that would normally be used in a valence-bond description of the molecular electronic structure, the method is called multiconfiguration SCF (MCSCF) whereas if all possible determinants that can be constructed from the occupied and empty valence orbitals important to the bond beaking and forming steps are considered, then it is called complete active-space SCF (CASCF).

3.4 The semi-empirical MNDO-PM3/PM6 methods

MNDO-PM3/PM6 are valence-electron self-consistent-field (SCF) molecular orbital (MO) methods which employ a minimal basis set of atomic orbitals $\{\phi_\mu\}$ and the neglect of diatomic differential overlap (NDDO) integral approximation. The NDDO approximation retains the higher multipoles of charge distributions in the two-centre interactions. The NDDO Fock matrix elements are given as the sum of parametric one-centre and two-centre terms. The one-centre terms are taken from atomic

spectroscopic data, with the refinement that slight adjustments are allowed in the optimization to account for possible differences between free atoms and atoms in a molecule. The experimentally derived one-centre two-electron integrals are considerably smaller than their analytically calculated values which is (at least partly) attributed to an average incorporation of electron correlation effects. The two-centre two-electron integrals are evaluated from semi-empirical multipole-multipole interactions and again are at intermediate distances smaller than their analytical counterparts reflecting some inclusion of electron correlation effects. The MNDO-PM3/PM6 methods have been parameterized primarily with respect to ground-state properties, with particular emphasis on the energies and geometries of organic molecules. The difference between PM3 and PM6 lies in the treatment of the core-core interaction and leads to an improved modeling of hydrogen bonds in PM6 [5].

3.5 The Density Functional Theory

The Density functional theory (DFT) is a powerful, formally exact theory that must be solved approximately because a key operator has an unknown analytical form. In the Density Functional Theory, the interacting electrons are replaced by a fictitious system of non-interacting electrons characterized by an overall ground-state density identical to the density of the real system. The electronic Hamiltonian of such a system can be expressed as a sum of one-electron operators. The Kohn-Sham (KS) one-electron operator is defined as $h_i^{KS} = -\frac{1}{2}\nabla_i^2 - \sum_{k=1}^{M}\frac{Z_k}{|\mathbf{r}_i - \mathbf{r}_k|} + \int \frac{\rho(\mathbf{r}')}{|\mathbf{r}_i - \mathbf{r}'|} d\mathbf{r}' + V_{xc}$

where $V_{xc}(\rho)$ is the exchange-correlation potential operator. It is the analytical form of $V_{xc}(\rho)$, defined as the functional derivative with respect to the density of the

exchange-correlation density functional energy, $V_{xc}(\rho) = \frac{\delta E_{xc}(\rho)}{\delta \rho}$, that is unknown and prevents from computing exact solutions. The exchange-correlation energy, $E_{xc}(\rho)$, not only includes the effects of quantum mechanical exchange and correlation, but also the correction for the classical self-interaction energy and the correction for the difference in kinetic energy between the fictitious non-interacting system and the real one.

In molecular quantum chemistry, Von Karman boundary conditions are used and the density is expanded in a finite basis set, the Kohn-Sham orbitals. This is unlike the approach used in solid state where periodic boundary conditions are used and the basis set is typically made of plane waves.

The numerical approach used to determine the electron density and subsequently derive the other molecular properties, implies to decompose the density on a basis set, $\rho(\mathbf{r}) = \sum_{i}^{N} |\chi_i(\mathbf{r})|^2$. The KS orbitals, $\chi_i(\mathbf{r})$, are then, in turn, expressed as a linear combination of functions $\{\phi_\mu\}$, typically atomic orbitals. The individual coefficients are determined by solving a secular equation entirely analogous to that employed for HF theory. Since the density is determined using the orbitals derived by solving the secular equation, $\rho(\mathbf{r}) = \sum_{i}^{N} |\chi_i(\mathbf{r})|^2$, the Kohn-Sham process must be carried out as an iterative SCF procedure. After each iteration, $\rho(\mathbf{r}) = \sum_{i}^{N} |\chi_i(\mathbf{r})|^2$ and $E(\rho)$ are calculated until both change by less than a predefined threshold.

The exchange-correlation functional used in the present work is the hybrid functional B3LYP. It is a so-called *hybrid* functional because it includes a fraction of exact Hartree-Fock exchange in addition to density functional exchange. Since density based functionals typically overestimate a quantity which HF theory will underestimate (for example, bond lengths) [6], Stephens *et al.* [7] proposed a three-parameter functional expression denoted B3LYP: $E_{xc}^{B3LYP} = (1-a_0-a_x)E_x^{LSDA} + a_0 E_x^{HF} + a_x E_x^{B88} + (1-a_c)E_c^{VWN} + a_c E_c^{LYP}$. It involves the local spin density approximation (LSDA) exchange functional, the Hartree-Fock (HF) exchange functional, Becke's 1988 (B88) functional [8], Vosko Wilk Nusair (VWN) correlation functional [9], and Lee Yang Parr (LYP) correlation functional [10]. The three parameters a_0=0.20, a_x=0.72 and a_c=0.81 were initially determined by Becke [11, 12] by minimizing the atomization energies, ionization energies, electron affinities and proton affinities of the G2 dataset with Perdew-Wang correlation functional E_c^{PW91} instead of E_c^{LYP}. B3LYP shows surprising accuracy for thermochemistry, structures and spectroscopic properties of first row molecules [13]. The high accuracy of B3LYP has made it perhaps the most popular functional of modern density functional theory although it does not, for instance, include the dispersive forces correctly for non-bonded molecular structures and therefore yield incorrect interaction energies [14, 15, 16].

3.6 Geometry optimization and vibrational modes

Once the electronic problem is solved, the motion of the nuclei can be solved under the same assumptions (e.g. Born-Oppenheimer approximation). For *M* nuclei, the geometry optimization problem is a minimization problem in $\Re^{3M}$ that can be written as $\inf\{E_{tot}(\mathbf{R}), (\mathbf{R}) \in \Re^{3M}\}$, where $E_{tot}(\mathbf{R})$ designate the sum of the Coulombic

repulsion energy between the nuclei $\sum_{k}^{M}\sum_{l>k}^{M}\frac{Z_k Z_l}{|\mathbf{R}_k - \mathbf{R}_l|}$ and the fundamental electronic energy $E_{el}(\mathbf{R})$ corresponding to the nuclei positions $\{\mathbf{R}\}$. From a numerical point of view because the configuration space is large (M can reach several hundreds for the *ab initio* models and several thousands for semi-empirical models) and because evaluation of $E_{tot}(\mathbf{R})$ at a given point of $\Re^{3M}$ is computationally expensive, the number of $E_{tot}(\mathbf{R})$ evaluations needs to be as small as possible.

In Gaussian™ geometry optimization is performed by default using the Berny algorithm [17, 18] in internal coordinates. The function $E_{tot}(\mathbf{R})$ in internal coordinates depends on 3M-6 variables, R_i. The (3M-6)-dimensional gradient of this function is given by $g_i = \frac{dE_{tot}(\mathbf{R})}{dR_i}$. Berny algorithm is an iterative method aiming at constructing a sequence $\{\mathbf{R}\}_n$ that converges to a minimum of $E_{tot}(\mathbf{R})$.

At step p+1, the value of the function E_{tot}^{a}, and its gradient $\mathbf{g}^a$, at m+1 points $(0 \le a \le m \le p)$ are recorded. The information is arranged so that $\mathbf{R}^0$ is the current point, $\mathbf{R}^1$ the most recent previous point, and so on with $\mathbf{R}^m$ the oldest. From the previous step there is also an $(3M-6)\times(3M-6)$ matrix **F** that is an approximation to the true second derivative matrix, i.e. $F_{ij} = \frac{d^2 E}{dR_i dR_j}$.

The first part of one step aims at obtaining corrections to the approximate second derivative matrix. An orthonormal basis set of vectors $\mathbf{e}^a$ is constructed for the space

spanned by the vectors $\left(\mathbf{R}^a - \mathbf{R}^0\right)$ by Schmidt orthogonalization.

$$\begin{aligned} \mathbf{r}^a &= \left(\mathbf{R}^a - \mathbf{R}^0\right) - \sum_{b=1}^{a-1} \mathbf{e}^b \left(\left(\mathbf{R}^a - \mathbf{R}^0\right) \cdot \mathbf{e}^b\right) \\ \mathbf{e}^a &= \frac{\mathbf{r}^a}{\left|\mathbf{r}^a\right|} \end{aligned} \tag{3.5}$$

If a point is too far from the current point $\left(\left|\mathbf{R}^a - \mathbf{R}^0\right| > r_{\max}\right)$ or if points are nearly collinear $\left(\left|\mathbf{r}^a\right| < r_{thresh}\right)$, then the point is discarded. Thus at step *p+1*, a total of *m+1* energy and gradient evaluations remain for use in correcting the approximate force constant matrix.

In the space spanned by the vectors $\mathbf{e}^a$, the new and the old estimates of the second derivatives, k_n^{ab} and k_0^{ab}, are respectively obtained:

$$k_n^{ab} = \frac{\left(\mathbf{g}^a - \mathbf{g}^0\right) \cdot \mathbf{e}^b - \sum_{c=1}^{a-1} \mathbf{k}_n^{cb} \left(\left(\mathbf{R}^a - \mathbf{R}^0\right) \cdot \mathbf{e}^c\right)}{\left(\mathbf{R}^a - \mathbf{R}^0\right) \cdot \mathbf{e}^a}, \text{ and } k_0^{ab} = k_0^{ba} = \mathbf{e}^a \cdot \mathbf{F} \cdot \mathbf{e}^b \tag{3.6}$$

These values are then used to update the current estimate of $\mathbf{F}$.

$$\mathbf{F}^{new} = \mathbf{F}^{old} + \sum_{b \geq a}^{m} \left(k_n^{ab} - k_0^{ab}\right) \left[\mathbf{e}^a \otimes \mathbf{e}^b + \left(1 - \delta_{ab}\right) \mathbf{e}^b \otimes \mathbf{e}^a\right] \tag{3.7}$$

The second part of one step is dedicated to searching for a minimum along the line between the current point and the previous point, $\left(\mathbf{R}^1 - \mathbf{R}^0\right)$ by fitting a quartic polynomial constrained to have only one minimum to E^0, $\mathbf{g}^0$, E^1, $\mathbf{g}^1$, and interpolating the energy and the gradient $\tilde{\mathbf{g}}$ at the minimum $\tilde{\mathbf{R}}$.

Using the new estimate of the second derivative matrix **F**, and the result from the one-dimensional search, the next estimate of the location of the stationary point is given by $\mathbf{R}^{new} = \tilde{\mathbf{R}} - \mathbf{F}^{-1}\tilde{\mathbf{g}}$.

The inverse of the second derivative matrix is calculated by first diagonalizing the matrix. The eigenvalues are tested to ensure that the matrix is positive definite and thus that the optimization step proceeds towards a minimum. If a negative value is found, its sign is reversed. The net effect is to force a steepest descend step along the direction of the eigenvector possessing the negative eigenvalue. The next step is carried out in a similar manner, retaining information from at most *n* previous steps and discarding the oldest information if necessary. At each step the gradient and displacement vectors are tested to see if the optimization has converged.

Once the stationary state localized, it is possible to calculate the normal modes of vibration and the associated frequencies by solving the eigenvalue equation $\mathbf{H}^{(m)}\mathbf{Q}_k = \lambda_k \mathbf{Q}_k$ where $\mathbf{H}^{(m)}$ is the mass-weighted Cartesian Hessian, $\lambda_k = 2\pi\nu_k^2$ with ν_k being the kth vibrational frequency and $\mathbf{Q}_k$ the associated normal mode. The elements of the Hessian are the mass-weighted second derivatives of the total electronic energy with respect to nuclear Cartesian coordinates

$$H_{lk}^{(m)} = \frac{1}{(m_l m_k)}\left(\frac{\partial E_{tot}}{\partial R_l^{(m)} \partial R_k^{(m)}}\right)_{eq} \qquad (3.8)$$

3.7 Vibrational spectroscopy

In general, experimental vibrational spectra of large molecules with many degrees of freedom are too complex to yield detailed information about the vibrational motions. In most cases assignment of the peaks to particular modes of vibration is not possible

at all. Accurate quantum-chemical calculations of vibrational frequencies and intensities make the interpretation of experimental spectra much easier.

At the heart of spectroscopic experiments is the exchange of energy between radiation and matter. Matter can emit or absorb light (photons) by undergoing transitions between quantized energy levels. Light is a superposition of electromagnetic radiations. These radiations are classically described as transverse waveforms consisting of orthogonal oscillating electric and magnetic fields which point transversely to the direction of propagation of the wave. Both the electric and magnetic fields oscillate at the same frequency $\nu = \frac{c}{\lambda}$ where c is the speed of light. Conventional spectroscopic measurements are concerned with the intensity of light absorption (IR spectroscopy), emission (fluorescence spectroscopy), or scattering as a function of the frequency of radiation. Scattering of a monochromatic electromagnetic (EM) radiation (photons) of frequency ν by a molecule can occur either elastically (Rayleigh scattering) or inelastically (Raman scattering). In the case of vibrational spectroscopy, the fraction of the photons that exchange energy with the molecule induces transitions between its vibrational states. Vibrational spectra are generally dominated by fundamental transitions, in which the number of quanta in one normal mode increases (or decreases) by one and all other normal modes remain in the same state.

In the presence of an electromagnetic radiation (photon), a time-dependent electric dipole moment is induced by the oscillating electric field in the molecule. The expansion in a power series in the applied field of the molecular dipole moment is

given by: $\boldsymbol{\mu} = \sum_{i=0}^{\infty} \boldsymbol{\mu}^{(i)} = \boldsymbol{\mu}^{(0)} + \boldsymbol{\alpha} \cdot \mathbf{E} + \frac{1}{2} \boldsymbol{\beta} : \mathbf{E}\mathbf{E} + \cdots$ with the first-rank tensor $\boldsymbol{\mu}^{(0)}$, the permanent dipole moment and the second rank tensor $\alpha_{ij} = \left(\frac{\partial \mu_i}{\partial E_j} \right)_0$, the polarizability tensor. The zero subscript means that the derivative is evaluated at zero field.

3.7.1 Infrared spectroscopy

The interaction responsible for the one photon absorption and the one photon emission by one molecule, is given by $H'(t) = -\mathbf{E}_{\omega}(t) \cdot \boldsymbol{\mu}$, where $\boldsymbol{\mu}$ is the transition dipole moment and $\mathbf{E}_{\omega}(t)$ is the incident electric field. In particular for infrared vibrational spectroscopy the transition dipole moment can be approximated by the electric dipole moment dependent on the normal modes of vibration $\boldsymbol{\mu}^{(0)} = \boldsymbol{\mu}_0^{(0)} + \sum_{k=1}^{3N-6} \left(\frac{\partial \boldsymbol{\mu}^0}{\partial Q_k} \right)_0 Q_k + \ldots.$ The intensity of the infrared absorption corresponding to a given vibrational transition $\left| v_i^k + 1 \right\rangle \leftarrow \left| v_i^k \right\rangle$ is then proportional to the square of the transition matrix elements

$$\left\langle v_f^k \left| \boldsymbol{\mu}_{if} \right| v_i^k \right\rangle = \left(\frac{\partial \boldsymbol{\mu}^{(0)}}{\partial Q_k} \right)_0 \left\langle v_f^k \left| Q_k \right| v_i^k \right\rangle \qquad (3.9)$$

3.7.2 Raman spectroscopy

The present section introduces Raman spectroscopy and the hypotheses made in the theoretical derivation of the intensity of Raman active modes according to the treatment of Placzek [4, 19, 20].

Scattering is a two photon process involving the interaction between two electric fields due to their mutual interaction with a molecule. In the linear approximation in the electric field, the molecular dipole induced by the incident field $\mathbf{E}_{\omega}(t)$ is equal to $\boldsymbol{\mu}^{ind} = \boldsymbol{\alpha} \cdot \mathbf{E}$. The interaction potential of this dipole with the resultant field $\mathbf{E}_{\omega'}(t)$ is given by $H'(t) = -\mathbf{E}_{\omega'}(t) \cdot \boldsymbol{\mu}^{ind} = -\mathbf{E}_{\omega'}(t) \cdot \boldsymbol{\alpha} \cdot \mathbf{E}_{\omega}(t)$. The different transitions induced by this interaction are two-photon absorption, two-photon emission, Rayleigh scattering $(\omega' = \omega)$, Stokes-Raman scattering $(\omega' < \omega)$, and anti-Stokes-Raman scattering $(\omega' > \omega)$. In what follows the focus is on the non-resonance Raman spectrum, the spectrum observed when the exciting light is distant in frequency from any absorption band.

The response of the molecule may be calculated quantum mechanically while the fields remain classical. The differential Raman scattering cross-section for the $i \to f$ transition, $\frac{d\sigma_{fi}}{d\Omega}$, is equal to the ratio of the power per steradian (irradiance, W/sr) at the detector divided by the incident intensity (W/cm^2). Within the Born-Oppenheimer approximation and the long wavelength approximation (electric field vector **E** constant within the whole molecule), the application of Fermi's golden rule yields the following expression for the Raman-scattering differential cross section from an initial state $|i\rangle$ to a final $|f\rangle$, $\frac{d\sigma_{fi}}{d\Omega} = \frac{\omega^3 \omega'}{c^4} \left| \mathbf{e}_s \cdot \boldsymbol{\alpha}_{fi} \cdot \mathbf{e}_0 \right|^2$. The unit vectors $\mathbf{e}_0$ and $\mathbf{e}_s$ point along the polarization directions of the incident and scattered radiations and do the job of projecting out the part of the induced polarization that is detected. According to Placzek, the polarizability tensor, $\boldsymbol{\alpha}_{fi}$, for the $i \to f$ transition from vibrational state $|i\rangle$ to a final vibrational state $|f\rangle$ of the non-

degenerate electronic ground state is given by

$$\left(\alpha_{\rho\sigma}\right)_{fi} = \frac{1}{\hbar}\sum_{n=1}^{\infty}\left[\frac{\langle f|\mu_\rho|n\rangle\langle n|\mu_\sigma|i\rangle}{\omega_0 + \omega_{nf} + i\Gamma_n} - \frac{\langle f|\mu_\sigma|n\rangle\langle n|\mu_\rho|i\rangle}{\omega_0 - \omega_{ni} - i\Gamma_n}\right] \tag{3.10}$$

In this expression μ_ρ is the ρ component of the transition dipole moment, $|n\rangle$ an intermediate state, $i\Gamma_n$ is a damping factor which is inversely proportional to the lifetime of the state $|n\rangle$, and ω_0 is the incident radiation frequency.

It is the basis of the standard method for calculating relative intensities for polyatomic molecules.

Since the ground state polarizability tensor parametrically depends on the nuclear coordinates, it can be expanded in a Taylor series about the equilibrium geometry,

$$\boldsymbol{\alpha}_{\sigma\rho}(\mathbf{Q}) = \left(\boldsymbol{\alpha}_{\sigma\rho}\right)_0 + \sum_{k=1}^{3N-6}\left(\frac{\partial\boldsymbol{\alpha}_{\sigma\rho}}{\partial Q_k}\right)_0 Q_k + \ldots \tag{3.11}$$

In the harmonic approximation, the first term in the expansion accounts for Rayleigh scattering $\left(|v_f\rangle = |v_i\rangle\right)$ and the second term for the first Stokes-Raman lines and anti-Stokes-Raman lines $\left(|v_f\rangle = |v_i \pm 1\rangle\right)$.

Evaluation of the total matrix elements (neglecting quadratic and higher order terms), $\langle v_f|\boldsymbol{\alpha}_{\sigma\rho}|v_i\rangle = \left(\boldsymbol{\alpha}_{\sigma\rho}\right)_0\langle v_f|v_i\rangle + \sum_{k=1}^{3N-6}\left(\frac{\partial\boldsymbol{\alpha}_{\sigma\rho}}{\partial Q_k}\right)_0\langle v_f|Q_k|v_i\rangle$, gives for transitions $|v_i^k + 1\rangle \leftarrow |v_i^k\rangle$ the following expression $\langle v_f^k|\boldsymbol{\alpha}_{\sigma\rho}|v_i^k\rangle = b_{v_k}\left(v_{k,i}+1\right)^{\frac{1}{2}}\left(\frac{\partial\boldsymbol{\alpha}_{\sigma\rho}}{\partial Q_k}\right)_0$ with $b_{v_k}^2 = \frac{\hbar}{4\pi\nu_k}$. The derivatives of the ground state polarizability tensor are often carried out as numerical or analytical derivatives of the energy since according to the

Hellmann-Feynman theorem $\boldsymbol{\alpha}_{\rho\sigma} = -\left(\frac{d^2 E_{el}}{d\mathbf{E}_\rho d\mathbf{E}_\sigma} \right)_0$, $\rho, \sigma = \{x, y, z\}$. Given the normal modes, all Raman intensities can be calculated at a cost comparable to that of an energy and gradient calculation at a single nuclear energy.

References

[1] A. Szabo, N. S. Ostlund, *Modern Quantum Chemistry* (Dover Publications, Mineola, 1996).

[2] G. C. Schatz, M. A. Ratner, *Quantum Mechanics in Chemistry* (Dover Publications, Mineola, 2002).

[3] J. I. Steinfeld, *Molecules and Radiation, 2nd Edition* (Dover Publications, Mineola, 2005).

[4] D. Long, *The Raman Effect* (Wiley, Chichester, 2002).

[5] W. Thiel, *Semiempirical Methods, published in Modern Methods and Algorithms of Quantum Chemistry, NIC Series, Vol. 3, p 261-283.* (John von Neumann Institute for Computing, Jülich).

[6] M. M. Morrell, R. G. Parr, M. Levy, *Journal of Chemical Physics* **62**, 549 (1975).

[7] P. J. Stephens, F. J. Devlin, C. F. Chabalowski, M. J. Frisch, *Journal of Physical Chemistry* **98**, 11623 (1994).

[8] A. D. Becke, *Physical Reviews A* **38**, 3098 (1988).

[9] S. H. Vosko, L. Wilk, M. Nusair, *Canadian Journal of Physics* **58**, 1200 (1980).

[10] C. Lee, W. Yang, R. G. Parr, *Physical Reviews B* **37**, 785 (1988).

[11] A. D. Becke, *Journal of Chemical Physics* **97**, 9173 (1992).

[12] A. D. Becke, *Journal of Chemical Physics* **98**, 1372 (1993).

[13] V. Barone, *Chemical Physics Letters* **226**, 392 (1994).

[14] S. Tsuzuki, H. P. Luthi, *Journal of Chemical Physics* **114**, 3949 (2001).

[15] X. Wu, M. C. Vargas, S. Nayak, V. Lotrich, G. Scoles, *Journal of Chemical Physics* **115**, 8748 (2001).

[16] T. van Mourik, R. J. Gdanitz, *Journal of Chemical Physics* **116**, 9620 (2002).

[17] H. Schlegel, *Journal of Computational Chemistry* **3**, 214 (1982).

[18] H. B. Schlegel, *Optimization of Equilibrium Geometries and Transition Structures, in Ab initio Methods in Quantum Chemistry-I* (Wiley, Chichester, 1987).

[19] A. C. Albrecht, *Journal of Chemical Physics* **34**, 1476 (1961).

[20] J. Tang, A. C. Albrecht, *Journal of Chemical Physics* **49**, 1144. (1968).

Chapter 4. Ion-molecule reaction studies

The present chapter discusses the characterization of 2'-deoxyguanosine and C_{60} using ion-molecules reactions in the gas phase. Gas-phase ion-molecule reactions are one of the available techniques to gain information on the intrinsic properties of ionized molecules in a solvent free environment. Since its introduction as a structural probe for gas-phase ions in 1972 by Hunt and coworkers [1], gas-phase hydrogen/deuterium (H/D) exchange has been used to distinguish isomeric species [2] and to probe conformational changes by mass spectrometry [3, 4]. Deuterium incorporation occurs at exchange sites (i.e. amine, amide, and hydroxyl) accessible to the reagent gas [5]. Gas-phase H/D exchange is also, to some extent, affected by charge location on the molecule [5, 6]. It has been used in the present work (see section 4.1) to probe the fragmentation of 2'-deoxyguanosine and to provide supporting evidence for its fragmentation mechanism. 2'-deoxyguanosine is a purine deoxynucleoside composed of guanine linked by its N9 nitrogen to the C1 carbon of 2'-deoxyribose. It is a component of deoxyribonucleic acid (DNA) in which repeats of 2'-deoxyguanosine monophosphate can be found, among other places, in the telomeric deoxyguanosine-rich sequences. These sequences undergo a monovalent cation-induced transition to a folded conformation called G-quadruplex with guanines forming planar G-quartet structures. These structures have attracted considerable attention both for their structural and potential physico-chemical properties [7, 8, 9, 10, 11, 12].

Gas-phase reactions have also been used to study C_{60} reactivity towards methanol (see section 4.2). Fullerenes such as C_{60} are closed caged molecules exclusively composed of carbon. They are considered to be the 3rd carbon allotrope in addition to diamond

and graphite. Unlike aromatics, fullerenes have no hydrogen atoms or other group attached, and so are unable to undergo substitution reactions. However, a vast number of products may arise from addition of just one reagent [13]. The chemistry of fullerenes is therefore concerned with investigating these additions and examining the structures and reactivity of its derivatives. The second section of this chapter is dedicated to the reactivity of the radical monoanion $C_{60}^{\bullet -}$ towards neutral methanol in the gas phase.

4.1. Collision induced dissociation of deuterium enriched protonated 2'-deoxyguanosine

Studies of the fragmentation of nucleosides and nucleotides are instrumental to the understanding of the cleavage of oligonucleotides for sequencing purposes. Typical activation techniques in mass spectrometry include low and high energy collisions, infrared multiphoton activation, UV-visible photoactivation, and electron capture [14, 15, 16, 17] (see discussion in chapter 2). Depending on the activation technique used and the ergodicity of the fragmentation mechanism involved, different reaction channels are followed and different fragments generated. In order to understand a fragmentation mechanism, one must obtain information about the reaction channel, for example about the atoms and the conformations involved [18].

Nucleosides and nucleotides have been studied by a large range of experimental techniques, from X-ray[19], NMR[20, 21, 22], Raman spectroscopy[23, 24, 25], mass spectrometry[26, 27, 28, 29] to photoelectron measurements[30, 31]. Conformers with different relative orientations of their subunits were reported and it appeared that the physicochemical properties, e.g. reactivity, of nucleosides were influenced by their conformation[23, 32, 33]. The conformation of 2'-deoxyguanosine is defined by five

main torsion angles among which the most important is the torsion angle around the C1'-N9 glycosidic bond, χ, which defines the orientation of the nucleobase with respect to the ribose (see Fig. 4.1.1). Conformers are typically divided according to their *anti* (χ ranging from 90° to 270°) or *syn* (χ ranging from -90° to +90°) character. In crystals[19, 34] and solutions[21, 35] nucleosides preferentially adopt an *anti* conformation in which the base is oriented away from the sugar. However NMR data in solution indicate that 2'-deoxy-5'-monophosphateguanosine has a significant propensity to adopt a *syn* orientation, with the nucleobase oriented over the furanose ring[20, 36]. Guanine containing nucleotides have also been shown to adopt the *syn* orientation in a number of crystal structures of nucleosides [37].

In the gas phase, the influence of the desorption / desolvatation and ionization processes on the conformational population and fragmentation pathways of molecules with a large number of degrees of freedom is most often not known. Some results are therefore expected to be dependent on the gas-phase ion production method and even involve, in some cases, several gas phase conformers. However, collision cross-sections measurements by ion mobility in helium of the deprotonated and protonated 2'-deoxy-5'-monophosphatenucleosides (dNMP), performed by Gidden and Bowers[38], indicate that only one family of conformers is present for each of the dNMP. The gas-phase conformations of the deprotonated dNMP deduced from the mobility measurements are in the *anti* orientation, except for the deprotonated 2'-deoxy-5'-monophosphateguanosine (dGMP) which is *syn*. For protonated dNMP the orientation is *syn* except for dGMP which is *anti*[38]. To our knowledge, similar results are not available for (deoxy)nucleosides.

McCloskey *et al*. [26, 27, 28, 29] have studied nucleosides fragmentation using electron impact and chemical ionization mass spectrometry. Their study of purine nucleosides focused on adenosine and adenosine analogs since guanosine was not directly vaporizable due to its high polarity and low volatility[26]. For both ionization techniques one of the most abundant fragment species of nucleosides was found to correspond to the base fragment [b] plus two hydrogens [bH_2]. However, the fragment ions from chemical and electron impact ionizations are formed by different mechanisms. The main ion population of bH_2 resulting from electron impact ionization arises from double hydrogen transfer from labile hydrogens of the sugar[26], whereas in the chemical ionization of nucleosides, the bH_2 fragments arise preferentially by initial base protonation followed by transfer of hydrogen from one of the hydroxyl groups, most likely located in C2', with cleavage of the glycosidic bond[27, 28, 29]. For the 2'-deoxyguanosine investigated here, electrospray ionization is used and the only hydroxyl hydrogen atoms available for hydrogen transfer are located in O5' and O3' (see Fig. 4.1.1).

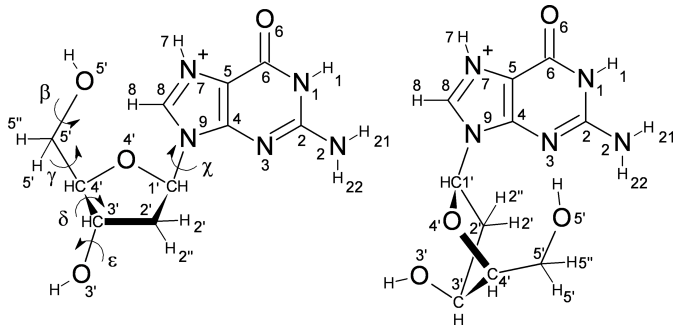

Fig. 4.1.1. Atom numbering of the 2'-deoxyguanosine protonated in N_7. Illustration of the five principal torsion angles. Among the torsion angles, χ=∠O4'-C1'-N9-C4 defines the orientation of the nucleobase with respect to the 2'-deoxyribose, γ=∠O5'-C5'-C4'-C3' characterizes the orientation of the O5' atom with respect to the 2'-deoxyribose ring. The molecule on the left is in the *anti* conformation whereas on the right it is *syn*.

However, collision induced fragmentation following electrospray ionization also yields, exclusively, a bH_2 fragment at m/z equal to 152 (see Fig. 4.1.2).

Experimentally, isotopic labelling of exchangeable or skeleton atoms (on carbon atoms) plays a key role in the interpretation of mass spectra. In the present study partial and complete labelling of the labile hydrogen atoms as well as incorporation of deuterium atoms in the 2'-deoxyguanosine skeleton upon synthesis are used to identify the hydrogen transferred upon fragmentation from the 2'-deoxyribose to the protonated guanine fragment. Two different notations are used for deuterium atoms: ^2H for the skeleton atoms labelled using deuterium and D for the hydrogen atoms exchanged in solution or in the gas phase.

Any hydrogen residing on a heteroatom, such as exposed amino, imino, hydroxyl groups, is considered to be exchangeable[39]. Besides local inductive effects caused by adjacent atoms, the intrinsic rate of exchange for a particular proton depends on several factors, including the degree of solvent exposure, temperature, pH, and the concentration of exchange catalyst[6]. Several exchange mechanisms can account for H/D exchange in solution. From the extensive study of the H/D exchange for glycine oligomers, five mechanisms have been proposed for the H/D exchange with reagent bases: the onium ion, relay, saltbridge, flip-flop, and tautomer mechanisms[6]. Deuterium oxide with its proton affinity of about 166 kcal mol^{-1} [40, 41] is the least basic of the commonly used exchange reagents. In gas phase, it is likely that the H/D exchange predominantly occurs via formation of a hydrogen bonded species for compounds whose proton affinities differ from deuterating species by less than 20 kcal/mol whereas compounds whose proton affinity differ by significantly more than 20 kcal/mol would use a relay mechanism to facilitate exchange[6, 40].

Green-Church *et al.* extensively studied the gas-phase exchange behaviour of protonated 5'- and 3'-mononucleotides with D_2O, D_2S, and ND_3 to elucidate the gas-phase structural features of these molecules and to determine the effect of reagent gas basicity on the H/D exchange profiles. They reported that except for 2'-deoxyguanosine-3'-monophosphate, the 3'- or 5'-hydroxyl sites all have proton affinities less than 190 kcal/mol at the AM1 restricted Hartree-Fock level of theory. Consequently, they suggested that although the rate of exchange represented most likely the sum of individual rate constants for exchange at several different labile hydrogens, the sugar hydroxyl hydrogens should be among the first to exchange or back-exchange. Intramolecular hydrogen bonding was also pointed out to explain the incompletely exchanged nucleotides[39, 41].

In addition to the tracer use of deuterium for the hydrogen transfer, the significant kinetic isotope effects taking place provide means to study the hydrogens involved either directly or via a concerted mechanism in the fragmentation.

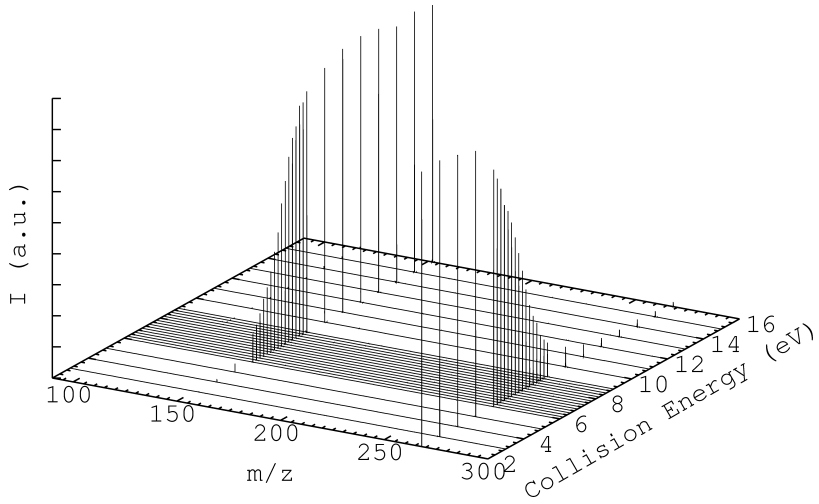

Fig. 4.1.2. Collision Induced Fragmentation of the most abundant isotopic form of the protonated 2'-deoxyguanosine (m/z=268). The only fragment signal corresponds to the protonated guanine (bH2 at m/z=152); the sugar fragment is not detected. No parasite fragmentation is observed. The collision energy is given in the laboratory frame.

In short, the study reported here aims at: (1) giving experimental evidence of the origin of the hydrogen transferred from the deoxyribose to the nucleobase using H/D exchange and deuterium labelling, (2) discussing which hydrogen atoms are involved in the fragmentation based on the kinetic isotope effect (3) proposing a fragmentation mechanism for the protonated 2'-deoxyguanosine in gas phase, (4) demonstrating the feasibility of modulated in-source Deuterium/Hydrogen back-exchange using a conventional nano-electrospray source.

4.1.1. Experimental

If the exchange of the labile hydrogen atoms of the 2'-deoxyguanosine in D_2O is experimentally simple, the principal experimental difficulty arises from partial reexchange of deuterium atoms by collision with atmospheric water molecules in the ion source after sample vaporization[26]. In the present study the hydrogen atoms are exchanged in solution with D_2O and use is made of back-exchange in the gas-phase (by collision with atmospheric water in the high pressure region of the ion-source) to modulate the number of labile deuterium substituted and study the origin of the hydrogen transferred.

The back-exchange is performed by collisions with atmospheric H_2O in our open nano-electrospray source with the H_2O partial pressure unknown. To control or prevent the back-exchange prior to ion entrance in the low pressure region of the instrument, the H_2O partial pressure is modulated by means of a controlled saturation in nitrogen of the source. For the back-exchange experiments, all ions were allowed to react for the same duration with the atmospheric water. The charge is a proton or a deuteron depending on the solvent nebulized, H_2O or D_2O respectively. Once in the

instrument and under vacuum conditions, the protonated 2'-deoxyguanosine ions were mass selected by a quadrupole and then fragmented by collisions with argon.

Back-exchange essentially provides the same information as direct-exchange in gas phase. It is however far easier to implement. The number of labile hydrogens back-exchanged is determined from a comparison of ESI spectra obtained from D_2O solutions with a source saturated or not in N_2. CID spectra were obtained for parent $[M+H]^+$ ions and the exchanged analogs $[M(D_x) +D]^+$. Composition of product ions was determined and mechanisms of decomposition elucidated by comparison of the CID mass spectra of the undeuterated and deuterated species. The hydrogen transfer from the deoxyribose to the nucleobase was studied by monitoring the mass of the sole charged fragment, the protonated guanine, for parent molecules with different numbers of hydrogens substituted by deuterium atoms.

The analytes were prepared by dissolving each mononucleoside to a concentration of 10 µM either in a 100% H_2O or a 100% D_2O solution. The non-deuterated 2'-deoxyguanosine was obtained from Sigma-Aldrich and used without further purification. Partial or total replacement of the seven exchangeable hydrogen atoms of the neutral 2'-deoxyguanosine by deuterium atoms was done by dissolving the non-deuterated 2'-deoxyguanosine in pure D_2O. The extended exchange was performed by annealing the molecule in pure D_2O at a temperature of 95°C and letting the solution stand for several weeks to ensure the replacement of the H8 hydrogen atom. The molecules with deuterium on carbon atoms, [1'-^{2}H]2'-deoxyguanosine, [2',2''-$^2H_2$]2'-deoxyguanosine (Deuterium enrichment 97 atom-% for 2'-H and 89% for 2"-H as

determined by ^{1}HNMR) and [5',5''-$^{2}H_2$]2'-deoxyguanosine, were purchased from Omicron Biochemicals Inc. (South Bend, IN, USA).

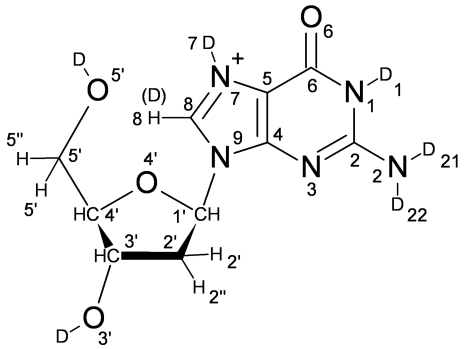

Fig. 4.1.3. Sites of deuteration by exchange of the protonated labile hydrogens. The exchange of H8 is also known to occur upon heating, prolongated exchange or at basic pH.

In the present work a distinction is made between exchange(-able) and transfer(-able) atoms. The exchangeable atoms are those that can be replaced by deuterium/hydrogen upon collisions with water. The transferable atoms are those which can be ceded to the nucleobase upon fragmentation. For all gas phase experiments done on partially or totally exchanged 2'-deoxyguanosine electronebulized from D_2O the protonation is effected by a deuteron.

Collision-induced dissociation (CID), commonly used in tandem mass spectrometry to extract information on the primary structure of molecules emitted in gas phase, was used to promote fragmentation.

The instrument used in the present study is a hybrid Q-TOF Ultima Global™ mass spectrometer (Micromass Ltd., UK) with an open atmospheric pressure nanospray source.

4.1.2. Results

As discussed in the introduction, the chemical incorporation of deuterium followed by mass spectrometry plays a major role in the structural characterization of molecules, in gaining information on the mechanisms of chemical or enzymatic reactions and the interpretation of mass spectra. Gas-phase hydrogen/deuterium exchange, on the other hand, can be used to determine the number of labile hydrogens, distinguish between isomers of a molecule, deduce structural features of the molecule, and infer thermochemical properties such as proton affinities[39, 6, 41, 42]. The aim of the collision induced dissociation of protonated 2'-deoxyguanosine parent ions with hydrogens replaced by deuterium atoms is to determine experimentally the origin of the hydrogen atom transferred from the 2'-deoxyribose to the protonated guanine upon fragmentation.

4.1.2.1. Unlabelled 2'-deoxyguanosine

The fragment signal shown in Fig. 4.1.2 and 4.1.6a corresponds to the neutral guanine augmented by a single proton. As in chemical ionization[29], a rearrangement between the sugar and the nucleobase takes place. This rearrangement involves the transfer of a hydrogen atom from the sugar to the protonated guanine. Indeed, from the mass spectrometer characteristics – argon being used as collision gas and no hydrogen being transferred between molecules once the ions have been mass selected by the quadrupole – the only possible origin of this hydrogen is the sugar. On the basis of mass spectra, it is not possible to assess if the N-glycosidic bond breaking occurs before, simultaneously with, or after the hydrogen transfer. Assuming that no undetected fragmentation of the sugar occurs, collision induced fragmentation of the

protonated 2'-deoxyguanosine yields two closed shell fragments: the protonated guanine and the neutral dehydrogenated deoxyribose.

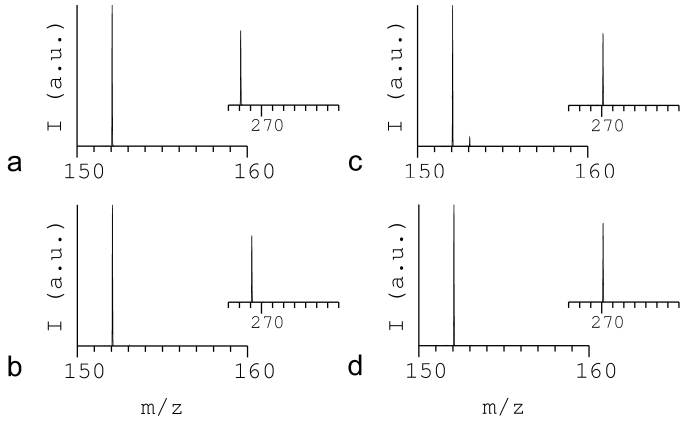

Fig. 4.1.4 Collisional Induced Fragmentation of the most abundant isotopic form of the protonated 2'-deoxyguanosine (spectrum a, 268m/z), of protonated [1'-^{2}H]2'-deoxyguanosine (spectrum b, 269m/z), of protonated [2',2''-$^{2}H_2$]2'-deoxyguanosine (spectrum c, 270m/z), and of protonated [5',5''-$^{2}H_2$]2'-deoxyguanosine (spectrum d, 270m/z). The observed fragment signals correspond to the protonated guanine (bH2 at 152 m/z).

4.1.2.2. [1'-^{2}H]2'-, [2',2''-$^{2}H_2$]2'-, and [5',5''-$^{2}H_2$]2'-deoxyguanosine

Fragmentation of [1'-^{2}H]2'-, [2',2''-$^{2}H_2$]2'-, and [5',5''-$^{2}H_2$]2'-deoxyguanosine yield the same fragment as the unlabelled dG as can be seen on Fig. 4.1.4. Apparently, the labelled deuterium atoms (^{2}H), incorporated at carbon sites upon synthesis, are not directly involved in the fragmentation since only the protonated nucleobase without deuterium atoms is observed.

4.1.2.3. 2'-deoxyguanosine with partial or total exchange of the labile hydrogen atoms

Control of the back-exchange extent was achieved by varying the source saturation in nitrogen (partial pressure unknown) as shown in Fig. 4.1.5. For a given incorporation

level of deuterium, the back-exchange in gas phase of the deuterium exchanged in solution increases as the volume rate of nitrogen leaked into the source is reduced. Spectra 4.1.5-a to 4.1.5-d were obtained following a two hours exchange in solution (spectrum a further required annealing in D_2O at a temperature ~90°C prior to the two hours exchange). Spectra 4.1.5-a' to 4.1.5-d' are the result of annealing in D_2O at a temperature ~90°C followed by weeks of exchange in D_2O at room temperature. The maximum number of deuterium atoms incorporated is 7 (spectrum 4.1.5-a') which corresponds to the replacement of all the exchangeable hydrogens, H1, H21, H22, H on O3', H on O5', H7 (the "protonation" site) and H8 (see Fig. 4.1.3). In solution, the slowest exchange most likely involves the hydrogen in H8 as will be further discussed in the next section. From the comparison of mass shift for the pairs of spectra (4.1.5-a, 4.1.5-d) and (4.1.5-a', 4.1.5-d') it is found that from the 6 and 7 hydrogens respectively exchanged on short and long time scales only 3 are back-exchanged by collisions with H_2O in the gas phase.

Experimental conditions reducing the amount of ^{13}C in the isotopic signal singled out were used for the CID measurements (see Fig. 4.1.6). Spectrum 4.1.5-b for example illustrates experimental conditions for a negligible ^{13}C contribution of the labelled ion at m/z 272 to the m/z 273 ion signal which corresponds to one more deuterium exchanged.

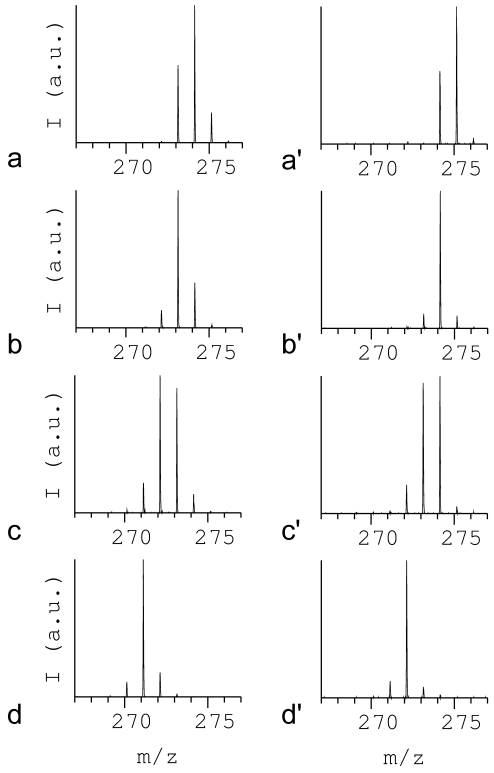

Fig. 4.1.5. Partial back-exchange in the gas phase of 2'-deoxyguanosine deuterated in solution. Ion abundances observed for the same back exchange reaction times from the reaction of protonated 2'-deoxyguanosine at different controlled levels of saturation of the instrument source in N_2. The N_2 partial pressure is decreased from a to d, and from a' to d', respectively. The right column corresponds to extended exchange in solution.

Collision induced dissociation of partially and fully exchanged 2'-deoxyguanosine is reported in Fig. 4.1.6. Spectra 4.1.6-a and 4.1.6-a' show that fragmentation of dG with respectively 6 and 7 exchangeable hydrogens substituted yields the protonated guanine with 5 and 6 deuterium atoms. The presence of seven deuterium on the parent ion implies that all exchangeable hydrogens were replaced by deuterium. Six deuterium atoms on the protonated guanine fragment imply H1, H21, H22, H7 (the "protonation" site), H8 and the hydrogen transferred from the sugar unit are exchanged in solution.

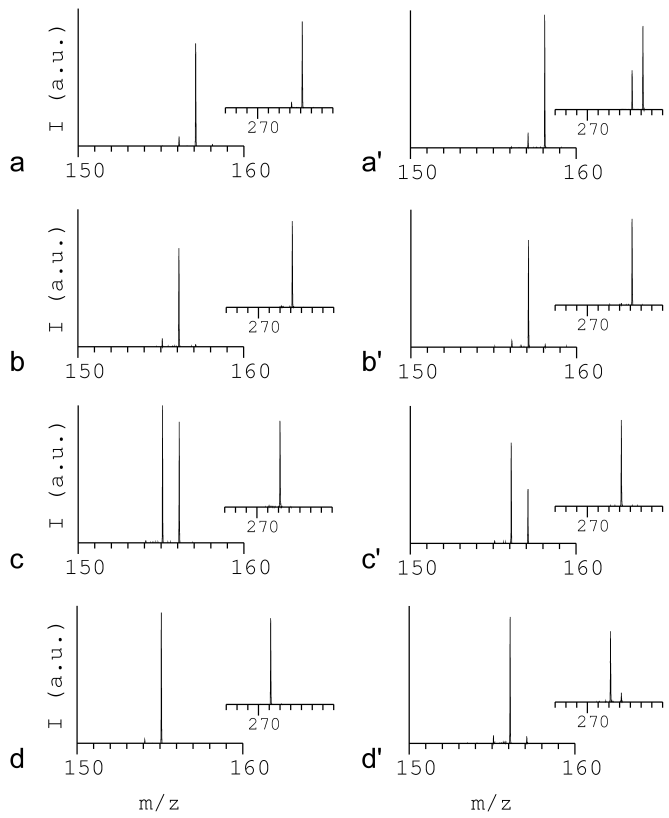

Fig. 4.1.6. Collision induced dissociation spectra of 2'-deoxyguanosine with partial or total exchange of the labile hydrogen atoms. a-a') 6 -7 labile hydrogen atoms exchanged. [274-275 Da parent gives 157-158 Da fragment] b-b') 5-6 labile hydrogen atoms exchanged. [273-274 Da parent gives 156-157 Da fragment] c-c') 4-5 labile hydrogen atoms exchanged. [272-273 Da parent gives 155-156 Da and 156-157 Da fragments] d-d') 3-4 labile hydrogen atoms exchanged. [271-272 Da parent gives a 155-156 Da fragment]. The MSMS spectra correspond to the isolation and fragmentation of one peak the MS spectra of Fig. 4.1.5.

The spectra 4.1.6-c and 4.1.6-c' are most interesting since no ^{13}C contribution can be accounted for in order to explain the isotopic pattern of the fragments. As can be inferred from the fragment isotopic patterns the deuterium involved can end up either on the protonated guanine or on the neutral 2'-deoxyribose fragments. This implies either scrambling or a competition between two sites with comparable back-exchange rates. This will be further discussed in the next section. Since the protonated guanine fragment has a mass to charge ratio of 155 and 156 m/z respectively compared to 152

m/z for the non-deuterated fragment, spectra 4.1.6-d and 4.1.6-d' show, respectively, that the 3 and 4 deuterium atoms exchanged in solution and that are not back-exchanged in the gas phase are already or end up being on the guanine. Finally, at least one of the three most labile deuterium atoms back-exchanged by collision with H_2O has to be one of the hydroxyls on the 2'-deoxyribose since the mass of the protonated guanine fragment only decreases by two units between 4.1.6-a and 4.1.6-d or between 4.1.6-a' and 4.1.6-d' while the mass of the parent ion decreases by three units.

4.1.3. Discussion

In solution, (2'-deoxy)guanosine is known to hydrolyze through fast initial protonation followed by a hydrolysis rate limiting process of cleavage of the N-glycosidic bond[43, 44]. The available theoretical and experimental data show that the protonation of 2'-deoxyguanosine in the keto-N9R form preferentially occurs at the acceptor site N7 of the nucleobase[41, 45, 46, 47]. It is also known that upon fragmentation a hydrogen atom is transferred to the nucleobase unit, the guanine. For molecules in solution this hydrogen can originate from water molecules. However, for nucleosides isolated in gas phase the only source of this hydrogen is the ribose.

2'-deoxyguanosine differs from guanosine by the absence of a hydroxyl group in C-2' of the ribose, even though it yields the same charged fragment, the protonated guanine, as shown in Fig. 4.1.4. The mass of the dominant isotope of the non-deuterated 2'-deoxyguanosine is 267 amu. Upon protonation the mass increases to 268 amu. Fragmentation yields, as charged fragment, the protonated guanine of mass 152 amu. All the deuterated 2'-deoxyguanosine ions studied in the present work yield the same charged fragment with a varying number of hydrogen atoms substituted by

deuterium atoms and thus different masses. The interference of ^{13}C in the collision induced fragmentation signal of all the different isotopes studied can be neglected since care has been taken to isolate isotopes with a negligible lower mass neighbour. In other words, the difference of mass between two isotopes is the consequence of a different number of deuterium atoms almost exclusively.

4.1.3.1. Labelled 2'-deoxyguanosine

The most stable tautomer of the protonated guanine fragment is known to have hydrogens in N7 and N9, not N3 [48]. However N9 is also known to be the least basic site of 2'-deoxyguanosine[49]. Consequently transfer of the hydrogen atom located in C-1' was considered. The collision induced dissociation of the [1'-^{2}H]2'-deoxyguanosine (see Fig. 4.1.4b) shows that the deuterium in C-1' is not transferred since the mass of the protonated guanine fragment is the same for both the deuterated and non deuterated precursors (see Fig. 4.1.4). However, it is interesting to note that the replacement of the hydrogen atom in C-1' by a deuterium atom influences not only the spectroscopic properties of the 2'-deoxyguanosine[23] but also its fragmentation threshold as can be seen from the survival yield curves in Fig. 4.1.7.

The collision induced dissociation of [2',2''-$^{2}H_2$]2'-deoxyguanosine and of [5',5''-$^{2}H_2$]2'-deoxyguanosine shows that the deuterium atoms in C-2' and C-5' are not transferred since the mass of the protonated guanine fragment is the same for both the deuterated and non deuterated precursors (see Fig. 4.1.4). However, noticeable kinetic isotope effect is observed for the [2',2''-$^{2}H_2$]2'-deoxyguanosine whereas none is observed for the [5',5''-$^{2}H_2$]2'-deoxyguanosine. This suggests the involvement of the hydrogen atoms in C-2' in a concerted fragmentation/transfer mechanism.

4.1.3.2. 2'-deoxyguanosine with partial or total exchange of the labile hydrogen atoms

When no annealing is done, only 5 (spectrum 4.1.6-b) of the 6 labile hydrogen atoms typically exchangeable by D_2O in solution are replaced by deuterium atoms. Upon annealing one more exchange takes place and traces of a seventh deuterium can be found (spectra 4.1.6-a). Substitution at the C8 position is most likely the last exchange to take place in solution. Reaction at the C8 position in a D_2O solution, involves the abstraction from the neutral or N7-protonated deoxyguanosine of the hydrogen in C8 by OH^- giving rise to an ylide type intermediate, which then is "reprotonated" at C8. In the case of guanosine, the protonation of the N7 could also occur due to the formation of a zwitterion[50, 51, 52]. Numerous pH-dependent kinetic studies of exchange processes have been performed[52, 53]. The reaction is usually carried out in a slightly alkaline (pH = 7.8) solution[53] or by incubation of guanosine triphosphate and guanosine monophosphate in neutral ^2H_2O at 50°C for 24 hours[54]. In the present work, however, nucleosides, not nucleotides, are considered. Complete exchange of the 7 exchangeable hydrogen atoms was achieved by annealing in D_2O at a temperature ~90°C followed by weeks of exchange in D_2O at room temperature.

The hydroxyls of the 2'-deoxyribose are assumed to be very labile and easily replaced in the gas phase by collisions with H_2O molecules with the possible exception of O5' which can be involved in a hydrogen bond when 2'-deoxyguanosine is in the *syn* form[45]. From spectrum 4.1.6-a' it is found that upon replacing the 7 exchangeable hydrogens by deuterium atoms, 6 end up on the protonated guanine fragment. Furthermore, one of the deuterium atoms that can be back-exchanged in the gas phase does not lead to a mass increase of the protonated guanine fragment. This can be seen from the mass difference between the fragments of spectra 4.1.6-a and 4.1.6-d, or

4.1.6-a’ and 4.1.6-d’ (see Fig. 4.1.6) since the mass of the parent ion decreases by one more unit than the fragment ion. Consequently one of the hydroxyls of the 2’-deoxyribose transfers its deuterium to the guanine whereas the other one does not. Since geometrically the H on O3’ does not easily interact with the nucleobase, the hydrogen transferred is very likely to come from O5’.

From spectra 4.1.6-d and 4.1.6-d’ and the mass of the fragment, the 3 and 4 deuterium atoms respectively exchanged in solution that do not back-exchange in gas phase are found to be or end up being on the guanine. The deuterium in O5’ could be among those since it is transferred and would consequently end up on the protonated guanine; however, this would require the *syn* conformation to be dominant in gas phase and the involvement of the deuterium in O5’ in hydrogen bond strong enough to prevent back-exchange.

The two mass to charge ratios observed for the fragment signal in spectra 6-c and 6-c’ are only observed for a given H_2O partial pressure. We suggest a competition between the back-exchange of the hydroxyl in O3’ and either the hydroxyl in O5’ or an exchangeable deuterium on the guanine since the competition must involve two sites, one leading to a guanine fragment higher in mass by one unit than the other one. Exchange of hydrogen or deuterium between H5’ and H22 cannot be held responsible for the observed isotopic patterns since the atom in O5’ would nonetheless be transferred to the guanine. Based on the proton affinities calculated by Green-Church *et al.*[29] the competition most likely occurs between O5’ and O3’.

4.1.3.3. Kinetic Isotope Effect (KIE)

A kinetic isotope effect [55] is observed for the 2’-deoxyguanosine upon the substitution of some of its hydrogen atoms by deuterium, as can be observed for the

shifted survival yield curves in Fig. 4.1.7. The KIE is expected to be measurable only for deuterium atoms directly involved in the hydrogen transfer process or in the close vicinity of the bonds formed or broken. It is related to the ZPE shift, to the kinetic shift related to the densities of vibrational states and caused by the limited time-window of the mass spectrometer, as well as to the different tunnelling probabilities for hydrogen and deuterium. A kinetic shift is typically assessed based on the ratio of the rate constants of the light (H) and heavy (D, ^{2}H) species at the same excitation energy E in the reactant. Using the quotient of RRKM rate constant, one gets

$$\frac{k_H(E)}{k_D(E)} \propto \frac{G_H^*\left(E-E_{0(H)}\right)N_D(E)}{G_D^*\left(E-E_{0(D)}\right)N_H(E)}$$

The sum of vibrational states functions, G*(y), for the transition states does not include the reaction coordinate but is nevertheless affected by the deuteration via the other vibration modes; hence, at the same energy, one has $G_D^*(y) > G_H^*(y)$ because most of the isotopically substituted vibrational modes have lower frequencies. Deuteration also reduces the zero point energy of the reactant molecule – probably much less so that of the transition state if the deuteration occurs for one of the atoms involved in the reaction coordinate – and therefore affects the critical energy, $E_{0(D)} \gtrsim E_{O(H)}$, which tends to reverse the inequality of the G*(y) functions, so that overall, $\frac{G_H^*\left(E-E_{0(H)}\right)}{G_D^*\left(E-E_{0(D)}\right)} \gtrsim 1$. But because the $\frac{G_H^*\left(E-E_{0(H)}\right)}{G_D^*\left(E-E_{0(D)}\right)}$ is evaluated at a lower energy than $\frac{N_D(E)}{N_H(E)}$, the latter ratio is more important. Since $\nu_D < \nu_H$, one gets $\frac{N_D(E)}{N_H(E)} > 1$ and the overall result is then that $\frac{k_H(E)}{k_D(E)} > 1$. The decomposition of the deuterated reactant with a smaller rate constant, when the rates are compared at the same excitation energy in the reactant, is called normal KIE [56]. Figure 4.1.7

illustrates the influence of deuteration on the fragmentation threshold of several of the species studied. Under identical experimental conditions, the survival yield curves are shifted to the higher collision energies for 2-deoxyguanosine deuterated in C1' or in C2',2" (normal KIE); deuteration in C5' has no significant effect. A normal KIE is also observed for the most extensively exchanged – 5 and 6 exchangeable hydrogen replaced by deuterium – 2'-deoxyguanosine ions.

Toyama *et al.*[23] reported for guanosine, using Ultraviolet resonance Raman spectroscopy, that upon deuteration in C1' most of the in-plane vibrations of the guanine rings in the 1420-1100 cm^{-1} were upshifted, while those in the 1100-700 cm^{-1} region were downshifted. The frequency shifts associated with the C(1') deuteration have been explained by assuming couplings of the guanine vibrations with a ribose C(1')-H bending mode, which involves a hydrogen motion in the plane of N(9)-C(1')-H [5]. Furthermore the N(9)-C1' stretching mode showed the largest (+60 cm^{-1}) shift upon C(1') deuteration[5]. Although these observations alone are not sufficient to explain the KIE observed for [1'-^{2}H] 2'-deoxyguanosine, they concur with the observed influence of C(1')-^{2}H on fragmentation.

A similar effect of C2'-deuteration on the in-plane vibrations of thymine has been reported by Tsuboi *et al.*[57]. No results are however available, to our knowledge, for [2',2''-$^{2}H_2$]2'-deoxyguanosine which precludes the assessment of C2'-deuteration of 2'-deoxyguanosine normal modes. However, since the hydrogen atoms in C2' are remote from O5' and from the glycosidic bond, a weaker kinetic isotope effect than the one observed might have been expected. This suggests a fragmentation mechanism involving at least one of the two hydrogens in C2'. The following

mechanism is proposed to explain the strong KIE observed upon deuteration in C2'. The cleavage of the N-glycosidic bond and the transfer of the hydrogen in O5' would yield a highly unstable bi-radical species with a carbonyl and a radical oxygen. The bi-radical would then rearrange by transferring one of the two hydrogens in C2' to O5'. This mechanism involves a highly endothermic fragmentation followed by an exothermic intramolecular rearrangement. It has been reported by Hine[58, 59] that stepwise bond makings and breakings in a reaction involving highly unstable reaction intermediate may be avoided by combining such bond changes into a concerted step. The fragmentation could thus occur in only one step with the C2'-deuteration responsible for a primary KIE explaining the rate determining role of H-2'.

The absence of effect for the [5',5''-$^{2}H_2$]2'-deoxyguanosine suggest that the hydrogen atoms in C-5' are not involved in the hydrogen transfer mechanism or at least not in a rate determining step.

For the species emitted from D_2O, only the species with the higher number of deuterium atoms replacing labile hydrogen (respectively 5 and 6 hydrogen exchanged) present an increase of the fragmentation threshold. These two species are believed to correspond to exchanged hydroxyl groups. The involvement of the hydroxyl in hydrogen bonds, their impact on the other vibrations is indeed likely to affect the fragmentation.

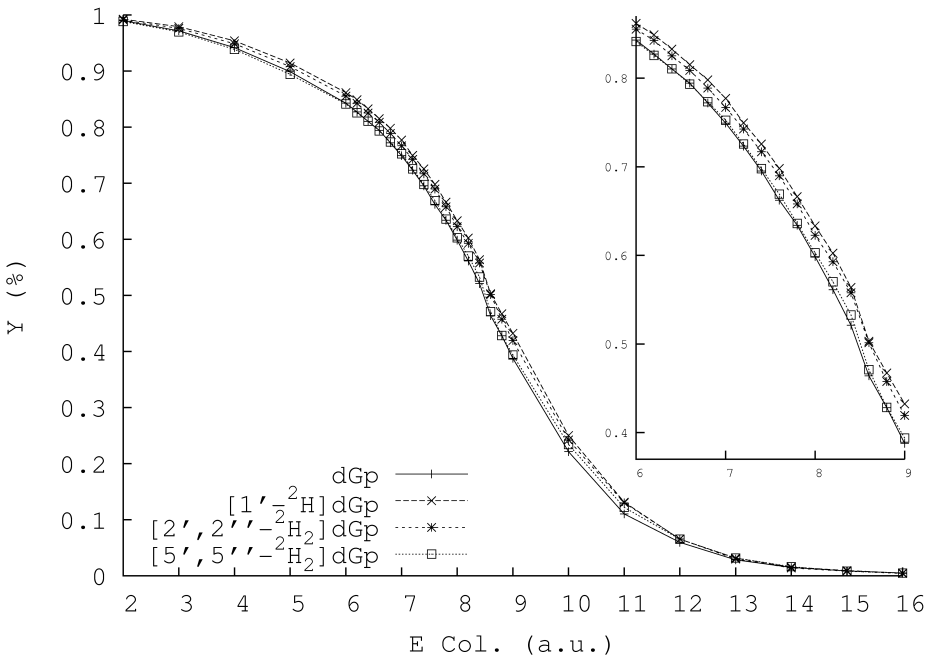

Fig. 4.1.7.: Survival yield (Y) curves of unlabelled and labelled protonated 2'-deoxyguanosine. The collision energy units correspond to energy in the laboratory frame, however, no calibration of the collision energy scale was made.

Finally, although it is likely that several conformations are populated in the gas phase as supported by the dependence of the conformational inhomogeneity of 2'-deoxynucleoside crystals and solutions on *e.g.* the temperature, the nature of the solvent and a possible residual influence of the solution or electronebulization conditions on the protonated 2'-deoxyguanosine gas phase conformations, the hydrogen transfer most likely proceeds from a *syn* conformer since it is the only conformation that allows to transfer a hydroxyl hydrogen from the sugar to an acceptor site on the nucleobase.

4.1.4. Conclusion

Few results were so far available in the literature on the protonated 2'-deoxyguanosine. The present systematic study of the protonated 2'-deoxyguanosine aimed at giving experimental evidence of the origin of the hydrogen transferred from

the 2'-deoxyribose to the nucleobase using H/D exchange and chemical incorporation of deuterium and proposing a mechanism to explain the fragmentation of the protonated 2'-deoxyguanosine. The number of hydrogens replaced by deuterium atoms is shown to be tunable. The present results however do not allow determining the exact location of the exchanged labile hydrogens on the nucleobase.

Based on the mass of the nucleobase fragment, the hydrogen transferred from the 2'-deoxyribose to the nucleobase originates from O5'. The significant isotope effects observed for deuteration in C1' and C2' suggest the involvement of the hydrogen atoms on these two carbons in the fragmentation process. The normal KIE of C1'-deuteration is easily explained by its close vicinity to the glycosidic bond and its impact on the normal modes of vibration whereas the intense normal KIE observed for the hydrogen atoms in C2' supports a fragmentation mechanism with a rearrangement step involving one of these. The fragmentation mechanism proposed for protonated 2'-deoxyguanosine in the gas phase involves the cleavage of the N-glycosidic bond followed by the concerted transfer of the hydrogen in O5' to the nucleobase and of one of the hydrogen atoms in C2' to O5'. It is suggested that the fragmentation proceeds from the *syn* conformation with N3 as acceptor site since for the hydrogen transferred it is the only conformation that allows the direct transfer from O5' to the nucleobase.

The *syn* conformer intermediate of reaction is further supported by the theoretical calculations performed. The conformational space of the 2'-deoxyguanosine protonated in N7 (the most likely protonation site based on the published results currently available) has been explored at the B3LYP/6-31+G(d,p) level. The total energies, including zero point energy (ZPE) corrections, of all model complexes have

been compared, and it was found that *anti* conformers were the most stable by ~5 kcal/mol. The lowest energy transition state related to the fragmentation found – it corresponds to the transfer of the hydrogen atom located in O5' to the N3 nitrogen atom for a C1'-N9 distance of 3.44 Å – corresponds to a *syn* conformation and is ~25 kcal/mol higher in energy than the lowest ground-state *anti* conformer. These theoretical results are not reported in the present work; they will be complemented by further exploration of the phase space and intrinsic reaction channel (IRC) determination.

4.2. Gas phase formation of fullerene hydrides by reaction of C_{60} anions with methanol at room temperature

Hydrogen, easily generated from renewable energy sources, has great potential as a fuel. Its storage however involves pressures of hundreds of atmospheres in the gas state and cryogenic temperatures in the liquid state, limiting its use in hydrogen fuel cells (HFCs). In most near-term applications, hydrogen has been supplanted by hydrocarbons and alcohols. The current methane and direct-methane fuel cells either include a reformer that converts hydrocarbon fuel into hydrogen or involve temperatures of several hundred Celsius degrees. Direct methanol fuel cells (DMFCs) use polymers as electrolytes, and suffer from methanol permeating the membrane. In order to increase the use of HFCs and DMFCs in portable and embedded systems, further improvements of the hydrogen storage materials and proton-conducting membranes are required. Fullerenes and functionalized fullerenes have respectively been investigated as potential hydrogen storage material and, dispersed within membranes, as reducers of methanol permeation. The present section reports on $C_{60}^{\bullet -}$ reaction with methanol, on the formation of C_{60} hydride anions and on their

reversible dehydrogenation using CO_2 laser irradiation in the gas phase, at room temperature, and pressures in the microbar range. It supports an enhancement effect of fullerene anions within DMFC membranes and suggests that the release of hydrogen from fullerenes and related materials such as carbon fullerenes, nanotubes, peapods,… could be efficiently performed using CO_2 laser irradiation. Finally, it provides evidence that contaminants added to $C_{60}^{\bullet -}$ upon methanol reduction can be efficiently removed using CO_2 laser irradiation contributing to achieve and help maintain high performance DMFCs and HFCs. Both the hydrogen storage capabilities of fullerene hydrides [60, 61] and the enhancing proton conductivity ability of polyhydroxylated fullerenes [62, 63] have been patented for use in hydrogen storage materials and proton conducting membranes.

The present investigation focuses on $C_{60}^{\bullet -}$ hydrogenation under mild conditions. Most of the synthetic approaches described in the literature to produce fullerene hydrides, $C_{60}H_x$ ($2 \leq x < 60$), involve extreme conditions with temperatures of several hundreds Kelvin, pressures on the order of several mega Pascal, or condensed phase condition [1]. These synthetic approaches include the Birch reduction (443-543 K, $x \leq 36$, in the presence of t-BuOH) [64, 65, 66] (195 K, in liquid NH_3-tetrahydrofuran, in the presence of t-BuOH) [67] (240 K, in liquid ammonia) [68], the Benkeser reduction (363 K, $36 \leq x \leq 44$) [69], polyamine reduction (at boiling temperature, x=18) [70] (at boiling temperature with Co catalyst, $x \leq 34$) [71], reduction by anhydrous hydrazine (in benzene in presence of methanol, $x \leq 8$) [72], reduction by diimides (at room temperature, in benzene, $x \leq 4$) [73], hydroboration (in toluene, x=2) [74] (273-293 K, in toluene in presence of tetrahydrofuran, $x \leq 4$) [75], hydrogen transfer reduction (by 9,10-Dihydroanthracene, 623 K, $x \leq 36$) [76, 68] (by 9,10-Dihydroanthracene, 523 K

with [7H]benzanthrene added as catalyst, x≤44) [77, 66], photoreduction (by 10-methyl-9,10-dihydroacridine, at room temperature, x=2) [78], transition metal catalyzed hydrogenation (at room temperature, 0.1 MPa H_2, x=2) [79] (573-673 K, 5-10 MPa H_2, x≤36) [80] (423-523 K, in toluene while bubbling H_2) [60], Zinc – concentrated hydrochloric acid reduction (at reflux temperature, in benzene or toluene, x≤8) [81] (at room temperature with light exclusion, in benzene or toluene, x≤40) [82, 83], Zn(Cu) reduction (323 K, in toluene in presence of water, x≤6) [84, 85, 86], hydrozirconation (at room temperature, in benzene, x≤6) [87], hydrogen radical induced hydrogenation (using iodoethane as hydrogen radical promoter, 673K, 6.9 MPa H_2 (cold), x≤36) [88], electrochemical reduction [89, 90, 91], sonication [92], direct reduction by hydrogen (573-623K, 50-85 MPa, x≤18) [93] (~960K, W filament at ~1900 K, ~3 kPa, x~18) [94] (673 K, 5-10 MPa H_2, x≤37) [80, 95], (using $LiAlH_4$ as hydrogen source, 723-823K, 2 GPa, 44≤x≤52) [96], and direct exposure to atomic hydrogen [97, 98].

Mass spectrometry (MS) combined with field desorption (FD) [69, 76, 99], desorption electron ionization (DEI) [82, 100], matrix-assisted laser desorption ionization (MALDI) [66, 101], atmospheric pressure photoionization (APPI) [102], and chemical ionization [103] has mostly been used to characterize the $C_{60}H_x$ produced by the synthetic approaches listed above. Fullerene hydride cations and anions undergoing no fragmentation within the observation time window of the mass analyzer used are expected to be indicative of their neutral precursors. Few results have, however, been reported up to now on the gas phase reactivity of C_{60} mono-charged ions. $C_{60}^{\bullet-}$ was reported to lack reactivity in the gas phase with H_2O, $(CH_3)_2CHOH$, CF_3CH_2OH, C_2H_5COOH, CF_3COOH [104] but its reactivity with

methanol has not been investigated. $C_{60}^{\bullet+}$ was also observed to be essentially unreactive with alcohols and esters such as CH_3OH, C_2H_5OH, CH_3OCH_3, $C_2H_5OC_2H_5$, c-C_4H_8O, n-C_3H_7OH, i-C_3H_7OH, and H_2O [105]. It undergoes, however, hydrogenation in the gas phase upon reaction with atomic hydrogen [106].

Fullerene hydride dehydrogenation, on the other hand, has been investigated using thermal activation [65, 67, 76, 82, 83, 107, 108], transition metal catalysts and photochemical catalytic dehydrogenation [109], and electrochemical oxidation [91]. Thermal decomposition of $C_{60}H_x$ ($x \leq 36$) into C_{60} with hydrogen release has been reported for temperatures ranging from 660 to 923 K [76, 82, 108, 61] with, for the higher hydrogen contents, some degradation into various hydrocarbon species (methane, ethane, benzene, etc.) [82, 80]. Electrochemical oxidation in solution has provided evidence of the electrochemical reversibility of C_{60} hydrogenation following cathodic reduction, and of $C_{60}H_x$ dehydrogenation upon anodic oxidation [91].

In short, the present work (summarized in Fig. 4.2.1) demonstrates the gas phase hydrogenation of $C_{60}^{\bullet-}$ by methanol at room temperature and low vapour pressures. C_{60} hydrides anions with up to eleven hydrogen atoms are identified via elemental composition analysis using Fourier transform ion-cyclotron resonance (FT-ICR) mass spectrometry. Dehydrogenation of the C_{60} hydride anions and reformation of $C_{60}^{\bullet-}$ have been achieved using infrared multiphoton activation with a low intensity continuous-wave CO_2 laser within the ion cyclotron resonance cell of FT-ICR mass spectrometer.

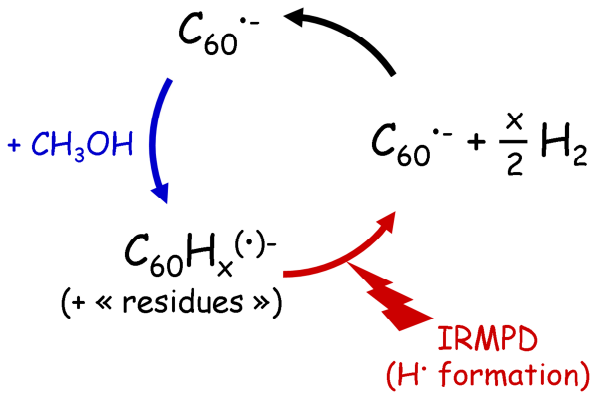

Fig. 4.2.1. Schematic representation of the results discussed in the present section.

4.2.1. Experimental

The [60]fullerene was purchased from MER Corporation at a purity of 99.9%. The HPLC grade toluene (+99% purity, water content < 0.01%) and acetonitrile (LC-MS grade, water content < 0.02%) were purchased from Biosolve (Valkenswaard, The Netherlands). The CH_3OH (99.9 % purity, spectrophotometric grade) was purchased from Sigma-Aldrich (St-Louis, The U.S.A.) and CD3OD (>99.96 % purity), CH3OD (>99% purity) and CD3OH (>99% purity) from Euriso-Top (Gif sur Yvette, France)..

The experiments were performed on a hybrid quadrupole-FT-ICR mass spectrometer, APEX-Qe 9.4T (Bruker Daltonics, Billerica, MA), equipped with a standard Appolo I electrospray source. A slightly rust colored solution of C_{60} in toluene:acetonitrile (4:1 or 3:2) was electrosprayed at a flow rate of 120 µL/h with the assistance of N_2 as nebulizing gas (250 °C). After a while the signal decreases due to C_{60} tendency to precipitate within the injection capillary. Pure acetonitrile can be used in these conditions to elute the C_{60} and obtain an over long periods of time stable signal. Even though no differences were detected between the different electronebulization conditions used, the electrospray conditions for a given set of experiments were kept constant in order to permit comparison. For all solution conditions used, the off axis

needle was grounded with the end-plate and inlet capillary respectively set to 3.54 kV and 4.1 kV.

A given bunch of ions formed in the source region of the mass spectrometer enter the mass selector quadrupole (see Fig. 4.2.2, region A) and either the full isotopic $C_{60}^{\bullet-}$ distribution is transferred, or the signal corresponding to $^{12}C_{60}^{\bullet-}$ only. For the selection of the ^{12}C signal, since the characteristics of the quadrupole used do not allow to select only one isotopic signal, the selected m/z was downshifted, with the upper m/z cutoff shifted between the first and second isotopic signals. The bunch of ions transmitted by the quadrupole used for mass selection is trapped within the reaction cell (see. Fig. 4.2.2, region B). The bunch of ions trapped within the reaction cell hexapole is allowed to react with room temperature methanol (CH_3OH) for variable periods of time ranging from 10 ms to 512s. Methanol vapor at 20°C continuously diffuses within the reaction cell via a nozzle valve. A pressure at the vacuum gauge adjacent to the reaction cell of 5.0 ± 0.1 nbar is maintained throughout the experiments, approximately corresponding to 1 µbar within the reaction cell. The bunch of ions is then ejected from the reaction cell and captured by static trapping in the ion cyclotron resonance (ICR) cell of the mass spectrometer (see Fig. 4.2.2, region C). Within the ICR cell, the fullerene hydrides can again be mass selected and/or undergo infrared multiphoton activation using the laser intensity delivered by a continuous wave Synrad 48-2 CO_2 laser (20-40 W/cm^2 at 10.6 µm) through a BaF_2 window for irradiation times of several hundreds of milliseconds. The overlap between the ions within the ICR cell and the IR beam is confirmed by the complete dissociation of the species stored. The current setup does not allow the fine tuning of the laser power nor its measure within the ICR cell, only the irradiation time being

practically tunable. The ions present in the ICR cell are then detected, prior to allowing a new bunch of ions within the reaction cell. A scheme of the experimental setup is provided in Fig. 4.2.2.

In FT-ICR mass spectrometry one should ideally use FT absorption-mode spectral peak areas to determine the relative numbers of different species [110]. In a frequency-domain spectrum obtained by discrete Fourier transformation (FFT) of the time-domain response following a delta-function excitation, the absorption-mode spectral peak relative areas are directly proportional to the time-domain relative initial amplitudes of the sinusoidal signals, which in turn are proportional to the numbers of oscillators at those frequencies [110]. However, it is not always possible to phase-correct a complex FT spectrum to obtain its pure absorption-mode component. This results into unavoidable auxiliary "wiggles" in each spectral peak [110]. In the present work, due to difficulties in integrating areas and also, for some of the spectra, to the existence of some overlap between peaks with different numbers of H, ^{12}C, and ^{13}C atoms, the peak intensities as defined in DataAnalysis 3.4 (Bruker) – not the peak areas – were used to determine the relative numbers of different species.

Mass spectra were internally calibrated, and elemental composition assignments were based on accurate mass measurements. The mass resolving power is typically very high ($100000 \leq m/\Delta m_{50\%} \leq 700000$) and mass accuracy is typically better than 1.0 ppm.

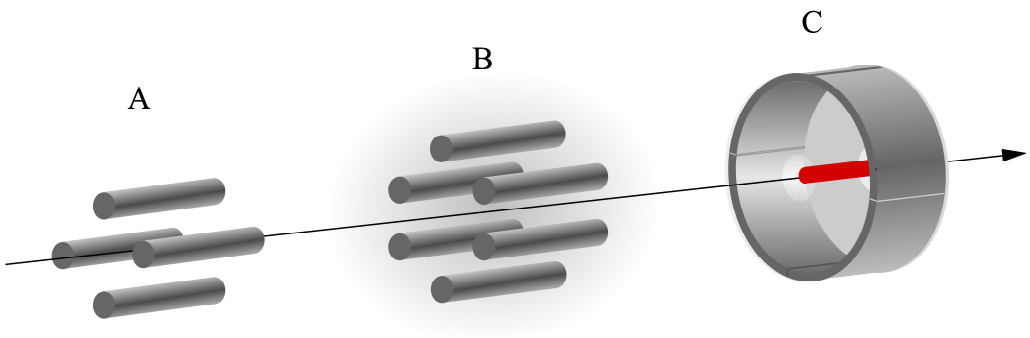

Fig. 4.2.2. Experimental setup used in the present section: a) quadrupole used for mass pre-selection, b) reaction cell, c) ICR cell where both infrared multiphoton activation and mass analysis take place. The numbers represent the different steps on the timeline.

4.2.2. Results

Reaction of the full isotopic signal of $C_{60}^{\bullet -}$ (see. Fig. 4.2.3-a) for 256 s with CH_3OH or CD_3OD at room temperature yields the mass spectrum of Fig. 4.2.3-b and 4.2.3-c, in opposition to $C_{60}^{\bullet +}$ found to be unreactive to methanol [105]. Using deuterated methanol, CD_3OD, the presence of different isotopic distributions can easily be assessed. However, even for the deuterated species, the superposition of the ^{13}C isotopic signal of the different hydrides complicates the determination of the number of hydrogen atoms added and of the related ion intensities.

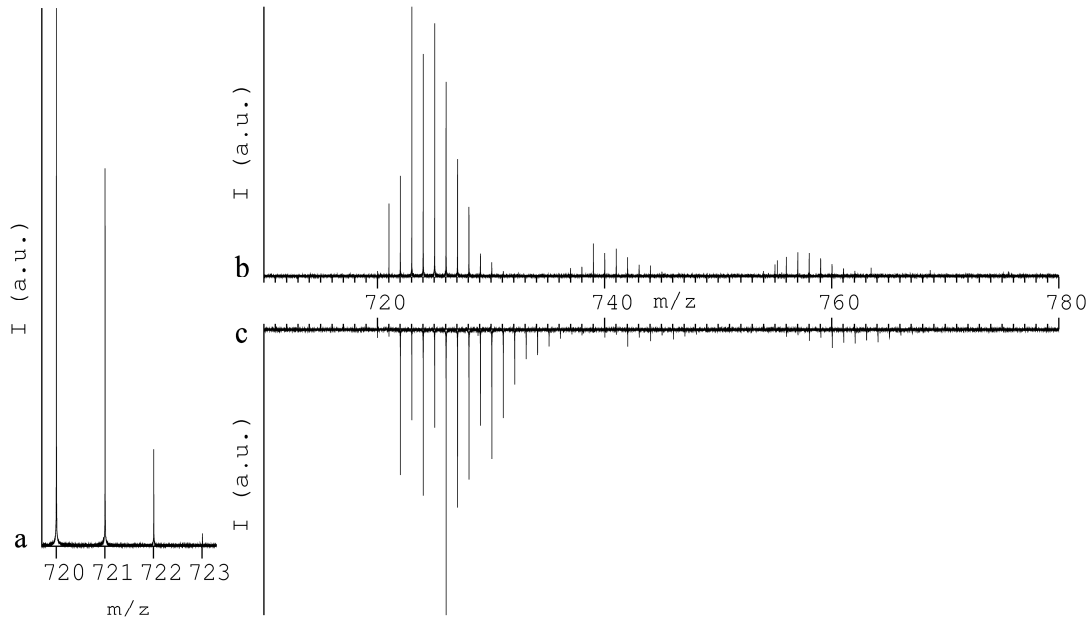

Fig. 4.2.3. $C_{60}^{\bullet-}$ full isotopic signal before (a) and after reaction with CH_3OH (b) and with CD_3OD (c) for 256 s at room temperature (~20°c) at a pressure of about 1 µbar (the spectrum is oriented bottom-up in order too facilitate comparison). The reaction products are mostly $C_{60}H_x^-$ (b) and $C_{60}D_x^-$ (c) with some traces of oxygen or hydroxyl adducts. A small isotopic effect can also be inferred from the comparison of the two spectra.

Elemental composition determination allows us to identify the different isotopic distributions (Fig. 4.2.4.B-b, B-c, and B-d) and the extent of hydrogenation. The isotopic distributions below 736 m/z correspond to fullerene hydrides, $C_{60}H_x^-$, exclusively, with a maximum of eleven added hydrogen atoms detected. The higher m/z isotopic distributions correspond to $C_{60}H_xO_y^-$ with y>0. The three high resolution scale-ups of Fig. 4.2.4.B illustrate the contributions to the ion signal of $^{12}C_{60}H_9^-$, $^{12}C_{59}{}^{13}C_{59}H_8^-$, and $^{12}C_{58}{}^{13}C_2H_7^-$ (Fig. 4.2.4.B-b) and their equivalent for species containing one (Fig. 4.2.4.B-c) and two (Fig. 4.2.4.B-d) oxygen atoms. The presence of oxygen containing adducts pertains to the formation of fullerenols and degradation of fullerene hydrides into fullerenols [73, 111]. In the present conditions, it has to involve either direct abstraction of hydroxyls from methanol or the replacement of

hydrogen atoms by hydroxyls. Direct addition of $O^{\bullet}$ or O_2 is expected to be negligible due to their very low partial pressure within the reaction cell. Finally, the recovery of the $C_{60}^{\bullet-}$ ion signal upon infrared multiphoton activation using a CO_2 laser of all the ion species present (see Fig. 4.2.4.C) with only negligible CH_x and C_2H_x losses, points to reversible addition processes and suggests that the C_{60} cage remains intact.

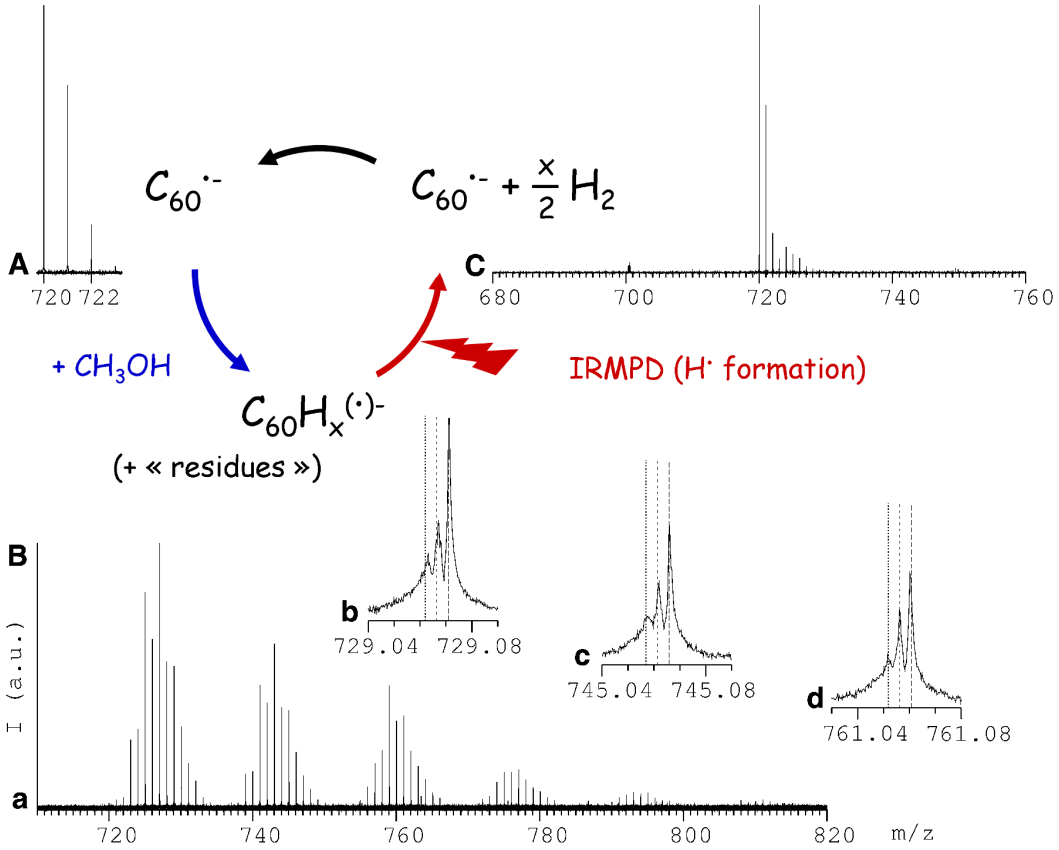

Fig. 4.2.4. $C_{60}^{\bullet-}$ full isotopic signal before (A) and after reaction with CH_3OH for 512s at room temperature (~20°c) at a pressure of about 1 µbar (B-a). The scale-ups (B-b, B-c, and B-d) make elemental composition determination possible. The dashed vertical lines drawn in scale-up (B-b) correspond from left to right to $^{12}C_{58}{}^{13}C_2H_7^-$, $^{12}C_{59}{}^{13}C_{59}H_8^-$, and $^{12}C_{60}H_9^-$. Their equivalents are also drawn in scale-ups (B-c) and (B-d) describing species respectively containing one and two oxygen atoms. Spectrum (C) represents the result of 1.2 s infrared multiphoton activation (IRMPA) (~20W) applied to an ion mixture corresponding to the (B-a) spectrum.

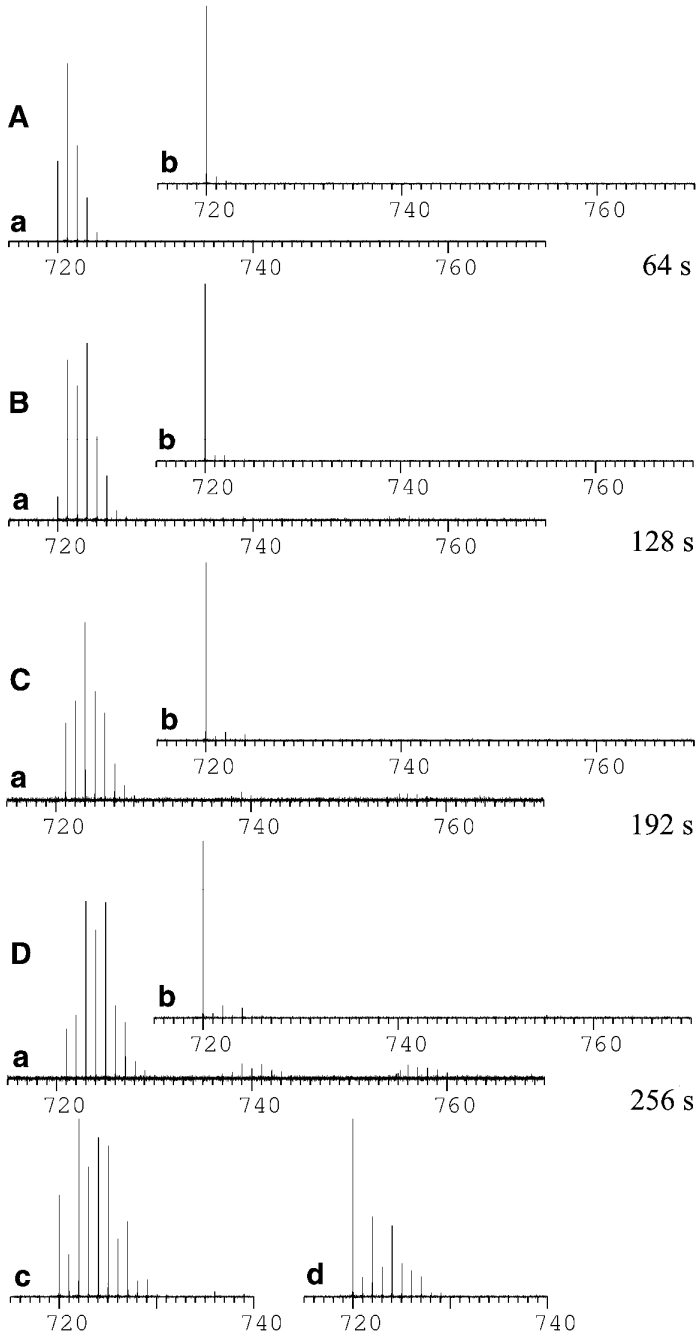

Fig. 4.2.5. Mass spectra of the product ions formed by reacting $^{12}C_{60}^{\bullet-}$ with CH_3OH for 64 (A-a), 128 (B-a), 192 (C-a) and 256 (D-a) s. The spectra A-b, B-b, C-b, D-b correspond to the result of 1.2 s infrared multiphoton activation (IRMPA) of the previous ion signals with recovery rates (ion signal after IRMPA / ion signal before) of 83, 88, 108, 106 % respectively (with the rates > 100% a consequence of the uncertainty on the intensities of the oxygen containing species). *Per se* the residual signal of ^{13}C containing species is negligible, it amounts to less than 2.5% of the total ion signal. The mass spectra D-c and D-d result of the IRMPA during 0.6 s (D-c) and 0.8 s (D-d) of the ion signal reported in d.

In order to accurately measure the ion intensities for $C_{60}H_x^{(\bullet)-}$ with x=0-7 and extract kinetic information, it is necessary to avoid the ^{13}C contributions. The $^{12}C_{60}^{\bullet-}$ ions were thus mass selected and reacted with CH_3OH for 14 time periods ranging from 10 ms to 256 s (see Fig. 4.2.5). The highest level of hydrogenation for $^{12}C_{60}H_x^-$ and $^{12}C_{60}H_xO^-$, confirmed by elemental composition analysis (errors < 0.5 ppm) corresponds again to eleven hydrogen atoms added. Infrared multiphoton activation during 1.2 s and for ~20 W laser intensity at 10.6 µm yields back the $^{12}C_{60}^{\bullet-}$. The conclusions obtained for $^{12}C_{60}^{\bullet-}$ are expected to hold also for ^{13}C containing anions.

4.2.3. Discussion

Information about the kinetics of the successive hydrogenation steps can be extracted using a model described in Fig. 4.2.6. With a pressure in the µbar range within the constant flow reaction cell, methanol can be considered to be in large excess compared to the ions, leading to successive pseudo first-order hydrogenation reactions. Only $C_{60}^{\bullet-}$ anions with up to seven hydrogen atoms added are explicitly considered in the model. The signals of all other ions ($C_{60}H_{x>7}$, $C_{60}H_xO_{y>1}$) are summed up and included in a residual contribution. The total ion intensity is normalized to one and neutralization of fullerene anions is neglected. In order to accurately measure the relative ion populations for $C_{60}H_x^{(\bullet)-}$ with x=0-7, it is necessary to avoid the ^{13}C contributions to the ion intensities. The $^{12}C_{60}^{\bullet-}$ ions were thus mass selected and reacted with CH_3OH for 14 time periods ranging from 10 ms to 256 s (Fig. 4.2.5). The conclusions obtained for $^{12}C_{60}^{\bullet-}$ are expected to hold also for ^{13}C containing anions. The highest level of hydrogenation for ^{12}C isotopically pure $^{12}C_{60}H_x^-$ and $^{12}C_{60}H_xO^-$, confirmed by elemental composition analysis (error < 0.5

ppm) also corresponds to eleven hydrogen atoms added and the infrared multiphoton activation during 1.2 s and for ~20W laser intensity at 10.6 µm yields back the $^{12}C_{60}^{\bullet-}$.

Each $C_{60}H_x^-$ (x=0-7) ion is potentially involved in two kinds of reactions with methanol, respectively yielding $C_{60}H_{x+1}^-$ with rate constant k_{x+1} and $C_{60}H_uO_y^-$ (u=x or x+1, y>0) with rate constant r_{x+1} (Fig. S2). The rate constants (see Fig. 4.2.8 and Table 1) leading to $C_{60}H^-$ (x=1-7) and $C_{60}H_uO_y$ (y>0) are obtained from the fit (Fig. 4.2.7.) of the relative population of ions measured at 14 different times, 4 of which are shown in Fig. 4.2.5. Formation of $C_{60}H_{x+2}^-$ and formaldehyde, a by-product detected in direct methanol fuel cells (DMFCs) [112], upon transfer of two hydrogen atoms from one methanol molecule yields, when inserted into the model, negligible rate constants and has been ruled out. The $C_{60}H_x^-$ ions can be organized in two groups respectively corresponding to radical (x even) and to closed-shell (x odd) ions.

The origin (CH_3 or OH groups of CH_3OH) of the hydrogen(s) transferred to the fullerene was probed using isotopically labelled methanol (CH_3OD and CD_3OH). Even though the ion signal distributions differ, the observation of the anion $C_{60}H^-$ in both cases – suggesting that either both CH_3 and OH groups contribute or that exchange takes place following hydrogen addition to the C_{60} – and the unresolved $C_{60}H_2^{-\bullet}$ and $C_{60}D^-$ signals did not allow to reach a definite conclusion using this approach.

The ion intensities corresponding to three independent sets of experiments were then fitted to the kinetic model of Fig. 4.2.6 using the MATLAB multi-experiment fitting toolbox PottersWheel [113]. The kinetic parameters were estimated via the

minimization of the weighted $\chi^2 = \sum_{i=1}^{N} \frac{(y_{\mathrm{mod}\,el}(i) - y_{meas.}(i))^2}{\sigma^2_{meas.}(i)}$ value where N is the total number of data points and $\sigma_{meas.}(i)$ is the standard deviation of measurement *i*, $y(i)$ (see Fig. 4.2.7). The inferred reaction rates are reported in table 1.

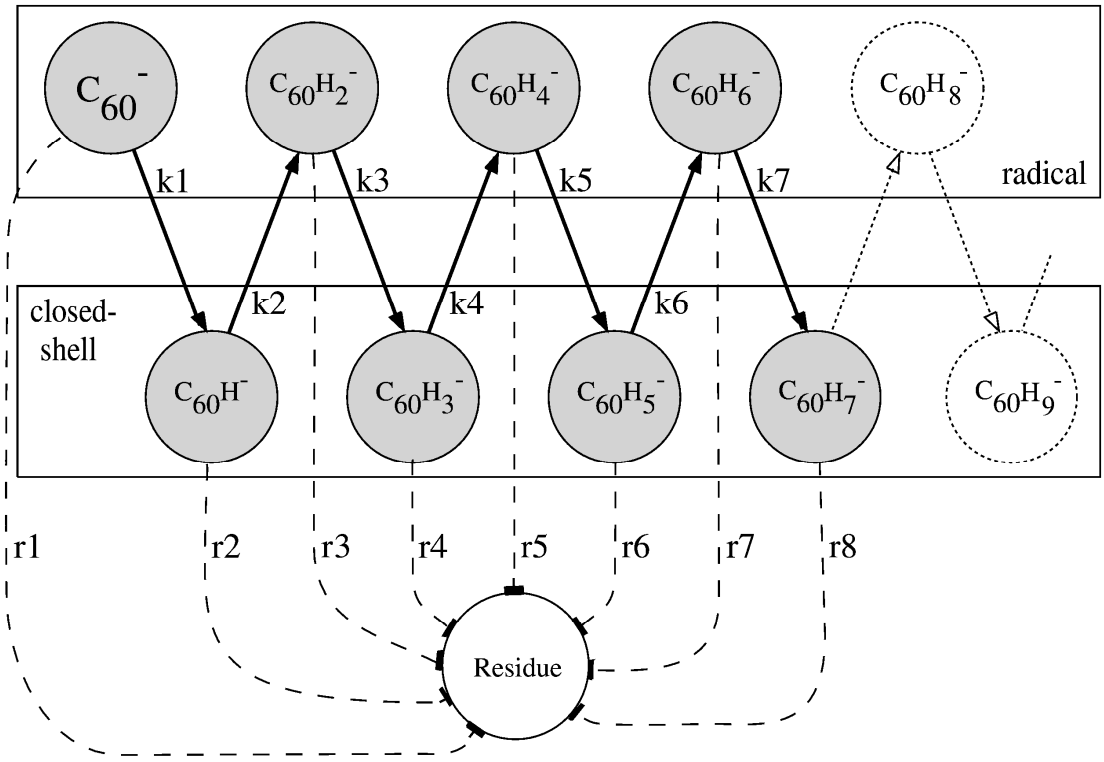

Fig. 4.2.6. Kinetic model used to describe the formation of fullerene hydrides from $C_{60}^{\bullet -}$ by reaction with CH_3OH. Each $C_{60}H_x^-$ (x=1-7) reagent is assumed to be involved in two different reactions respectively yielding $C_{60}H_{x+1}^-$ and $C_{60}H_uO_y^-$ (u=x or x+1), with rate constants labelled k_i and r_i. Only $C_{60}H_x^-$ (x=1-7) are explicitly considered due to increasing errors on the intensities measured and the inferred rate constants for x>7. "Residue" represents all the reaction products detected that do not qualify as $C_{60}H_x^-$ (x=1-7).

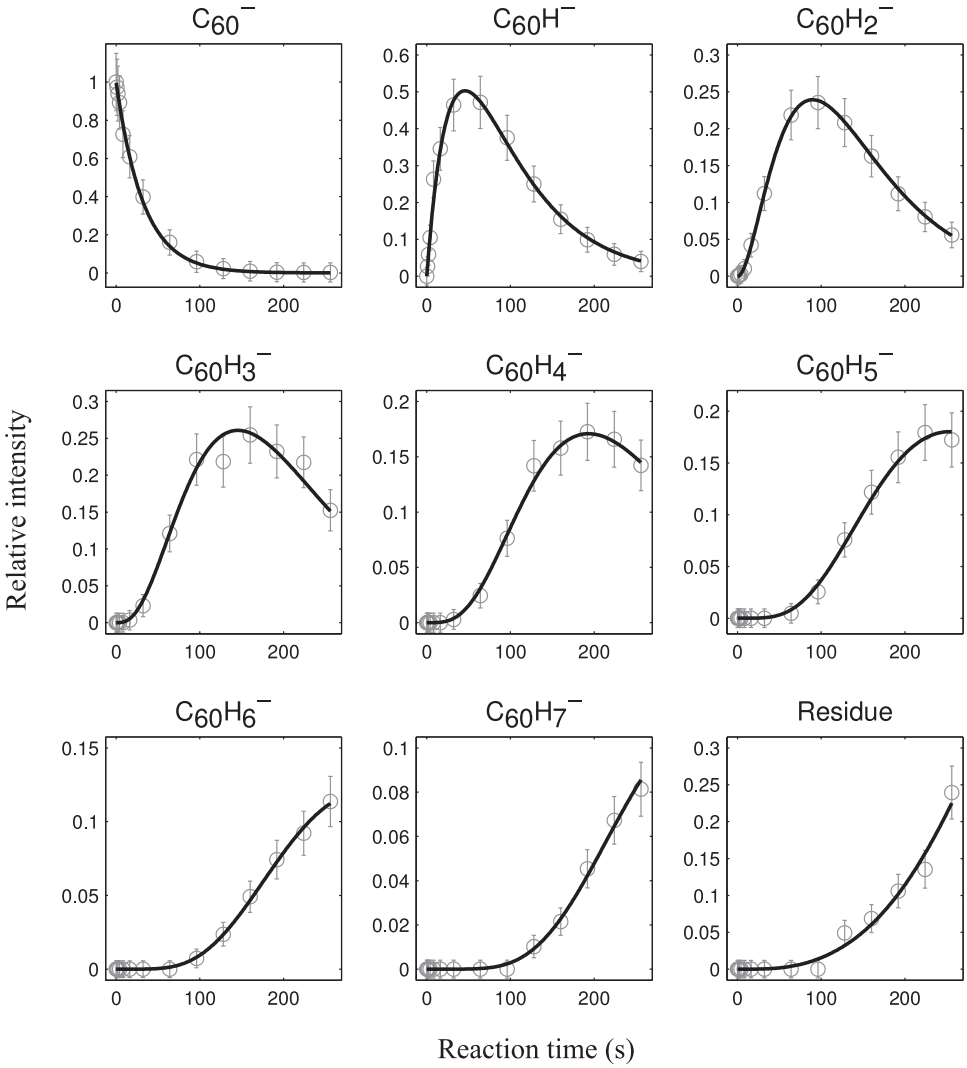

Fig. 4.2.7. Example of normalized ion intensities fitted using the model of Fig. 4.2.6.

Table 4.2.I. reaction rate constants (in s^{-1}) and their standard deviations obtained for the reaction model described in Fig. 4.2.6.

i	k_i	$\sigma(k_i)$	r_i	$\sigma(r_i)$
1	0.029	0.002	0.000	0.000
2	0.015	0.001	0.000	0.000
3	0.023	0.002	0.000	0.001
4	0.015	0.002	0.000	0.001
5	0.019	0.001	0.002	0.003
6	0.015	0.001	0.000	0.000
7	0.017	0.005	0.007	0.010
8	-	-	0.012	0.009

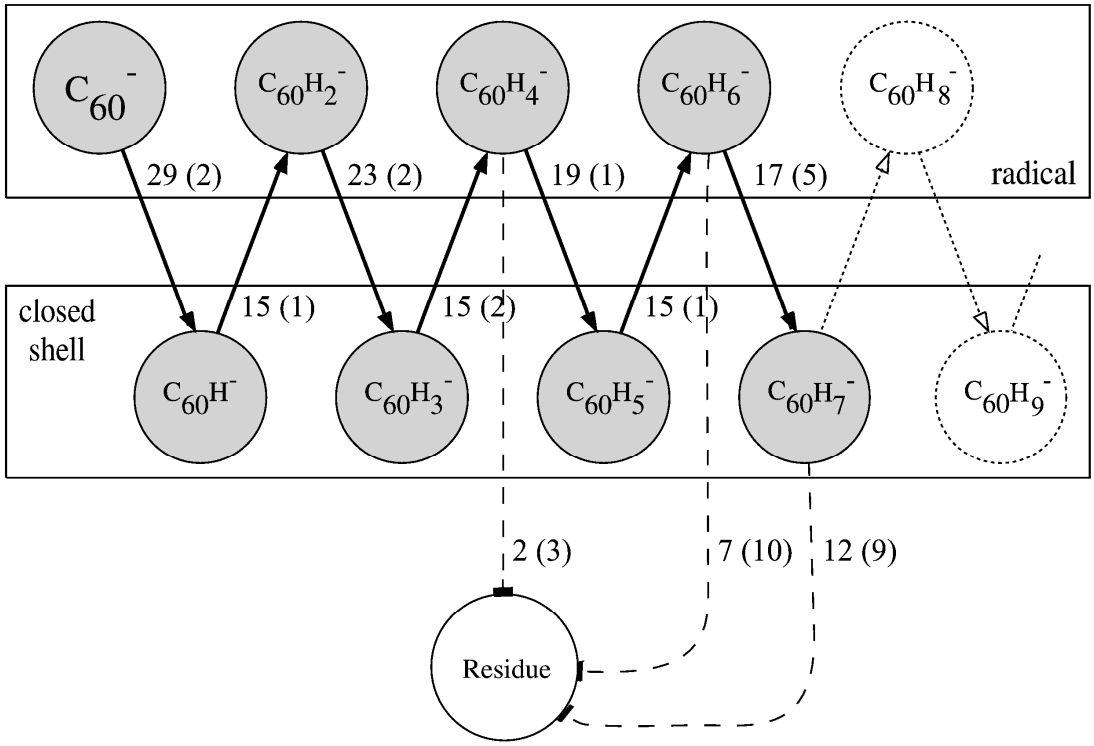

Fig. 4.2.8. Summary of the kinetic model used to describe the formation of fullerene hydrides from $C_{60}^{\bullet-}$ by reaction with CH_3OH. The rate constants (in 10^{-3} s^{-1}) are displayed next to the reaction arrows with their standard deviation in parentheses.

The reversible dehydrogenation of C_{60} hydride anions is demonstrated using IRMPA (Fig. 4.2.4 and Fig. 4.2.5.). Upon low intensity IRMPA using a continuous-wave CO_2 laser, the hydrides and oxygen containing adducts stored in the ICR cell of the mass spectrometer and resulting from the reaction of $C_{60}^{\bullet-}$ with methanol during 512 s yield back $C_{60}^{\bullet-}$ isotopic distribution with only negligible CH_x and C_2H_x losses (see Fig. 4.2.4.C). The recovery rates of the $^{12}C_{60}^{\bullet-}$ ion signal upon IRMPA (see Fig. 4.2.5.A-b, B-b, C-b, and D-b) also points to reversible addition processes. This suggests that the C_{60} cage remains intact with the oxygen containing adducts being hydroxyls [99]. Dehydrogenation is favoured upon other reaction channels, since the relatively slow IRMPA process leads to selective dissociation through the lowest threshold channel [114]. No evidence of electron detachment from $C_{60}^{\bullet-}$ or its hydrides upon IRMPA

was observed; the fluctuations observed in the $C_{60}^{\bullet-}$ signal intensities and thus in the signal recovery rates measured upon IRMPA have been assigned to small instabilities in the electrospray process.

The approach generally used to discuss multiphoton excitation involves a set of spectroscopic molecular states (eigenstates of the molecular Hamiltonian in absence of electromagnetic field) interacting with the radiation field [115, 116]. Some mechanisms of interest in multiphoton excitation in arbitrary many level systems are [115, 116]:

(i) a direct multiphoton process between two states without interference from any further states by electric dipole coupling if the number of photon exchanged is odd;

(ii) a Goeppert-Mayer process involving necessarily coupling to intermediate states, that are assumed to be so far off resonance that they can always be treated by perturbation theory. These intermediate levels are hardly populated and Goeppert-Mayer process is possible for any number of photons (even and odd);

(iii) a quasiresonant stepwise process involving intermediate levels close to resonance. An arbitrary borderline can be drawn at an off-resonance energy of the intermediate levels of $\Delta\nu \geq \nu/2$ with $\Delta\nu$ the mismatch and ν the excitation frequency, beyond which the definition of the quasiresonant approximation is of little use [117];

(iv) an incoherent stepwise excitation that can be rigorously described using Einstein coefficients for thermal radiation.

All these processes occur under appropriate conditions. Direct transitions (i) between spin states have been proved in the radiofrequency range, Goeppert-Mayer (ii) two photon excitation appears to exist abundantly in the visible laser excitation of polyatomic molecules and there is no reason to question the Einstein coefficient transition rates for excitation with thermal radiation (iv) [116]. In the infrared multiphoton high-intensity regime, there is however overwhelming evidence that the IR-multiphoton excitation of polyatomic molecules is dominated by the coherent quasiresonant-stepwise excitation mechanism (iii) [116].

From the dehydrogenation of $C_{60}H^-$ and the spectra of Fig. 4.2.5. (D-c and D-d), it is clear that one of the observed dissociation mechanism involves $H^\bullet$ loss, in agreement with the theoretical predictions reported by Bettinger *et al.* [118]. This does not however preclude the parallel H_2 loss mechanism. Indeed, the ion signals enriched in $C_{60}H_{2x}^{\bullet-}$ after weak IRMPA could be explained either by a H_2 loss or by two different $H^\bullet$ loss rates, one for radical species, $C_{60}H_{2x}^{\bullet-}$, and another one for closed-shell species, $C_{60}H_{2x+1}^-$. The presence of different isomers formed upon hydrogenation of $C_{60}^{\bullet-}$ by methanol is also expected to affect the dehydrogenation process.

Provided that (i) energy relaxation processes are at least as fast as laser up-pumping for molecules near the dissociation threshold, (ii) the dissociation kinetics is governed by the laser up-pumping processes near threshold and not by the rate of crossing a low-energy bottleneck, (iii) collisional relaxation is unimportant compared with spontaneous radiative relaxation, the infrared multiphoton low-intensity regime corresponds to an incoherent stepwise thermal-like excitation [114, 119] leading to extensive internal energy randomization [120]. Since the previous assumptions are

most likely to hold for a low-intensity (~20W) continuous wave laser (10.6 µm), low pressure (10^{-14} bar) conditions, and large molecules with a quasi-continuum of vibrational states at room temperature (C_{60} has about 10^{10} states per cm^{-1} at the average thermal energy of 0.5 eV, at 300 K [121, 122, 123]), $C_{60}^{\bullet-}$ and its hydrides may be assumed to undergo upon IRMPA a thermal-like dehydrogenation comparable to the thermal dehydrogenation previously reported [76, 82, 83, 65, 107, 108, 67]).

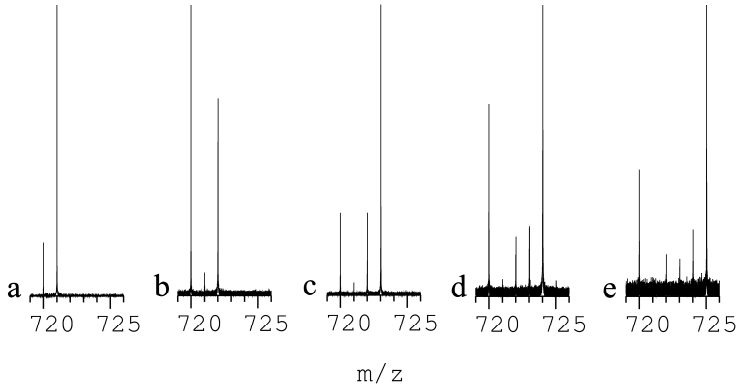

Fig. 4.2.9. Selective infrared multiphoton activation of hydrides $C_{60}H_x^-$ with hydrogen content ranging from 1 to 5. The parent ions produced by reaction with methanol during 96 (a-c) and 256 s (d-e) are isolated within the ICR cell by multiple ejection pulses prior to infrared multiphoton activation. Formation of $C_{60}H_{x-1}^-$ is observed for all $C_{60}H_x^-$ parent ions whereas the spectra (for example b) with marked two m/z differences could also be explained by a difference in reactivity between closed-shell and radical ions.

4.2.4. Conclusion

Overall, $C_{60}^{\bullet-}$ hydrogenation in the gas phase by reaction with methanol vapour was demonstrated at pressures of the order of one microbar in methanol and room temperature conditions. For the experimental condition used, a maximum of eleven hydrogen atoms were added to $C_{60}^{\bullet-}$. Kinetic studies are compatible with the

assumption that only one hydrogen atom is transferred to the fullerene or its hydrides upon reaction with a single methanol molecule. For the longer reaction times, a second addition mechanism comes into play and leads to the addition of oxygen atoms or hydroxyl groups to the hydride fullerene anions. Hydrogen release from $C_{60}^{\bullet-}$ anions was successfully performed using low-intensity infrared multiphoton activation with a 10.6 µm continuous-wave CO_2 laser. Based on the experimental evidence, a multistep mechanism for radical hydrogen loss is most probable, in agreement with previously published theoretical results [118]. Fullerene hydrides therefore appear to be a potentially interesting source of hydrogen radicals when irradiated by infrared radiation. Molecular hydrogen losses cannot, however, be dismissed based on the experimental evidence. Infrared multiphoton activation was also found to lead to the successful removal of impurities such as hydroxyl or oxygen adducts from fullerene anions.

The present work pertains to the study of the hydrogen storage capabilities of fullerenes as well as of the reactions between mono-reduced fullerene and methanol for applications in direct methanol fuel cells or hydrogen generation from methanol. It further suggests that infrared multiphoton activation in the µm range is potentially well suited for the recycling of fuel cell membranes and electrodes covered by or embedding fullerenes.

References

[1] D. F. Hunt, C. N. McEwen, R. A. Upham, *Analytical Chemistry* **44**, 1292 (1972).

[2] A. Ranasinghe, R. G. Cooks, S. K. Sethi, *Organic Mass Spectrometry* **27**, 77 (1992).

[3] T. D. Wood, *et al.*, *Proceedings of the National Academy of Sciences USA* **92**, 2451 (1995).

[4] X. B. Wang, C. F. Ding, L. S. Wang, *Journal of Chemical Physics* **110**, 8217 (1999).

[5] T. Wyttenbach, M. T. Bowers, *Journal of the American Society of Mass Spectrometry* **10**, 9 (1999).

[6] S. Campbell, M. T. Rodgers, E. M. Marzluff, J. L. Beauchamp, *Journal of the American Chemical Society* **117**, 12840 (1995).

[7] D. Sen, W. Gilbert, *Nature* **334**, 364 (1988).

[8] S. L. Forman, J. C. Fettinger, S. Pieraccini, G. Gottareli, J. T. Davis, *Journal of the American Chemical Society* **122**, 4060 (2000).

[9] F. L. Gervasio, P. Carloni, M. Parrinello, *Physical Review Letters* **89**, 108102 (2002).

[10] A. Calzolari, R. Di Felice, E. Molinari, A. Garbesi, *Applied Physics Letters* **80**, 3331 (2002).

[11] R. Di Felice, A. Calzolari, E. Molinari, *Physical Review B* **65**, 045104 (2002).

[12] A. B. Kotlyar, *et al.*, *Advanced Materials* **17**, 1901 (2005).

[13] R. Taylor, D. R. M. Walton, *Nature* **363**, 685 (1993).

[14] M. T. Rodgers, S. Campbell, E. M. Marzluff, J. L. Beauchamp, *International Journal of Mass Spectrometry and Ion Processes* **148**, 1 (1995).

[15] K. M. Keller, J. S. Brodbelt, *Analytical Biochemistry* **326**, 200 (2004).

[16] K. Håkansson, R. R. Hudgins, A. G. Marshall, R. A. J. O'Hair, *Journal of the American Society of Mass Spectrometry* **14**, 23 (2003).

[17] C. W. Chou, P. A. Limbach, R. B. Cole, *Journal of the American Society of Mass Spectrometry* **13**, 1407 (2002).

[18] J. Gidden, M. T. Bowers, *European Physical Journal D* **20**, 409 (2002).

[19] A. Gelbin, *et al.*, *Journal of the American Chemical Society* **118**, 519 (1996).

[20] T. D. Son, J. Thiéry, W. Guschlbauer, J. J. Dunand, *Biochimica Biophysica Acta* **281**, 289 (1972).

[21] D. B. Davies, S. S. Danyluk, *Biochemistry* **13**, 4417 (1974).

[22] W. K. Olson, J. L. Sussman, *Journal of the American Chemical Society* **104**, 270 (1982).

[23] A. Toyama, Y. Takino, H. Takeuchi, I. Harada, *Journal of the American Chemical Society* **115**, 11092 (1993).

[24] W. S. Oh, M. S. Kim, S. W. Suh, *Journal of Raman Spectroscopy* **18**, 253 (1987).

[25] B. Pergolese, A. Bonifacio, A. Bigotto, *Physical Chemistry Chemical Physics* **7**, 3610 (2005).

[26] S. J. Shaw, D. M. Desiderio, K. Tsuboyama, J. A. McCloskey, *Journal of the American Chemical Society* **92**, 2510 (1970).

[27] M. S. Wilson, I. Dzidic, J. A. McCloskey, *Biochemica Biophysica Acta* **240**, 623 (1971).

[28] J. A. McCloskey, *et al.*, *Journal of the American Chemical Society* **95**, 5762 (1973).

[29] M. S. Wilson, J. A. McCloskey, *Journal of the American Chemical Society* **97**, 3436 (1975).

[30] M. Yu, H. S. Kim, P. R. LeBreton, *Biochemical and Biophysical Research Communications* **184**, 16 (1992).

[31] H. S. Kim, M. Yu, Q. Jiang, P. R. LeBreton, *Journal of the American Chemical Society* **115**, 6169 (1993).

[32] L. Rivas, S. Sanchez-Cortes, J. V. Garcia-Ramos, *Journal of Raman Spectroscopy* **33**, 6 (2001).

[33] L. Rivas, S. Sanchez-Cortes, J. V. García-Ramos, *Physical Chemistry Chemical Physics* **4**, 1943 (2002).

[34] C. Altona, M. Sundaralingam, *Journal of the American Chemical Society* **94**, 8205 (1972).

[35] C. Altona, M. Sundaralingam, *Journal of the American Chemical Society* **95**, 2333 (1973).

[36] T. D. Son, W. Guschlbauer, *Nucleic Acids Research* **2**, 873 (1975).

[37] N. Yathindra, M. Sundaralingam, *Biopolymers* **12**, 2075 (1973).

[38] J. Gidden, M. T. Bowers, *Journal of Physical Chemistry B* **107**, 12829 (2003).

[39] J. M. Robinson, M. J. Greig, R. H. Griffey, V. Mohan, D. A. Laude, *Analytical Chemistry* **70**, 3566 (1998).

[40] S. Campbell, M. Rodgers, E. Marzluff, J. Beauchamp, *Journal of the American Chemical Society* **116**, 9765 (1994).

[41] K. B. Green-Church, P. A. Limbach, *Journal of the American Society of Mass Spectrometry* **11**, 24 (2000).

[42] M. E. Hemling, J. J. Conboy, M. F. Bean, M. Mentzer, C. S. A., *Journal of the American Society for Mass Spectrometry* **5**, 434 (1994).

[43] J. A. Zoltewicz, D. F. Clark, T. W. Sharpless, G. Grahe, *Journal of the American Chemical Society* **92**, 1741 (1970).

[44] R. Rios-Font, L. Rodrigez-Santiago, J. Bertran, M. Sodupe, *Journal of Physical Chemistry B* **111**, 6071 (2007).

[45] K. B. Green-Church, P. A. Limbach, M. A. Freitas, A. G. Marshall, *Journal of the American Society for Mass Spectrometry* **12**, 268 (2001).

[46] H. T. Miles, J. Howard, F. B.and Frazier, *Science* **142**, 1458 (1963).

[47] P. Buchner, W. Maurer, H. Rüterjans, *Journal of Magnetic Resonance* **29**, 45 (1978).

[48] C. Colominas, F. J. Luque, M. Orozco, *Journal of the American Chemical Society* **118**, 6811 (1996).

[49] P. Cysewski, D. Bira, K. Bialkowski, *Journal of Molecular Structure (Teochem)* **678**, 77 (2004).

[50] M. Tomasz, J. Olson, C. M. Mercado, *Biochemistry* **11**, 1235 (1972).

[51] J. A. Elvidge, J. R. Jones, C. O'Brien, E. A. Evans, H. C. Sheppard, *Journalof the Chemical Society, Perkin Transactions 2* p. 174 (1974).

[52] M. J. Lane, G. J. J. Thomas, *Biochemistry* **3839**, 18 (1979).

[53] J. M. Benevides, D. Lemeur, T. G. J. Jr., *Biopolymers* **23**, 1011 (1984).

[54] J. D. Puglisi, J. R. Wyatt, I. J. Tinoco, *Journal of Molecular Biology* **214**, 437 (1990).

[55] B. S. Rabinovitch, D. W. Setser, *Advances in Photochemistry* **3**, 1 (1964).

[56] W. Forst, *Theory of unimolecular reactions* (Academic press, New York., 1973).

[57] M. Tsuboi, *et al.*, *Journal of the American Chemical Society* **119**, 2025 (1997).

[58] J. Hine, *Journal of the American Chemical Society* **94**, 5766 (1972).

[59] M. E. Crestoni, S. Fornarini, M. Lentini, M. Speranza, *Journal of Physical Chemistry* **100**, 8285 (1996).

[60] T. Osaki, T. Tanaka, Y. Tai, *Physical Chemistry Chemical Physics* **1**, 2361 (1999).

[61] A. A. Peera, L. B. Alemany, W. E. Billups, *Applied Physics A: Material Sciences Processes* **78**, 995 (2004).

[62] K. Hinokuma, M. Ata, *Chemical Physics Letters* **341**, 442 (2001).

[63] H. Wang, *et al.*, *Journal of Membrane Science* **289**, 277 (2007).

[64] R. E. Haufler, *et al.*, *Journal of Physical Chemistry* **94**, 8634 (1990).

[65] W. E. Billups, *et al.*, *Tetrahedron Letters* **38**, 175 (1997).

[66] Y. Vasil'ev, *et al.*, *Journal of the Chemical Society, Chemical Communications* p. 1233 (2000).

[67] M. Banks, *et al.*, *Journal of the Chemical Society, Chemical Communications* p. 1149 (1993).

[68] J. Nossal, *et al.*, *Journal of the American Chemical Society* **123**, 8482 (2001).

[69] A. Peera, *et al.*, *European Journal of Organic Chemistry* p. 4140 (2003).

[70] J. B. Briggs, M. N. Montgomery, L. L. Silva, G. P. Miller, *Organic Letters* **7**, 5533 (2005).

[71] J. Kintigh, J. B. Briggs, K. Letourneau, G. P. Miller, *Journal of Materials Chemistry* **17**, 4647 (2007).

[72] W. E. Billups, *et al.*, *Tetrahedron Letters* **38**, 171 (1997).

[73] A. G. Avent, *et al.*, *Journal of the Chemical Society, Perkin Transactions 2* p. 15 (1994).

[74] C. C. Henderson, P. A. Cahill, *Science* **259**, 1885 (1993).

[75] C. C. Henderson, C. M. Rohlfing, R. A. Assink, P. A. Cahill, *Angewandte Chemie International Edition in English* **33**, 786 (1994).

[76] C. Rüchardt, *et al.*, *Angewandte Chemie International Edition in English* **32**, 584 (1993).

[77] M. Gerst, H. D. Beckhaus, C. Rüchardt, E. E. B. Campbell, R. Tellgmann, *Tetrahedron Letters* **34**, 7729 (1993).

[78] S. Fukuzumi, T. Suenobu, S. Kawamura, A. Ishida, K. Mikami, *Journal of the Chemical Society, Chemical Communications* p. 291 (1997).

[79] L. Becker, T. Evans, J. L. Bada, *Journal of Organic Chemistry* **58**, 7630 (1993).

[80] A. V. Talyzin, Y. M. Shul'ga, A. Jacob, *Applied Physics A* **78**, 1005 (2004).

[81] M. S. Meier, *et al.*, *Tetrahedron Letters* **35**, 5789 (1994).

[82] A. D. Darwish, *et al.*, *Journal of Chemical Society, Perkin Transactions 2* p. 2359 (1995).

[83] A. D. Darwish, *et al.*, *Synthetic Metals* **77**, 303 (1996).

[84] M. S. Meier, B. R. Weedon, H. P. Spielmann, *Journal of the American Chemical Society* **118**, 11682 (1996).

[85] R. G. Bergosh, M. S. Meier, J. A. L. Cooke, H. P. Spielmann, B. R. Weedon, *Journal of Organic Chemistry* **62**, 7667 (1997).

[86] M. S. Meier, *et al.*, *Carbon* **38**, 1535 (2000).

[87] S. Ballenweg, R. Gleiter, W. Krätschmer, *Tetrahedron Letters* **34**, 3737 (1993).

[88] M. L. Attalla, A. M. Vassalo, B. N. Tattam, J. V. Hana, *Journal of Physical Chemistry* **97**, 6329 (1993).

[89] D. E. Cliffel, A. J. Bard, *Journal of Physical Chemistry* **98**, 8140 (1994).

[90] M. E. Niyazymbetov, D. H. Evans, S. A. Lerke, P. A. Cahill, C. C. Henderson, *Journal of Physical Chemistry* **98**, 13093 (1994).

[91] R. Nozu, O. Matsumoto, *Journal of the Electrochemical Society* **143**, 1919 (1996).

[92] D. Mandrus, *et al.*, *Journal of Physical Chemistry B* **101**, 123 (1997).

[93] C. Jin, *et al.*, *Journal of Physical Chemistry* **98**, 4215 (1994).

[94] S. M. C. Vieira, W. Ahmed, P. R. Birkett, C. A. Rego, *Chemical Physics Letters* **347**, 355 (2001).

[95] T. Wågberg, *et al.*, *Organic Letters* **7**, 5557 (2005).

[96] A. V. Talyzin, *et al.*, *Chemical Physics* **325**, 445 (2006).

[97] J. A. Howard, *Chemical Physics Letters* **203**, 540 (1993).

[98] P. A. Brühweiler, *et al.*, *Chemical Physics Letters* **214**, 45 (1993).

[99] A. V. Talyzin, *et al.*, *Journal of Physical Chemistry B* **109**, 12742 (2005).

[100] A. D. Darwish, A. G. Avent, R. Taylor, D. R. M. Walton, *Journal of the Chemical Society, Perkin Transactions 2* p. 2051 (1996).

[101] I. Rogner, P. Birkett, E. E. B. Campbell, *International Journal of Mass Spectrometry and Ion Processes* **156**, 103 (1996).

[102] A. V. Talyzin, *et al.*, *Journal of Physical Chemistry A* **110**, 8528 (2006).

[103] Y. V. Vasil'ev, R. R. Absalimov, S. K. Nasibullaev, A. S. Lobach, T. Drewello, *Journal of Physical Chemistry A* **105**, 661 (2001).

[104] L. S. Sunderlin, *et al.*, *Journal of the American Chemical Society* **113**, 5489 (1991).

[105] G. Javahery, S. Petrie, H. Wincel, J. Wang, D. K. Bohme, *Journal of the American Chemical Society* **115**, 6295 (1993).

[106] S. Petrie, G. Javahery, J. Wang, D. K. Bohme, *Journal of the American Chemical Society* **114**, 6268 (1992).

[107] E. L. Brosa, J. Davey, F. H. Garson, S. Gooesfeld, *Journal of Materials Research* **14**, 2138 (1999).

[108] P. A. Dorozhko, A. S. Lobach, A. A. Popov, V. M. Senyavin, M. V. Korobov, *Chemical Physics Letters* **336**, 39 (2001).

[109] N. X. Wang, J. P. Zhang, *Journal of Physical Chemistry A* **110**, 6276 (2006).

[110] Z. Liang, A. G. Marshall, *Analytical Chemistry* **62**, 70 (1990).

[111] N. S. Schneider, A. D. Darwish, H. W. Kroto, R. Taylor, D. R. M. Walton, *Journal of the Chemical Society, Perkin Transactions 2* p. 463 (1994).

[112] Z. Jusys, R. J. Behm, *Journal of Physical Chemistry B* **105**, 10874 (2001).

[113] T. Maiwald, J. Timmer, Potterswheel multi-experiment fitting toolbox, *Tech. rep.*, www.PottersWheel.de.

[114] D. S. Bomse, R. L. Woodin, J. L. Beauchamp, *Journal of the American Chemical Society* **101**, 5503 (1979).

[115] D. W. Lupo, M. Quack, *Chemical Reviews* **87**, 181 (1987).

[116] M. Quack, *Infrared Physics* **29**, 441 (1989).

[117] M. Quack, *Advances in Chemical Physics* **50**, 395 (1982).

[118] H. F. Bettinger, *et al.*, *Chemical Physics Letters* **360**, 509 (2002).

[119] R. L. Woodin, D. S. Bomse, J. L. Beauchamp, *Journal of the American Chemical Society* **100**, 3248 (1978).

[120] R. C. Dunbar, *Journal of Chemical Physics* **95**, 2537 (1991).

[121] R. E. Haufler, *et al.*, *Chemical Physics Letters* **179**, 449 (1991).

[122] J. U. Andersen, C. Gottrup, K. Hansen, P. Hvelplund, M. O. Larsson, *European Journal of Physics D* **17**, 189 (2001).

[123] J. U. Andersen, P. Hvelplund, S. B. Nielsen, U. V. Pedersen, S. Tomita, *Physical Review A* **65**, 053202 (2002).

Chapter 5. Covalent modification of C_{60}

The remarkable spectroscopic, photochemical, and redox properties of C_{60} make it an interesting constituent for sensing systems. Most relevant to the present chapter are its high electron affinity, and low reorganization energy that results into rapid charge separation and rather slow charge recombination[1, 2, 3, 4]. C_{60}-based donor-acceptor or donor-bridge-acceptor systems have been investigated for their possible application as photovoltaic devices and as component of sensing devices[5, 6, 7, 8, 9, 10, 11]. DNA strands linked to C_{60} have been shown, for example, to induce the selective cleavage of a DNA sequence incorporating the complementary strand[12, 13].

Incorporation of C_{60} in molecular systems involved in photovoltaic and sensing devices can be achieved through either functionalization or complexation [14, 15, 16, 17]. The present chapter discusses the interaction between C_{60} and the covalently added 3'-azido-3'-deoxythymidine (AZT), a thymidine analog, using mass spectrometry and related techniques. The synthesis of this compound was first reported by Ungurenasu *et al.*[18]. The study of the 3'-imino[60]fulleryl-3'-deoxythymidine is motivated by its use as model system [17] for conformational analysis, for rearrangement studies, and for spontaneous or photoinduced electron transfers characterization between a DNA strand and C_{60}, the two being covalently bonded. The model system is well suited for the present purpose. Indeed, 3'-imino[60]fulleryl-3'-deoxythymidine has the ability to form Watson-Crick base pairs with 2-aminopurine, a fluorescent reporter molecule and adenine analogue widely used to probe the structures and dynamics of nucleic acids. Quenching of its fluorescence occurs when, involved in a hydrogen complex with an acceptor molecule, electron transfer to the acceptor takes place [8]. Furthermore, the free 5'-

end of the deoxythymidine caped at the 3'-end by an imino[60]fullerene can serve as precursor for the synthesis of DNA strands by addition of nucleotides using phosphoramidite chemistry [19]. Thymine high photoreactivity can also lead upon absorption of ultraviolet light by adjacent thymines to the formation of a cyclobutane photodimer [20, 21, 22, 23]. Finally, thymine, thymidine, and 3'-azido-3'-deoxythymidine, are also known to adsorb on silver and gold surfaces [24, 25, 26, 27, 28]. The present system can thus bind a C_{60} molecule to metallic surfaces via the adsorption of the nucleobase subunit, the [60]fullerene being available to further functionalization.

The present chapter describes work published in reference [29] (section 5.1.) and reference [30] (section 5.2.). Section 5.1 describes the synthesis of 3'-imino[60]fulleryl-3'-deoxythymidine and the characterization of its ions using collision induced dissociation. Section 5.2 focuses on deprotonated 3'-imino[60]fulleryl-3'-deoxythymidine and its different behavior compared to cationized and reduced species. The rearrangements and the charge transfer occurring upon deprotonation are probed using action spectroscopy and *ab initio* calculations.

5.1. Synthesis and mass spectrometric characterization of 3'-imino[60]fulleryl-3'-deoxythymidine

Covalent attachment of a single functionalizing adduct on a [60]fullerene can in principle yield up to four different isomeric products: [6,6]-closed (**a**), [6,6]-open (**b**), [5,6]-closed (**c**), [5,6]-open (**d**) as illustrated in Fig. 5.1.1. Among these four, the [6,6]-closed and [5,6]-open, in which the adduct is placed respectively at the junctions of two hexagons or across the single bond at the hexagon-pentagon junction, are dominant. Furthermore, as a general rule, the [5,6]-open derivatives synthesized are

less stable and less abundant than the [6,6]-closed isomers. For some compounds such as methanofullerenes, conversion from the [5,6]-open into the thermodynamically more stable [6,6]-closed isomer can even occur [31, 32, 33, 34, 35, 36, 37, 38, 39, 3, 40].

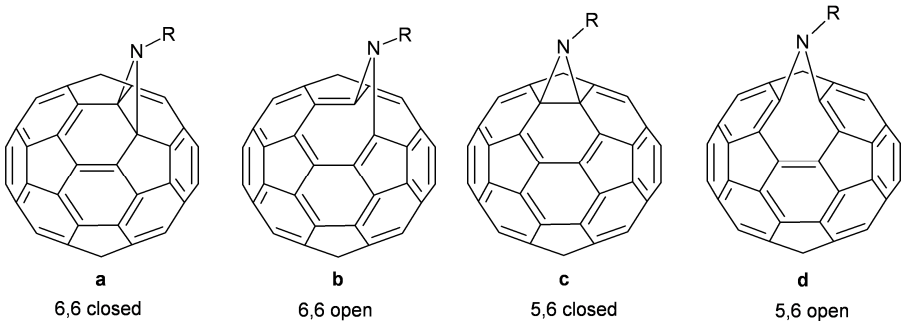

Fig. 5.1.1. The four isomeric products that can in principle be obtained upon functionalization of a [60]fullerene by imino bonding: **a** [6,6]-closed, **b** [6,6]-open, **c** [5,6]-closed and **d** [5,6]-open.

Iminofullerenes are obtained by the direct addition of nitrenes [36, 37] or through the addition of organic azides [31, 34, 38, 39, 3, 40] followed by thermal or photochemical N_2 elimination. These reactions are the only general routes that currently provide access to [5,6]imino adducts [40]. The imino-[60]fullerenes formed through the 1,3-dipolar cycloaddition (1,3-DC) of organic azides followed by the thermal elimination of N_2 differ from the methano-adducts case; they result in the open [5,6]-imino[60]fullerene, **d**, as major or even only product [31, 34, 38, 39, 3, 40] and the open [5,6]-imino structure is not known to convert into the closed [6,6]-imino configuration even though this isomer is still thermodynamically more stable [31, 3]. The preferential formation of the [5,6] adducts by thermal elimination of nitrogen can be explained by the stepwise mechanism first proposed by Luh and coworkers [39] and further studied by Solà and coworkers [40] (see Fig. 5.1.2). From their results, the azide addition takes place on a [6,6] bond and is followed by the cleavage of the N-N

bond. The cleavage of the C-N bond occurs simultaneously with the formation of the new C-N bond. However, since the N_2 molecule sterically prevents the nitrene substituent from adding to the originally attacked [6,6] bond, the nitrene substituent is forced to attack either of the two adjacent [5,6]-ring junctions [39, 3, 40]. The 3'-imino[60]fulleryl-3'-deoxythymidine synthesis by addition of 3'-azido-3'-deoxy-thymidine on a [60]fullerene followed by nitrogen elimination is described in Fig. 5.1.2. The elimination can also be followed using mass spectrometry (see Fig. 5.1.3).

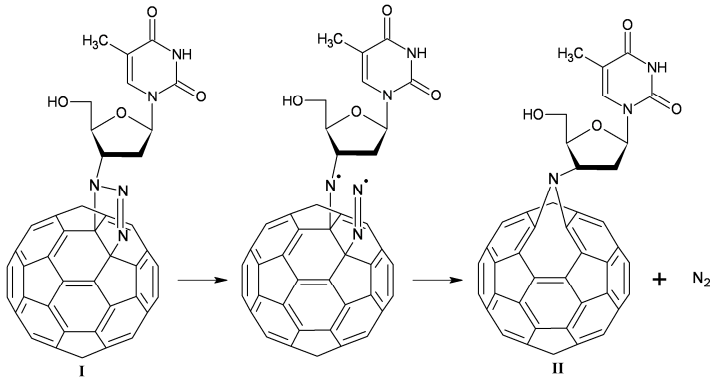

Fig. 5.1.2. Formation of the 3'-imino[60]fullerene-3'-deoxythymidine (**II**). The cycloaddition of the azido group followed by the thermal elimination of nitrogen results in the [5,6]-open isomer as illustrated.

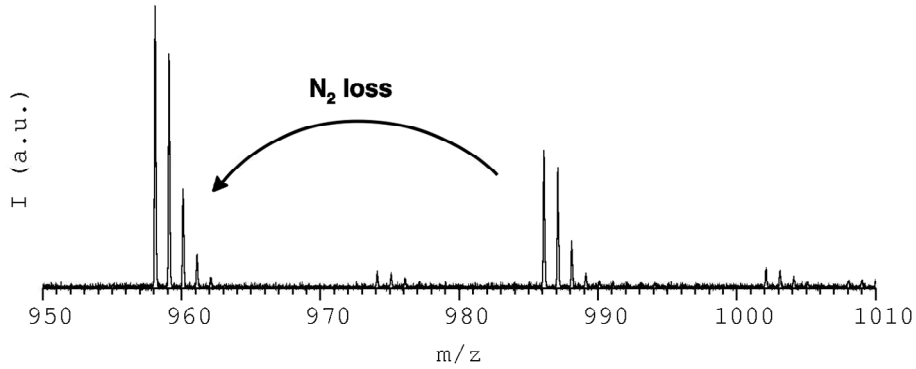

Fig. 5.1.3. Negative ion electrospray mass spectrum of 3'-azido-3'-deoxythymidine reacted with [60]fullerene at a temperature of 60°C for 24 h. The isotopic pattern starting at 986 m/z corresponds to the deprotonated 3'-azido-[60]fulleryl-3'-deoxythymidine whereas at 958 m/z we have the deprotonated 3'-imino-[60]fulleryl-3'-deoxythymidine obtained by nitrogen elimination. The ions present in traces (at 974 m/z and 1002 m/z) are the mono-oxidized products. The electronebulized solution was composed of Toluene:ACN (80:20 v:v) with 1% TEA.

The electronic structure of the [5,6]-open imino derivative is very appealing because it largely conserves the 60 π-electron system of the fullerene core even though the presence of the nitrogen atom affects the excited-state energies due to an electronic interaction between the nitrogen lone pair and the fullerene core [3]. This system can furthermore undergo the attachment of virtually any functionalizing group [3]. This is particularly relevant for the functionalization of a [60]fullerene by polyadducts.

The present section aims at: (1) describing the synthesis, the purification and the experimental characterization of the system composed of a fullerene molecule functionalized by 3'-azido-3'-deoxythymidine (2) discussing fragmentation and an intramolecular charge transfer using mass spectrometry with electrospray ionization (3) discussing interaction between the thymine nucleobase and the [60]fullerene.

5.1.1. Experimental

The [60]fullerene and the 3'-azido-3'-deoxythymidine used in the synthesis were purchased from Sigma-Aldrich respectively at purities of 99.5% and 98%. The HPLC grade toluene (+99% purity, water content < 0.01%) was purchased from Biosolve (Valkenswaard, The Netherlands).

The 3'-imino[60]fulleryl-3'-deoxythymidine (see Fig. 5.1.2.**II**) was prepared according to the general procedure for the addition of azides developed by Prato et al. [31]. A mixture of C_{60} (74 mg) and 3'-azido-3'-deoxythymidine (25 mg) was heated at a temperature of 80°C in 60 mL of toluene under constant agitation for about 96 hours. Reaction at 80°C yields the monoadduct (**II**) exclusively whereas polyadducts are observed for temperatures above 120°C. The prolonged heating was required for the total conversion of the triazolino- (**I**) to iminofullerene (**II**) by nitrogen emission. Figure 3 presents the mass spectrum of the products formed when the reaction takes place at 60°C for 24 hours; the conversion from (**I**) to (**II**) is only partial.

The 3'-imino[60]fulleryl-3'-deoxythymidine obtained is easily separated from the unreacted [60]fullerene by liquid phase chromatography using a C-18 column [41, 42, 43, 44]. The purification was carried out on a semi-preparative HPLC system with a 10 x 250 mm C-18 PrincetonSPHER Semi-PREP HPLC column (60 Å pore size, carbon load of 20%, 5 µm particle size, Princeton Chromatography, Cranbury, NJ, USA) at a temperature of 20°C. The eluent used under isocratic conditions was acetonitrile-toluene (27:73, v:v) at a 2 mL min^{-1} flow rate. 200 µL of sample were injected repetitively. A Waters 2487 UV-visible detector set at 320 nm was used for automatic peak detection and collection.

The collision induced dissociation mass spectrometric measurements were performed on a hybrid quadrupole time-of-flight, Q-Tof Ultima (Waters), equipped with either a standard or a nano-electrospray source. The ions are mass selected using a quadrupole, activated by collisions with argon in an octopole and analysed in a time-of-flight operated in reflectron mode calibrated using phosphoric acid. The identification of the 736 m/z fragment was performed by exact mass determination using a hybrid quadrupole-FT-ICR, APEX-Qe 9.4T (Bruker), equipped with a standard electrospray source. The ions are mass selected using a quadrupole, activated by Infrared Multi-Photon Dissociation (IRMPD) and analysed in the ICR cell. The time of irradiation (~60 ms) is adjusted so that both the parent ion and its fragments are observed. Internal calibration was performed versus the isotopes of $C_{60}^{\bullet -}$ and the first isotope of the deprotonated 3'-imino[60]fulleryl-3'-deoxythymidine using linear interpolation.

5.1.2. Results

The structural integrity of the synthesized C_{60} derivative, the 3'-imino[60]fulleryl-3'-deoxythymidine, was controlled by tandem mass spectrometry and ^{1}H NMR spectroscopy.

A. NMR spectra

The ^{1}H NMR spectral data (Not shown) obtained in 100% deuterated toluene (Aldrich) revealed peaks corresponding to the deoxyribose and thymidine units. As observed by Prato *et al.* for other adducts and by Ungurenasu *et al.* [18] the ^{1}H NMR spectrum of the nucleoside unit is very similar to that of the starting nucleoside analog with a small downfield shift due to the influence of the fullerene. No apparent hydrogen transfer from the nucleoside to the [60]fullerene is detected.

B. Mass spectrometry

The ESI-MS and nanoESI-MSMS spectra were obtained in positive ion mode from a solution of acetonitrile-toluene (20:80, v:v) saturated in sodium chloride and in negative ion mode from a solution of acetonitrile-toluene (20:80, v:v) with or without 1% of triethylamine added to induce deprotonation. In positive ion mass spectrometry the 3'-imino[60]fulleryl-3'-deoxythymidine was observed sodiated. In negative ion mass spectrometry, on the other hand, two different ion production mechanisms were observed to take place leading to two different negatively charged species. Depending on the amount of triethylamine in the solution and on the diameter of the capillary used for electronebulization, deprotonation (leading to an isotopic distribution starting at 758 m/z) and/or reduction (leading to an isotopic distribution starting at 759 m/z) can occur (see Fig. 5.1.4).

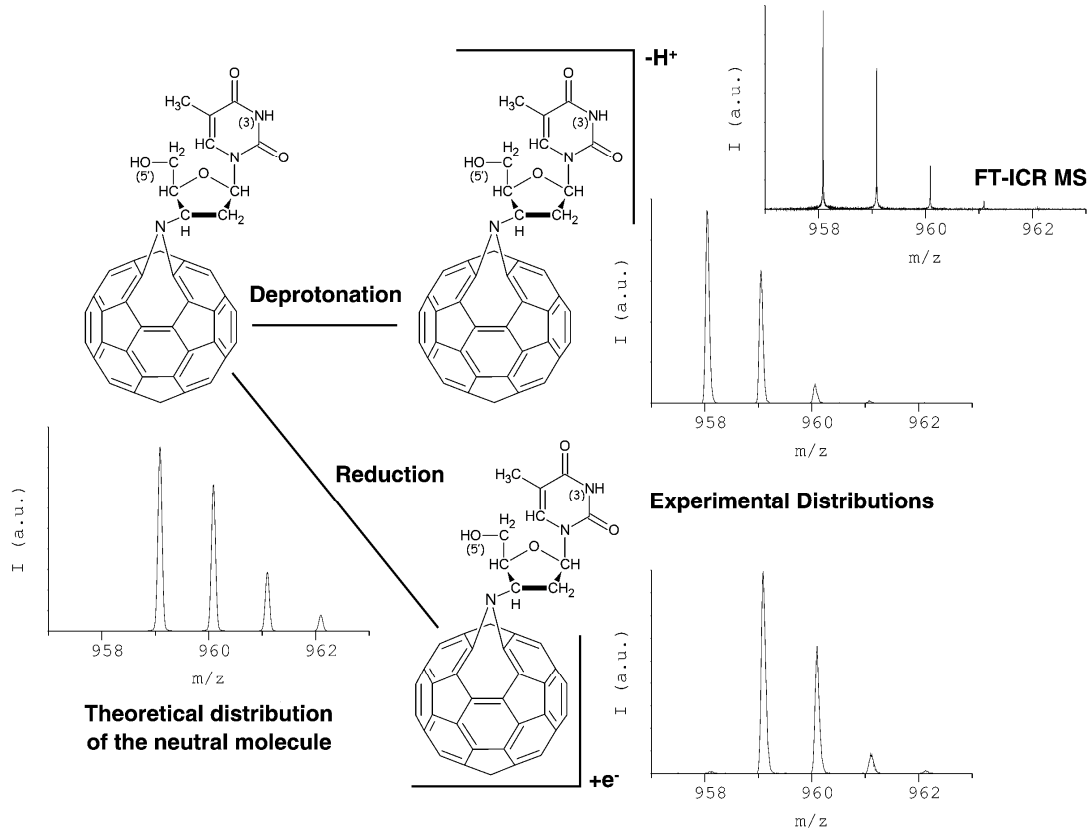

Fig. 5.1.4. The two ion production mechanisms of 3'-imino[60]fulleryl-3'-deoxythymidine taking place in negative ion mode electrospray mass spectrometry. The deprotonation spectrum (isotopic distribution starting at 758 m/z) was obtained using standard electrospray from a solution with 1% TEA added both on a Q-FT-ICR and a Q-ToF. The reduction spectrum (isotopic distribution starting at 759 m/z) was obtained using nanoelectrospray without triethylamine on a Q-ToF.

The electronebulization of the solution containing triethylamine results in standard electrospray – flow rate about 4 µL/min and a capillary diameter about 300 microns – only in the formation of deprotonated molecules (see Fig. 5.1.4). In nanoelectrospray on the other hand – flow rate ranging from 0.5 to 1 µl/hour and a capillary diameter of the needle about 1 micron – both deprotonation and reduction can take place. Reduction occurs when the electrospray source behaves as an intrinsic electrochemical cell and was first demonstrated for fullerenes by Dupont *et al.* [45] and for fullerene derivatives using nanoelectrospray by Drewello and coworkers [46].

Since reduction also takes place in nanoelectrospray in the absence of triethylamine, triethylamine is not required for the radical ion formation. Consequently ion production by photoinduced electron transfer between the excited singlet C_{60} and the amine can be ruled out [47, 48].

Collision induced dissociation (CID) using argon as collision gas of the mass selected parent ions in positive and negative mode was carried out. Nanospray was used for the CID measurements because of the improved sensitivity and lower sample consumption. Larger needle diameters and triethylamine were used to study the deprotonated ions in presence of negligible reduction. Experimental conditions can also be devised to study simultaneously deprotonation and reduction (see Fig. 5.1.5). The Laboratory frame collision energies are given only as indications. The amount of energy transferred to the ions upon emission in gas phase from an acetonitrile/toluene solution is highly dependent on the ion production/desolvatation mechanism and the source conditions e.g. needle diameter and voltages.

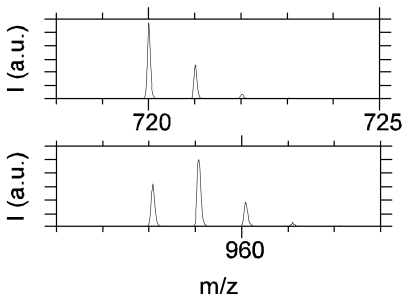

Fig. 5.1.5. The isotopic abundance of ^{12}C and ^{13}C obtained from the experimental mass spectrum of the pristine [60]fullerene, top spectrum, are respectively p=0.99*24* and (1-p)=0.00*76*. They are used to extract the two contributions to the experimental spectrum of the 3'-imino[60]fulleryl-3'-deoxythymidine obtained using nanoelectrospray ion production with 1% triethylamine added. The two contributions to the isotopic pattern of bottom spectrum about 5*4*% and 4*6*% respectively correspond to the deprotonated and radical anions of 3'-imino[60]fulleryl-3'-deoxythymidine.

The different fragments observed upon collision induced dissociation of the protonated, deprotonated and radical 3'-imino[60]fulleryl-3'-deoxythymidine ions and discussed below are summarized in Fig. 5.1.6.

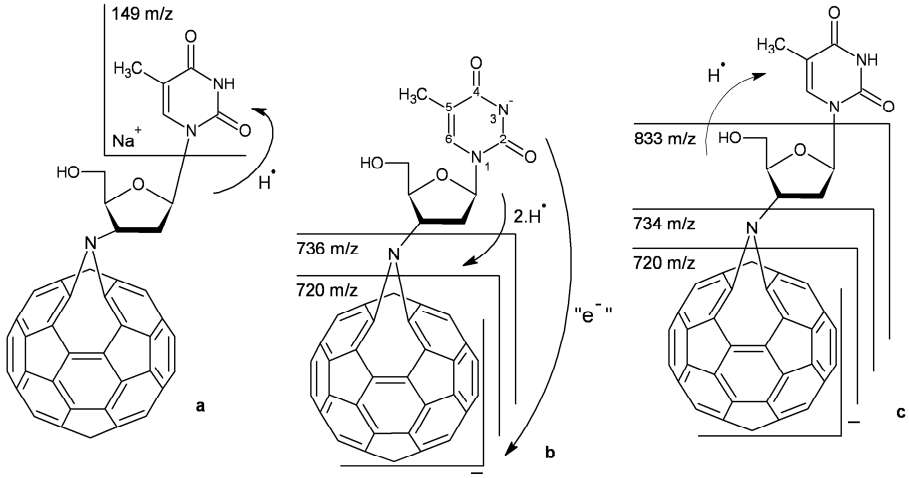

Fig. 5.1.6. Fragments of the 3'-imino[60]fulleryl-3'-deoxythymidine observed upon collision induced dissociation of the parent ions resulting from cationization by Na^+ **a**, from deprotonation (N-3 is one of the two possible deprotonation sites, the hydroxyl on the deoxyribose is the other one) **b** and from reduction **c**.

B.1. Fragmentation in positive mode

For collision energies in the laboratory frame up to ~70eV, the collision induced dissociation of the sodiated 3'-imino[60]fulleryl-3'-deoxythymidine yields the sodiated thymine ion exclusively (see Fig. 5.1.7). Higher collision energies lead to the increasing observation of the C_{60}^+, $C_{60}H^+$ cations. The thymine fragment of mass to charge ratio 149 m/z corresponds to the closed shell cation $[Thymine + Na]^+$. The transfer of a radical hydrogen atom from the deoxyribose to the nucleobase upon the cleavage of the N-glycosidic bond is commonly observed in nucleosides [49].

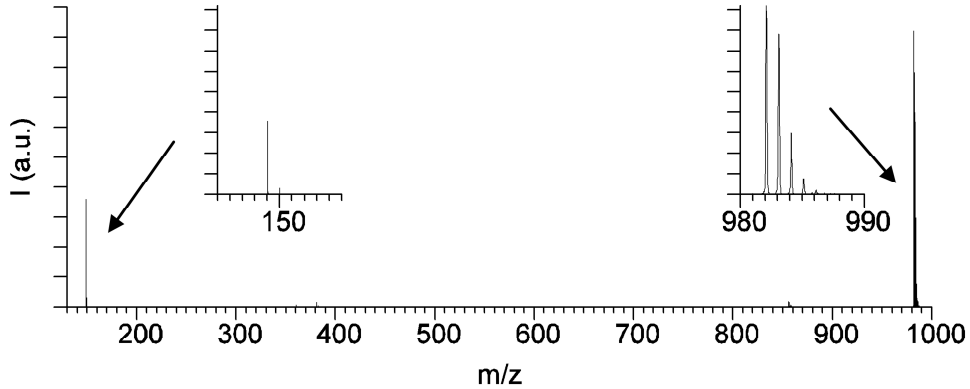

Fig. 5.1.7. MSMS CID spectra of the sodiated 3'-imino[60]fulleryl-3'-deoxythymidine parent ion (**Fig. 5.1.6-a**) (982 m/z) with a collision energy in the laboratory frame about 50 eV. The only fragment observed at 149 m/z for low activation energies is the sodiated thymidine.

B.2. Fragmentation in negative mode

When 3'-imino[60]fulleryl-3'-deoxythymidine is nanosprayed from a solution of acetonitrile-toluene (20:80, v:v) with 1% triethylamine both deprotonated and radical ions formed by reduction can contribute to the isotopic pattern of the parent ion as can be seen in Fig. 5.1.5. Deprotonation results from the addition of triethylamine to the solution. Reduction, on the other hand, is significant or even dominant when gold coated needles made of borosilicate with an orifice about 1 micrometer in diameter are used. The percentage of radical and deprotonated species strongly depends on the capillary used and the amount of triethylamine added.

To discuss the collision induced fragmentation of the deprotonated and radical parent ions, the ions responsible for the "^{12}C only" peak of the parent ion isotopic patterns (see Fig. 5.1.8 and 5.1.9) were mass selected and fragmented, see Fig. 5.1.10 (ions of m/z 958) and 5.1.11 (ions of m/z 959).

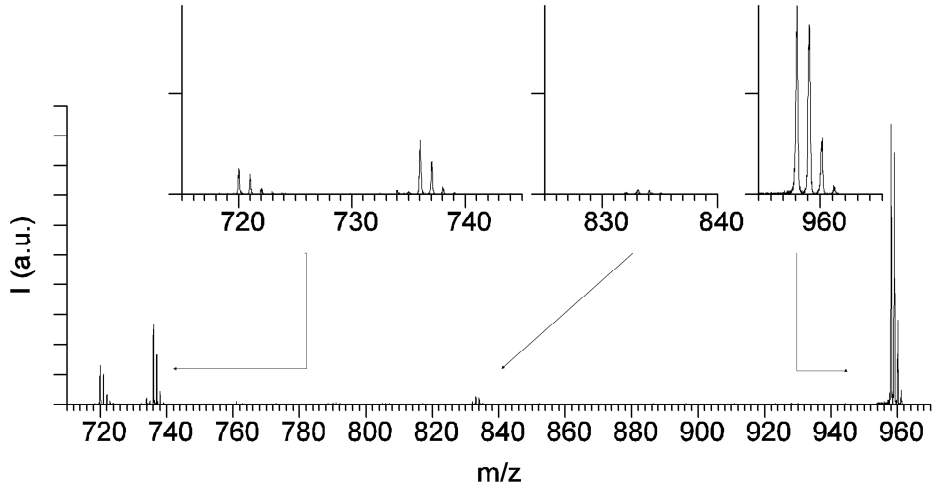

Fig. 5.1.8. MS spectrum of the deprotonated 3'-imino[60]fulleryl-3'-deoxythymidine (**Fig. 5.1.6-b**) (958 m/z for the "^{12}C only" isotopic signal) as major ion obtained at a collision energy about 70 eV with argon in the laboratory frame. A small contribution of the radical 3'-imino[60]fulleryl-3'-deoxyribose can be inferred from the isotopic pattern of the parent ion (intensity of the 959 m/z isotopic signal) and the negligible signal at 833 m/z (see Fig. 5.1.7).

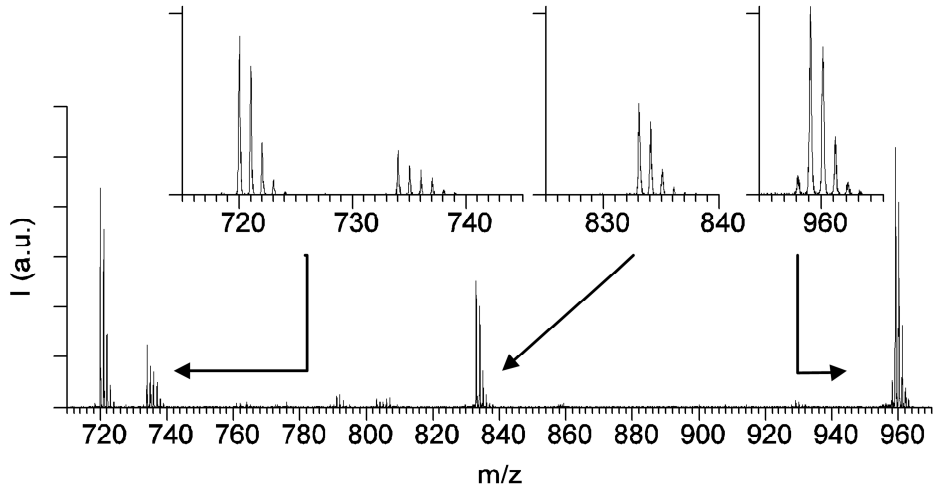

Fig. 5.1.9. MS spectrum of the radical 3'-imino[60]fulleryl-3'-deoxythymidine anion (**5.1.6-c**) (959 m/z for the "^{12}C only" isotopic signal) as major ion obtained at a collision energy about 70 eV with argon in the laboratory frame. The negligible presence of deprotonated 3'-imino[60]fulleryl-3'-deoxyribose can be assessed from the isotopic signal at 958 m/z.

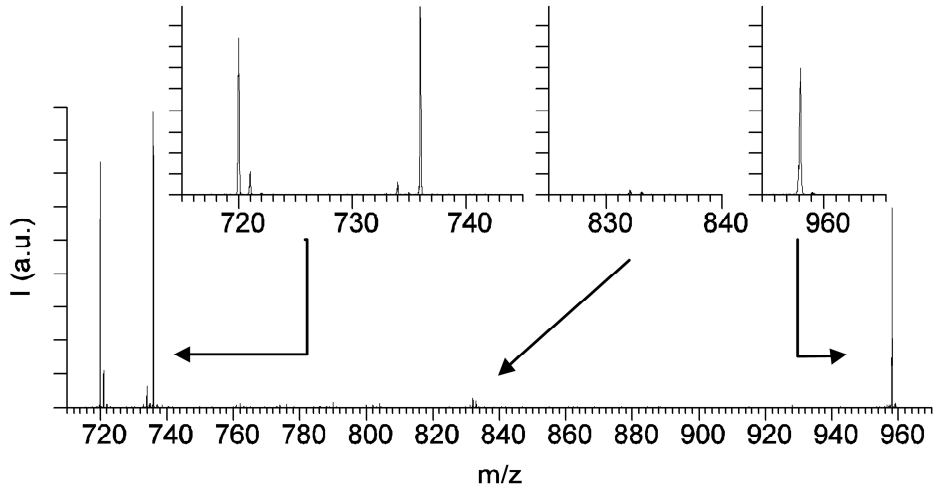

Fig. 5.1.10. MSMS CID spectrum of the first peak (958 m/z) of the isotopic pattern of the deprotonated 3'-imino[60]fulleryl-3'-deoxythymidine parent ion (**5.1.6-b**) obtained at a collision energy about 70 eV in the laboratory frame. Reduction does not contribute to the fragments since the 959 m/z isotopic signal has been excluded upon mass selection. The small peak at 721 m/z likely corresponds to $C_{60}H^-$.

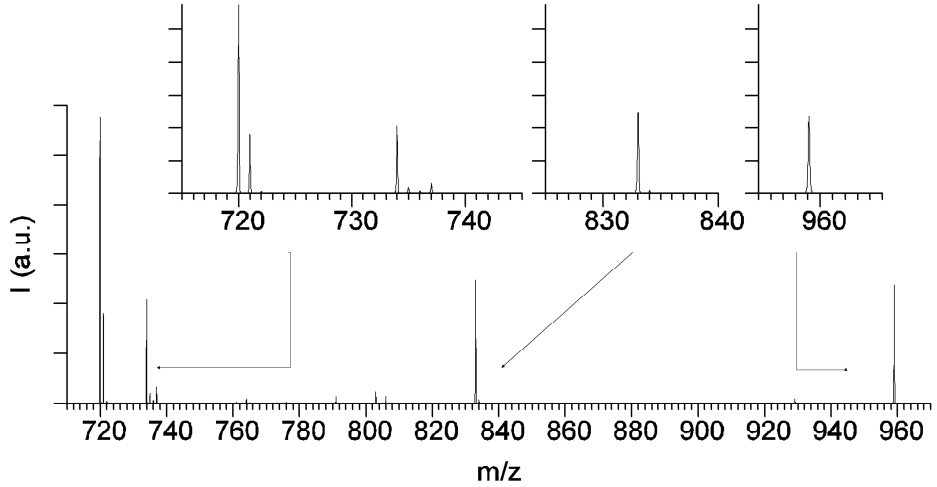

Fig. 5.1.11. MSMS CID spectrum of the radical 3'-imino[60]fulleryl-3'-deoxythymidine parent ion (**5.1.6-c**) of mass to charge ratio equal to 959 m/z at a collision energy about 70 eV in the laboratory frame. The contribution of the deprotonated ions to the signal is negligible as can be inferred from the negligible signals at 736 and 737 m/z. The main fragments observed are the [3'-imino[60]fullerene-3'-deoxyribose]$^-$, the radical $C_{60}^{\bullet -}$ and the $C_{60}N^-$ anions. The small peak at 721 m/z likely corresponds to $C_{60}H^-$.

5.1.3. Discussion

In most fullerene based donor-acceptor dyads studied, molecular spacers are used to avoid electronic delocalization and electron transfer typically occurs upon photoexcitation [15]. In the present system a thymine nucleobase is linked to a [60]fullerene by a 2',3'-deoxyribose. Ion production is observed to take place via cationization in positive mode, deprotonation and reduction in negative mode. Discussion of the charge carrying site will be performed according to the methodology used in MALDI by Fati *et al.* [50, 51] for amphiphilic and dendrimeric fullerene derivatives and by Zenobi and coworkers [6] for donor-acceptor and donor-bridge-acceptor fullerenes.

Depending on the ion production mechanism different fragments are observed upon collision induced fragmentation (see Fig. 5.1.7, 5.1.10 and 5.1.11). The different charged fragments observed are summarized in the partial reaction schemes hereunder.

$$[3'\text{-N-}C_{60}\text{-}3'\text{-deoxythymidine} + Na]^+ \rightarrow [\text{Thymine} + Na]^+$$

$$[3'\text{-N-}C_{60}\text{-}3'\text{-deoxythymidine}]^{\bullet -} \rightarrow [3'\text{-N-}C_{60}\text{-}3'\text{-deoxyribose} - H^{\bullet}]^-$$

$$[3'\text{-N-}C_{60}\text{-}3'\text{-deoxythymidine}]^{\bullet -} \rightarrow C_{60}N^-$$

$$[3'\text{-N-}C_{60}\text{-}3'\text{-deoxythymidine}]^{\bullet -} \rightarrow C_{60}^{\bullet -} \text{ and } C_{60}H^-$$

$$[3'\text{-N-}C_{60}\text{-}3'\text{-deoxythymidine} - H]^- \rightarrow C_{60}NH_2^-$$

$$[3'\text{-N-}C_{60}\text{-}3'\text{-deoxythymidine} - H]^- \rightarrow C_{60}^{\bullet -} \text{ and } C_{60}H^-$$

Functionalization of fullerene molecules by compounds, such as crown ethers, containing a binding site for alkali metals was first reported by Wilson and Wu [52]. Collision induced dissociation of the sodiated 3'-imino[60]fulleryl-3'-deoxythymidine (982 m/z) in tandem mass spectrometry yields the sodiated thymine fragment (149

m/z); see Fig. 5.1.7. This result is consistent with alkali metals interacting with the nucleobase rather than with the sugar units [25, 26, 53].

In negative mode two ion production mechanisms can take place: reduction and deprotonation (see Fig. 5.1.4). For some experimental conditions the two ion production mechanisms can be present simultaneously as seen in Fig. 5.1.5.

Even though Guldi *et al.* [54] showed that stepwise functionalization of C_{60} caused a gradual destruction of the fullerene π system and correlated linearly with its redox properties, the radical electron is most likely located on the fullerene due to the small predicted electron affinity [55], 0.44 eV, and cross section of the thymidine compared to the 2.7 eV electron affinity [56] and cross section of the [60]fullerene. Collision induced dissociation of the radical anion 3'-imino[60]fulleryl-3'-deoxythymidine yields two fragment anions resulting from the cleavage of the N-glycosidic bonds as well as the radical anion $C_{60}^{\bullet -}$. The radical anion [3'-N-C_{60}-3'-deoxyribose – $H^{\bullet}$]$^-$ (833 m/z) results from the cleavage of the N-glycosidic bond between the deoxyribose and the thymine and the transfer of a radical hydrogen from the sugar to the nucleobase. This cleavage is similar to the cleavage taking place in positive mode for the sodiated parent ion that yields the sodiated thymine fragment (149 m/z). The [3'-N-C_{60}]$^-$ (734 m/z) fragment results from the cleavage between the deoxyribose and the imino[60]fullerene. The observation of the radical ion $C_{60}^{\bullet -}$ (720 m/z) is likely a direct consequence of the charge location on the [60]fullerene. Guldi *et al.* [3] showed that the fullerene π-system was affected by the free electron pair of the imino bond nitrogen atom. From their theoretical and experimental results the [6,5]-open isomer of the imino[60]fullerene is characterized by a 62 π-electron system [3] that does not isomerize upon extensive illumination. The presence of a radical electron on the [60]fullerene core however increases the number of electrons by one and is likely

responsible for the destabilization of the bond between the fullerene and the N-glycosidic nitrogen, yielding the $C_{60}^{\bullet-}$ fragment. Eiermann *et al.* [33] indeed observed that [5,6]-open isomers of methano[60]fullerene could convert to [6,6]-closed isomers when a radical electron was added to the fullerene core. Their suggested mechanism adapted to the present system would involve the transition structure between the [5,6]-open and the [5,6]-closed imino[60]fullerene with one of the C-N bond broken as intermediate structure before the cleavage of the remaining C-N bond.

Upon deprotonation, the closed-shell deprotonated 3'-imino[60]fulleryl-3'-deoxythymidine anion has its charge initially localized on the thymidine subunit since there is no proton on C_{60}. Analysis of the Raman spectra of thymine, 2'-deoxythymidine and 3'-azido-3'-deoxythymidine both in solution at different pH and adsorbed on Ag colloids by Rivas *et al*. [25, 26] gives evidence that their deprotonation takes place in N-3 of the nucleobase unit (see Fig. 5.1.6). However, in the present case, C_{60} presence might affect the deprotonation site as will be further discussed in the next section. The fragments present in the CID spectra of the deprotonated 3'-imino[60]fulleryl-3'-deoxythymidine are the radical anion $C_{60}^{\bullet-}$ and an anion of mass to charge ratio equal to 736 m/z (see Fig. 5.1.8). Based on the mass obtained using the hybrid quadrupole time-of-flight, this fragment corresponds either to $C_{60}O^{\bullet-}$ (735.9955 m/z) or to $C_{60}NH_2^-$ (736.0193 m/z). Exact mass determination was performed using a hybrid quadrupole FT-ICR mass spectrometer. Deprotonated 3'-imino[60]fulleryl-3'-deoxythymidine was selected in the quadrupole, transferred to the ICR cell and partially fragmented using infrared multi-photon dissociation (IRMPD) since collisional activation with Argon within the collsion cell of the FTMS spectrometer proved unsuccessful. The fragments obtained correspond to the radical anion $C_{60}^{\bullet-}$ and an anion of mass to charge ratio equal to 736.0184 m/z (see Fig.

5.1.12). The only composition found for this m/z ratio with an error less than 2 ppm is $C_{60}NH_2^-$ with an error of 1.2 ppm. It is believed that collisional activation with argon results in the same fragments as with IRMPD – both are slow activation techniques allowing rearrangements – provided multiple collisions occur, which is the case on our hybrid time-of-flight instrument. Identification of the hydrogen atoms transferred from the thymidine unit to the C_{60} has proved elusive. Hydrogen/deuterium exchange was inconclusive due to hydride attachment when methanol was used for the exchange in gas phase.

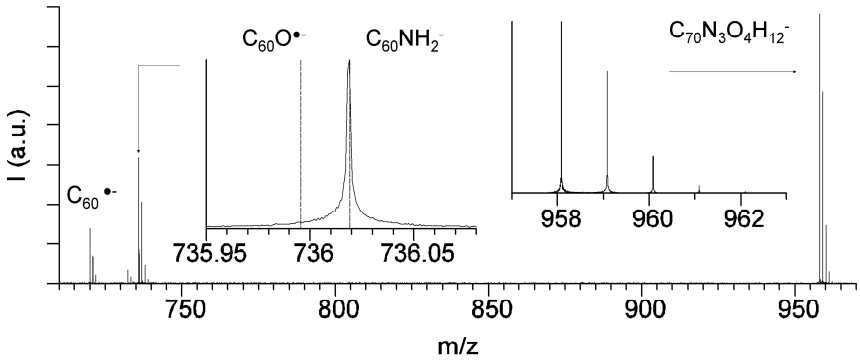

Fig. 5.1.12. MSMS IR-MPD FT-ICR spectrum of the deprotonated 3'-imino[60]fulleryl-3'-deoxythymidine parent ion ($C_{70}N_3O_4H_{12}^-$). A 736.0184 m/z ratio is obtained for the first isotopic peak of the most intense fragment signal, following linear internal calibration using the first three isotopes of $C_{60}^{\bullet -}$ and the first isotope of the parent ion. It corresponds within a 1.2 ppm error to the $C_{60}NH_2^-$ anion. No signal corresponding to a $C_{60}O^{\bullet -}$ anion is detected. The resolution at half height is higher than $3\ 10^5$. The three small peaks about 732.3847 m/z are interferences.

However, since all the fragments include the [60]fullerene, a charge transfer from the thymidine subunit to the C_{60} occurs. The detection of the $C_{60}^{\bullet -}$ fragment is an argument in favour of this transfer since the additional electron on the [60]fullerene core would destabilize the bond between the N-glycosidic nitrogen and the [60]fullerene in the same way as for the radical ions as discussed before.

The presence of the $C_{60}H^-$ fragment of m/z 721 (see Fig. 5.1.10 and 5.1.11) could be explained by the 62 π-electron system characterizing the fullerene core and the nitrogen free electron pair of the [6-5]-open isomer studied [23] or follow from the transfer of an additional electron to the fullerene core (63 π-electron system). Indeed Cliffel and Bard [42] showed that $C_{60}^{\bullet -}$ is a very weak base whereas the dianion is a relatively strong one. No evidence of the origin of the hydrogen transferred to the C_{60} has been obtained even though it is expected, as for the $C_{60}NH_2^-$ fragment ion, to come from the 2',3'-deoxyribose.

5.1.4. Conclusion

Successful synthesis, purification and characterization were demonstrated for the 3'-imino[60]fulleryl-3'-deoxythymidine. Characterization was performed using electrospray mass spectrometry both in positive and in negative ion mode. In negative mode mass spectrometry two ion production mechanisms take place, reduction and deprotonation. The ion production mechanism and consequent charge localization can be experimentally controlled by using gold coated needles with a very small diameter for reduction and by using triethylamine for deprotonation.

Interaction between the C_{60} and the deoxythymidine was studied using collision induced dissociation (CID) in mass spectrometry. CID of the sodiated 3'-imino[60]fulleryl-3'-deoxythymidine yields the sodiated thymine with a radical hydrogen atom transferred from the deoxyribose to the thymine upon cleavage of their shared N-glycosidic bond. Upon reduction the charge is located on the [60]fullerene and similarly to the sodiated 3'-imino[60]fulleryl-3'-deoxythymidine, the cleavage of the N-glycosidic bonds is observed. Deprotonation on the other hand is known to take

place on the thymidine subunit, and results in a CID spectrum different from those of the other 3'-imino[60]fulleryl-3'-deoxythymidine ions.

5.2. Characterization of 3'-imino[60]fulleryl-3'-deoxythymidine using electron photo-detachment and ab-initio calculations

As described in the previous section, both the sodiated and reduced 3'-imino[60]fulleryl-3'-deoxythymidine fragments include the ionic site, respectively the thymine and C_{60} subunits and the only observed rearrangement for these two species involves a radical hydrogen transfer from the deoxyribose to the thymine upon the cleavage of their shared N-glycosidic bond. The deprotonated 3'-imino[60]fulleryl-3'-deoxythymidine behaves differently. Firstly, upon collision induced and infrared multiphoton dissociation the fragments do not include the most likely deprotonation sites, N-3 and O-5'. Secondly, elemental composition analysis of the fragments formed by infrared multi-photon dissociation of the deprotonated 3'-imino[60]fulleryl-3'-deoxythymidine resulted in their identification as $C_{60}^{\bullet -}$ and $C_{60}NH_2^-$ ($C_{60}O^{\bullet -}$ was ruled out, see Fig. 5.1.12) [29]. This implies that both an electron transfer and a double radical hydrogen transfer to the C_{60} take place. Understanding of these processes and of the mechanisms involved is required prior to studying the interaction with 2-aminopurine.

If the electron affinity of C_{60} has been extensively studied and is reported to be in the 2.65-269 eV range [57, 56, 58], only a limited number of experimental and theoretical results are available in the literature on those of neutral and dehydrogenated thymine and thymidine. The reported experimentally measured values of the thymine electron affinity are ~0 and > 0 [59, 60]. Theoretically, the adiabatic electron affinities

calculated at the B3LYP/DZP++ level for thymidine and thymine are respectively equal to 0.44 (0.31) and 0.20 (0.06) eV with (and without) zero-point vibrational correction [55]. The vertical detachment energy for thymidine was calculated to be 0.94 eV [55]. The adiabatic electron affinities with (and without) zero-point vibrational correction, vertical electron affinities and vertical detachment energies calculated for thymine dehydrogenated in N3 (see Fig. 5.1.6) at the B3LYP/DZP++ level are respectively equal to 3.69 (3.74), 3.27 and 3.89 eV [61]. If dehydrogenation occurs in C6 (see Fig. 5.1.6), the values are respectively 2.61 (2.60), 2.08 and 3.13 eV whereas if it occurs in N1 (see Fig. 5.1.6), the values are respectively 3.21 (3.22), 3.05, 3.27 eV, in agreement with recent measurements [62].

In the present section, the focus is on charge (re)localization and molecular rearrangements following deprotonation of the deprotonated 3'-imino[60]fulleryl-3'-deoxythymidine (FuNdT). Different questions arise from their observation. What is the deprotonation site? Two deprotonation sites are possible, the N3 site on the thymine known to be the preferential deprotonation site of thymidine in aqueous solution and the site in O5' on the deoxyribose unit (see Fig. 5.2.1). What is the origin of the hydrogen atoms transferred? The most plausible hydrogen atoms are located in C1', C5' and O5'. How does the rearrangement take place? Where is the charge located on the molecule? If deprotonation occurs in N3, the negative charge is initially localized on the thymine unit. However, since the only fragments detected in mass spectrometry are C_{60}^- and $C_{60}NH_2^-$, an electron migration to the acceptor C_{60} unit accompanied or not by H migration must take place. The present set of experiments and theoretical calculations aim at clarifying these issues [29, 30].

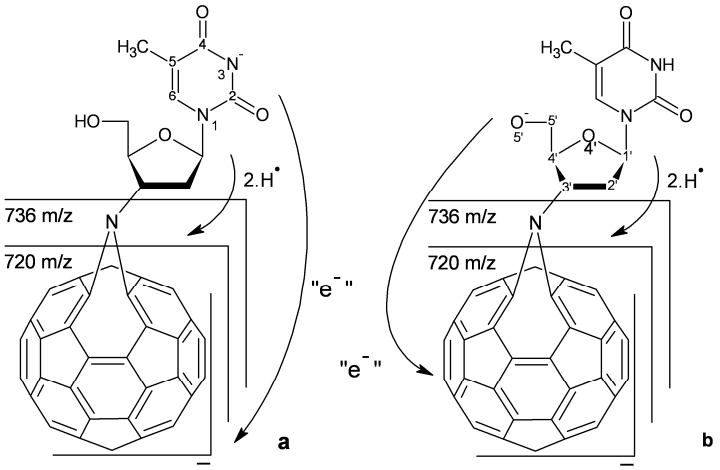

Fig. 5.2.1. The two potential deprotonation sites of 3'-imino[60]fulleryl-3'-deoxythymidine, respectively N-3 (**a)** and O-5' (**b).** The deprotonation is performed by addition of 0.4-1% TEA in a toluene : ACN 80:20 v:v solution. Also shown are the fragments of the deprotonated 3'-imino[60]fulleryl-3'-deoxythymidine.

5.2.1. Experimental and modelization

The action spectroscopy measurements were performed at the Heinrich-Heine-Universität in Professor Weinkauf group and the results published in reference [30].

The molecules are brought into the gas phase by electrospray ion production at atmospheric pressure and transferred through several pumping stages into the Paul trap of the mass spectrometer. Prior to undergoing photodetachment or detection, the ions stored in the Paul trap thermalize by collisions with helium. However, due to the heating and cooling processes inherent to the transfer form the solution to the gas-phase, some of these ions may exist as higher energy conformers or tautomers. As a consequence and since the composition of the conformer mixture cannot be assessed, averaging over the whole ion population stored takes place. The ion populations stored in the ion trap are photoexcited by overlapping their trajectory with 5 laser shots (1 to 4 mJ/shot) at wavelengths corresponding to the five first harmonics of a Nd:YAG of 1064nm fundamental (see Fig. 5.2.2). The successive harmonics are used

to bracket the electron photodetachment threshold of the deprotonated 3'-imino[60]fulleryl-3'-deoxythymidine anions.

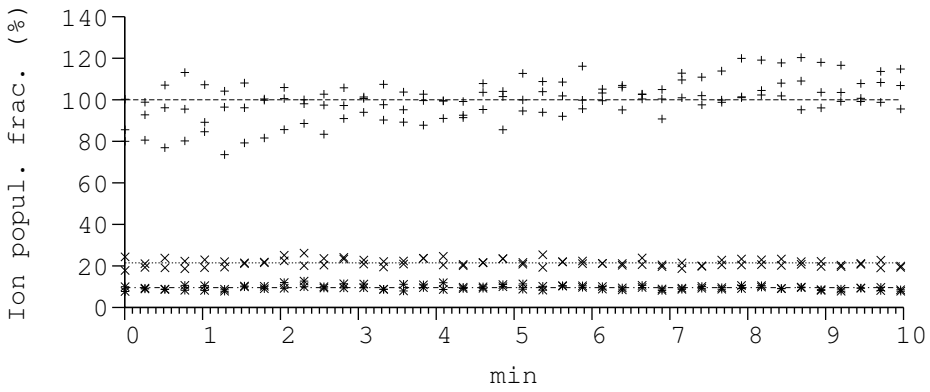

Fig. 5.2.2. Typical set of raw photodetachment data: Total ion currents associated with deprotonated FdT in absence (+) and in presence (x) of laser excitation at 535 nm (5shots 1mJ/shot). The contribution of the fragment ions in presence of laser excitation to the total ion current is also shown (*). Note that the laser effects are much larger than ESI source fluctuations over time.

All the computations were carried out at the B3LYP/3-21G level using the quantum chemistry package GAUSSIAN 03 [63]. The 3-21G is a good compromise in view of the size of the system, e.g. C_{60} bond lengths at this level are equal to 1.39 and 1.46 Å in good agreement with the experimentally reported values: 1.41 and 1.46 Å, respectively [64]. A few conformers were further optimized at the B3LYP/6-31G(d) and B3LYP/6-31+G(d) levels with no significant geometrical changes found. Thermodynamically, the enthalpies and entropies were estimated from the partition functions calculated at room temperature (298.15 K) under a pressure of 1 atm, using Boltzmann thermostatistics, the rigid-rotor-harmonic-oscillator approximation, and unscaled harmonic vibrational frequencies.

5.2.2. Results and discussion

For photons ranging from 5.08 (5^{th} harmonic) to 2.32 eV (2^{nd} harmonic) electron detachment (corresponding to a loss of signal by neutral formation) is observed to be predominant with for photons of 2.32 eV more than 70% of the ion population detached.

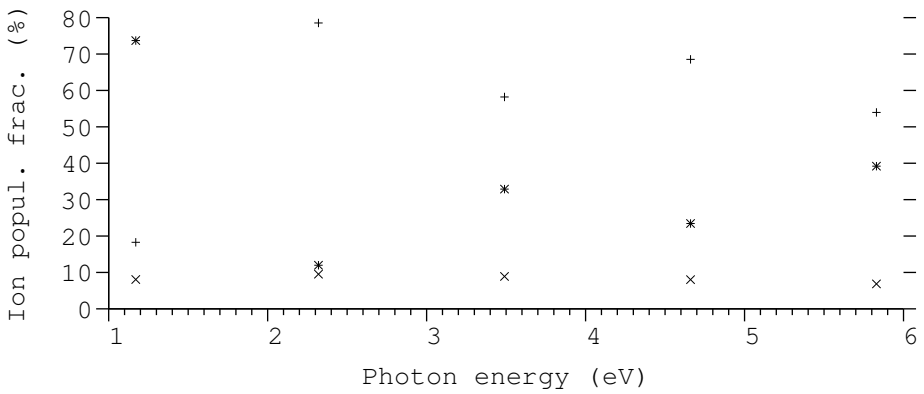

Fig. 5.2.3. Percentage of the ion populations undergoing detachment (+), fragmentation (x) and not affected (*) by laser excitation using 5 shots of 1 mJ at 213.5, 266, 355, 535 and 1064 nm.

Using 5 shots of 1 mJ at 1064 nm (1.17 eV), limited photodetachment and photofragmentation of deprotonated 3'-imino[60]fulleryl-3'-deoxythymidine are observed (see Fig. 5.2.3). Since $C_{60}^{\bullet -}$ photodetachment at 1064 nm corresponds to a multiphoton process and already occurs at a pulse energy of 1 mJ, the observed excitation is most likely resonant. Indeed, C_{60}^{-} absorbs at 1080 nm in solution [65, 66, 67, 68, 69] and C_{60}^{-} undergoes delayed detachment at 1064 nm in the gas phase. Deprotonated thymine, on the other hand, does not absorb 1064 nm radiation even at high pulse energies (6 mJ/pulse) and high shot numbers (up to 50 laser shots). Detachment at 1064 nm suggests either that the charge migrates to the C_{60} immediately following deprotonation, or that formation of fragments with the charge sitting on the C_{60} precede photo-detachment.

$$[3'\text{-N-}C_{60}\text{-}3'\text{-deoxythymidine} - H]^- \rightarrow C_{60}NH_2^-$$

$$[3'\text{-N-}C_{60}\text{-}3'\text{-deoxythymidine} - H]^- \rightarrow C_{60}^{\bullet -} \text{ and } C_{60}H^- \text{ (negligible)}$$

The second harmonics (532 nm, 2.32 eV) radiation can detach with high efficiency. In a simplified approach 3'-imino[60]fulleryl-3'-deoxythymidine can be considered as composed of two chromophores, a C_{60} and a thymine, linked by a non absorbing spacer, the deoxyribose. In that case, the EA affinities of the isolated C_{60} and thymine hold locally, and detachment occurs although the photon energy of the second harmonic, 2.32 eV, is below the measured EA of C_{60}, ≈ 2.67 eV [57, 56, 58]. Within the local ionization potential (IP) hypothesis [70, 71, 72, 73, 74] different explanations are possible:

i) The amount of vibrational energy present is sufficient to allow direct detachment at lower excitation energies. Indeed, C_{60} average excitation energy at 300K is 0.52 eV [75, 76] and additional internal energy could potentially be retained after the ion production and electro-nebulization processes.

ii) The electron affinity of deprotonated 3'-imino[60]fulleryl-3'-deoxythymidine is lower than that of C_{60}. However, because photodetachment is observed for both the deprotonated 3'-imino[60]fulleryl-3'-deoxythymidine and the $C_{60}^{\bullet -}$ anions with comparable yields at a photon energy below the C_{60} electron affinity, the detachment mechanism, their cross sections and their electron affinities are expected to be similar.

iii) Two or more photons are absorbed and cause electron detachment. Because $C_{60}^{\bullet -}$ absorbs green light at 532 nm [57, 5], a cyclic multiphoton

excitation mechanism can happen: The $C_{60}^{\bullet -}$ anion is electronically excited by one photon to S_n. Then the electronic energy is converted to vibrational energy by internal conversion (IC). In a subsequent photoexcitation the same electronic excitation can be performed as in the first step; IC happens again and so on. The resulting high internal energy can then lead to a delayed statistical electron detachment as previously observed also with 532 nm excitation by Wang et al. [57]. Obviously the optical cross section at 532 is already so big that 1 mJ slightly focused with a 200 mm lense allows this multiphoton scheme.

Theoretically, in order to assess the contribution of different conformers, a conformational analysis was performed. The conformational space of the 3'-imino[60]fulleryl-3'-deoxythymidine molecule is, however, too large to allow a fully systematic study. The conformational space of the 3'-imino[60]fulleryl-3'-deoxythymidine was thus explored using the educated guess approach. Four families of neutral conformers have been identified (see Fig. 5.2.4).

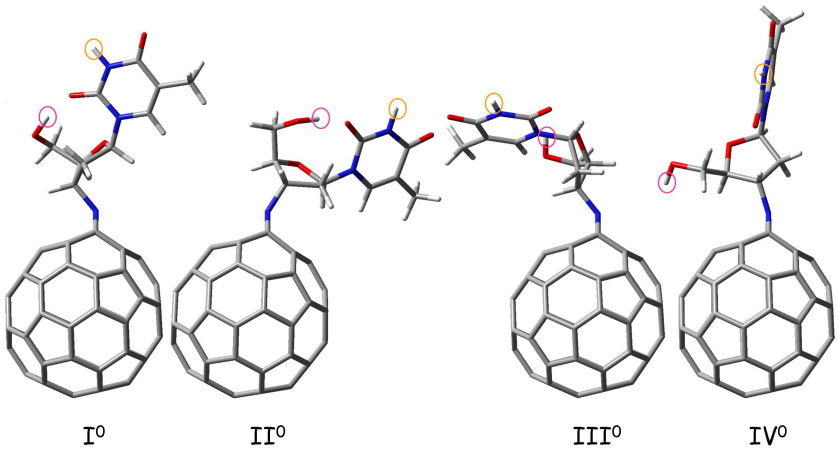

Fig. 5.2.4. The neutral four conformers of 3'-imino[60]fulleryl-3'-deoxy-thymidine investigated. I^0 and II^0 are stabilized by an intramolecular H-bond involving O5'-H of the deoxyribose unit. The N3 and O5' deprotonation are respectively circled in orange and pink.

The four lower-energy neutral conformers computationally investigated differ by the values of the dihedral angles, that is, by the orientation of the spacer deoxyribose unit with respect to both the thymine cycle and the $C_{60}N$ unit. Their geometries are drawn in Fig. 5.2.4. They are energetically ordered as

$$\begin{matrix} & 0.17 & & 0.04 & & 0.41 & \\ I^0 & < & II^0 & < & III^0 & < & IV^0 \end{matrix}$$

where the quantity above the inequality sign indicates the zero-point corrected energy difference (in eV) between the isomers.

The neutral conformers can be subdivided based on the presence of an intramolecular H-bond between the sugar and the thymine and on their spatial extension. In the conformers I^0 and II^0, the O_5'-H group of the deoxyribose residue forms the intramolecular hydrogen bond with the $O_2=C_2$ group of thymine, which is an additional stabilizing factor. The O_5'-H_5'$\cdots O_2$ H-bond of I^0 is characterized by R(O_5'-H_5') = 0.977 Å, r(H_5'$\cdots O_2$) = 1.877 Å, and a stretching frequency ν(O_5'-H_5') = 3291 cm^{-1} (IR intensity amounts to 696 $km \cdot mol^{-1}$). In conformers I^0 (χ=59°), II^0 (χ=60°) and IV^0 (χ=64°) the orientation of the nucleobase relatively to the deoxyribose is *syn* whereas in conformer III^0 (χ=-140°) it is *anti*. In conformers I^0 (γ=38°), II^0 (γ=32°) and III^0 (γ=71°) the hydroxyl group in O5' interacts with the nucleobase, whereas in IV^0 (γ=-178°) such interaction is negligible. (The conformer angles χ and γ are defined according to the IUPAC convention). Additionally, the neutral conformers differ by the orientation of the hydrogen in C1' relatively to the C_{60}. In I^0 and III^0, H1' is above the hexagon involved in the imino bond whereas in II^0 and IV^0, H1' is above one of the carbons bonding the nitrogen N3'. They also differ by the inclination of the

C3'-N3' bond relatively to the C_{60}. When measured relatively to the segment joining N3' to the opposite summit of the pentagon involved in the imino bond, the values of the angle in I^0, II^0, III^0 and IV^0 are respectively 177°, 108°, 176°, 154°.

Deprotonation of 3'-imino[60]fulleryl-3'-deoxythymidine either takes place in N3 on the thymine nucleobase (see Fig. 5.2.5) or in O_5' of the deoxyribose residue (see Fig. 5.2.6). The deprotonation energies (DPE) are reported in Table I. There is clear trend in the DPE's for the I^0 - II^0 and for the III^0 -IV^0 families. In absence of rearrangement, i.e. for the two lowest energy neutral conformers, I^0 and II^0, and in general for deprotonation in N3, the anions deprotonated in N3 are more stable than those deprotonated in O5'. The higher O5' deprotonation energy is easily explained by the extra energy needed to break the sugar-base intramolecular H-bond. Furthermore, N3 deprotonation strengthens the intramolecular O5'–H···O2 ; the H-bond becomes shorter by 0.18 Å and 0.15 Å upon deprotonation of I^0 and II^0. Thermodynamically, the calculated deprotonation energies of the N3 deprotonated anions (see Table 5.2.I), $DPE_{I\text{-}IV}$(N3), fall within a range of 346 - 353 kcal/mol in agreement with ref. [77]. On the other hand, when a stabilizing rearrangement occurs, e.g. for the conformers III^0 and IV^0 deprotonated in O5', the O5' deprotonation site becomes the most favourable. The conformer $(III\text{-}H_{O5'})^-$ is stabilized by a O5' – C bond (1.546Å), while the conformer $(IV\text{-}H_{O5'})^-$ undergoes a H atom transfer from C5' of the sugar to the C3 (using the numbering used in Schlegel diagram) of the C_{60} moiety, forming a C-H bond (1.098Å).

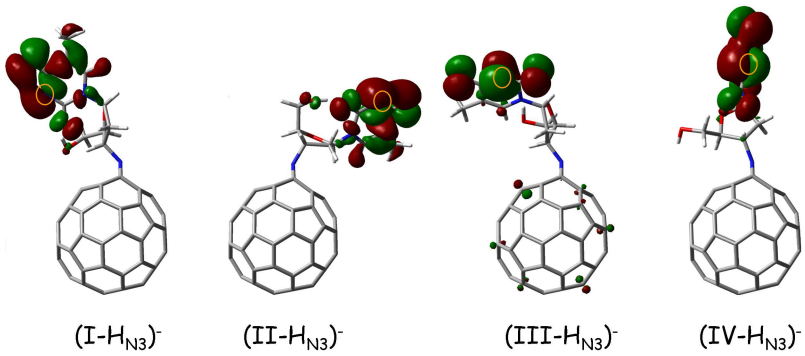

Fig. 5.2.5. Optimized geometries and isocontour of the highest occupied molecular orbital for the I-IV conformers depronated in N3. Deprotonation at N3 reinforces the intramolecular H-bond O5'-H...O2. The orange circle represents the N3 deprotonation site.

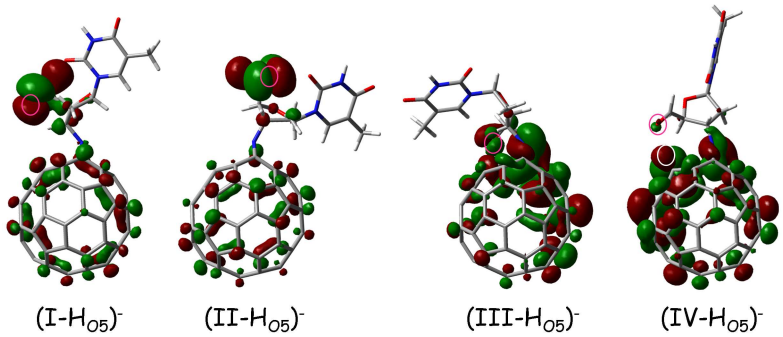

Fig. 5.2.6. Optimized geometries and isocontour of the highest occupied molecular orbital for the I-IV conformers depronated in O5'. The deprotonation at O5' leads to the formation of a C-O bond (1.546Å) for the (III-H)$^-_{O5'}$ conformer and of a C-H covalent bond (1.098Å) for (IV-H)$^-_{O5'}$. (III-H)$^-_{O5'}$ is the most stable deprotonated conformer investigated (see Table I). The pink circle represents the O5' deprotonation site.

Table 5.2.I. ZPVE-corrected energy differences, ΔE, ZPVE-corrected deprotonation energies, DPE, and deprotonation Gibbs free energies (ΔG) of the conformers I to IV at N3 and O5' (in kcal/mol).

	(I-H)$^-$	(I-H)$^-$	(II-H)$^-$	(II-H)$^-$	(III-H)$^-$	(III-H)$^-$	(IV-H)$^-$	(IV-H)$^-$
	O5'	N3	O5'	N3	O5'	N3	O5'	N3
ΔE_{ZPVE}	43.9	25.9	47.7	30.3	0.0	38.2	3.2	44.3
DPE_{ZPVE}	364.3	346.3	364.1	346.7	315.4	353.6	309.1	350.3
ΔG_{DPE}^{298K}	364.7	346.6	364.9	346.4	317.3	353.0	310.1	350.2

Table 5.2.II. Mulliken charges on the C_{60} subunit for conformers I to IV, deprotonated at N3 and O5'. Conformers IIIp and IVp are nearly isoenergetic with III and IV respectively, and differ by the spatial extension.

	$(I-H)^-$	$(II-H)^-$	$(III-H)^-$	$(IV-H)^-$	$(IIIp-H)^-$	$(IVp-H)^-$
	N3	N3	N3	N3		
$C60(H)_x$	0.019	0.146	0.154	0.211		
$C60N(H)_x$	-0.590	-0.501	-0.470	-0.462		
	O5'	O5'	O5'	O5'	O5'	O5'(1H)
C60(H)	-0.147	-0.103	-0.282	-0.520	-0.340	-0.504
$C60N(H)_x$	-0.768	-0.754	-0.920	-1.210	-0.967	-1.142

Table 5.2.III. Electron affinities (eV) of conformers I-IV deprotonated at N3 and O5'. EA, EA_{ZPVE} and ΔG_{EA}^{298K} are computed for the relaxed geometry of the dehydrogenated species. EA_v is computed for the dehydrogenated species at the geometry of the deprotonated one.

	$(I-H)^-$	$(II-H)^-$	$(III-H)^-$	$(IV-H)^-$	$(I-H)^-$	$(II-H)^-$	$(III-H)^-$	$(IV-H)^-$
	N3	N3	N3	N3	O5'	O5'	O5'	O5'
EA	3.82	3.64	3.29	3.51	1.84	1.83	2.98	2.81
EA_{ZPVE}	3.78	3.63	3.32	3.51	1.96	1.95	3.02	2.84
ΔG_{EA}^{298K}	3.72	3.60	3.30	3.47	1.97	1.94	2.98	2.84
EA_v	4.10	3.94	3.64	3.78	2.15	2.16	3.19	2.98

According to our computational model, when the loss of the proton occurs in N3 on the thymine, the negative charge is mostly delocalized on the dT moiety. This can be seen from the analysis of the Mulliken charges of the conformers deprotonated in N3 reported in Table 5.2.II. It is also supported by their adiabatic electron affinities in the 3.3-3.8 eV range (Table 5.2.III) that compared well with the electron affinities computed for thymine at higher levels [61]. The highest EA ($I-H_{N3}$) is equal to 3.82 eV. Since it is larger than the EA of C_{60}, the negative charge formed upon the loss of the proton in N3 is expected to be mostly localized on the dT subunit. Another

indication of the charge localization on the thymine is the gross strengthening of the O_5'-H_5'···O_2 H-bond of I^0 upon deprotonation in N3; it is characterized by an elongation $\Delta R(O_5'\text{-}H_5') = 0.03$ Å, a contraction, $\Delta r(H_5'\cdots O_2) = -0.18$ Å, and a red-shift of $\nu(O_5'\text{-}H_5')$ by 543 cm^{-1} consistent with the H-bond acquiring an anionic character $[O_5'\text{-}H_5'\cdots O_2]^-$. Finally, for all the conformers deprotonated in N3, the HOMO of the deprotonated (see Fig. 5.2.5) and unpair spin densities of the dehydrogenated molecule prior to geometrical relaxation (see Fig. 5.2.7) are localized on the thymine moiety. The HOMO of the deprotonated species represents the less bounded electrons, those most susceptible to undergo detachment. The unpair spin density corresponds to the unpaired electron generated upon detachment. By comparison with the HOMO, it gives additional evidence about the origin of the detached electron.

When the loss of the proton takes place at the O5' of the deoxyribose residue of dT, the picture of localization of the negative charge is significantly different. The electron detachment energies of the species deprotonated in O5' are significantly lower. The EA_{ZPVE} of (I-$H_{O5'}$) and (II-$H_{O5'}$) are ~1.95 eV while the conformers III and IV have EA_{ZPVE} of 3.02 and 2.84 eV respectively, closer to the zero point corrected electron affinity of C_{60} computed for this study at the B3LYP/3-21G level and equal to 2.56 eVand that of $C_{60}N^-$ (3.13 eV). The lowest values of the adiabatic EA correspond to a localization of the HOMO of the O5'-dehydrogenated species mostly on the deoxyribose (see Fig. 5.2.6). When the rearrangement occurs and the lowest energy conformers are formed, the HOMO is localized on the C_{60} (see Fig. 5.2.6) and the unpair spin densities of the dehydrogenated species also (see Fig. 5.2.7). This

clearly supports a charge migration from the sugar to the C_{60} subunit upon geometry relaxation, in agreement with the experiments.

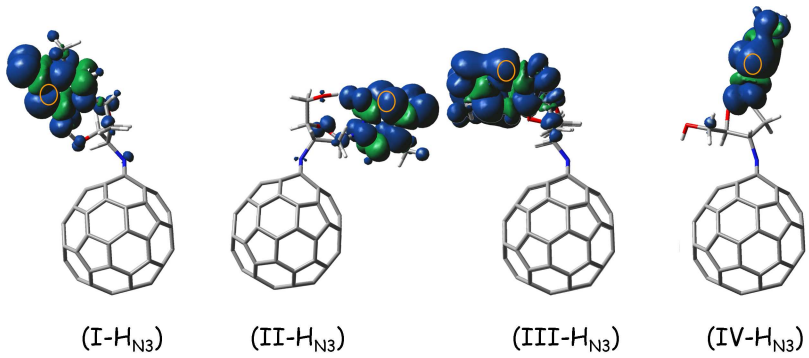

Fig. 5.2.7. Isocontours of the unpaired spin density of the (I,II,III,IV-H) N3-dehydrogenated conformers computed for a vertical detachment at the geometry of the deprotonated species.

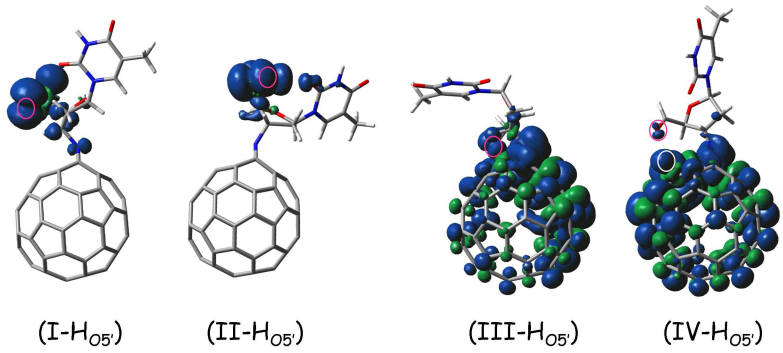

Fig. 5.2.8. Isocontours of the unpaired spin density of the (I,II,III,IV-H) O5'-dehydrogenated conformers computed for a vertical detachment at the geometry of the deprotonated species.

In short, deprotonation takes place on the 3'-deoxythymidine (dT) subunit, either on the thymine at N3 or on the deoxyribose residue at O5'. Deprotonation in N3 leads to negatively charged molecules with an extended geometry and the excess charge largely localized on the dT. Deprotonation in N3 is more favourable for the neutral conformers for which the proton on O5' is engaged into an intramolecular H-bond

with the thymine subunit. The O5'-deprotonation leads to lower-energy folded conformers for two of the four families of conformers investigated. For these conformers deprotonation in O5' is accompanied by a rearrangement and the formation of the O5'-C_{60} bond or the transfer of a hydrogen atom to the C_{60}, forming a negative $C_{60}NH$ unit. Additional work is however necessary to elucidate the mechanism for the double H atom transfer and explaining the $C_{60}NH_2^-$ formation. Experimentally, multiphoton photodetachment experiments at 1064 nm indicate the negative charge to be on the C_{60} unit in good agreement with deprotonation occurring in O5'. No indication for a photoinduced charge transfer was found.

5.2.3. Conclusion

Based on the experimental and theoretical evidence gathered, the most likely deprotonation site on -imino[60]fulleryl-3'-deoxythymidine is O5' on the deoxyribose bridge between the C_{60} and the thymine. Upon geometry relaxation, it is suggested that the charge migrates to the subunit of the highest electron affinity, i.e. C_{60}. The present work suggests that steric hindrance should help prevent charge migration following e.g. rearrangement from deprotonated groups to the C_{60}.

References

[1] H. Imahori, Y. Sataka, *Advanced Materials* **9**, 537 (1997).

[2] H. Imahori, Y. Sakata, *European Journal of Organic Chemistry* p. 2445 (1999).

[3] D. M. Guldi, H. Hungerbuhler, I. Carmichael, K. D. Asmus, M. Maggini, *Journal of Physical Chemistry A* **104**, 8601 (2000).

[4] F. D'Souza, O. Ito, *Coordination Chemical Reviews* **249**, 1410 (2005).

[5] J. Baffreau, *et al.*, *Journal of Physical Chemistry A* p. 066415 (2006).

[6] V. E. Frankevich, *et al.*, *Physical Chemistry Chemical Physics* **7**, 1036 (2005).

[7] J. Roncali, *Chemical Society Reviews* **34**, 483 (2005).

[8] F. D'Souza, *et al.*, *Journal of Physical Chemistry B* **108**, 11333 (2004).

[9] D. M. Guldi, *Journal of the Chemical Society, Chemical Communications* p. 321 (2000).

[10] J. L. Segura, N. Martin, D. M. Guldi, *Chemical Society Reviews* **34**, 31 (2005).

[11] H. Yamada, *et al.*, *Journal of the American Chemical Society* **125**, 9129 (2003).

[12] H. Tokuyama, S. Yamago, E. Nakamura, T. Shiraki, Y. Sugiura, *Journal of the American Chemical Society* **115**, 7918 (1993).

[13] A. S. Boutorine, *et al.*, *Angewandte Chemie International Edition in English* **33**, 2462 (1994).

[14] A. Hirsch, *Synthesis-Stuttgart* p. 895 (1995).

[15] F. Diederich, M. Gomez-Lopez, *Chemical Society Reviews* **28**, 263 (1999).

[16] D. M. Guldi, N. Martin, *Journal of Materials Chemistry* **12**, 1978 (2002).

[17] R. Marczak, *et al.*, *Journal of Material Chemistry* **12**, 2123 (2002).

[18] M. Ungurenasu, C. Pinteala, B. C. Simionescu, *Synthesis-Stuttgart* **3**, 361 (2005).

[19] G. M. Bonora, G. Biancotto, M. Maffini, C. L. Scremin, *Nucleic Acids Research* **21**, 1213 (1993).

[20] T. P. Begley, *Accounts in Chemical Research* **27**, 394 (1994).

[21] I. Husain, J. Griffith, A. Sancar, *Proceedings of the National Academy of Sciences of the U.S.A.* **85**, 2558 (1988).

[22] I. Husain, A. Sancar, *Nucleic Acids Research* **15**, 1109 (1987).

[23] S. T. Kim, A. Sancar, *Biochemistry* **30**, 8623 (1991).

[24] B. Roefls, *et al.*, *Journal of Physical Chemistry B* **101**, 754 (1997).

[25] L. Rivas, S. Sanchez-Cortes, J. V. Garcia-Ramos, *Journal of Raman Spectroscopy* **33**, 6 (2001).

[26] L. Rivas, S. Sanchez-Cortes, J. V. García-Ramos, *Physical Chemistry Chemical Physics* **4**, 1943 (2002).

[27] M. Ostblom, B. Liedberg, L. M. Demers, C. A. Mirkin, *Journal of Physical Chemistry B* **109**, 15150 (2005).

[28] K. H. Cho, J. Choo, S. W. Joo, *Journal of Molecular Structure* **738**, 9 (2005).

[29] J. F. Greisch, E. De Pauw, *Journal of Mass Spectrometry* **42**, 304 (2007).

[30] J. F. Greisch, R. Weinkauf, E. De Pauw, E. S. Kryachko, F. Remacle, *Israel Journal of Chemistry* **47**, 25 (2007).

[31] M. Prato, Q. C. Li, F. Wudl, V. Lucchini, *Journal of the American Chemical Society* **115**, 1148 (1993).

[32] M. Prato, *et al.*, *Journal of the American Chemical Society* **115**, 8479 (1993).

[33] M. Eiermann, F. Wudl, M. Prato, M. Maggini, *Journal of the American Chemical Society* **116**, 8364 (1994).

[34] T. Grosser, M. Prato, V. Lucchini, A. Hirsch, F. Wudl, *Angewandte Chemie International Edition in English* **34**, 1343 (1995).

[35] A. Curioni, P. Giannozzi, J. Hutter, W. Andreoni, *Journal of Physical Chemistry* **99**, 4008 (1995).

[36] M. Banks, *et al.*, *Journal of the Chemical Society, Chemical Communications* **8**, 885 (1995).

[37] M. R. Banks, *et al.*, *Journal of the Chemical Society, Chemical Communications* **8**, 887 (1995).

[38] J. Averdung, J. Mattay, *Tetrahedron* **52**, 5407 (1996).

[39] C. K. F. Shen, H. H. Yu, C. G. Juo, G. R. Chien, K. M. Her, T. Y. Luh, *Chemistry - a European Journal* **3**, 744 (1997).

[40] M. Cases, M. Duran, J. Mestres, N. Martín, M. Sola, *Journal of Organic Chemistry* **66**, 433 (2001).

[41] K. Jinno, T. Uemura, H. Ohta, H. Nagashima, K. Itoh, *Analytical Chemistry* **65**, 2650 (1993).

[42] H. Ohta, Y. Saito, K. Jinno, H. Nagashima, K. Itoh, *Chromatographia* **39**, 453 (1994).

[43] H. Ohta, *et al.*, *Chromatographia* **40**, 507 (1995).

[44] H. Ohta, *et al.*, *Journal of Chromatography A* **883**, 55 (2000).

[45] A. Dupont, J. P. Gisselbrecht, E. Leize, L. Wagner, A. Van Dorsselaer, *Tetrahedron Letters* **35**, 6083 (1994).

[46] M. P. Barrow, *et al.*, *Chemical Physics Letters* **330**, 267 (2000).

[47] H. N. Ghosh, H. Pal, A. V. Sapre, J. P. Mittal, *Journal of the American Chemical Society* **115**, 11722 (1993).

[48] G. Lawson, A. Kitaygorodskiy, Y. Sun, *Journal of Organic Chemistry* **64**, 5913 (1999).

[49] M. S. Wilson, J. A. McCloskey, *Journal of the American Chemical Society* **97**, 3436 (1975).

[50] D. Fati, *et al.*, *Journal of the American Society for Mass Spectrometry* **13**, 1448 (2002).

[51] D. Fati, Y. V. Vasil'ev, N. K. Wachter, R. Taylor, T. Drewello, *International Journal of Mass Spectrometry* **229**, 3 (2003).

[52] S. R. Wilson, Y. Wu, *Journal of the Chemical Society, Chemical Communication* p. 784 (1993).

[53] T. Aggerholm, S. C. Nanita, K. J. Koch, R. G. Cooks, *Journal of Mass Spectrometry* **38**, 87 (2003).

[54] D. M. Guldi, H. Hungerbuhler, K. D. Asmus, *Journal of Physical Chemistry* **99**, 9380 (1995).

[55] N. A. Richardson, J. Gu, S. Wang, Y. Xie, H. F. Schaeffer III, *Journal of the American Chemical Society* **126**, 4404 (2004).

[56] C. Brink, L. H. Andersen, P. Hvelplund, D. Mathur, J. D. Voldstad, *Chemical Physics Letters* **233**, 52 (1995).

[57] L. S. Wang, J. Conceicao, C. M. Jin, R. E. Smalley, *Chemical Physics Letters* **182**, 5 (1991).

[58] X. B. Wang, C. F. Ding, L. S. Wang, *Journal of Chemical Physics* **110**, 8217 (1999).

[59] V. Periquet, A. Moreau, J. P. Carles, S.and Schermann, C. Desfrancois, *Journal of Electron Spectroscopy and related phenomena* **106**, 141 (2000).

[60] M. A. Huels, I. Hahndorf, E. Illenberger, L. Sanche, *Journal of Chemical Physics* **108**, 1309 (1998).

[61] L. T. M. Profeta, J. D. Larkin, H. F. Schaefer, *Molecular Physics* **101**, 3277 (2003).

[62] B. F. Parsons, *et al.*, *Physical Chemistry Chemical Physics* **9**, 3291. (2007).

[63] M. J. Frisch, *et al.*, *Gaussian 03, Revision B.04* (2003).

[64] C. S. Yannoni, P. P. Bernier, D. S. Bethune, G. Meijer, J. R. Salem, *Journal of the American Chemical Society* **113**, 3190 (1991).

[65] D. R. Lawson, *et al.*, *Journal of the Electrochemical Society* **139**, L68 (1992).

[66] T. Kato, *et al.*, *Chemical Physics Letters* **180**, 446 (1991).

[67] G. A. Heath, J. E. McGrady, R. L. Martin, *Journal of the Chemical Society, Chemical Communications* p. 1272 (1992).

[68] R. J. Sension, A. Z. Szarka, G. R. Smith, R. M. Hochstrasser, *Chemical Physics Letters* **185**, 179 (1991).

[69] J. W. Arbogast, C. S. Foote, M. Kao, *Journal of the American Chemical Society* **114**, 2277 (1992).

[70] R. Weinkauf, *et al.*, *Journal of Physical Chemistry* **100**, 18567 (1996).

[71] R. Weinkauf, P. Schanen, D. Yang, S. Soukara, E. W. Schlag, *Journal of Physical Chemistry* **99**, 11255 (1995).

[72] F. Remacle, R. D. Levine, E. W. Schlag, R. Weinkauf, *Journal of Physical Chemistry A* **103**, 10149 (1999).

[73] R. Weinkauf, F. Lehrer, E. W. Schlag, A. Metsala, *Faraday Discussions* **115**, 363 (2000).

[74] R. Weinkauf, L. Lehr, A. Metsala, *Journal of Physical Chemistry A* **107**, 2787 (2003).

[75] J. U. Andersen, C. Gottrup, K. Hansen, P. Hvelplund, M. O. Larsson, *European Journal of Physics D* **17**, 189 (2001).

[76] J. U. Andersen, P. Hvelplund, S. B. Nielsen, U. V. Pedersen, S. Tomita, *Physical Review A* **65**, 053202 (2002).

[77] A. K. Chandra, M. T. Nguyen, T. Zeegers-Huyskens, *Journal of Physical Chemistry A* **102**, 6010 (1998).

Chapter 6. Non-covalent complexes of C_{60}

Many molecular systems can be assembled through non-covalent interactions using cyclodextrins [1, 2, 3], calixarenes [4, 5, 6, 7], crown ethers [8, 9, 10], cyclens [11], cryptands… and their derivatives [3, 12]. Section 6.1 of the present chapter reports on the non-covalent C_{60}:γ-cyclodextrin complex 1:2 formation and on its characterization using electrospray ionization mass spectrometry, probes the strength of the interactions stabilizing the gas-phased ionized complex by collisional activation, and discusses the electron and radical hydrogen transfers observed upon the dissociation of the gas phase deprotonated complex. Section 6.1 results have been published in reference [13]. Section 6.2 reports on the gas phase mobilities of the [C60:(γ-CyD)$_2$] complex ions, infers additional structural information on the encapsulation of a C_{60} molecule by a γ-cyclodextrin dimer by the comparison of the experimental cross sections obtained from gas phase ion mobility measurements with those obtained from semi-empirical and *ab initio* calculations, compares the three dimensional structures of the deprotonated and sodiated [C_{60}:(CyD)$_2$] ions and highlights the influence of the ionization mechanism, and finally infers the area of the C_{60} accessible to reagents or to the solvent in aqueous solution and discusses the influence of the ionization method influence on the complex stability.

The complexation of C_{60} aims at different purposes. Firstly, the negligible solubility of the [60]fullerene in polar solutions hinders its use in many applications. Among the strategies developed to increase water solubility of fullerenes is the inclusion of C_{60} within water-soluble hosts such as cyclodextrins [14, 15, 16, 17, 18, 19, 20, 21, 22, 23, 24, 25, 26]. Secondly, the encapsulation of the C_{60} by cyclodextrins inhibits reactions with dissolved species, since the capsule provides a mechanical barrier [16,

17, 18, 19, 20]. C_{60} complexation can also help prevent direct interaction between C_{60} and DNA strands fullerene-DNA systems. C_{60} in the close vicinity of DNA strands has been reported to induce cleavages of DNA strands at guanine positions [27, 28]. Finally, numerous regio-selective additions on C_{60} have been reported in the literature [29, 30, 31]. C_{60} encapsulation can be used to direct additions to the unprotected areas. In short, the aim of the present section is to contribute to the description of the complex structure using gas phase techniques, to discuss the interactions taking place between the cyclodextrins and the C_{60}, and to open the road to applications relying on complexation to enhance C_{60} water-solubility, regio-selective additions, and protection against unwanted side-reactions.

The γ-cylodextrin (γ-CyD) is a macrocyclic oligosaccharide consisting of eight D-glucose residues connected by α-1,4-linkage (see Fig. 6.1.1). Since all the glucoses are aligned in *cis* with the secondary O2 and O3 hydroxyls connected by O2(n)…O3(n-1) hydrogen bonds on one side, and the primary O6 hydroxyls on the other side, γ-CyD has the overall shape of a hollow, truncated cone with the wide side occupied by O2 and O3 and the narrow side by O6 [32]. The inside of its cavity, due to the C3-H and C5-H hydrogen atoms and glucosidic ether-like O4 oxygen atoms, is hydrophobic whereas the periphery, because the rims are lined with primary and secondary hydroxyl groups, is hydrophilic [33, 34, 35].

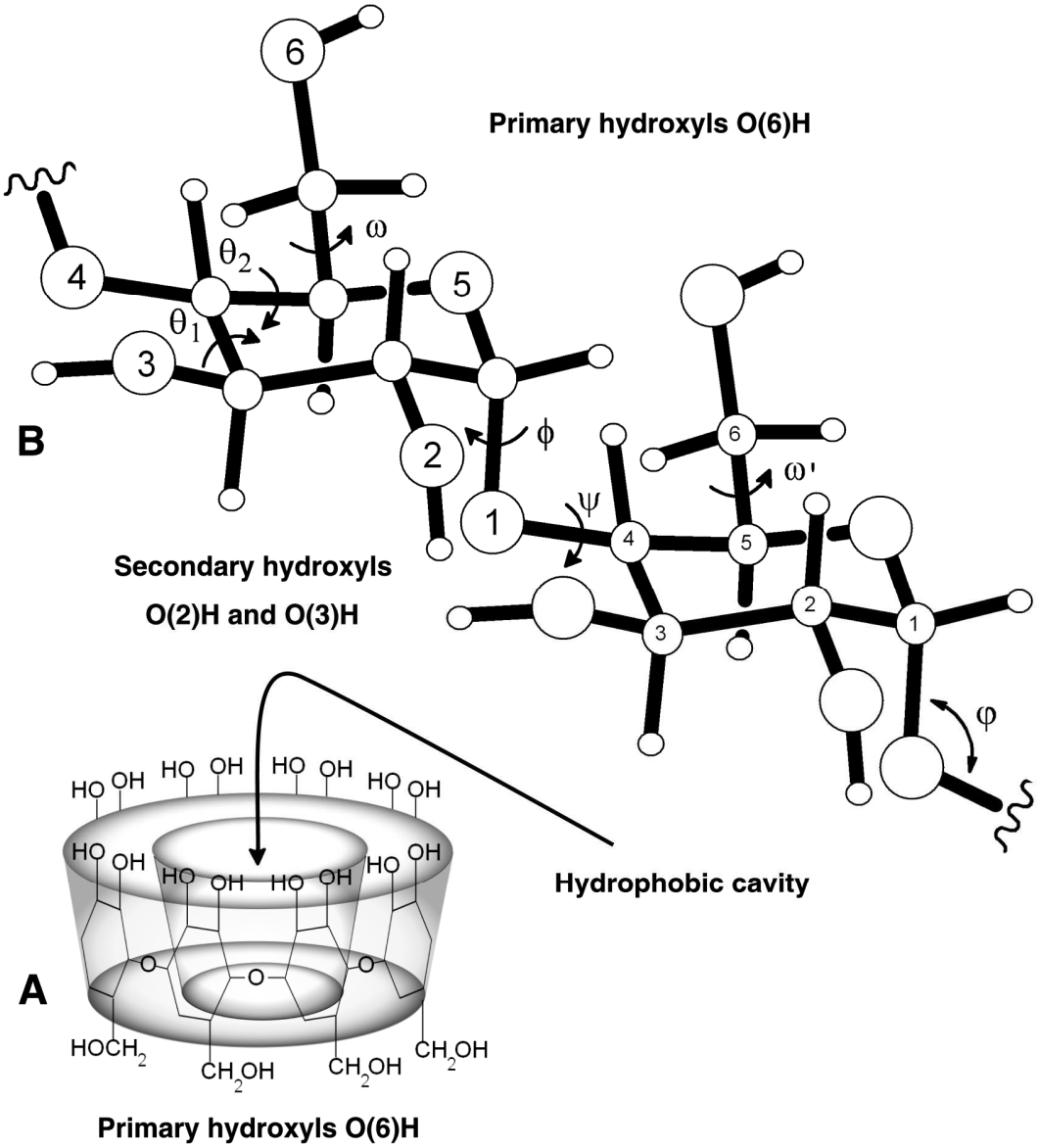

Fig. 6.1.1. (A) Hollow, truncated cone shape of the γ-Cyclodextrin. (B) Labelling convention for γ-cylodextrin D-glucose residues. φ(C1-O1-C4') is the inter-D-glucose bond angle. ϕ(O5-C1-O1-C4') and ψ(C1-O1-C4'-C3') are the torsion angles about the glycosidic linkages. θ_1(C2-C3-C4-C5) and θ_2(C3-C4-C5-O5) are the two endocyclic ring torsions around C_4. ω(O5-C5-C6-O6) describes the orientation of the primary 6-OH relative to the pyranose ring.

Saenger *et al.* [32] based on X-ray and neutron diffraction measurements describe the glucose residues as fairly rigid and the structural rigidity of the CyD macrocycle, especially of β- and γ-CyD [36], as remarkable [32]. The structural rigidity of the

macrocycle appears primarily due to the formation of intramolecular hydrogen bonds between O2-H and O3-H hydroxyl groups of adjacent glucose residues [32, 37]. The O2(n) and O3(n-1) atoms are part of a three center hydrogen bond. The minor component donates to the O4 atom linking the two respective glucose residues and strengthens the major O2(n)…O3(n-1) hydrogen bonding interactions, adding rigidity to the macrocycle [32] (see Fig. 6.1.1).

The description of the D-glucose units forming a cyclodextrin can be reduced to five torsion angles, one bond angle and one tilt angle. The torsion angles ϕ ($O5_n$-$C1_n$-$O1_n$-$C4_{n-1}$) and ψ ($C1_n$-$O1_n$-$C4_{n-1}$-$C3_{n-1}$) describe the rotations about the glucosyl $C1_n$-$O1_n$ and $O1_n$-$C4_{n-1}$ bonds [38]. The endocyclic torsion angles, e.g. θ_1(C2-C3-C4-C5) and θ_2(C3-C4-C5-O5), of the glucose residues (see Fig. 6.1.1) are confined within a narrow range of the (+)- or (-)-gauche rotameric states whatever the guest included in the cavity [32]. The primary O6-H hydroxyl groups, on the other hand, can rotate about the C5-C6 bond. The O5-C5-C6-O6 torsion angle ω (see Fig. 6.1.1) can, in principle, adopt three staggered orientations (+)gauche, (-)gauche, and anti/trans. Crystal phase measurements report a marked preference for the (-)gauche over the (+)gauche state whereas the anti form is not observed [32]. The angle φ(C1-O1-C4') is the inter-D-glucose bond angle and the angle τ (see Fig. 6.1.2) describes the tilt of the least-square fit plane of the pyranose ring relatively to the least-square fit plane of all the inter-glycosidic oxygen atoms. Absolute values $|\tau| > 90°$ are associated with the 6-CH_2-OH group turned towards the cavity center. Guests (inside the γ-cyclodextrin cavity) have been reported to have little or no influence on the glucose conformations, only slightly distorting the macrocycle of the cyclodextrin [32].

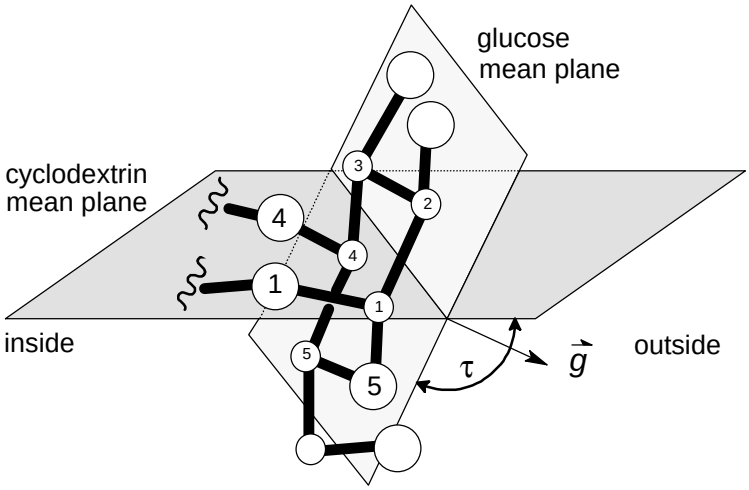

Fig. 6.1.2. Definition of the angle τ as the tilt angle between the least-square fit plane of the pyranose ring and the least-square fit plane of all the interglycosidic oxygen atoms as defined by Lichtenthaler *et al.* [39].

The formation and stability of cyclodextrin inclusion complexes with guests of similar volume but of different shape usually results from several attractive forces whose effective contribution depends on the nature of host and guest. Most intermolecular interactions responsible for noncovalent assemblies are described by the non-relativistic molecular Hamiltonian of chapter 3. Using perturbation theory, the total intermolecular interaction energy between closed shell molecules in their ground states and forming noncovalent complexes can be partitioned into several fundamental long- and short-range intermolecular contributions. In practice, the long-range terms are conveniently expressed in terms of multi-pole series (monopoles, dipoles, quadrupoles, octopoles, etc.) about several points, typically the atom centres and bond midpoints [40, 41]. The interaction energy can then be calculated using the expressions for classical multipolar interactions. The free energies of interaction of the different types of noncovalent interactions that occur between particles that are either charged, or carry a dipole moment, or are polarisable, are given in table 6.1.I [42, 43].

The perturbation theory and the distributed multipole analysis allow decomposition of the noncovalent interactions as follows. (1) The electrostatic interaction is the interaction between the molecular or atomic permanent mono- and multi-poles. It can be attractive or repulsive depending on the sign of the monopoles and the relative angular orientation of the interacting multi-poles. (2) The induction interaction is the interaction between the permanent mono- and multi-poles on one molecule (or atom) and the induced multi-poles resulting from the polarization of the other molecule (or atom) in the electric field of the first one. (3) The dispersion interaction arises from dynamic electron correlation: fluctuations in electron density give rise to instantaneous electronic multi-poles, which in turn induce multi-pole in neighbouring atoms or molecules. The instantaneous dipoles are correlated (in absence of retardation effect) so that they do not average to zero. When two molecules (or atoms) are an appreciable distance apart (on the order of 100 nm), the time taken for the electric field of the first entity to reach the second one and return can become comparable with the period of the fluctuating dipole itself. When this happens the field returns to find that the direction of the instantaneous dipole of the first atom is now different from the original and less favourably disposed to an attractive interaction. This so called retardation effect (Casimir-Polder effect) will not be further discussed [42]. (4) The exchange repulsion arises from the Pauli Exclusion Principle. It occurs when two molecules are brought close enough and their charge densities overlap. (5) The charge penetration interaction also occurs when two molecules are brought close enough, so that their charge densities overlap. In that case, the nuclei on one molecule will no longer be shielded by its own electron density, and will experience a greater attraction for the electron density associated with the other species. The energy difference resulting from this increased attraction is referred to as

charge penetration [44]. (6) Finally, the intermolecular charge transfer interaction is characterized by electronic transition(s) to an excited state in which there is a partial transfer of electronic charge from one molecular entity, called the electron donor, to another, called the electron acceptor.

The long-range interactions are due to electrostatics, polarization (induction), and dispersion; while exchange repulsion, charge penetration, and charge transfer are considered to be short-range [45].

Table 6.1.I. Types of noncovalent interactions

Type of noncovalent interactions	Formula	Name
charge-charge	$\frac{Z_1 Z_2}{\varepsilon_r r}$	Coulomb energy
charge-dipole (fixed dipole)	$-\frac{Zu\cos\theta}{\varepsilon_r r^2}$	
charge-dipole (freely rotating dipole)	$-\frac{Z^2 u^2}{6(\varepsilon_r)^2 kTr^4}$	
dipole-dipole (fixed dipole)	$-\frac{u_1 u_2}{\varepsilon_r r^3}(2\cos\theta_1\cos\theta_2 - \sin\theta_1\cos\phi\sin\theta_2)$	
dipole-dipole (freely rotating dipole)	$-\frac{u_1^2 u_2^2}{3(\varepsilon_r)^2 kTr^6}$	Keesom energy (van der Waals energy $\propto \frac{1}{r^6}$)

charge-nonpolar	$-\frac{Z^2\alpha}{2(\varepsilon_r)^2 r^4}$	
dipole-nonpolar (fixed dipole)	$-\frac{u^2\alpha(1+3\cos^2\theta)}{2(\varepsilon_r)^2 r^6}$	
dipole-nonpolar (freely rotating dipole)	$-\frac{u^2\alpha}{(\varepsilon_r)^2 r^6}$	Debye energy (van der Waals energy $\propto \frac{1}{r^6}$)
nonpolar-nonpolar	$-\frac{3}{2}\frac{\alpha_{01}\alpha_{02}}{(\varepsilon_r)^2 r^6}\left(\frac{I_1 I_2}{I_1+I_2}\right)$	London dispersion energy (van der Waals energy $\propto \frac{1}{r^6}$)
hydrogen bond	special, directed interaction	
hydrophilic interaction	special interaction	
hydrophobic interaction	special interaction	

Adapted from Israelachvili [42, 43]. *Z*= charge, *u*=dipole, *r*=distance, α =polarizability, ε =dielectric constant, *I*=first ionization potential, θ =angle between dipole and vector connecting the interacting particles, ϕ =polar angle of second dipole.

Although it is often referred to, hydrogen bonding does not correspond to a single and unique type of interaction. “Hydrogen bonding” is commonly used to describe extremely different interactions involving a hydrogen atom and can be summarized by the isoelectronic sequence, $(FHF)^-$, HF•••HF, and Ne•••HF, suggested by Legon [46]. In $(FHF)^-$, the hydrogen bond is very strong with a binding energy [47] of ~167 kJ

mol-1, that borders a covalent bond. In HF•••HF, the typical hydrogen bond has a binding energy [48] of ~19 kJ mol-1, that is dominated by electrostatic forces. Finally in Ne•••HF, the weak interaction has a binding energy [49] about ~1 kJ mol-1, dominated by dispersive and inductive interactions.

Another interaction – not described above – is the so called hydrophobic interaction. It represents the tendency of non-polar surfaces to associate in aqueous solutions. Different models have been proposed to explain this interaction, i.e. entropic effects due to molecular rearrangement of water near hydrophobic surfaces, electrostatic effects, correlated charge fluctuations or correlated dipole interactions, the bridging of sub-microscopic bubbles, and cavitation due to the metastability of the intervening fluid [50, 51]. However, no existing model seems capable of explaining the hydrophobic interaction over the entire range of observed distances, solution conditions, methods of hydrophobization, surface roughness and fluidity, and "hydrophobicity" of specific chemical groups [51].

As discussed in chapter 2, the transferability of the present gas phase results to the solution phase is unknown. They are nevertheless expected to provide useful information for dehydrated media.

6.1. Synthesis and mass spectrometric characterization of the C_{60}:(γ-Cyclodextrin)$_2$ Inclusion Complex

The formation of an inclusion complex of γ-cyclodextrins with the apolar [60]fullerene was first reported by Andersson et al. [14]. This water soluble complex of stoechiometry 1:2 [$C_{60:}$ (γ-CyD)$_2$] has been studied using UV-VIS and IR spectroscopy [14, 15, 19, 22], NMR spectroscopy [15, 21, 26], circular dichroïsm

[21], powder X-ray diffraction [19, 26], thermogravimetry [19, 25], fast atom bombardment mass spectrometry [23, 24, 52], flash photolysis and pulse radiolysis [16, 17, 18, 19, 20].

The initial experimental characterization of the [C_{60}:(γ-CyD)$_2$] complex was performed by Andersson *et al.* [14] using UV-VIS spectroscopy. Using molecular modeling, Andersson *et al.* [14, 15] also reported that the hydrophobic cavity in γ-CyD was just a little too small to accommodate C_{60}. Whereas in a 1:1 complex, the C_{60} molecule would present a relatively large area towards water, in a 1:2 complex, the guest is perfectly enclosed by the two host molecules, which are close enough to allow for hydrogen bonding between their respective secondary hydroxyl groups, with the access to the solvent phase significantly reduced (see Fig. 6.1.1).

Mass spectrometric characterization of the [C_{60}:(γ-CyD)$_2$] complex was first achieved by Andersson *et al.* [23], Giesa *et al.* [24] and Her *et al.* [52] using fast atom bombardment (FAB) on a solid "magic bullet" matrix (dithiothreithol : dithioerythritol, 5:1) both in positive and negative mode. The negative-ion FAB spectra exhibited peaks due to $C_{60}^{-\bullet}$ (719.9 m/z), [(γ-CyD) -H]$^-$ (1295.2 m/z), [C_{60}:(γ-CyD) -H]$^-$ (2016.5 m/z), [C_{60}:(γ-CyD)$_2$ -H]$^-$ (3313.9 m/z) and [(γ-CyD)$_2$ -H]$^-$ (2591.9 m/z) [24]. Andersson *et al.* [23] raised the question whether the monocharged [C_{60}:(γ-CyD)$_2$] complex anions consist of a negative $C_{60}^{\bullet-}$ surrounded by an intact γ-CyD dimer or a neutral C_{60} surrounded by a deprotonated γ-CyD dimer. Both Andersson *et al.* [23] and Giesa *et al.* [24] conclude from the relative abundances of the different isotopic signals that a contribution of the radical ion [C_{60}:(γ-CyD)$_2$]$^{-\bullet}$ may be assumed to be superposed to the signal of [C_{60}:(γ-CyD)$_2$ -H]$^-$ (the two isotopic distributions

overlap). Giesa *et al.* [24] also observed that the isotopic pattern of the C_{60} ions (starting at 720 m/z) revealed that the intensities at higher mass (e.g. 721 m/z corresponding to $^{13}C\,^{12}C_{59}$) are too high to represent $C_{60}^{-\bullet}$ alone. The 721 m/z peak is the base peak instead of having a 66% relative intensity compared to the peak at m/z 720. This was interpreted in terms of hydride attachment. Her *et al.* [52] observed using fast-atom bombardment mass spectrometry that many C_{60} derivatives form stable complexes with γ-cyclodextrin in a ratio 1:2. They also reported the first CID spectra of the C_{60}/γ-cyclodextrin complex. From their results they concluded that it is likely that the negative C_{60}/γ-cyclodextrin 1:2 complex mono-anion detected in FAB-MS mainly consists of a C_{60}^{-} ion in the cavity of a γ-cyclodextrin dimer.

Finally, Priyadarsini, Guldi *et al.* [20] carried out pulse radiolysis experiments on the reaction of the [C_{60}:(γ-CyD)$_2$] complex with primary radiolytic species, such as $OH^{\bullet}$, $H^{\bullet}$ and e^{-} in aqueous solution. Their results showed that $OH^{\bullet}$ led mainly to hydrogen abstraction from the cyclodextrin followed by the reaction of the resulting radical with C_{60} to yield a radical adduct which absorbs at 290 nm. From the similitude of the transient spectra and all the formation and decay kinetics of the $H^{\bullet}$ case as compared to the $OH^{\bullet}$ case, Priyadarsini, Guldi *et al.* concluded that the reactions of [C_{60}:(γ-CyD)$_2$] with $OH^{\bullet}$, $H^{\bullet}$ radicals are of similar nature. They react with the γ-CyD moiety via hydrogen abstraction rather than with the fullerene and the γ-CyD radical is suggested to add subsequently to C_{60} [20].

In short, section 6.1. aims at: (1) describing the electronebulization and ionization of the [C_{60}:$(CyD)_2$] complex in electrospray mass spectrometry, (2) probing in gas phase by tandem mass spectrometry and collision induced dissociation the strength of the interactions involved in the complex stability, (3) discussing the electron and radical hydrogen transfers observed in gas phase upon the dissociation of the deprotonated complex.

6.1.1. Experimental

The [60]fullerene : γ-cyclodextrin complexation was performed according to a method similar to that described by Yoshida *et al.* [21]. 20 ml of a $5.2x10^{-3}$ M aqueous solution of γ-cyclodextrin were stirred at a temperature not exceeding 80°C for 48 hours in presence of 20 ml of a $2.8x10^{-3}$ M toluene solution of [60]fullerene. Removal of part of the excess of free γ-cyclodextrin from the aqueous phase was performed by repetitive collection of the violet precipitate and resolubilization in water (about 20°C). The violet residue was then lyophilized at room temperature. Prior to characterization and analysis using electrospray mass spectrometry partial elimination of the uncomplexed cyclodextrin was performed again by suspension in MQ water at room temperature of an excess of complex, decantation and separation of the precipitate from the supernatant. The remaining [C_{60}:$(\gamma\text{-CyD})_2$] complex was dissolved in pure water at room temperature. A volume of the saturated aqueous solution obtained was then mixed with 2 to 3 volumes of a solution 30% in methanol and 20-40 mM in ammonium acetate (NH_4OAc) for analysis in negative mode ion mass spectrometry whereas a solution 30% in methanol without ammonium acetate was used in positive mode to avoid ammonium adducts. The concentration, whose

precise value is unknown due to the washing steps, was optimized to obtain a stable signal of maximum intensity using electrospray ionization.

6.1.2. Results

A number of parameters including the flow rate, applied voltage, conductivity, and liquid surface tension must be properly balanced in order to accomplish stable electrospray (ESI) operation [53, 54]. In the present study, nanoelectrospray was performed in absence of back pressure which allows the flow rate to automatically adjust to the correct value. The conductivity of the ESI solution, necessary for the process of charge separation at the tip, depends on the amount of ionic analyte, added electrolyte (such as acetic acid or ammonium acetate), and/or of charge products of the electrochemical reaction. By varying systematically the instrumental parameters and the solution composition, the best conditions for the ionization of $[C_{60}{:}(\gamma\text{-CyD})_2]$ using nano-ESI were determined empirically. In negative mode, the optimal solution composition was 20 % methanol and ~15 mM NH_4OAc. In positive mode, Na^+ adducts are commonly observed and NH_4OAc is best avoided (as described in section 6.1.1) to prevent additional ammonium adducts formation (see Fig. 6.1.3-B and 6.1.3-C). Low concentrations of sodium (on the order of 10^{-6} M) typically derive from glassware and storage bottles [54].

The mass spectra were obtained using electrospray and tandem mass spectrometry on a Q-ToF Ultima Global™ mass spectrometer (Micromass Ltd.). For the collision induced dissociation experiments, the ions are mass selected using a quadrupole, activated by collisions with argon in an octopole and analysed in a time-of-flight operated in reflectron mode calibrated using phosphoric acid. Typical MS spectra of

the [C_{60}:(γ-CyD)$_2$] complex are presented in Fig. 6.1.3. The signals at 1655.4, 1657.4 and 1679.4 m/z correspond to the [C_{60}:(γ-CyD)$_2$] complex doubly charged, those at 1295.4, 1297.4 and 1319.4 m/z to the γ-cyclodextrin monomer monocharged or dimer doubly charged and those at 647.2, 649.2 and 671.2 m/z to the monomer doubly charged. The successive m/z ratios correspond to the deprotonated, protonated and sodiated ions respectively. Besides γ-cyclodextrin dimers (see Fig. 6.1.3), which are known to form easily in electrospray, small differences are observed upon comparison of the electrospray mass spectra with the FAB mass spectra [23, 24]. Andersson *et al.* [23] state that both 1:2 and 1:1 complexes between C_{60} and γ-CyD are believed to exist in water and both species are detected using FAB mass spectrometry even though the intensity of the 1:1 complex is very small. Only the [C_{60}:(γ-CyD)$_2$] complex was detected in our electrospray mass spectra (see Fig. 6.1.3). There was no evidence of a [C_{60}:(γ-CyD)] complex. A reason might be an excess of free γ-cyclodextrin contained in the aqueous solution compared to the FAB conditions.

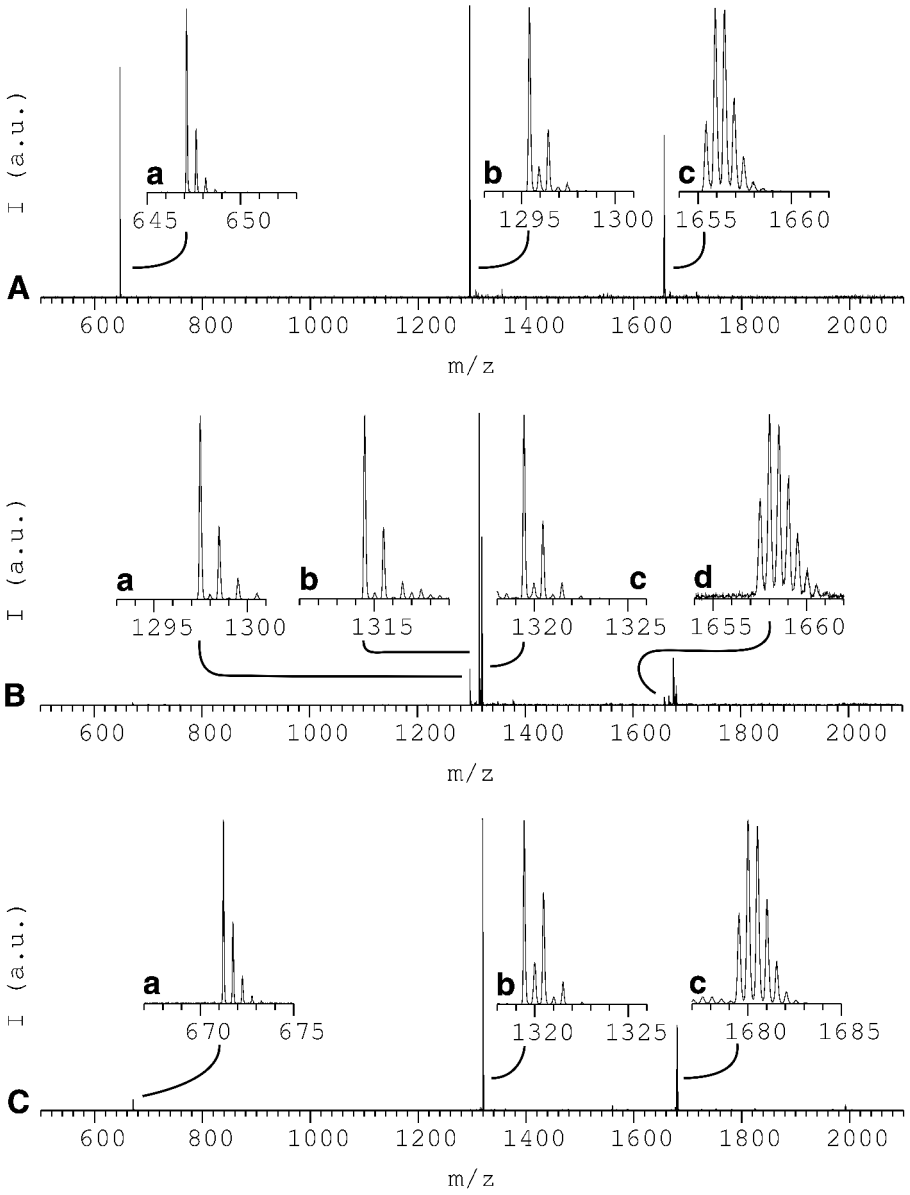

Fig. 6.1.3. MS spectra of the [C_{60}:(γ-CyD)$_2$] complex in negative (A) and positive (B and C) modes. The signals at 1655.4 (scale-up A-c), 1657.4 (scale-up A-d) and 1679.4 (scale-up A-c) correspond to the doubly deprotonated, doubly protonated and doubly sodiated [C_{60}:(γ-CyD)$_2$] ions respectively. The other scale-ups are assigned as follows: (A-a) doubly deprotonated γ-cyclodextrin (CyD), (A-b) mono deprotonated CyD, (B-a) protonated CyD, (B-b) ammoniated (NH_4^+) CyD, (B-c) sodiated CyD, (C-a) doubly sodiated CyD and (C-b) sodiated CyD. Traces of doubly charged dimers can be seen. Spectrum B was obtained from the same solution as spectrum A which is 15mM in NH_4OAc. Protonation of γ-cyclodextrins is observed to be inefficient compared to cationization. Spectrum C was obtained from a [C_{60}:(γ-CyD)$_2$] complex solution without NH_4OAc added.

The $[C_{60}:(\gamma\text{-CyD})_2]$ complex is unambiguously identified from the comparison of the experimental mass and isotopic distribution of its parent ions (see the insets of Fig. 6.1.3) with the corresponding theoretical spectra. The experimental ^{13}C isotopic abundance for the C_{60} was determined experimentally (see Fig. 6.1.4) and yields a ^{13}C isotopic abundance (0.00*7(6)*) lower than the expected value (0.011). This might explain the small difference between the experimental and expected theoretical spectra. However, from the isotopic pattern of the $[C_{60}:(\gamma\text{-CyD})_2]$ complex, it can be asserted that no hydride attachment to the complex as a whole takes place upon electronebulization.

In positive mode both protonation and cationization by sodium cations take place even though protonation is less efficient. In negative mode, only deprotonation takes place. Indeed, if deprotonation and reduction took place simultaneously, the center of the resulting isotopic distribution would be shifted to the higher masses. Furthermore the isotopic patterns of the deprotonated, protonated and sodiated ions match almost perfectly, which suggests only one species to be present in negative mode.

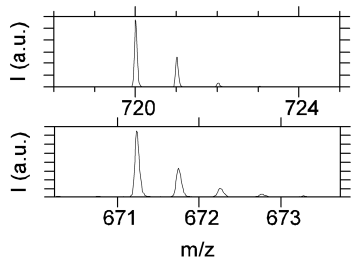

Fig. 6.1.4. The isotopic abundance of ^{12}C and ^{13}C obtained from the experimental mass spectrum of the pristine [60]fullerene, are respectively p=0.992(4) and (1-p)=0.007(6). The isotopic abundances obtained from the doubly charged γ-cyclodextrin monomer are respectively p=0.98(7) and (1-p)=0.01(2).

A straightforward strategy for measuring bond strength is to deliver progressively increasing amounts of internal energy into the ion and observe the threshold at which bond cleavage begins or the value of the collision energy at which the parent ion survival yield amounts to 50% of the total ion current. Collision-induced dissociation (CID), surface-induced dissociation (SID), heated capillary dissociation (HCD), and blackbody infrared radiation dissociation (BIRD) are commonly used in mass spectrometry to probe the strength of interactions in gas phase. In CID, the translationally excited parent ion is collided with gaseous atoms or molecules to induce dissociation.

Collision induced dissociation of the [C_{60}:(γ-CyD)$_2$] inclusion complex ions only allows to probe the interactions responsible for their stability – hydrogen bonding, charge transfer, electrostatic and Van der Waals interactions – as a whole. Furthermore, since mass spectrometry cannot be used to study neutral molecules, direct assessment of the interactions for the neutral complex is not possible. Finally since the ions produced by electronebulization are doubly charged, intramolecular coulombic repulsion has to be considered although it cannot be easily evaluated due to unknown location of the charge. Collision induced dissociation provides, however, besides purely structural data, some useful mechanistic information as will be further discussed in the next section. The MSMS spectra for different collision energies are presented in Fig. 6.1.5, 6.1.6 and 6.1.7 for the doubly deprotonated, doubly protonated and doubly sodiated ions respectively.

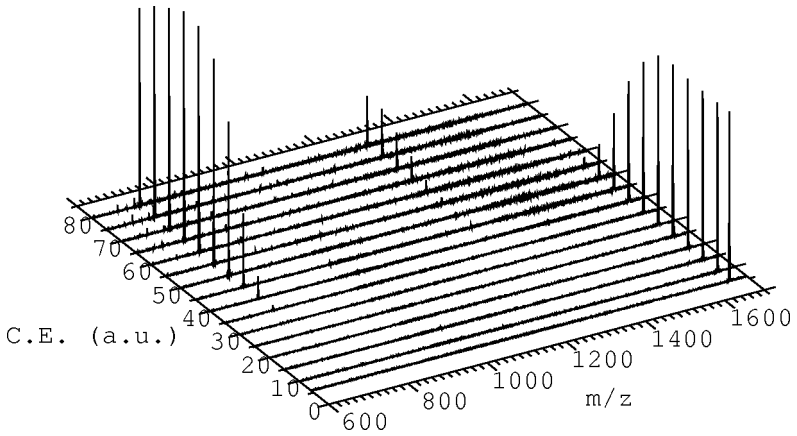

Fig. 6.1.5. CID spectra of the $[C_{60}:(\gamma\text{-CyD})_2\text{-}2H]^{2-}$ complex ion normalized to the total ion current. The amount of fragments in the [1700:3500] m/z range is negligible, see Fig. 6.1.8 for the isotopic distribution of the only fragment observed above 1700 m/z.

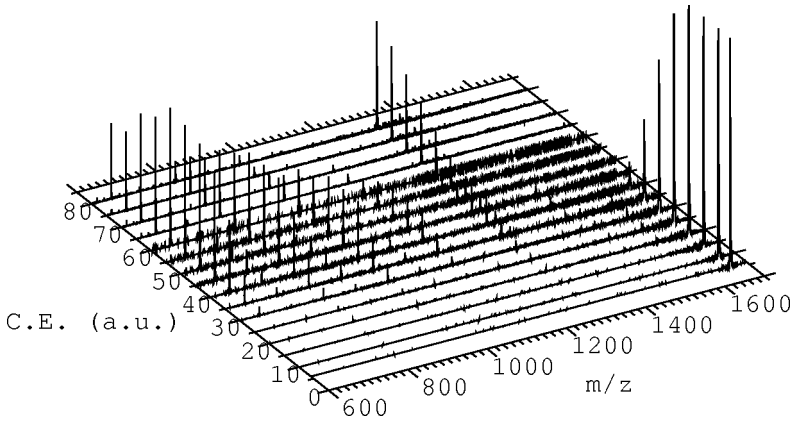

Fig. 6.1.6. CID spectra of the $[C_{60}:(\gamma\text{-CyD})_2+2H]^{2+}$ complex ion normalized to the total ion current. Negligible amounts of fragments (not shown) are also observed in the [1700:2200] m/z range.

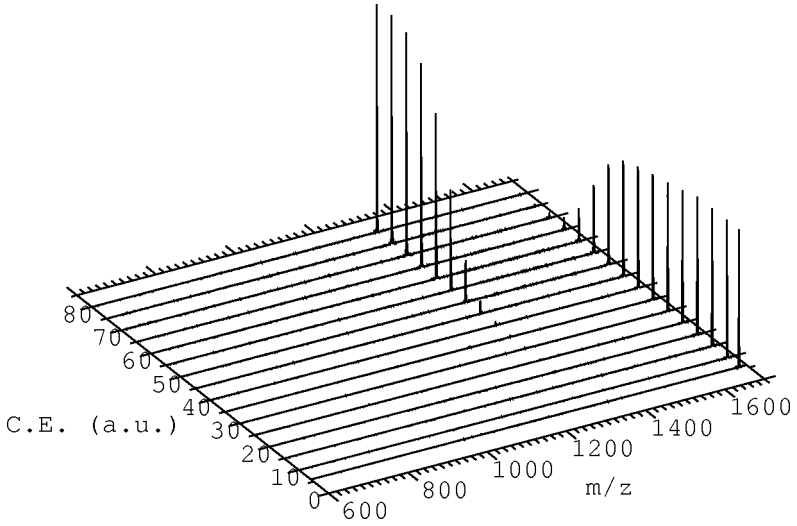

Fig. 6.1.7. CID spectra of the $[C_{60}:(\gamma\text{-CyD})_2+2Na]^{2+}$ complex ion normalized to the total ion current. No fragments are detected in the [1700:3500] m/z range. See Fig. 6.1.9 for the isotopic distribution of the fragments detected.

Since for the low collision energies only one monocharged fragment, $C_{60}^{\bullet -}$ or $C_{60}H^-$, is detected per complex dissociated and for the higher collision energies the $C_{60}H^-$ and γ-CyD intensities are not proportional, charge conservation in negative mode suggests that a small fragment of a deprotonated γ-cyclodextrin of m/z outside the mass range of our mass spectrometer in MS/MS (< 90 m/z) goes undetected. Different fragmentation mechanisms occur depending on the ion mode and the collision energy used to induce dissociation. For the deprotonated parent ions, as can be seen from the spectra in Fig. 6.1.5 and scaled up in Fig. 6.1.8, the dominant fragment for collision energies above 30 eV is $C_{60}H^-$. The protonated ions (see Fig. 6.1.6), fragment into γ-cyclodextrin sub-units while de sodiated ions, Fig. 6.1.7, yield a sodiated γ-cyclodextrin as main fragment. As can be seen from Fig. 6.1.8 and 6.1.9, the deprotonated and sodiated parent ions also yield for low collision energies, respectively in the [30:60] a.u. and [20:40] a.u. energy ranges, a doubly charged γ-cyclodextrin dimer fragment. This fragment likely converts to monocharged γ-cyclodextrin monomers at the higher collision energies.

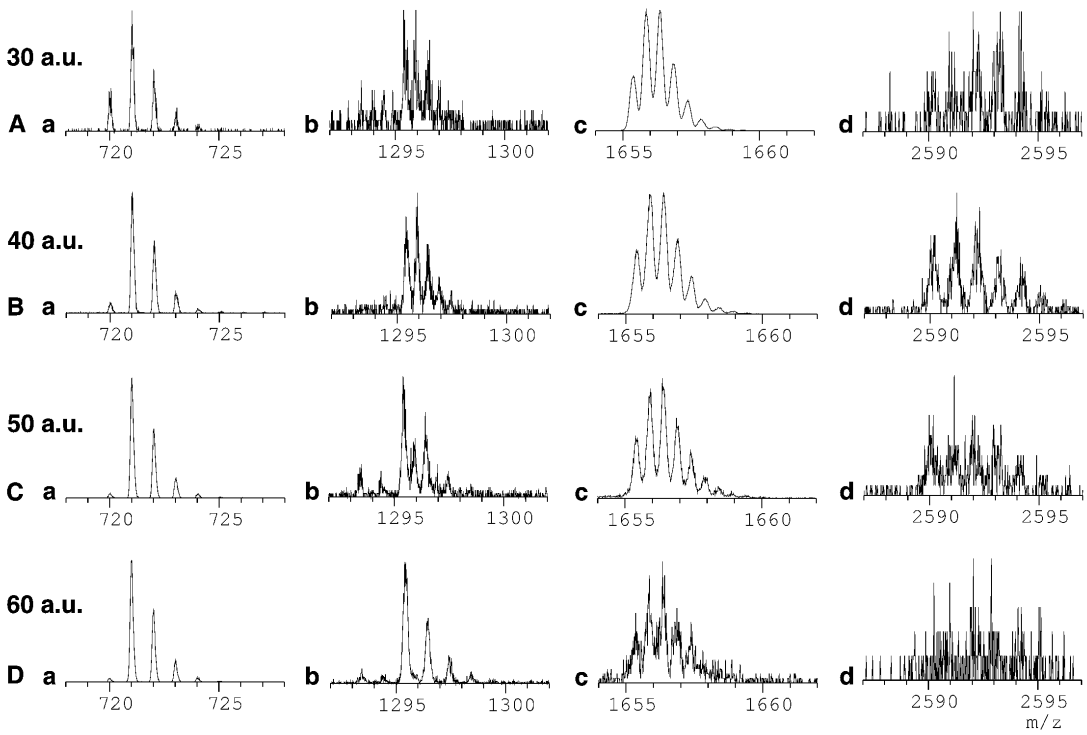

Fig. 6.1.8. Isotopic distributions of the ions detected upon collision induced dissociation of the $[C_{60}:(\gamma\text{-CyD})_2 - 2.H]^{2-}$ complex anion for collision energies ranging from 30 to 60 a.u. The first column corresponds to the superposed isotopic distributions of $C_{60}^{\bullet-}$ and $C_{60}H^-$. The second column corresponds to the superposed $[(\gamma\text{-CyD})_2 - 2.H]^{2-}$ (dominant in spectrum A-b) and $[(\gamma\text{-CyD}) - H]^-$ (dominant in spectrum D-b). The third column corresponds to the parent anion, $[C_{60}:(\gamma\text{-CyD})_2 - 2.H]^{2-}$. The fourth column spectra corresponds most likely to the monocharged $[(\gamma\text{-CyD})_2 - 3.H]^-$ ions (2590.3 m/z).

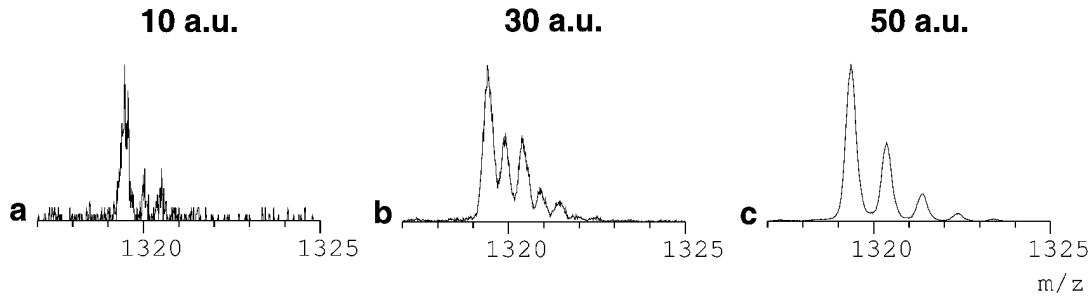

Fig. 6.1.9. Isotopic distributions of the ions detected upon collision induced dissociation of the $[C_{60}:(\gamma\text{-CyD})_2 + 2.Na]^{2+}$ complex cation for collision energies ranging from 10 to 50 a.u.. Superposition of the $[(\gamma\text{-CyD}) + Na]^+$ and $[(\gamma\text{-CyD})_2 + 2.Na]^{2+}$ isotopic distributions is observed.

The survival yield curves for the $[C_{60}:(\gamma\text{-CyD})_2 - 2.H]^{2-}$, $[C_{60}:(\gamma\text{-CyD})_2 + 2.H]^{2+}$ and $[C_{60}:(\gamma\text{-CyD})_2 + 2.Na]^{2+}$ ions are presented in Fig. 6.1.10. No fragmentation occurs for collision energies below 20 eV. The values of the collision energy corresponding to a 50% survival yield and inferred from Fig. 6.1.10 are respectively equal to 37, 48 and 59 eV in the laboratory frame.

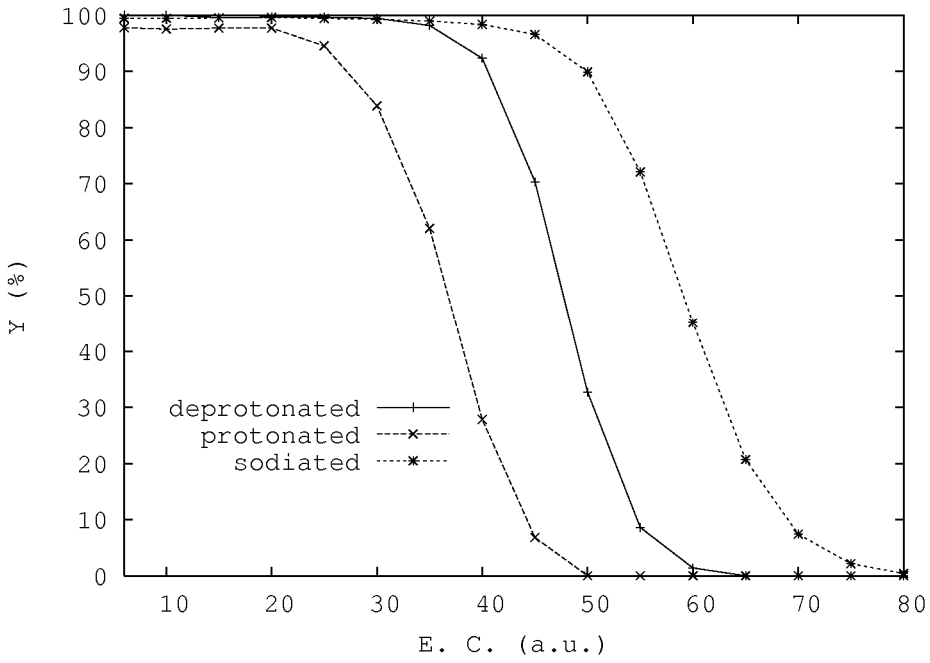

Fig. 6.1.10. Survival yield curves of $[C_{60}:(\gamma\text{-CyD})_2 - 2.H]^{2-}$, $[C_{60}:(\gamma\text{-CyD})_2 + 2.H]^{2+}$ and $[C_{60}:(\gamma\text{-CyD})_2 + 2.Na]^{2+}$ ions. The survival curves obtained from the signals ranging from 90 to 3500 m/z and taking into account "charge conservation".

6.1.3. Discussion

In mass spectrometry, the ions detected are usually expected to mirror the molecular species present in solution. According to Fenn [55], "electrospray ionization" refers to a complex of independent component processes, the two most important of which are electrospray dispersion, the electrostatic dispersion of sample liquid into charged droplets, and ionization, i.e., the transformation of solute species in those droplets to free ions in the gas phase. Electrospray dispersion involves the high electric field applied between the metal capillary and the counter-electrode which causes the

accumulation, at the solution-air interface, of ions of the same polarity as the voltage applied to the capillary [53, 55, 56, 57, 58]. The accumulation of charged species destabilizes the liquid at the capillary tip and causes the emission of charged droplets in gas phase [53, 55, 56, 57, 58]. The rate of the charge separation process which determines the average current that flows between the electrodes is determined by the flow rate, applied voltage, conductivity and liquid surface tension [53, 54, 55]. The involvement of electrochemical processes in the operation of electrospray sources was emphasized by Kebarle and coworkers [57] as well as by many others [55, 57, 58, 59]. As summarized by Van Berkel [55, 58], reduction /oxidation reactions involving solvents or analytes, and/or the elimination of cations /anions from solution, must occur during the negative/positive ion mode of operation to supply the necessary excess negative /positive charge. However the details of the ionization step and the different agents involved are often not controlled.

The optimal solution composition for the electronebulization and ionization of the $[C_{60}:(CyD)_2]$ complex is empirically determined to be 20 % methanol and 15 mM NH_4OAc in negative mode, and 20% methanol in presence of a sodium concentration on the order of 10^{-6}M in positive mode. The bicapped structure of the $[C_{60}:(\gamma\text{-}CyD)_2]$ inclusion complex is unambiguously identified from the mass to charge ratio, the isotopic patterns and the fragments of its doubly deprotonated, protonated and sodiated ions (see Fig. 6.1.3, 6.1.5, 6.1.6 and 6.1.7).

The formation of the $[C_{60}:(\gamma\text{-}CyD)_2\ -2H]^{2-}$ anion in negative mode is significantly increased by the addition of ammonium acetate to the electronebulized solution. Charge separation induces the accumulation of acetate anions in negative ion mode

and sodium cations in positive ion mode at the water-air interface as reported by Kebarle and coworkers [60]. These ions accumulated on the surface of the leaving droplets contribute to the analyte ionization, *e.g.* double acetate adducts observed under particularly soft experimental conditions can be seen in Fig. 6.1.11.

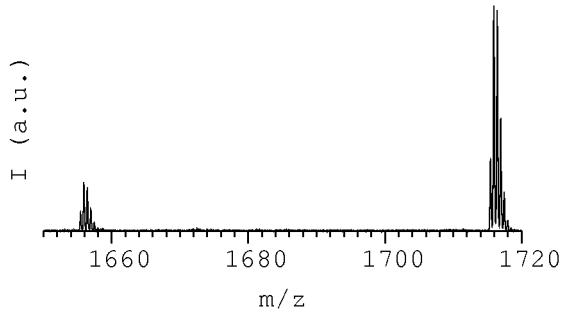

Fig. 6.1.11. Negative ion mode MS spectrum of a $[C_{60}:(\gamma\text{-CyD})_2]$ solution 20% in methanol and 150mM in NH_4Ac. The isotopic pattern at 1715.4 m/z corresponds to the $[C_{60}:(\gamma\text{-CyD})_2+2.Ac]^{2-}$ ion. The ion composition was checked using tandem mass spectrometry. The signal at 1655.4 m/z corresponds to the $[C_{60}:(\gamma\text{-CyD})_2\text{-}2.H]^{2-}$ ions. The reason for the absence of the acetate (Ac) mono adduct is not known.

Furthermore, electron accumulation at the gold coated capillary tip causes the formation and accumulation, at the capillary tip where the solution is in contact with the gold coating, of hydroxyl anions according to the following half-reaction:

– in negative mode: $O_2 + 2.H_2O(l) + 4.e^- \rightarrow 4.OH^-(aq)$ $(E^0_{red} = 0.16$ V vs. SCE)

pH changes resulting from the electrochemical reaction of water can affect the appearance of the mass spectrum [61, 62]. The effect is particularly pronounced when low flow-rates such as those common to the nanospray mode (tens of nl min^{-1}) are employed and non-buffered solutions are used [53, 62]. As suggested by Wang and Agnes [63] and Van Berkel and coworkers [55], the products of the electrolysis reaction may be concentrated on the surface of the liquid exiting the capillary.

In conclusion for the negative mode, the ionization of the C_{60}:(γ-CyD)$_2$ complex ions likely involves the following reactions:

$$C_{60}:(\gamma\text{-CyD})_2 + 2.OH^- \rightarrow [C_{60}:(\gamma\text{-CyD})_2 - 2.H]^{2-} + 2.H_2O \quad \textbf{(1)}$$

$$C_{60}:(\gamma\text{-CyD})_2 + 2.CH_3COO^- \rightarrow [C_{60}:(\gamma\text{-CyD})_2 - 2.H]^{2-} + 2.CH_3COOH \quad \textbf{(2)}$$

In positive mode, the $[C_{60}:(\gamma\text{-CyD})_2 + 2H]^{2+}$ ions result from the electron depletion at the gold coated capillary tip causing the formation and accumulation of protons, where the solution is in contact with the gold coating, according to the following half-reaction:

– in positive mode: $2.H_2O(l) \rightarrow O_2(g) + 4.H^+(aq) + 4.e^-$ (E^0_{red} = 0.99 V vs. SCE)

The $[C_{60}:(\gamma\text{-CyD})_2 + 2.Na]^{2+}$ ions, on the other hand, result from the charge separation that induces the accumulation of sodium cations in positive ion mode at the water-air interface as reported by Kebarle and coworkers [60].

In conclusion for the positive mode, the ionization of the C_{60}:(γ-CyD)$_2$ complex ions likely involves the following reactions:

$$C_{60}:(\gamma\text{-CyD})_2 + 2.H^+ \rightarrow [C_{60}:(\gamma\text{-CyD})_2 + 2.H]^{2+} \quad \textbf{(3)}$$

$$C_{60}:(\gamma\text{-CyD})_2 + 2.Na^+ \rightarrow [C_{60}:(\gamma\text{-CyD})_2 + 2.Na]^{2+} \quad \textbf{(4)}$$

The fact that only doubly charged ions were detected might be a consequence of the decreasing sensitivity of the instrument for the higher masses or result from the dimeric nature and symmetrical structure of the complex and of the mechanisms responsible for the ionization.

The interactions responsible for the complex stability were probed in gas phase using collision induced dissociation with Argon. The collision induced dissociation

experiments were performed by varying only the collision energy in the laboratory frame with all the other parameters, including the voltage differences in the negative and positive mode, kept constant. In our experimental setup the activation takes place in a stepwise fashion due to multiple collisions. The time between the collision steps and before the dissociation is long compared to the vibrational periods so that reactions can occur during the activation process or more generally before the detection step [64].

As discussed in the experimental section, activation by multiple collisions of a large molecular complex in mass spectrometry can only be used to probe the interactions responsible for the ion stability as a whole. Furthermore, in gas phase, the interactions responsible for the complex stability – hydrogen bonding, charge transfer, electrostatic and Van der Waals interactions – can be strengthened and may completely mask weaker interactions since ionic or ion-dipole interactions are no longer screened by the solvent molecules. The existence of the complex and the influence of dehydratation were studied by Yoshida *et al.* [21] using circular dichroism (CD). Since γ-CyD is chiral but nonchromophoric and C_{60} chromophoric but achiral, circular dichroism can be used to study the encapsulation of C_{60} by γ-CyD [21]. Increasing dehydration was observed to give rise to more intense negative and positive CD bands suggesting an increasing interaction due to orbital steering between C_{60} and the functional groups (active sites $–O^{(4)}-$ and $–O^{(3)}H$) of γ-cyclodextrin units and supporting a charge transfer interaction. Finally, besides the solvatation conditions, the stability of the molecular complex also depends on their charge state and on the charge location. In the case of doubly charged ions, C_{60} can act as a dielectric and reduce the perception of the two charges. However, for the

deprotonated complex, an electron and radical hydrogen transfer to C_{60} occurs prior to dissociation. This is likely to affect the repulsion between the two charges and therefore the complex structure and stability. According to the values of the collision energy corresponding to survival yields of the parent ions of 50% (Fig. 6.1.10), the deprotonated, protonated and cationized ions follow the following stability order $[C_{60}:(\gamma\text{-CyD})_2 + 2.H]^{2+} < [C_{60}:(\gamma\text{-CyD})_2 - 2.H]^{2-} < [C_{60}:(\gamma\text{-CyD})_2 + 2.Na]^{2+}$.

From the collision induced dissociation of the $[C_{60}:(\gamma\text{-CyD})_2 - 2.H]^{2-}$ and $[C_{60}:(\gamma\text{-CyD})_2 + 2.Na]^{2+}$ complex ions which yields intact γ-cyclodextrin ions, it is suggested that the release of the [60]fullerene occurs from an open γ-cyclodextrin cavity. The detection of the $[(\gamma\text{-CyD})_2\text{-}2.H]^{2-}$, $[(\gamma\text{-CyD})_2\text{-}3.H]^{-}$ (see Fig. 6.1.8) and $[(\gamma\text{-CyD})_2\text{+}2.Na]^{2+}$ (see Fig. 6.1.9) dimers even suggest an opening of the cavity similar to a bivalve shellfish.

Besides γ-cyclodextrins, γ-cyclodextrin dimers and their fragments (see Fig. 6.1.5 to 6.1.9), $C_{60}H^-$ and $C_{60}^{\bullet-}$ fragments of the $[C_{60}:(\gamma\text{-CyD})_2 - 2.H]^{2-}$ complex ion are also detected (see Fig. 6.1.8). Both fragments were observed by Giesa *et al.* [11] using fast atom bombardment (FAB) mass spectrometry. The $C_{60}H^-$ fragment was interpreted in terms of hydride attachment. It contributes as a second process in the ionization of C_{60} in FAB. The abundance of the $C_{60}H^-$ is lower in FAB than in electrospray.

The $C_{60}^{\bullet-}$ formation can be easily explained by the transfer of one electron from the deprotonated cyclodextrins to the C_{60} due to its large electron affinity, 2.7 eV [65]. Two mechanisms are proposed to explain the formation of the $C_{60}^{\bullet-}$ and $C_{60}H^-$ fragments, involving an electronic transfer (a or a') and an acid-base reaction (b):

Mechanism 1:

$$C_{60}:[(\gamma\text{-CyD})_2 - 2.H]^{2-} \rightarrow [C_{60}:(\gamma\text{-CyD})_2 - 2.H]^{\bullet -} + \text{“ } e^- \text{ “}$$

$$[C_{60}:(\gamma\text{-CyD})_2 - 2.H]^{\bullet -} \rightarrow [C_{60}:(\gamma\text{-CyD}) - H]^- + [(\gamma\text{-CyD}) - H]^{\bullet}$$

$$[C_{60}:(\gamma\text{-CyD}) - H]^- \rightarrow C_{60}^{\bullet -} + [(\gamma\text{-CyD}) - H]^{\bullet} \qquad \textbf{(a)}$$

Mechanism 2:

$$C_{60}:[(\gamma\text{-CyD})_2\text{-}2.H]^{2-} \rightarrow C_{60}^{2-}:[(\gamma\text{-CyD})_2\text{-}2.H] \qquad \textbf{(a')}$$

$$C_{60}^{2-}:[(\gamma\text{-CyD})_2\text{-}2.H] \rightarrow C_{60}H^-:[(\gamma\text{-CyD})_2\text{-}3.H]^- \qquad \textbf{(b)}$$

$$C_{60}H^-:[(\gamma\text{-CyD})_2\text{-}3.H]^- \rightarrow C_{60}H^- + \{[(\gamma\text{-CyD})_2\text{-}H]^- + [(\gamma\text{-CyD})_2\text{-}2.H]\}$$

The electronic transfer steps (a or a') are supported by the following arguments. First, Yoshida *et al.* [21] concluded from the chemical shifts of the ^{1}H NMR and ^{13}C NMR spectra that the specific interaction leading to chirality induction in the circular dichroism experiments and to the stability of the complex is the charge transfer from the n-donor oxygen atoms ($-O^{(4)}-$ and $-O^{(3)}H$) to the C_{60} (see Fig. 6.1.12). The reasons are that 1) C_{60} does not behave as a π base but as an extremely strong electron acceptor (E.A. = 2.7 eV [65]) and ether oxygen and alcoholic oxygen are known to serve as n-donor in the formation of charge-transfer complexes; 2) molecular models and X-ray structure of γ-CyD and C_{60} indicate that the ether oxygen atom ($O^{(4)}$) and the strongly hydrogen-bonded oxygen atom at C3 ($O^{(3)}$) between adjacent glucose units are favourably situated for charge transfer to C_{60} [21]. However, since the characteristic NIR and ESR spectra of the anions of C_{60} were not observed, the amount of charge transfer in the neutral $[C_{60}:(\gamma\text{-CyD})_2]$ complex is considered to be smaller than one elemental charge [21]. Secondly, in the present study using negative

mode mass spectrometry, deprotonation of two hydroxyl groups of the $[C_{60}:(\gamma\text{-CyD})_2]$ complex yields two alkoxide groups. Yoshida and coworkers [21] reported, using VIS/NIR spectroscopy, the generation of γ-cyclodextrin bicapped $C_{60}^{\bullet-}$ and C_{60}^{2-} by electron transfer to the C_{60} from alkoxide anion(s) following the addition of NaOH or $NaOH+Na_2SO_4$ to the $[C_{60}:(\gamma\text{-CyD})_2]$ complex solution, at 25°C under argon. The alkoxide groups of the $[C_{60}:(\gamma\text{-CyD})_2 - 2.H]^{2-}$ anion thus interact with the C_{60}, which acts as an electron acceptor and reduction of the C_{60} occurs. If C_{60} has a significant first electron affinity of 2.7 eV [65], C_{60}^{2-} anions have only been observed by mass spectrometry following highly energetic processes such as laser ablation [66, 67, 68] even though their lifetime is considerably greater than 1 ms [66]. This suggests for the present system that more than one electron is transferred to the fullerene core, the second electron likely being loosely bound. This leads in the case of mechanism 1 to an electron loss consistent with the observation that a small fragment negatively charged (below our mass spectrometer detection limit of 90 m/z) or an electron has to go undetected to respect charge conservation upon collision induced dissociation of the $C_{60}:[(\gamma\text{-CyD})_2 - 2.H]^{2-}$ complex anion.

The acid-base reaction (b) occurring in mechanism 2 is supported by the following arguments. The [60]fullerene dianion, C_{60}^{2-}, is known to have a significant basic character compared to C_{60} and $C_{60}^{\bullet-}$ [69, 70, 71]. Cliffel and Bard [69] showed that reduction of C_{60} to the radical anion, $C_{60}^{\bullet-}$, is unaffected by the presence of weak proton donors in *o*-dichlorobenzene, indicating that the monoanion is a weak base. They also observed that upon addition of triflic acid to a solution of C_{60}^{2-} in acetonitrile the near-IR spectrum of the resulting product resembles that of $C_{60}^{\bullet-}$. Two mechanisms were proposed to explain this result, a redox reaction ($C_{60}^{2-} + H^+ \rightarrow C_{60}^{\bullet-}$

+ $H^{\bullet}$) and a protonation ($C_{60}^{2-} + H^{+} \rightarrow C_{60}H^{-}$) [69]. Evans and coworkers [70] used voltametric techniques to monitor the acid-base reactions of reduced forms of C_{60} in dimethyl sulfoxide (DMSO) solution. They found the pK_a of C_{60}^{2-} to be in the [10.8:16.4] interval. Finally, Ohlendorf *et al.* [71] determined the pK_a of singly reduced C_{60} encapsulated in γ-cyclodextrin and dissolved in a water/propan-2-ol mixture to be 4.5(±0.5) on the basis of a specific IR absorption band for $C_{60}^{\bullet-}$- γ-CyD.

These results suggest that the [60]fullerene dianion formed in mechanism 2 by the electron transfer from the alkoxide groups of the γ-cyclodextrins captures a proton from one of its host molecules, as can be seen from the experimental tandem mass spectra (see Fig. 6.1.5 and 6.1.8). The mechanism proposed is also consistent with the results of Priyadarsini *et al.* [20] for the reaction of the C_{60}:(γ-CyD)$_2$ complex with the $OH^{\bullet}$ radical.

A radical or proton transfer to the [60]fullerene occurring in the bulk of the solution is unlikely to take place since the complex would have to lose three protons from the cyclodextrins to match the experimental isotopic pattern that corresponds to the $[C_{60}:(\gamma\text{-CyD})_2 - 2.H]^{2-}$ anion. Furthermore, in that case, the $[C_{60}:(\gamma\text{-CyD})_2 + 3.H]^{2+}$ and $[C_{60}:(\gamma\text{-CyD})_2 + H + 2.Na]^{2+}$ ions would also likely be present and the isotopic distributions shifted to the higher mass to charge ratios by 0.5 m/z (since the complex ions are doubly charged). Further indications supporting an intramolecular hydrogen transfer in gas phase are the double acetate adducts observed in standard electrospray (see Fig. 6.1.11) supporting a late double deprotonation as the ionization mechanism, and the trace fragments observed which include $C_{60}^{\bullet-}$and $[(\gamma\text{-CyD})_2\text{-}2H]^{2-}$ (see Fig. 6.1.8).

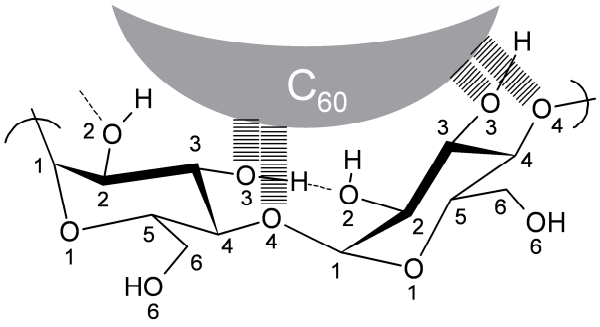

Fig. 6.1.12. Charge transfer interactions from the n-donor oxygen atoms of the γ-cyclodextrin units and the C_{60} (adapted from reference 8).

6.1.4. Conclusions

Electrospray mass spectrometry is suitable to study the $[C_{60}:(\gamma\text{-CyD})_2]$ inclusion complexes. The electrospray and collision induced dissociation spectra of $[C_{60}:(\gamma\text{-CyD})_2]$ ions are reported for the first time, both in positive and negative ion mode mass spectrometry. Structural information using MS and tandem MS has been obtained confirming the bicaped structure of the complex. Evidence for electron and proton transfers following double deprotonation of the complex has been provided. A stability order in gas phase has been provided for the doubly deprotonated, protonated and sodiated $[C_{60}:(CyD)_2]$ ions: $[C_{60}:(\gamma\text{-cyclodextrin})_2 + 2H]^{2+} < [C_{60}:(\gamma\text{-cyclodextrin})_2 - 2H]^{2-} < [C_{60}:(\gamma\text{-cyclodextrin})_2 + 2Na]^{2+}$. Finally, this work opens the way to further studies and applications of the $[C_{60}:(\gamma\text{-CyD})_2]$ inclusion complex ions in gas phase using electronebulization as the ionization technique.

6.2. Cross Section Measurements of the $C_{60}:(\gamma\text{-CyD})_2$ complex using gas phase ion mobility

In a non-covalent complex, the properties of the original subsystems are relatively unperturbed compared to the isolated molecules. Nevertheless, the formation of a

non-covalent complex does affect properties of the subsystems, and these changes are important for the detection of the complex formation. The stronger the non-covalent interaction, the larger the changes in the properties of the subsystem [72]. In order to gain information on [C_{60}:$(CyD)_2$] ions and their properties, to clarify the influence of desolvation, and to improve the description of the noncovalent interactions involved, the 3D structure of the complex in gas phase is required.

Gas phase conformations are typically inferred from indirect methods such as ion mobility measurements, ion-molecule and ion dissociation reactions [73, 74, 75]. The mobility of a polyatomic ion describes its ability to move through a buffer gas under the influence of a (weak) electric field [76, 77, 78]. It depends on its average collision cross section and can be used to separate structural isomers [76, 77, 78]. Compact isomers have higher gas phase mobilities and smaller cross-sections than distributed ones. Reduced ion mobilities/average cross sections can be respectively measured/inferred accurately and used to deduce information about the gas phase geometries of ions by comparison with their theoretically predicted equivalents [76, 77, 78].

Model structures of cyclodextrins were reported using force field based [79, 80, 81, 82, 83, 39], semi-empirical [84, 85, 86, 87] and *ab initio* [87] methods. Koehler *et al.* [79, 80] reported molecular dynamics simulations on α- and β-CyD with the Gromos package. Their molecular crystal simulations reproduced the distorted, collapsed molecular structure of α-CyD and the more regular, round structure of β-CyD as observed crystallographically [81]. Lipkowitz [82, 83] analyzed the inherent features of isolated cylodextrins void of water as well as crystal-lattice effects using AMBER

and MM2 empirical force fields. Symmetry breaking was found to lower their energy leading to considerable deviations from their regular, highly symmetrical shape. Using the PIMM empirical force field Lichtenthaler and Immel [39] reached a different conclusion, cyclodextrins are symmetrical due to the stabilizing interactions of the interglucose hydrogen bonds.

Avakyan *et al.* [85, 86, 87] and Guo *et al.* [84] performed semi-empirical studies of cyclodextrins using AM1 and PM3. PM3 is reported to be more accurate in reproducing the geometries of intermolecular hydrogen-bonded complexes [88], with cyclodextrins retaining the overall circular shape found in crystals. Structures of the free β-CyD having exact C_7 symmetry were reported to correspond, at the PM3 and AM1 levels, to the global minimum of the potential energy [86]. The α- and γ-CyD were also reported to be very close to the strictly symmetric forms at the PM3 level [87].

Avakyan *et al.* [87] also performed full geometry optimizations of α-, β-, and γ-CyD using the quantum chemical program Priroda [89, 90], the Perdew-Burke-Ernzerhof (PBE) exchange-correlation functional and a triple-zeta Gaussian basis set with the electron density expansion in an atom-centered auxiliary basis set [89]. All structures are stabilized by a ring of interglucose hydrogen bonds formed between the secondary hydroxyl groups [85, 86, 87]. The lowest energy orientation of the H bond ring corresponds either to the (2)OH and (3')OG groups respectively acting as H donor and H acceptor or the converse depending on the calculation level [85, 86, 87]. Clearly, in the case of γ-cyclodextrin, an accurate description of the molecule 24

hydroxyl groups (8 primary CH_2-OH and 16 secondary CH-OH) and related hydrogen bonds is desirable.

Finally, isolated cyclodextrins dimers were also studied in the three possible orientations between CyD units, i.e. the head-to-head (HH), tail-to-tail (TT), and head-to-tail (HT) structures [91, 92, 86]. Using molecular mechanics and dynamics simulations, Jaime *et al.* [91, 92] found the HH orientation of the isolated dimer to be the most stable for α-, β- and γ-CyD whereas Avakyan *et al.* [86] concluded the head-to-tail (HT) dimer of the β-CyD to be thermodynamically more stable at the PM3 level.

In the HH orientation, the γ-CyDs can interact via a maximum of sixteen intermolecular H bonds involving a system of four interglucose H bonds connecting (2)OH and (3')OH groups of adjacent and opposite glucose residues. Due to stereochemical restrictions, major intraresidue hydrogen bonding components between O(2) and O(3) of the same glucose cannot be formed [93]. X-ray and neutron diffraction studies have furthermore demonstrated the occurrence of circular chains of minimum four hydrogen bonds involved in a cooperative effect. The "cooperative effect" is the mutual polarization of hydrogen-bonding groups, which are interconnected to form larger arrangements [94, 95, 96]. It strengthens a H-bond if the donor accepts an H-bond from another donor [97]. In the γ-CyD dimer, three different orientations of the ring system of four interglucose H bonds connecting (2)OH and (3')OH groups of adjacent and opposite glucose residues are worth considering. In one case, the H bond ring on each of the γ-CyD is formed by H atoms of (2)OH groups and O atoms of (3')OH groups ((2)OH→O(3')H), called "clock-wise" (H),

with the γ-CyD linked through the secondary (3)OH groups. In the reciprocal case, the H bond ring on each of the γ-CyD is formed by H atoms of (3')OH groups and O atoms of (2)OH groups ((3')OH→O(2)H), called "trigonometric" (T), with the γ-CyD linked through the secondary (2)OH groups. The last case is the alternation of the two: (2)OH→O(3')H, (3')OH→O(2)H, etc. (see Fig. 6.2.1).

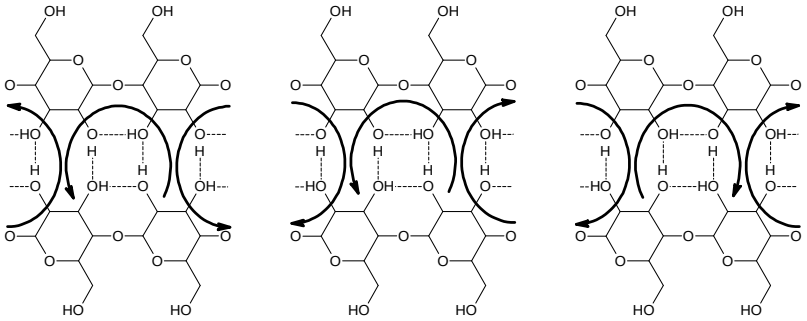

"T" orientation alternated orientation "H" orientation

Fig. 6.2.1. Schemes of the three inter-molecular H-bond orientations that can stabilize a γ-CyD dimer of the "head-to-head type". "Head-to-head" cyclodextrin complexes involve the cyclodextrins interacting *via* their secondary hydroxyls and are the only one relevant to the complexation of C_{60}.

Experimentally, Betzel *et al.* [96] found, while using neutron diffraction, that the interglucose O(2)…O(3') hydrogen bonds in crystallized cyclodextrins are of the flip-flop type [98, 96, 99], in dynamic equilibrium [93] (see Fig. 6.2.2) as well as attracted by the neighbouring glucosidic O(4) atoms [96]. Consequently both left and right orientations are expected to exist in the gas phase ion population.

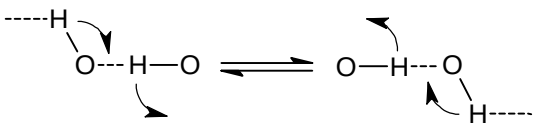

Fig. 6.2.2. Flip-flop hydrogen bonds in dynamic equilibrium adapted from reference [98].

Even though, the γ-CyD is more flexible than the β-CyD and could thus deviate from a round-shape symmetric structure, the C_{60} fullerene is expected to act as a template and constrain the γ-CyD to round-shape provided tight encapsulation occurs.

An overview of the experimental studies performed on the [C60:(γ-CyD)$_2$], first observed by Andersson *et al.* [14], can be found in section 6.1. Additional information can however be inferred from ^{1}H NMR and circular dichroism. The ^{1}H NMR spectra of the complex in solution obtained by Andersson *et al.* [15] and Yoshida *et al.* [21] show the presence of two different γ-CyD species; one with the same shifts as free γ-CyD, the other with slightly shifted proton signals. The substantial downfield ^{13}C shifts of C1 and C4 and ^{1}H shift of 3-H as well as the slightly upfield shifted 1-, 2-, 4- and 5-H led Yoshida *et al.* [21] to conclude that the specific interaction leading to chirality induction and stabilization of the complex was the charge transfer from the n-donor (the hydroxyl oxygen atom bound to C3 and the ether oxygen between adjacent glucose units) to C_{60}. In addition, since the observed induced ^{1}H NMR shifts for all but one of the protons are very small, only small conformational changes are expected for γ-CD upon complexation of C_{60}.

The [C_{60}:(γ-CyD)$_2$] complex has been the subject of a limited number of theoretical studies, all of them using empirical force field methods [14, 15, 100, 101]. Besides the results of Andersson *et al.* [14, 15] (see section 6.1), C_{60} was also reported to be perfectly enclosed in the [C_{60}:(γ-CyD)$_2$] complex with the secondary hydroxyl groups of two γ–cyclodextrin involved in intermolecular hydrogen bonds by Marconi and Coworkers [100]. Using the MM3 force field, Monte-Carlo simulations and semi-empirical methods to compare the measured and calculated induced circular

dichroism spectra, they found highly symmetric, tightly bound complexes to be the most probable structures. Jaime *et al.* [101] studied the [C_{60}:(γ-CyD)$_2$] complex by molecular dynamics simulations with the AMBER package. Dummy atoms were used to incorporate the various electron densities on the fullerene bonds into the molecular mechanics scheme. According to their molecular dynamics simulations the C_{60} is not completely encapsulated and the two γ-CyDs are not round-shaped but adopt a V-shape only strengthened by a few intermolecular hydrogen bonds.

In the present section as in the previous, electrospray ionization (ESI) effects the transfer of molecules from solution to gas phase, concurrently to their ionization and desolvation. Although solution specific complexes can be detected by electrospray mass spectrometry, the extent of the similitude between the structures in solution and ionized in gas phase as well as between the intramolecular interactions in both phases is unclear [75, 102, 103]. Interactions not present or not dominant in solution which form or strengthen during or after the ESI process have been shown to contribute significantly to the stability of some specific complexes in the gas phase. Among those interactions intermolecular hydrogen bonds can strongly influence the energetic and kinetic stability of gas phase complexes [75, 102, 103]. Klassen and coworkers [103] suggested that the solution phase interactions could impose conformational constraints preventing, in some cases, the gas phase complex from adopting a lower energy structure. Complementarily they also suggested that the disappearance of the solution phase interactions might allow the complex to explore a greater region of the conformational space and to relax to a lower energy structure [103].

In short the gas phase ion mobility measurements will provide accurate information on the gas phase structures of unknown transferability to the solution phase. Inter-studies transferability is further disputable since the [C_{60}:(γ-CyD)$_2$] can be produced and stored under different conditions [14, 16, 17, 18, 19, 21, 22, 24, 52, 25, 26]. Steiner and Koellner [104] suggested that the preparation and storage conditions could affect the structure of the cyclodextrins complexes. Indeed, a strengthening of the hydrogen bonds is expected to occur upon removal of water and the interactions between the γ-CyDs and the C_{60} increase under increasingly hydrophobic conditions [21]. Therefore, preparation conditions involving a lyophilization step, as used in the present study, could help overcome a complexation energy barrier and stabilize the [C_{60}:(γ-CyD)$_2$] complex in a lower energy compact structure with up to sixteen intermolecular hydrogen bonds between the two γ-CyD, closely related to the ion gas phase structures. This structure is expected to be relevant to both solution and gas phases.

In short, the present section aims at: (1) reporting the gas phase mobilities of the [C60:(γ-CyD)$_2$] complex ions (2) inferring additional structural information on the encapsulation of a C_{60} molecule by a γ-cyclodextrin dimer by the comparison of the experimental cross sections obtained from gas phase ion mobility measurements with those obtained from semi-empirical and *ab initio* calculations, (3) comparing the three dimensional structures of the deprotonated and sodiated [C_{60}:(CyD)$_2$] ions and inferring the area of the C_{60} accessible to the solvent and available for functionalization in aqueous solution, (4) discussing the ionization method influence on the interactions responsible for the stability order, [C_{60}:(γ-cyclodextrin)$_2$ + 2H]$^{2+}$ <

$[C_{60}:(\gamma\text{-cyclodextrin})_2 - 2H]^{2-} < [C_{60}:(\gamma\text{-cyclodextrin})_2 + 2Na]^{2+}$, determined by collision induced dissociation in the gas phase.

6.2.1 Experimental and Theoretical

The [60]fullerene : γ-cyclodextrin complexation was performed according to a method similar to that described by Yoshida *et al.* [21]. Both complexation and preparation for electrospray mass spectrometry were described in detail in section 6.1.1 and reference [13].

The ion mobility measurements were carried out at the University of California Santa-Barbara in Professor Bowers group.

Information about the shape of conformers present in the mobility data is obtained by comparing the collision cross sections derived from the mobility measurements to those calculated for trial structures. The experimental setup for the ion mobility measurements has been described in reference [105] and has provided mobility data for many systems, e.g. DNA and PNA [106]. The ions studied are electronebulized using nanospray and metalized boro-silicate (PROTANA) needles. They enter the instrument via an ion funnel and are injected into a 4.5 cm long drift cell filled with ~5 Torr of helium (at room temperature). After exiting the drift cell, the ions are mass analyzed in a quadrupole mass filter, which can be either set for the acquisition of a mass spectrum or for detecting one specific m/z as a function of time, yielding an arrival time distribution (ATD).

The mobility of a single isomer can be determined from its arrival time distributions (ATDs) by two different approaches.

In the first approach, the mean arrival times of a series of ATDs, obtained by changing only the voltage across the drift cell, are fitted by a straight line as a function of the voltage inverse. In that case the mobility of the isomer is extracted from the fit slope and the intercept equals the sum of the time spent outside the drift cell (equation 6.2.1).

$$t_A = t_d + t_0 = \left(\frac{L^2}{V} \frac{p}{760} \frac{273.15}{T} \frac{1}{K_0} \right) + t_0 \qquad (6.2.1)$$

with t_A the arrival time, t_d the drift time, t_0 the time spent outside the drift cell, L the drift cell length, V the voltage across the drift cell, p and T the pressure (Torr) and temperature of the buffer gas inside the drift cell and K_0 the reduced mobility.

The uncertainty associated with these measurements can be slightly affected by systematic effects such as penetration of the ions into the drift tube upon injection (which decreases the effective length of the drift tube). However, ion mobility distributions recorded at varying injection energies and buffer gas pressures yield similar mobilities and suggest that these effects are small. The statistical uncertainty of the mobility values obtained this way is usually better than $\pm 2\%$ [76].

In the second approach, if the time spent by the ions outside the cell is known, the mobility can be determined by fitting the arrival time distributions with a theoretical model. This approach allows extracting from the peak widths information about the number of conformers present within each peak of the total drift time distribution [76, 107]. When the measured drift time distribution is significantly broader than the calculated distribution, it indicates that at least two conformers with similar cross sections or conformers interconverting over the experiment time scale are present. In case good agreement is achieved between the measured and calculated drift time

distribution, either a single conformer or conformers having identical cross sections are present [108]. For a cylindrical drift tube and constant electric field [109, 110, 111, 76], the ATD of a single ion type can be modeled by equation 6.1.1.

$$\phi(t) = \frac{C\left(v_D + \frac{L}{t}\right)}{4(\pi D_l t)^{\frac{1}{2}}}\left[1 - \exp\left(\frac{-r_0^2}{4D_t t}\right)\right]\exp\left(-\frac{(L - v_D t)^2}{4D_l t}\right) \qquad (6.1.1)$$

where v_D is the measured drift velocity, L is the length of the drift cell, r_0 is the size of the drift cell entrance aperture, C is a scaling factor for the intensity, and D_l and D_t are the longitudinal and transversal diffusion coefficients. Under the low field conditions, D_l and D_t can be calculated from the Einstein relation, $D_L = D_t = \frac{Kk_BT}{ze}$ with $K = \frac{v_D L}{V} = \frac{760T}{p273.15}K_0$ the mobility. The above equation is valid for a delta pulse entering the cell. If the input pulse width is comparable to the width of the ATD, the above expression has to be convoluted with the width of the input pulse. For multiple ion types with different drift velocities (and therefore different diffusion coefficients), the resulting ATD is just the sum of the ATDs for the individual ions [76]. The ATD fitting is performed using the Levenberg-Marquard algorithm and the drift velocity $v_D = \frac{L}{t_D}$ as fitting parameter. If more than one isomer is present a linear combination of $\phi(t)$ is considered with the fractional abundances adding up to 1, a scaling factor, and the individual drift velocities as fitting parameters [76].

Only the first approach was used in the present work. The measured mobilities were converted for comparison with theoretical results into orientationally averaged collision integrals using

$$\Omega_{avg}^{1,1} = \frac{3ze}{16N_0}\left(\frac{2\pi}{\mu k_B T}\right)^{\frac{1}{2}}\frac{1}{K_0} \qquad (6.2.2)$$

with *ze* the ion charge, N_0 the buffer gas number density at standard temperature and pressure (STP), μ the ion-buffer gas reduced mass, k_B the Boltzmann constant and T the effective temperature [112, 111].

Three different approximations of decreasing complexity and computational cost can be used to infer orientationnally averaged cross sections from theoretical model structures: the trajectory approximation (TA), the enhanced hard sphere scattering approximation (EHSS) and the hard sphere projection approximation (HSPA). A fourth approximation (SIGMA) developed by the Bowers group and in some ways comparable to the trajectory approximation can also be used.

The trajectory calculation (TA) approach has been implemented by Mesleh *et al.* [112]. The average collision integral $\Omega_{avg}^{(1,1)}$ is used for comparison with experiments. It is obtained by averaging the first order transport cross section over the angles ϑ, φ, and γ that define the orientation of the polyatomic ion, and by averaging over the relative kinetic energy of the ion-neutral collision. The scattering angles, $\chi(\vartheta,\varphi,\gamma,v,b)$, used in the calculation of the collision integral for a given collision geometry, and relative velocity, v, are calculated for each impact parameter, b, by numerical integration of the equation of motion for a selected ion-atom interaction potential [112, 111].

$$\Omega_{avg}^{(1,1)} = \frac{1}{8\pi^2}\int_0^{2\pi}\mathrm{d}\vartheta\int_0^{\pi}\mathrm{d}\varphi\sin\varphi\int_0^{2\pi}\mathrm{d}\gamma\left(\frac{\mu}{2k_B T}\right)^3\int_0^{\infty}\mathrm{d}v\, e^{-\mu v^2/2k_B T}v^5\; 2\pi\int_0^{\infty}\mathrm{d}b\, b\left(1-\cos\chi(\vartheta,\varphi,\gamma,v,b)\right)$$

(6.2.3)

The ion-atom potentials used in the scattering angle determination are selected to mimic the true potential in a reasonable way [111]. In the MOBCAL program developed by Jarrold and Coworkers [112] each atom of the ion is represented by a (12, 6, 4) potential with the additional term compared to the Lennard-Jones potential describing the ion-induced dipole interaction [112]. The effective potential (taking into account the contributions of all the atoms constituting the molecule) is obtained by summing over the individual atomic contributions. It can take into account the long range interactions between the polyatomic ion and the buffer gas, the effect of temperature, and multiple collisions [112].

The exact hard sphere scattering model (EHSS) developed by Shvartsburg and Jarrold [113] is less computationally intensive than the trajectory approach. It models the ion by a collection of overlapping hard spheres with radii equal to hard sphere collision distances. It accounts for the details of the scattering process, such as multiple scattering by polyatomic ions with partially concave surfaces, but not the long range interactions [113]. The average collision integral $\Omega_{avg}^{(1,1)}$, obtained by averaging the first order transport cross section over the angles ϑ, φ, and γ, does not depend anymore on the relative velocity.

$$\Omega_{avg}^{(1,1)} = \frac{1}{8\pi^2}\int_0^{2\pi} \mathrm{d}\vartheta \int_0^{\pi} \mathrm{d}\varphi \sin\varphi \int_0^{2\pi} \mathrm{d}\gamma \, 2\pi \int_0^{\infty} \mathrm{d}b \, b\left(1-\cos\chi\left(\vartheta,\varphi,\gamma,b\right)\right) \qquad (6.2.4)$$

Calculating collision integrals for big molecules by the trajectory method uses a lot of computer power. The hard spheres scattering model can reproduce the results obtained by the trajectory method provided the small temperature dependence of the cross sections is taken into account by scaling the hard sphere contact distances used

in the exact hard spheres scattering model to reproduce the cross sections calculated by the trajectory method [114]. Shelimov and Coworkers [115] observed that the cross sections determined with the exact hard spheres scattering model for BPTI and cytochrome c are within 1% of the cross sections determined by trajectory calculations.

The less computationally demanding approach for the calculation of the average collision integral, $\Omega_{avg}^{(1,1)}$, is the hard sphere projection approximation [116, 76, 117] (HSPA). It involves the projection of the polyatomic ion structure on a plane. The area, σ_{PA} defined by the minimum impact parameters, $b_{\min}$, that avoid a hard sphere contact with the buffer gas atom for each atom of the polyatomic ion is calculated by Monte Carlo integration [76, 117]. The projected hard sphere cross section, σ_{PA}, is then averaged over all the orientations of the polyatomic ion.

$$\Omega_{avg}^{(1,1)} = \frac{1}{8\pi^2}\int_0^{2\pi} \mathrm{d}\vartheta \int_0^{\pi} \mathrm{d}\varphi \sin\varphi \int_0^{2\pi} \mathrm{d}\gamma\, \sigma_{PA} \qquad (6.2.5)$$

The values of $b_{\min}$ are defined as $b_{\min} = \frac{1}{2}\left(d_{atom} + d_{He}\right)$ with d_{He} and d_{atom}, the contact distances of the He atom and of the H, C, N, and O atoms respectively. The Hard Sphere Projection Approximation ignores the details of the momentum transfer, such as the scattering angle and multiple collisions, as well as long-range interactions [116, 112, 117]. Deviations larger than 20% have been shown to occur between the hard-spheres projection approximation and the exact hard-spheres scattering model due to the neglect of multiple scattering events. [108].

In addition to the three approximations reported above, Von Helden *et al.* [118, 119] developed a less computationally intensive approximation than the trajectory approximation [112] that reproduces the temperature dependence of the mobibility (SIGMA). They do not use the potential obtained by summing the contributions of all the atoms of the polyatomic ion to run trajectory calculations. Instead von Helden *et al.* [118, 119, 120] assume that the helium atom interacts in a pairwise fashion with each atom on the polyatomic ion. A generalized n-6-4 interaction potential is used to infer the atom-atom collision integral, $\Omega_{a-a}^{(1,1)}$ at temperature T. The contact distance between He and a given atom is equal to $\left(\frac{\Omega_{a-a}^{(1,1)}}{\pi}\right)^{\frac{1}{2}}$. These effective hard sphere radii are used to calculate the collision integrals by Monte Carlo integration [76, 119, 117].

Geometry optimization of the γ-CyD and its complexes is a multiple minima problem [83, 39, 121]. Sampling of the whole potential energy surface requires a significant amount of numerical resources. Furthermore, intermolecular interactions are difficult to model accurately using computational methods [122]. An accurate description of the $[C_{60}:(CyD)_2]$ complex and its ions would indeed require a good description of the electrostatic, induction (charge-induced dipole and dipole-induced dipole) and dispersion [123] (instantaneous dipole-induced dipole) forces. It is widely accepted that all currently available force-fields have weaknesses. Because each is tuned only to a limited number of molecular properties [38], they do not simultaneously describe carbohydrates and fullerenes accurately and are not suitable for the present study. The choice of the PM6 [124] and HF/sto-3g levels of theory (the less expensive in terms of numerical resources) was motivated by the huge size of the system studied (396

atoms), the numerous conformers to be screened, and the limited computer resources available.

Semiempirical methods such as PM6 are applicable to large molecules, and may give accurate results when applied to molecules that are similar to the molecules used for parameterization. In general, semiempirical results can be trusted only in situations when they are known to work well, e.g. systems similar to molecules in the parameterization set, they give satisfactory bond lengths and angles but the results are not as accurate as *ab ini*tio or DFT results with a suitable-size basis set. Furthermore, most semiempirical methods are not particularly well suited for predicting dihedral angles [125]. In spite of known drawbacks, e.g. dispersion is not described properly at the Hartree-Fock level [122], the *ab initio* HF/sto-3g gives fairly good predictions of bond distances and quite good predictions of bond and dihedral angles, but occasionally shows large bond-length errors [126].

In summary, it is acknowledged that a HF or B3LYP calculation with a bigger basis set, for example 6-31g(d,p) which has proven to produce reliable and consistent data on hydrogen bonding at the Hartree-Fock level [127] would provide more accurate results. However, a comparison of the results obtained using either PM6 or HF/sto3g methods is expected to provide some indication as to the relative importance of their limitations – for example the neglect of dispersion interactions by HF/sto-3g and not by PM6 – and help assess the accuracy of the conclusions reached. All *ab initio* calculations at the sto-3g level were executed using the Gaussian G03 package [128]; convergence to a minimum of the potential energy surface was checked by controlling the positive definite character of the Hessian. The structures were minimized with the

default criteria for convergence. The semi-empirical calculations at the PM6 level [124] were performed using MOPAC2007 version 127 [124]. The initial γ-CyD structure was initially obtained from the crystal structure determined by Harata [35].

6.2.2 Results

γ-cyclodextrin complexes are characterized by a large number of conformers. These conformers correspond (1) to the different values that can be taken by the angles (ψ, ϕ, θ_1, θ_2, ω, φ, and τ) of Fig. 6.1.1, (2) to the different combination of values when all eight D-glucose residues forming a single γ-cyclodextrins are considered, (3) to the combination of values when dimers of two cyclodextrin are considered, and finally, in the case of doubly charged ions, (4) to the different tautomers formed by different combinations of the ionization sites. Due to the limited numerical resources available, the theoretical conformational analysis was limited to educated guesses of the neutral [C_{60}:(γ-CyD)$_2$] complex structure with a complete hydrogen belt (sixteen intramolecular hydrogen bonds) postulated between the two γ-cyclodextrins. This rather limiting hypothesis will be reconsidered in the Discussion section.

The structures determined for the inclusion complex are reported in Appendix-1 Table A-1 with the main families of conformers illustrated in Fig. 6.2.3. All structures are characterized by the five torsion angles, the bond angle and the tilt angle described in the introduction. The simplified notation X0Y0X is used to describe the different conformers. 0 refers to the cyclodextrin conformer, X to the orientation of the primary hydroxyl groups and Y to the orientation of the hydrogen bonds involved in inter-glucose interactions. Both the primary (X) and secondary (Y) hydroxyl orientations can be described as trigonometric (T) or clockwise (H). The alternated orientations

(alt), possible for the secondary hydroxyls, were found to be energetically intermediate to the other two and will not be further discussed. For the [C_{60}:(γ-CyD)$_2$] complex each angle is described by one average value (of the eight contributing angles) and the associated standard deviation (Table 6.2. Appendix-1). The cross sections were obtained using the SIGMA [118, 119] method.

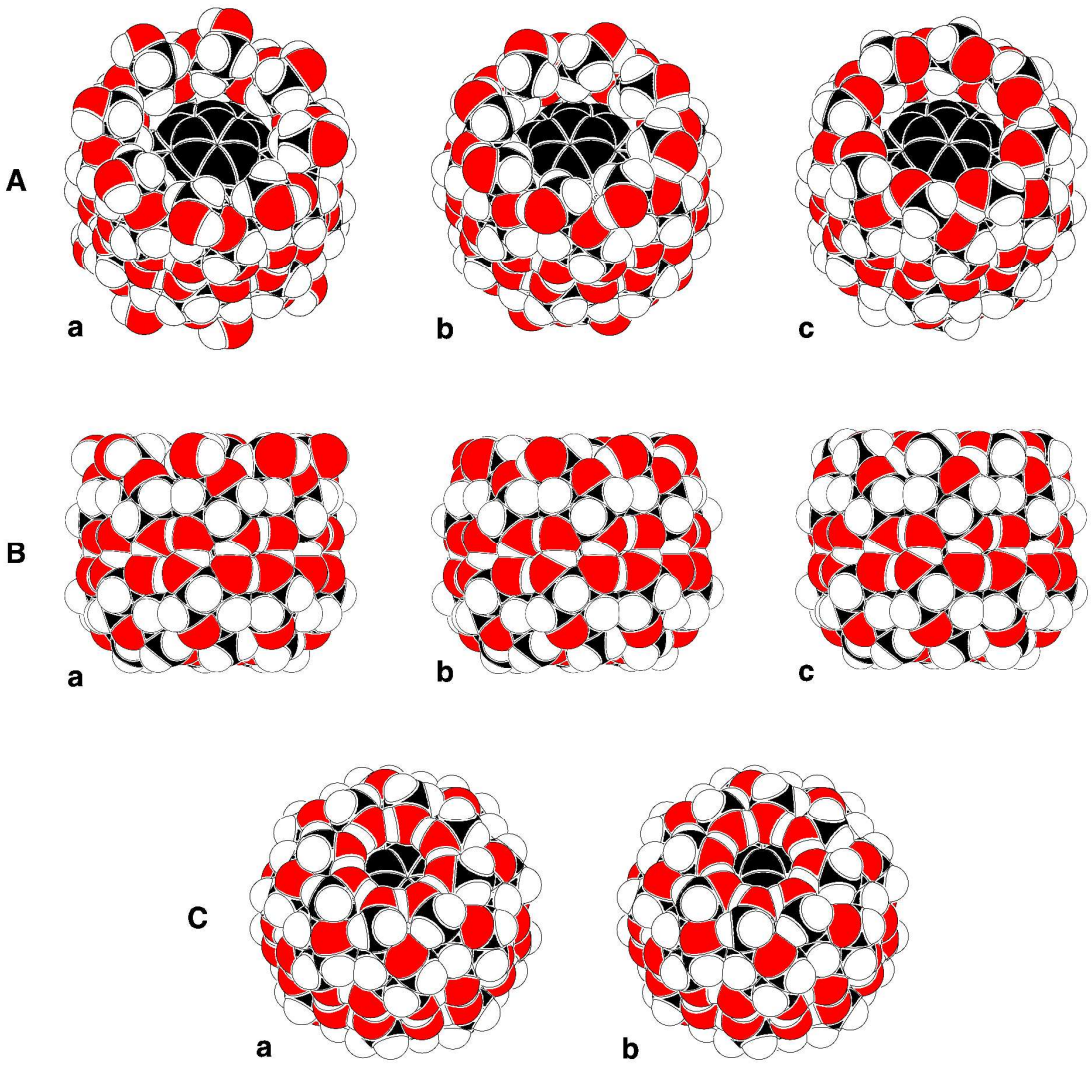

Fig. 6.2.3. The main conformer families formed upon the complexation of C_{60} by two γ-cyclodextrins. T1T1T (A.a), H4T4H (A.b), H3T3H (A.c) are symmetric barrel-shaped complexes. T1T5T (B.a), H4T5T (B.b), H3T5T (B.c) are cup-shaped complexes. T5H5T (C.a) and H5H5H (C.b) are sphere-shaped complexes. For a complete description of the different species see Appendix-1.

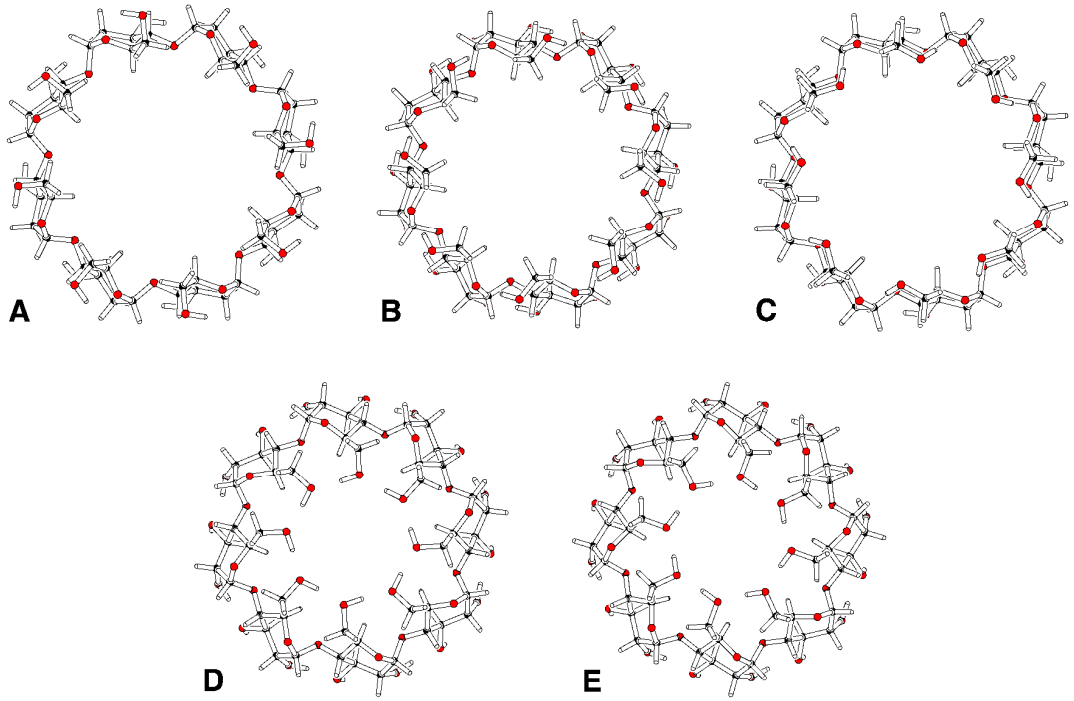

Fig. 6.2.4. Structures of the γ-cyclodextrins involved in the complexes: T1 (A), H4 (B), H3 (C), T5 (D), H5 (E). For a complete description of the different species see Appendix-1.

From the results displayed in table 6.2.1 Appendix-1, the conformers can be subdivided according to their cross-section into three groups: sphere- (sph), cup- (cup), and barrel-shaped (bar) (see Fig. 6.2.4 and Appendix-1 Fig. 1, 2, and 3). The sph, cup, and bar complexes respectively have cross-sections within the [363.4: 364.3], [378.3: 395.7], [394.7: 428.9] $Å^2$ ranges at the HF/sto-3g level and the [366.5: 368.8], [379.7: 392.1], [393.2: 415.4] $Å^2$ ranges at the PM6 level. The bar and cup complexes can be further subdivided according to the γ-cyclodextrin conformers involved (Appendix-1 Fig. 1). The different groups of conformers respectively have relative energies within the [0.0: 19.0], [11.8: 38.0], [24.6: 55.2] kcal/mol ranges at the HF/sto-3g level and within the [0.0: 31.6], [28.5: 62.1], [58.6: 92.6] kcal/mol ranges at the PM6 level.

The different conformations of the cyclodextrins involved in the $[C_{60}:(\gamma\text{-CyD})_2]$ complex are best summarized using the angle ω as conformational marker (Table 6.2.I) with their respective cross sections listed in Table 6.2.II.

Table 6.2.I. Values of the main conformational marker, ω, for the different conformers of the γ-cyclodextrin (see Fig. 6.2.4).

conformer	ω (HF/sto-3g)	ω (PM6)
T1	[-54.6: -54.0]	[-58.9: -56.5]
T2	[52.2: 53.3]	collapse → T5
H3	[164.5: 170.5]	[149.4: 164.7]
H4	[-91.9: -90.3]	[-115.5: -109.7]
T5	[122.7: 124.4]	[115.4: 116.5]
H5	[106.9: 109.2]	[108.3: 108.9]

Table 6.2.II. Cross-sections of the different conformations of the γ-cyclodextrin monomers in absence of C_{60} (see Fig. 6.2.4).

conformer	$\Omega_{avg}^{(1,1)}$ (HF/sto-3g)	$\Omega_{avg}^{(1,1)}$ (PM6)
T1	299.7 (0.6)	297.2 (0.6)
T2	289.5 (0.7)	collapse → T5
H3	283.5 (0.6)	284.2 (0.7)
H4	288.4 (0.6)	290.5 (0.7)
T5	275.3 (0.5)	278.1 (0.7)
H5	275.9 (0.5)	278.0 (0.7)

The experimental results obtained for the sodiated and deprotonated ions corresponding to the species described here above are being discussed hereafter.

A typical mass spectrum obtained for the deprotonated C_{60}:γ-cyclodextrin complex 2:1, $[C_{60}:(\gamma\text{-CyD})_2\text{-}2.H]^{2-}$, on the instrument used for the mobility experiments using a solution 15 % methanol and 20 mM NH4OAc is presented in Fig. 6.2.5. The mass to charge ratio of the $[C_{60}:(\gamma\text{-CyD})_2\text{-}2.H]^{2-}$ ions corresponds to 1655 m/z.

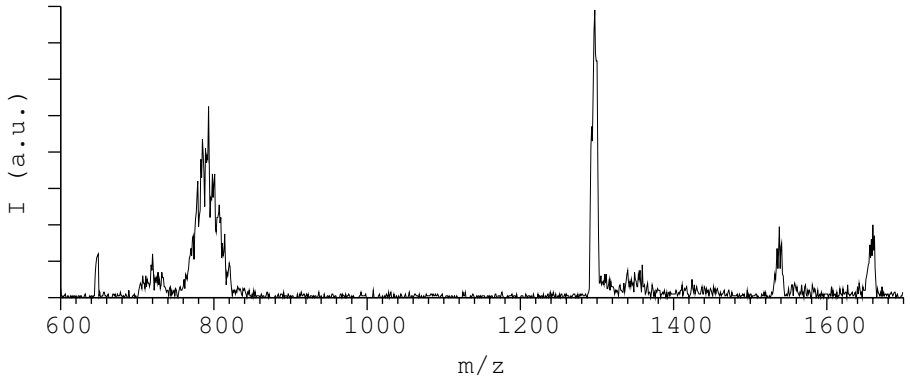

Fig. 6.2.5. Mass spectrum of the $[C_{60}:(\gamma\text{-CyD})_2]$ solution 15 % methanol and 20 mM NH_4OAc. The $[C_{60}:(\gamma\text{-CyD})_2\text{-}2.H]^{2-}$ and $[(\gamma\text{-CyD})\text{-}H]^-$ ions are respectively detected at 1655 and 1295m/z. The two lumps about 700 and 800 m/z are the consequence of a faulty reset of the acquisition, they do not affect the rest of the spectrum.

The arrival time distributions of the $[C_{60}:(\gamma\text{-CyD})_2\text{-}2.H]^{2-}$ anions were recorded with the quadrupole in the mass filter mode and the bandwidth centered on their mass to charge ratio, 1655 m/z (see Fig. 6.2.5). The ions were injected in the drift cell at voltages ranging from 15 to 55 V and the mobilities measured at five different drift voltages (see Fig. 6.2.6). The peaks of Fig. 6.2.6 correspond to the arrival time distributions of the $[C_{60}:(\gamma\text{-CyD})_2\text{-}2.H]^{2-}$ ions; the small shoulders on the left of each peak are small amounts of complex dimers, $[C_{60}:(\gamma\text{-CyD})_2 - 2.H]_2^{4-}$. The experimental conditions used to measure the cross sections were devised so as to reduce the amount of dimer to negligible quantities in order to avoid interferences due to its potential partial decomposition within the drift cell. The average cross section measured for $[C_{60}:(\gamma\text{-CyD})_2\text{-}2.H]^{2-}$ is equal to 386.0 $Å^2$ with a standard deviation of 1.0 $Å^2$ (only the

values obtained for drift voltages within the [15:40] V range are taken into account due to the increasing injection effect at higher voltages (see Fig. 6.2.7). The injection effect induces an apparent increase of the mobilities caused by the time required after injection for the ions to reach a stationary regime within the reaction cell).

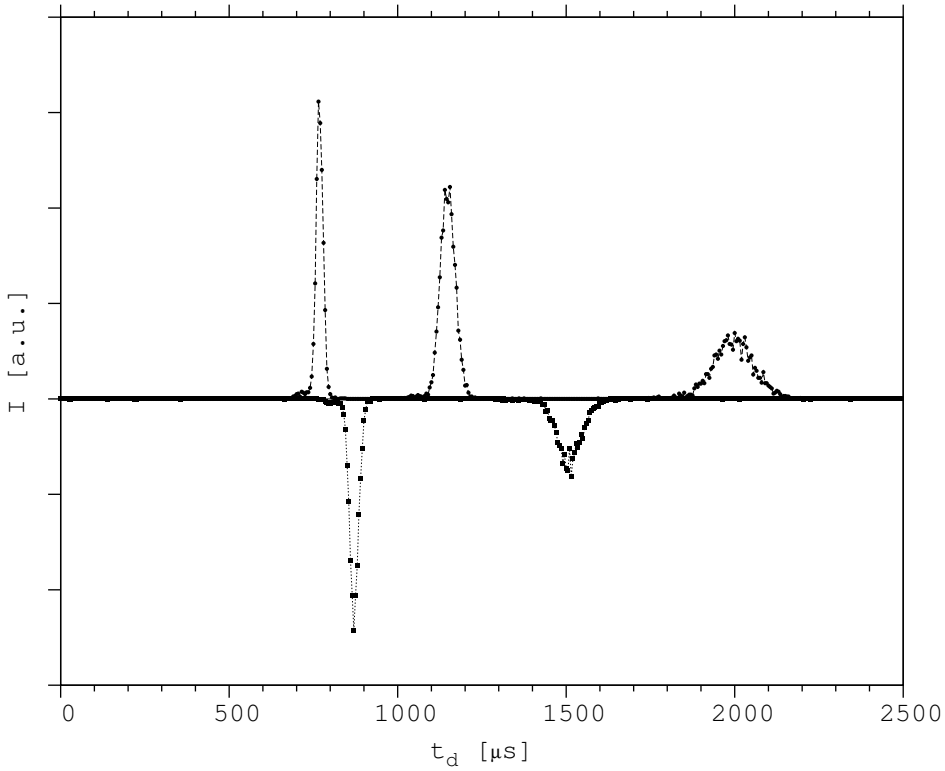

Fig. 6.2.6. Arrival time distributions of the $[C_{60}:(CyD)_2 - 2.H]^{2-}$ anions for an injection energy (IIE) of 40 V and drift voltages of 91.7, 75.2, 50.6, 35.5, 25.5 V. The five ATD have been superposed in order to facilitate global assessment.

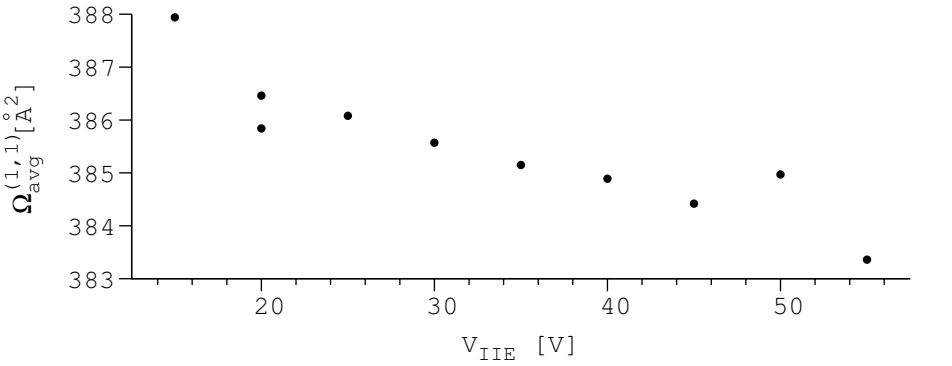

Fig. 6.2.7. The cross-sections inferred from the measured mobilities obtained for the $[C_{60}:(CyD)_2 - 2.H]^{2-}$ anions at different injection voltages.

A typical mass spectrum obtained for the sodiated C_{60}:γ-cyclodextrin complex 2:1, $[C_{60}:(\gamma\text{-CyD})_2+2.Na]^{2+}$, on the instrument used for the mobility experiments using a solution 15 % methanol and no NH_4OAc is presented in Fig. 6.2.8. The mass to charge ratio of the doubly sodiated complex corresponds to 1682 m/z.

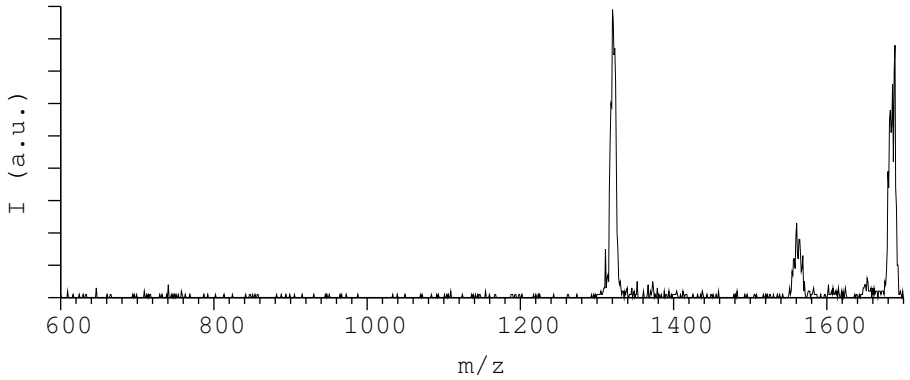

Fig. 6.2.8. Mass spectrum of the $[C_{60}:(\gamma\text{-CyD})_2]$ solution 15 % methanol without NH4OAc. The $[C_{60}:(\gamma\text{-CyD})_2+2.Na]^{2+}$ and $[(\gamma\text{-CyD})+Na]^{+}$ ions are respectively detected at 1682 and 1320 m/z. The $[C_{60}:(\gamma\text{-CyD})_2+2.H]^{2+}$ cations are found to be present in negligible amounts.

The arrival time distributions of the $[C_{60}:(\gamma\text{-CyD})_2+2.Na]^{2+}$ anions were recorded with the quadrupole in the mass analysis mode and the bandwidth centered on their mass to charge ratio, 1682 m/z (see Fig. 6.2.8). For V_{IIE}=40V in positive mode, the ATD distribution of the $[C_{60}:(\gamma\text{-CyD})_2+2.Na]^{2+}$ cations (1682 m/z) is mono modal (see Fig. 6.2.9). The negligible shoulder observed at higher mobilities (smaller arrival time) is assigned to a dimer of the complex $[C_{60}:(CyD)_2 + 2.Na]_2^{4+}$. Interferences from this dimer are removed at higher dilution rates.

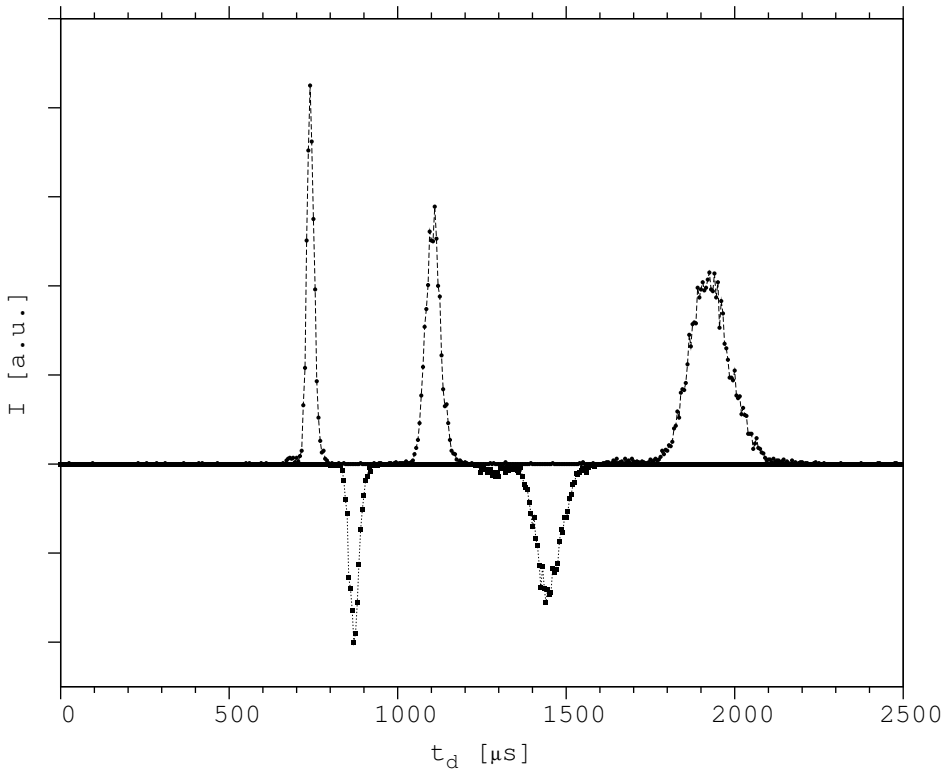

Fig. 6.2.9. Arrival time distributions of the $[C_{60}:(\gamma\text{-CyD})_2 + 2.Na]^{2+}$ cations for an injection energy (IIE) of 40V and drift voltages of 91.5, 70.8, 50.5, 35.4, 25.1 V.

The average cross section obtained from the measurements with injection energies within the [15,40] V range is equal to $\Omega_{avg}^{(1,1)} = 363.1 \text{Å}^2$ with a standard deviation of 0.7Å^2 (see Fig. 6.2.10).

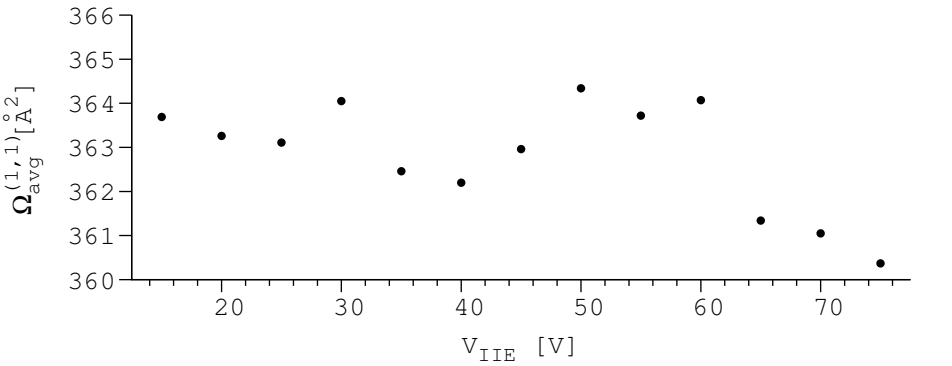

Fig. 6.2.10. The cross-sections inferred from the measured mobilities obtained for the $[C_{60}:(\gamma\text{-CyD})_2 + 2.Na]^{2+}$ cations at different injection voltages.

Finally, the cross-sections of the deprotonated and sodiated γ-cyclodextrins inferred from their respective mobility measurements are considerably smaller than those obtained from the theoretical structures reported above. They are furthermore dependent on the electrospray conditions. These results support the template influence of the C_{60} on the γ-cyclodextrins conformations. In absence of C_{60} the cyclodextrins collapse and their mobilities (cross-sections) cannot be assigned to the theoretical structures reported above. Consequently, they were not further investigated due to the tremendous number of theoretical conformers possible.

6.2.3. Discussion

Due to C_{60} size and shape, the only relevant guest position is within the γ-cyclodextrin cavities. However, in order to further reduce the exploration of the conformational space, the gas phase structure of the $[C_{60}:(\gamma\text{-CyD})_2]$ ions was postulated to be highly compact, with the C_{60} in close interaction with the two cyclodextrins as initially suggested by Yoshida *et al.* [21]. This led to the assumption that the two γ-cyclodextrins interact via the highest possible number of intermolecular hydrogen bonds, i.e. sixteen. In addition, although the experimentally observed charged state of the $[C_{60}:(\gamma\text{-CyD})_2]$ ions can be readily identified from the mass spectra, the exact locations of the deprotonation or cationization sites are not known. In order to avoid exploring the conformational space of the multiple isomers of position generated upon both deprotonation and cationization, the conformational analysis focused on the neutral form of the $[C_{60}:(\gamma\text{-CyD})_2]$ inclusion complex. Based on these two assumptions, multiple conformers characterized by different values of the torsion angles, especially the torsion angle ω and the tilt angle τ, were generated and their geometry optimized. Respectively six and five distinct families of conformers, mainly

characterized by different orientations of the primary hydroxyl groups, have been identified at the HF/sto-3g and PM6 levels of theory. In order to facilitate the discussion, these families can be divided into three groups: barrel- (Fig. 6.2.3.A), cup- (Fig. 6.2.3.B), and sphere- (Fig. 6.2.3.C) shaped complex ions. In the sphere-shaped ions the C_{60} is fully encapsulated by the two γ-cyclodextrins with only two small polar caps accessible to the solvent. In the cup-shaped ions, the C_{60} is fully encapsulated by one γ-cyclodextrin while the primary hydroxyl groups of the other γ-cyclodextrin are oriented so as to leave a large area of the C_{60} accessible to the solvent. In the barrel-shaped ions, the C_{60} is accessible from both sides of the complex.

Experimentally, the arrival time distributions (ATDs) of both the cationized (see Fig. 6.2.9) and the deprotonated (see Fig. 6.2.6) complex ions present a small peak on the left of the peaks respectively identified as $[C_{60}:(CyD)_2 + 2.Na]^{2+}$ and $[C_{60}:(CyD)_2 - 2.H]^{2-}$. At low injection energies, the ions entering the drift tube experience a rapid transient heating cycle as their kinetic energies is thermalized by collision with the buffer gas. As the injection energy is raised, the collisional heating increases and leads to the dissociation of the less stable complex dimers respectively into $[C_{60}:(CyD)_2 + 2.Na]^{2+}$ and $[C_{60}:(CyD)_2 - 2.H]^{2-}$. These small peaks whose intensity can be modulated by the solution concentration and electrospray conditions correspond to dimers of the ions of interest. For the cross-section measurement, the experimental conditions used minimize the presence of dimers at low injection energies so as to avoid delayed thermalization of the kinetic energy and artificially smaller cross-sections.

The experimentally inferred cross-section of the $[C_{60}:(CyD)_2 + 2.Na]^{2+}$ ions is equal to 363.1 $Å^2$ (0.7 $Å^2$). The cross-section inferred from the measured ion mobility of the $[C60:(\gamma\text{-}CyD)_2 + 2.Na]^{2+}$ ions are in excellent agreement with the predicted cross-section of the most compact conformers ([363.4: 364.3] $Å^2$ and [366.5: 368.8] $Å^2$ at the HF/sto-3g and PM6 levels respectively) of the neutral $[C_{60}:(CyD)_2]$. As explained in section 6.2.2, the theoretical predictions were limited to the study of the different conformers of the neutral complex. Due to the size of the present system and the absence of possible zwitterionic structure, the sodium adducts are expected to help stabilize the hydrogen bonds – as supported by the higher stability of the sodiated ions reported in section 6.1 – and lead to only minor changes in the theoretically predicted cross-sections. Therefore, since no conformers with a lower cross section may exist this leads to the formal identification of the gas-phase experimental structure of the $[C60:(\gamma\text{-}CyD)_2 + 2.Na]^{2+}$ ions. In the $[C60:(\gamma\text{-}CyD)_2 + 2.Na]^{2+}$ ions, the two γ-cyclodextrins are involved in sixteen intermolecular hydrogen bonds and the C_{60} is fully encapsulated with only two small polar caps accessible to the solvent. The C_{60} acts as a template reducing the conformational space accessible to the two γ-cyclodextrins. The sixteen intermolecular hydrogen bonds hypothesis is confirmed explaining the high stability of the cationized complexes observed using collision induced dissociation measurements.

The experimentally inferred cross-section of the $[C60:(\gamma\text{-}CyD)_2 – 2.H]^{2-}$ ions is equal to 386.0 $Å^2$ (1.0 $Å^2$). The cross-section inferred from the measured ion mobility of the $[C_{60}:(CyD)_2 - 2.H]^{2-}$ ions corresponds to the so-called cup-shaped conformers ([378.3: 395.7] $Å^2$ and [379.7: 392.1] $Å^2$ at the HF/sto-3g and PM6 levels respectively). However, it could also be explained by the destabilization of the hydrogen bond belt

between the two γ-cyclodextrins. Indeed, from their slightly acidic pK values, 12.1 [129], deprotonation is expected to take place at the secondary O(2), O(3) hydroxyl groups. Deprotonation of the secondary hydroxyl groups is further supported by the decreased stability of the deprotonated anions compared to the sodiated ones.

It is also worth mentioning that the 3D structure proposed by Bonnet *et al.*[101] for the [C60:(γ-CyD)$_2$] complex and illustrated in Fig. 6.2.11 does not agree with the experimental results reported in the present study. Its collision cross-section of 442 Å^2 is far too large.

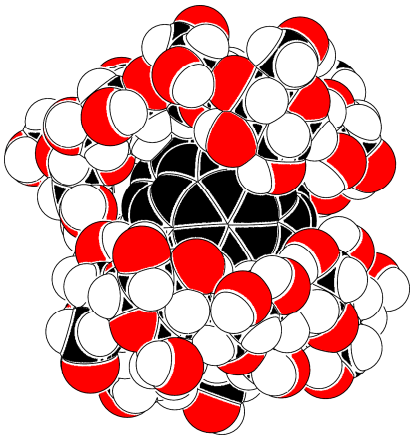

Fig. 6.2.11. 3D structure of the [C60:(γ-CyD)$_2$] complex proposed by Bonnet *et al.* [101]

Symmetric peaks appear in all of the ATDs. This indicates that either one family of conformers is present or, if multiple conformers exist, that they either have very similar cross-sections or rapidly interconvert in the drift cell. The extent of the transferability of the gas-phase inferred conformations to the solution phase is unknown. Most ESI-MS studies suggest that important structural features or large biomolecular assemblies are retained in the gas-phase. On the other hand, biomolecules are desolvated upon transfer into the vacuum of the mass spectrometer. This implies that electrostatic interactions and hydrogen bonds, that surely survive the

spray process, are largely responsible for maintaining structural features of the vaporized biomolecular ions. Hydrophobic interactions are believed to be partly or completely lost in the gas phase [43]. Moreover, both upon electronebulization and upon entering the drift tube, even at low injection energies, the ions experience rapid transient heating cycles [130, 74]. This causes some annealing and the conformation that dominates under these conditions is the one that dominates when the rate of isomerization becomes sufficiently small so that the isomer distribution is frozen [73].

6.2.4. Conclusion

The gas-phase conformational properties of the sodiated $[C60:(\gamma\text{-}CyD)_2 + 2.Na]^{2+}$ and deprotonated $[C60:(\gamma\text{-}CyD)_2 - 2.H]^{2-}$ complex ions were studied using ion mobility measurements and molecular modeling calculations. Six distinct families of conformers mainly characterized by different orientations of the primary hydroxyl groups have been identified theoretically. These families can be subdivided into three groups, sphere-, cup-, and barrel-shaped with increasing cross-sections and relative energies/heats of formation. The lowest energy group corresponds to the most compact conformers and thus the smallest cross-sections possible. The measured ion mobility of the $[C60:(\gamma\text{-}CyD)_2 + 2.Na]^{2+}$ ions are in excellent agreement with the predicted cross-section for these conformers. Since no conformers with a lower cross section may exist, this leads to the formal identification of the gas-phase experimental structure of the $[C60:(\gamma\text{-}CyD)_2 + 2.Na]^{2+}$ ions. In the $[C60:(\gamma\text{-}CyD)_2 + 2.Na]^{2+}$ ions, the two γ-cyclodextrins are involved in sixteen intermolecular hydrogen bonds and the C_{60} is fully encapsulated with only two small polar caps accessible to the solvent. The measured ion mobility of the $[C60:(\gamma\text{-}CyD)_2 - 2.H]^{2-}$ ions, on the other hand, are smaller and their cross sections thus larger. They may be related to the so called cup-

shaped conformers. It is also possible that the deprotonation takes place at the hydrogen belt between the two cyclodextrins and following its destabilization that the complex opens up like a bivalve shellfish. This would explain the decreased stability of the deprotonated complex ions compared to the sodiated ones.

References

[1] M. J. Frampton, H. L. Anderson, *Angewandte Chemie-International Edition* **46**, 1028 (2007).

[2] G. Wenz, *Angewandte Chemie-International Edition in English* **33**, 803 (1994).

[3] H. J. Schneider, *Angewandte Chemie-International Edition in English* **30**, 1417 (1991).

[4] R. M. Williams, J. M. Verhoeven, *Recueil des Travaux Chimiques des Pays-Bas* **111**, 531 (1992).

[5] J. L. Atwood, G. A. Koutsantonis, C. L. Raston, *Nature* **368**, 229 (1994).

[6] A. Ikeda, T. Hanato, M. Kawagushi, H. Suenaga, S. Shinkai, *Journal of the Chemical Society, Chemical Communications* p. 1403 (1999).

[7] S. Kunsági-Máté, K. Szabó, I. Bitter, G. Nagy, L. Kollar, *Tetrahedron Letters* **45**, 1387 (2004).

[8] S. R. Wilson, Y. Wu, *Journal of the Chemical Society, Chemical Communication* p. 784 (1993).

[9] M. Carano, *et al.*, *European Journal of Organic Chemistry* p. 374 (2003).

[10] F. Arias, L. A. Godinez, S. R. Wilson, A. E. Kaifer, L. Echegoyen, *Journal of the American Chemical Society* **118**, 6086 (1996).

[11] F. Diederich, *et al.*, *Angewandte Chemie International Edition in English* **31**, 1599 (1992).

[12] F. Diederich, M. Gomez-Lopez, *Chemical Society Reviews* **28**, 263 (1999).

[13] J. F. Greisch, S. Kyritsoglou, B. Leyh, E. De Pauw, *Journal of Mass Spectrometry* **43**, 242 (2008).

[14] T. Andersson, K. Nilsson, M. Sundahl, G. Westman, O. Wennerström, *Journal of the Chemical Society, Chemical Communications* **8**, 604 (1992).

[15] T. Andersson, G. Westman, O. Wennerström, M. Sundahl, *Journal of the Chemical Society, Perkin Transactions 2* **2**, 1097 (1994).

[16] D. M. Guldi, H. Hungerbühler, E. Janata, K. D. Asmus, *Journal of the Chemical Society, Chemical Communications* **1**, 84 (1993).

[17] D. M. Guldi, H. Hungerbuhler, E. Janata, K. D. Asmus, *Journal of Physical Chemistry* **97**, 11258 (1993).

[18] N. M. Dimitrijevic, P. V. Kamat, *Journal of Physical Chemistry* **97**, 7623 (1993).

[19] K. I. Priyadarsini, H. Mohan, A. K. Tyagi, J. P. Mittal, *Journal of Physical Chemistry* **98**, 4756 (1994).

[20] K. I. Priyadarsini, H. Mohan, J. P. Mittal, D. M. Guldi, K. D. Asmus, *Journal of Physical Chemistry* **98**, 9565 (1994).

[21] Z. I. Yoshida, H. Takekuma, S. I. Takekuma, Y. Matsubara, *Angewandte Chemie International Edition in English* **33**, 1597 (1994).

[22] P. Boulas, W. Kutner, M. Jones, K. Kadish, *Journal of Physical Chemistry* **98**, 1282 (1994).

[23] T. Andersson, C. Westman, G. Stenhagen, M. Sundahl, O. Wennerström, *Tetrahedron Letters* **36**, 597 (1995).

[24] S. Giesa, J. H. Gross, R. Gleiter, W. Kratschmer, *European Mass Spectrometry* **4**, 189 (1998).

[25] K. Komatsu, K. Fujiwara, Y. Murata, T. Braun, *Journal of the Chemical Society, Perkin Transactions 1* **20**, 2963 (1999).

[26] A. Buvari-Barcza, *et al.*, *Journal of the Chemical Society, Perkin Transactions 2* **2**, 191 (2001).

[27] H. Tokuyama, S. Yamago, E. Nakamura, T. Shiraki, Y. Sugiura, *Journal of the American Chemical Society* **115**, 7918 (1993).

[28] A. S. Boutorine, *et al.*, *Angewandte Chemie International Edition in English* **33**, 2462 (1994).

[29] F. Djojo, A. Herzog, I. Lamparth, F. Hampel, A. Hirsch, *Chemistry-a European Journal* **2**, 1537 (1996).

[30] U. Reuther, T. Brandmuller, W. Donaubauer, F. Hampel, A. Hirsch, *Chemistry-a European Journal* **8**, 2261 (2002).

[31] S. Sergeyev, F. Diederich, *Angewandte Chemie – International Edition* **43**, 1738 (2004).

[32] W. Saenger, *et al.*, *Chemical Reviews* **98**, 1787 (1998).

[33] J. M. Maclennan, J. J. Stezowski, *Biochemical and Biophysical Research Communications* **92**, 926 (1980).

[34] K. Harata, *Chemistry Letters, Chemical Society of Japan* **13**, 641 (1984).

[35] K. Harata, *Bulletin of the Chemical Society of Japan* **60**, 2763 (1987).

[36] K. Lindner, W. Saenger, *Biochemistry and Biophysics Research Communications* **92**, 933 (1980).

[37] K. Harata, *Chemical Reviews* **98**, 1803 (1998).

[38] J. Shimada, *Journal of Physical Chemistry B* **104**, 2136 (2000).

[39] F. W. Lichtenthaler, S. Immel, *Tetrahedron: asymmetry* **5**, 2045 (1994).

[40] A. J. Stone, *Chemical Physics Letters* **83**, 233 (1981).

[41] A. J. Stone, M. Alderton, *Molecular Physics* **100**, 221 (2002).

[42] J. N. Israelachvili, *Intermolecular and Surface Forces* (Academic Press, London, 1991).

[43] J. M. Daniel, S. D. Friess, S. Rajagopalan, S. Wendt, R. Zenobi, *International Journal of Mass Spectrometry* **216**, 1 (2002).

[44] M. A. Freitag, M. S. Gordon, J. H. Jensen, W. J. Stevens, *Journal of Chemical Physics* **112**, 7300 (2000).

[45] A. J. Stone, *The Theory of Intermolecular Forces* (Oxford University Press, Oxford, 1996).

[46] Iupac project number: 2004-026-2-100, “categorizing hydrogen bonding and other intermolecular interactions”, *Tech. rep.*.

[47] N. Elgobashi, L. González, *Journal of Chemical Physics* **124**, 174308 (2006).

[48] W. Klopper, M. Quack, M. A. Suhm, *Journal of Chemical Physics* **108**, 10096 (1998).

[49] M. Meuwly, J. M. Hutson, *Journal of Chemical Physics* **110**, 8338 (1999).

[50] E. E. Meyer, Q. Lin, T. Hassenkam, E. Oroudjev, J. Israelachvili, *Proceedings of the National Academy of Sciences of the U.S.A.* **102**, 6839 (2005).

[51] E. E. Meyer, K. J. Rosenberg, J. Israelachvili, *Proceedings of the National Academy of Sciences USA* **103**, 15739 (2006).

[52] C. G. Juo, L. L. Shiu, C. K. F. Shen, T. Y. Luh, G. R. Her, *Rapid Communications in Mass Spectrometry* **9**, 604 (1995).

[53] R. B. Cole, *Journal of Mass Spectrometry* **35**, 763 (2000).

[54] N. B. Cech, *Mass Spectrometry Reviews* **20**, 362 (2001).

[55] J. F. de la Mora, *et al.*, *Journal of Mass Spectrometry* **35**, 939 (2000).

[56] M. G. Ikonomou, A. T. Blades, P. Kebarle, *Analytical Chemistry* **63**, 1989 (1991).

[57] A. T. Blades, M. G. Ikonomou, P. Kebarle, *Analytical Chemistry* **63**, 2109 (1991).

[58] G. J. Van Berkel, F. Zhou, *Analytical Chemistry* **67**, 2916 (1995).

[59] G. S. Jackson, C. G. Enke, *Analytical Chemistry* **71**, 3777 (1999).

[60] M. Peschke, U. H. Verkerk, P. Kebarle, *Journal of the American Society of Mass Spectrometry* **15**, 1424 (2004).

[61] P. Kebarle, *Journal of Mass Spectrometry* **35**, 804 (2000).

[62] G. J. Van Berkel, F. Zhou, J. T. Aronson, *International Journal of Mass Spectrometry and Ion Processes* **162**, 55 (1997).

[63] H. J. Wang, G. R. Agnes, *Analytical Chemistry* **71**, 4166 (1999).

[64] S. A. McLuckey, *Journal of the American Chemical Society for Mass Spectrometry* **3**, 599 (1992).

[65] X. B. Wang, C. F. Ding, L. S. Wang, *Journal of Chemical Physics* **110**, 8217 (1999).

[66] R. L. Hettich, R. N. Compton, R. H. Ritchie, *Physical Review Letters* **67**, 1242 (1991).

[67] P. A. Limbach, *et al.*, *Journal of the American Chemical Society* **113**, 6795 (1991).

[68] O. Hampe, M. Neumaier, M. N. Blom, M. M. Kappes, *Chemical Physics Letters* **354**, 303 (2002).

[69] D. E. Cliffel, A. J. Bard, *Journal of Physical Chemistry* **98**, 8140 (1994).

[70] M. E. Niyazymbetov, D. H. Evans, S. A. Lerke, P. A. Cahill, C. C. Henderson, *Journal of Physical Chemistry* **98**, 13093 (1994).

[71] V. Ohlendorf, A. Willnow, H. Hungerbüler, D. M. Guldi, K. D. Asmus, *Journal of the Chemical Society, Chemical Communications* **7**, 759 (1995).

[72] K. Müller-Dethlefs, P. Hobza, *Chemical Reviews* **100**, 143 (2000).

[73] K. B. Shelimov, D. E. Clemmer, R. R. Hudgins, M. F. Jarrold, *Journal of the American Chemical Society* **119**, 2240 (1997).

[74] S. J. Valentine, D. E. Clemmer, *Journal of the American Chemical Society* **119**, 3558 (1997).

[75] E. N. Kitova, D. R. Bundle, J. S. Klassen, *Journal of the American Chemical Society* **124**, 5902 (2002).

[76] G. Von Helden, M. T. Hsu, N. Gotts, M. T. Bowers, *Journal of Physical Chemistry* **97**, 8182 (1993).

[77] J. M. Hunter, M. F. Jarrold, *Journal of the American Chemical Society* **117**, 10317 (1995).

[78] J. M. Hunter, J. L. Fye, E. J. Roskamp, M. F. Jarrold, *Journal of Physical Chemistry* **98**, 181 (1994).

[79] J. E. H. Koehler, W. Saenger, W. F. van Gunsteren, *European Biophysical Journal* **15**, 197 (1987).

[80] J. E. H. Koehler, *European Biophysical Journal* **15**, 211 (1987).

[81] W. Koehler, J. E. H.and Saenger, W. F. van Gunsteren, *European Biophysical Journal* **16**, 153 (1988).

[82] K. B. Lipkowitz, *Journal of Organic Chemistry* **56**, 6357 (1991).

[83] K. B. Lipkowitz, *Chemical Reviews* **98**, 1829 (1998).

[84] X. S. Li, L. Liu, T. W. Mu, Q. X. Guo, *Monatsh Chemie* **131**, 849 (2000).

[85] V. G. Avakyan, V. B. Nazarov, M. V. Alfimov, A. A. Bagatur´yants, *Russian Chemical Bulletin* **48**, 1833 (1999).

[86] V. G. Avakyan, V. B. Nazarov, M. V. Alfimov, A. A. Bagatur´yants, N. I. Voronezheva, *Russian Chemical Bulletin* **50**, 206 (2001).

[87] V. G. Avakyan, V. B. Nazarov, N. I. Voronezheva, *Russian Journal Physical Chemistry* **79**, S18 (2005).

[88] V. B. Luzhkov, C. A. Venanzi, *Journal of Physical Chemistry* **99**, 2312 (1995).

[89] D. N. Laikov, *Journal of Chemical Physics Letters* **281**, 151 (1997).

[90] D. N. Laikov, Y. A. Ustynyuk, *Russian Chemical Bulletin International Edition* **54**, 820 (2005).

[91] P. Bonnet, C. Jaime, L. Morin-Allory, *Journal of Organic Chemistry* **66**, 689 (2001).

[92] P. Bonnet, C. Jaime, L. Morin-Allory, *Journal of Organic Chemistry* **67**, 8602 (2002).

[93] T. Steiner, W. Saenger, *Journal of the Amrican Chemical Society* **113**, 5676 (1991).

[94] J. E. Del Bene, J. A. Pople, *Journal of Chemical Physics* **58**, 3605 (1973).

[95] G. A. Jeffrey, S. Takaji, *Accounts of Chemical Research* **11**, 264 (1978).

[96] C. Betzel, *Journal od the American Chemical Society* **106**, 7545 (1984).

[97] T. Steiner, W. Saenger, *Journal of the American Chemical Society* **114**, 7123 (1992).

[98] W. Saenger, *Nature* **296**, 581 (1982).

[99] V. Zabel, W. Saenger, S. A. Mason, *Journal of the American Chemical Society* **108**, 3664 (1986).

[100] G. Marconi, B. Mayer, C. T. Klein, G. Köhler, *Chemical Physics Letters* **260**, 589 (1996).

[101] P. Bonnet, I. Bea, C. Jaime, L. Morin-Allory, *Supramolecular Chemistry* **15**, 251 (2003).

[102] E. N. Kitova, D. R. Bundle, J. S. Klassen, *Journal of the American Chemical Society* **124**, 9340 (2002).

[103] W. Wang, E. N. Kitova, J. Sun, J. S. Klassen, *Journal of the American Society for Mass Spectrometry* **16**, 1583 (2005).

[104] T. Steiner, G. Koellner, *Journal of the American Chemical Society* **116**, 5122 (1994).

[105] T. Wyttenbach, P. R. Kemper, M. T. Bowers, *International journal of Mass Spectrometry* **212**, 13 (2001).

[106] E. S. Baker, J. W. Hong, B. S. Gaylord, G. C. Bazan, M. T. Bowers, *Journal of the American Chemical Society* **128**, 8484 (2006).

[107] G. Von Helden, T. Wyttenbach, M. T. Bowers, *Science* **267**, 1483 (1995).

[108] S. J. Valentine, D. E. Clemmer, *Journal of Physical Chemistry B* **101**, 3891 (1997).

[109] J. T. Moseley, *Physical Reviews Letters* **21**, 873 (1968).

[110] J. T. Moseley, *Physical Review* **178**, 234 (1969).

[111] E. Mason, E. McDaniel, *Transport Properties of Ions in Gases* (Wiley; New York, 1988).

[112] J. M. Mesleh, M. F.and Hunter, A. A. Shwartsburg, G. C. Schatz, M. F. Jarrold, *Journal of Physical Chemistry* **100**, 16082 (1996).

[113] A. A. Shvartsburg, M. F. Jarrold, *Chemical Physics Letters* **261**, 86 (1996).

[114] Y. Mao, J. Woencklaus, J. Kolafa, M. Ratner, J. M. F., *Journal of the AMerican Chemical Society* **121**, 2712 (1999).

[115] K. B. Shelimov, M. F. Jarrold, *Journal of the American Chemical Society* **119**, 2987 (1997).

[116] M. F. Jarrold, V. A. Constant, *Physical Review Letters* **67**, 2994 (1992).

[117] S. Lee, T. Wyttenbach, M. T. Bowers, *International Journal of Mass Spectrometry and Ion Processes* **167/168**, 605 (1997).

[118] G. Von Helden, T. Wyttenbach, M. T. Bowers, *International Journal of Mass Spectrometry and Ion Processes* **146/147**, 349 (1995).

[119] T. Wyttenbach, G. von Helden, J. J. Batka, D. Carlat, M. T. Bowers, *Journal of the American Chemical Society* **8**, 275 (1996).

[120] T. Wyttenbach, G. von Helden, M. T. Bowers, *Journal American Chemical Society* **118**, 8355 (1996).

[121] L. Liu, Q. X. Guo, *Journal of Inclusion Phenomena and Macrocyclic Chemistry* **50**, 95 (2004).

[122] E. R. Johnson, A. D. Becke, *Journal of Chemical Physics* **123**, 024101 (2005).

[123] J. C. S. Rüdiger, *Journal of the Chemical Society, Perkin Trans 2* p. 2119 (1996).

[124] J. J. P. Stewart, *Journal of Molecular Modeling* **13**, 1173 (2007).

[125] J. Stewart, *Journal of Computational Chemistry* **10**, 221 (1989).

[126] I. N. Levine, *Quantum Chemistry, fifth edition* (Prentice Hall, Upper Saddle River, New Jersey, 2000).

[127] U. Koch, P. L. A. Popelier, *Journal Physical Chemistry* **99**, 9747 (1995).

[128] M. J. Frisch, *et al., Gaussian 03, Revision B.04* (2003).

[129] R. L. Van Etten, G. A. Clowes, J. F. Sebastian, M. L. Bender, *Journal of the American Chemical Society* **89**, 3253 (1967).

[130] M. F. Jarrold, E. C. Honea, *Journal of the American Chemical Society* **114**, 459. (1992).

Chapter 7. Interactions of C_{60} with transition metals

Supramolecular architectures, in which photo-/electro-active donors and acceptors are pre-organized inter-molecularly *via* non-covalent linkages, are appealing for many applications, e.g. photovoltaic devices, since they may provide long-lived charge separated states [1, 2, 3]. However they often further require immobilization or positioning on surfaces, as for example [60]fullerenes used as potential Raman active nano-sensors [4]. The present chapter probes the interactions between C_{60}, its derivatives and transition metals such as silver, iron and manganese.

Direct adsorption and covalent linking are two approaches studied in the first part of this chapter. In aqueous solution, no evidence of the adsorption of C_{60} to silver colloids was found for the conditions used. Raman bands ($2A_g$+$8H_g$) characteristic of C_{60} [5] were not observed about 264(s), 430(m), *496(s)*, 709(w), 773(s), 1101(m), 1251(m), 1425(w), *1468(s)*, 1576(m) in cm^{-1}, in agreement with published work. For C_{60} to interact with aqueous colloids, an intermediate such as pyridine has to be used [6] or a C_{60} derivative having heteroatoms such as nitrogen, sulphur, or oxygen, or some functional groups such as CN, SO_3, SH, and COOH, which can interact with metal surfaces [7, 8]. Nucleic acids and thymidine and its analogues in particular (see chapter 5), are well known for their ability to bind silver and gold surfaces via their deprotonated N3 nitrogen atom [9, 10]. Their structure and assemblies have also been thoroughly studied using vibrational spectroscopy. Hydrogen bonding, base stacking, and metal coordination in nucleic acids can be revealed by the Raman and infrared spectra [11] (see Fig. 7.1).

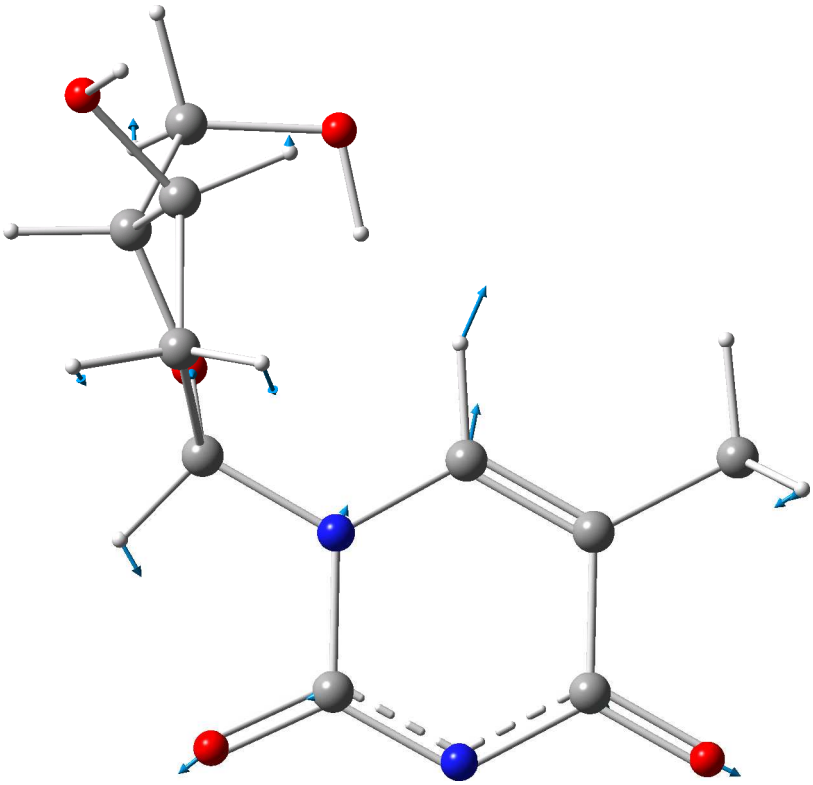

Fig. 7.0.1. In plane vibration mode acting as conformational marker.

Furthermore, the frequencies of several Raman bands have been correlated with the local conformations of nucleic acids, i.e. the ribose ring puckering and the glycosidic bond orientation. Most of the conformation marker bands are in-plane vibrations of the base ring and their sensitivity to the ribose ring puckering and glycosidic bond orientation has been ascribed to vibrational coupling between base and ribose vibrations [11]. Nucleic acids are thus choice compounds for functionalization of C_{60} in order to bind silver or gold surfaces, and for characterization using Raman spectroscopy (RS). Raman scattering, however, is a second-order process. In the absence of any resonance, the differential Raman cross-sections $\left(\frac{d\sigma}{d\Omega}\right)_{NRS}$ are less than 10^{-29} cm^2sr^{-1}, i.e. generally more than 10 orders of magnitude lower than that of infrared absorption [12, 13, 14]. Hence, the signal-to-noise ratio of the surface Raman signal expected for adsorbates is often too low to be detected. This intrinsically low

detection sensitivity is overcome in surface-enhanced Raman spectroscopy (SERS), both a surface selective and highly sensitive technique with a total enhancement at near-infrared nonresonant excitation for molecules absorbed to colloidal silver clusters as high as 10^{14} compared to RS [15, 16]. Besides the quenching of the fluorescence background of the adsorbed species by radiation-less energy transfer to the metal surface, the major SERS effect can be attributed to at least two factors [17, 18]: (i) an electromagnetic enhancement and (ii) a chemical enhancement. The electromagnetic enhancement occurs when the incident light is in resonance with the surface Plasmon modes of a metallic thin film or nanoparticle. The surface plasmons are collective oscillations of the free electrons in a metallic nanostructure that upon resonant interaction with light generate intense local electromagnetic fields responsible for the Raman signal amplification [19] (see Fig. 7.2).

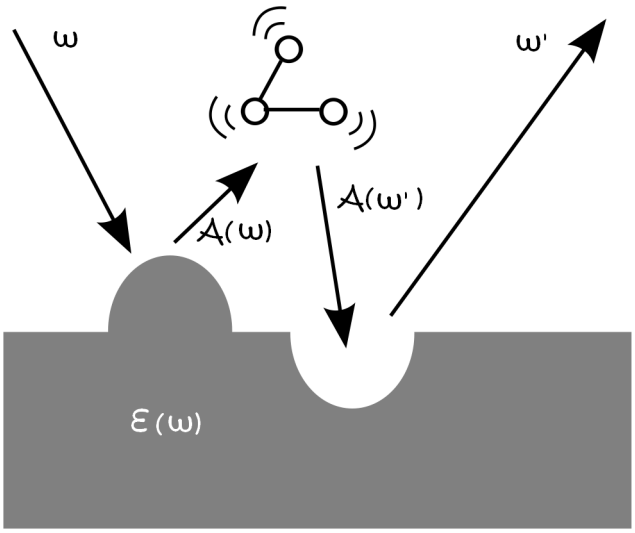

Fig. 7.0.2. Scheme of a molecule (not to scale) above a rough metal surface. A(ω) is the electromagnetic enhancement factor and ε(ω) the dielectric constant of the surface (adapted from reference [20]).

The chemical enhancement, on the other hand, is related to the possible chemical interactions – including charge transfer and polarization – that may occur between the

adsorbed molecules and the film or nanoparticle surface. For silver and gold, the electromagnetic field enhancement generated from a variety of metal nanostructures is dominant with the chemical enhancement contributing to only one or two orders of magnitude of the total enhancement[14]. This motivated our synthesis of nanoparticles suitable for surface enhanced Raman spectroscopy briefly discussed in the present chapter.

The last section of this chapter describes the complexation of C_{60} by metallo-porphyrins complexing iron and manganese ions. Non-covalent immobilization of C_{60} by complexation is attractive to position C_{60} while avoiding altering its properties [21]. Coordination of a fullerene ligand to a transition metal is also highly attractive because of the inherent assembling and positioning capabilities of this approach and of the efficiency of the related photo-driven processes. A photoactive supramolecular system, in which donor and acceptor moieties are linked via coordinative association, is relatively easily synthesized. Upon photo-illumination it triggers a sequential rapid electron transfer and a diffusional splitting of the charge-separated radical pair, mimicking a key step in natural photosynthesis [22, 23].

The present chapter is intended as a description of the prospective work undertaken. It does not provide a complete description of the systems studied; additional experiments using complementary techniques are required before definitive conclusions can be reached.

7.1. Surface-enhanced Raman spectroscopy of 3'-imino[60]fulleryl-3'-deoxythymidine

Metal colloids have been widely employed in surface enhanced Raman spectroscopy (SERS). The aggregation of metal particles leads to the formation of aggregates with a roughness and a fractal morphology necessary to yield intense Raman spectra [24, 25]. Among the methods used to obtain metal colloids, the chemical reduction of silver nitrate by citrate [26] is one of the most attractive since it produces very stable, highly sensitive and selective colloidal suspensions compared to other SERS substrates [27, 28, 29].

Prior to studying their adsorption on surfaces, thymine and thymidine Raman spectra obtained in water were vibrationally assigned *via* extensive isotopic labelling studies [30, 31, 32, 33, 34]. The 700-800 cm^{-1} region was found dominated by bands assigned to ring breathing modes of the thymine base [32]. In the 800-1200 cm^{-1} region different normal modes localized on the 2'-deoxyribose sugar ring were assigned, while in the 1200-1600 cm^{-1} region modes resulting form the coupling of the thymine base and the sugar ring were found to dominate [31, 32, 33, 34, 30]. Finally, the 1600-1800 cm^{-1} region corresponds to the C=C and C=O double bond stretches of the thymine. These previous assignments will be used to discuss the adsorption of 3'-imino[60]fulleryl-3'-deoxythymidine on silver colloids.

In the present study, SERS has been applied to the 3'-imino[60]fulleryl-3'-deoxythymidine molecule also studied by mass spectrometry (see chapter 5) (1) to find out, from the enhancement of different Raman bands, the most probable orientation of the adsorbed species relative to the metal surface, (2) to access

conformational information via Raman active conformational markers, and (3) to infer the localization of the C_{60} relatively to the silver surface.

7.1.1. Experimental

The synthesis, separation and characterization of 3'-imino[60]fulleryl-3'-deoxythymidine were described in chapter 5. The collected fractions of 3'-imino[60]fulleryl-3'-deoxythymidine separated from the reactants using a C18 column (Princeton Chromatography,USA) and toluene/ACN 77:23 isocratic conditions were lyophilized under low pressure conditions and a nitrogen trap for the solvent. Upon the solvent evaporation, the 3'-imino[60]fulleryl-3'-deoxythymidine forms a film on the glass vial.

The stable sodium citrate silver colloid used as SERS substrate was prepared according to the standard procedure reported by Lee and Meisel [26, 35]. 200 ml of Milli-Q water was rapidly heated to boiling point. The $AgNO_3$ was then added to reach a 10^{-3} M concentration, immediately followed by the addition of 4 ml of a 1% trisodium citrate solution. Further heating and agitation were performed using a magnetic stirrer/heater, with mixture kept at a temperature of 95°C for 2 hours under constant agitation. The resultant colloid was yellowish gray with a pH of 6.5, an absorption maximum at 420 nm and a long absorption tail in the IR. The 420 nm band is attributed to the dipole resonance of the spherical monomeric silver particles [36]. The shoulder on the low energy side of the 400 nm band is due to the presence of aggregated particles [36]. It has been established that these aggregates are responsible for the highest enhancement observed in SERS [37, 38, 39], and for the dependence of the signal enhancement in SERS on the excitation energy [40].

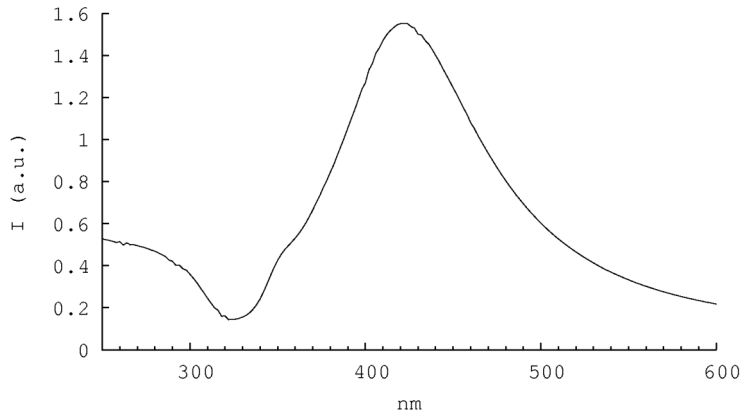

Fig. 7.1.1. UV-Vis spectrum of the silver colloid. The absorption maximum is at 420 nm.

The absence of signals, the minimal spectroscopic features attributed to the glass container excepted, ensures the signals recorded originate from the SERS substrate interaction with thymidine species (see Fig. 7.1.2.).

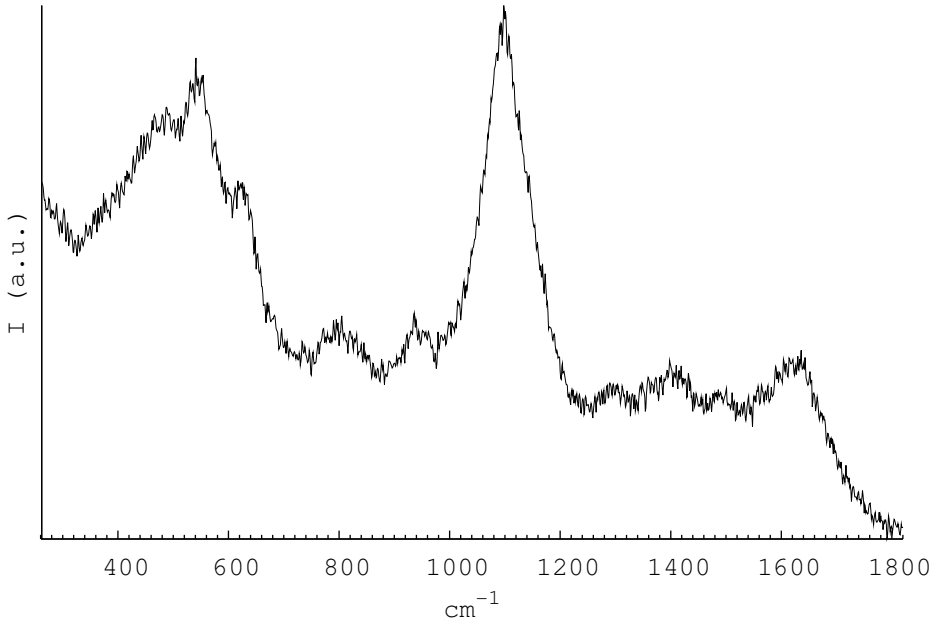

Fig. 7.1.2. Control SERS spectrum of the Ag colloid. The broad maximum about 1100 cm^{-1} is caused by the glass container.

3'-imino[60]fulleryl-3'-deoxythymidine solubility in water is negligible. In order to operate its transfer from the glassware surface to the silver nanoparticles forming the

colloid, a given volume of colloidal solution was added to the recipient containing the lyophilized 3'-imino[60]fulleryl-3'-deoxythymidine. The transfer of the 3'-imino[60]fulleryl-3'-deoxythymidine to the colloid was operated by simple contact *via* strong agitation. This simple method has been developed for this study and will be useful to SERS studies of other non water soluble compounds. Its main drawback is the inability to determine the amount of sample transferred to the colloid and thus its concentration. The SERS samples of 3'-azido-3'-deoxythymidine, on the other hand, were prepared by adding 1µL of a 10^{-2}M aqueous solution to 1 mL of the silver colloid, so that the final concentration was 10^{-5}M. The final pH of the SERS samples was that of the colloid, ~6.5.

Raman spectra were recorded on a Dilor LabRam (Jobrin-Yvan) coupled with a IFS66 FITR spectrometer in Professor Gilbert's Laboratory at ULg. Ar^{+} (at 514.5nm) radiation was used for excitation. The scattered light was collected at 180° to the excitation beam. Spectral resolution of ± 2 cm^{-1} is estimated for the Raman signals. The laser powers at the sample was equal to 20 mW (Ar^{*}).

7.1.2. Results and Discussion

Surface-enhanced Raman spectra were obtained for 3'-azido-3'-deoxythymidine and 3'-imino[60]fulleryl-3'-deoxythymidine (see Fig. 7.1.3-a and 7.1."-b, respectively). The SERS spectrum obtained for 3'-azido-3'-deoxythymidine agrees with the spectra reported by Rivas *et al.* [9] and allows mode assignments by comparison with their results. From the relative similarity observed between the Raman spectrum recorded at alkaline pH and the SERS spectrum – the appearance of bands at 1295 and 1139 cm^{-1} (see Fig. 7.1.3) respectively attributed to the ν(C-O) and ν(C-N) motions, the

intensity decrease of the 1203-1180 cm^{-1} bands, and the down shift of the ring breathing band and the ν(C=O) band – deprotonation is reported to take place in N3 as a consequence of its interaction with the metal [9, 41]. The SERS spectrum of the 3'-imino[60]fulleryl-3'-deoxythymidine resembles that of the 3'-azido-3'-deoxythymidine and allows similar conclusions to be drawn. The (minor) differences observed are likely consequences of the structural restrictions imposed by the C_{60} on the ribose moiety of the adsorbed molecule. As for 3'-deoxythymidine, the intense 792 cm^{-1} band is indicative of the existence of an interaction of the 3'-imino[60]fulleryl-3'-deoxythymidine with the surface *via* the thymine residue. Following the observation (see Fig. 7.1.3) of intense 792, 1247 cm^{-1} conformational marker bands (the 668 cm^{-1} band is not observed), the 3'-imino[60]fulleryl-3'-deoxythymidine adsorbed on the metal surface is reported to be in the C3'-*endo-anti* conformation [42, 43] in agreement with the spatial hindrance imposed by the C_{60}.

In SERS, the orientation of the adsorbed species relative to the metal surface can be determined based on the selective enhancement of the vibrations obeying the surface selection rules [44, 45, 46, 47]. According to these rules, the vibrational modes that involve a large change of the polarizability perpendicular to the metal surface are the most enhanced.

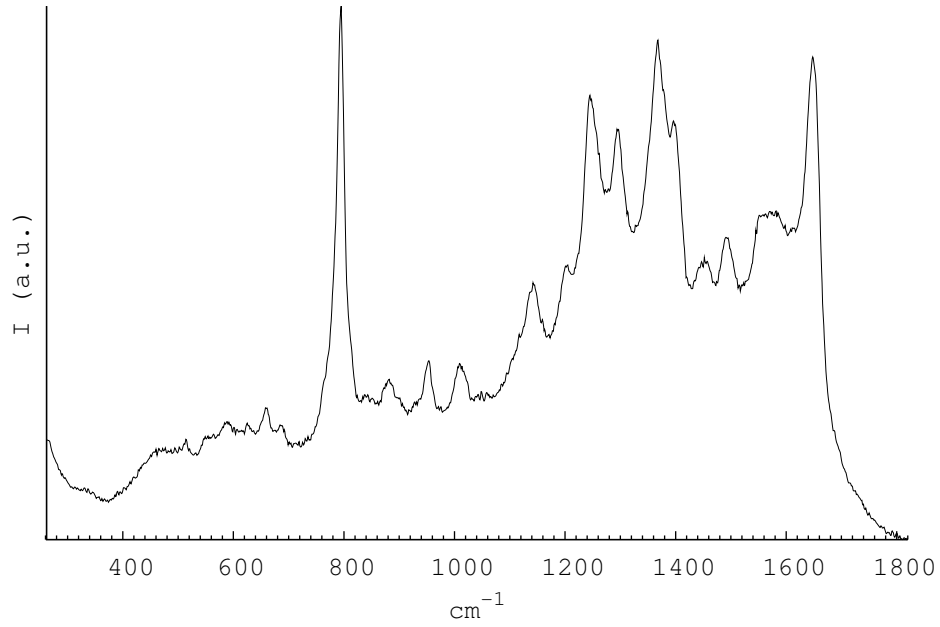

a.

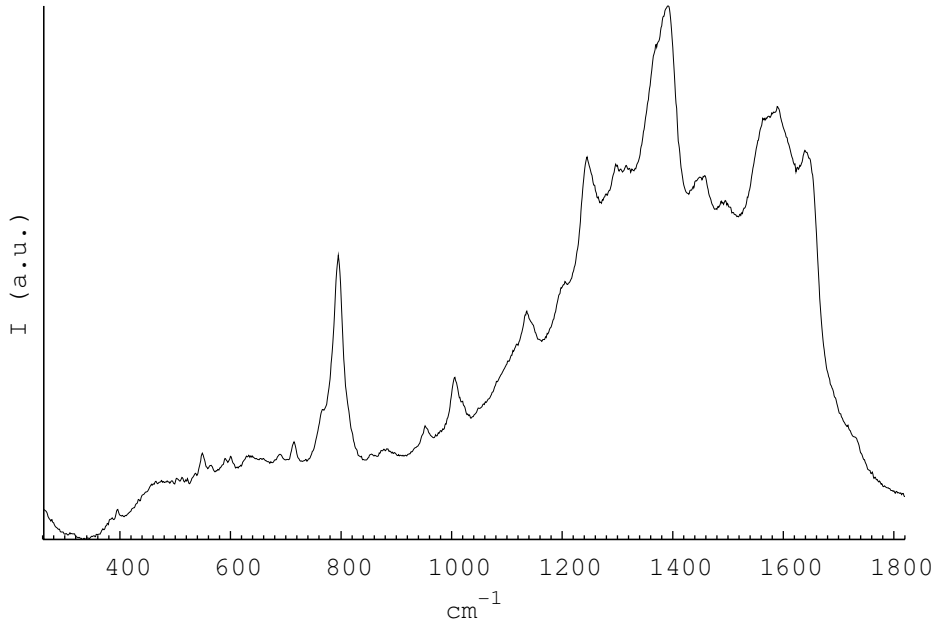

b.

Fig. 7.1.3. (a) SERS spectrum of 3'-azido-3'-deoxythymidine. (b) SERS soectrum of 3'-imino[60]fulleryl-3'-deoxythymidine.

By comparison of the SERS and Raman spectra in solution of the 3'-azido-3'-deoxythymidine molecule, it was observed that the 792 cm^{-1} band is highly enhanced in SERS. This vibration mode is assigned to a ring vibration mode of the thymine

moiety adsorbed on a silver nanoparticle *via* the deprotonated N3 atom. It involves a significant interaction between the surface and the oxygen O4 and considering that the two oxygens atoms, O2 and O4, concentrate the negative charge and thus stabilize the bonding at this position with the positively charged surface [9, 10], confirms the deprotonated N3 site as the adsorption site [48]. Consequently, by comparison of the SERS spectra of 3'-azido-3'-deoxythymidine and 3'-imino[60]fulleryl-3'-deoxythymidine, from their common intense 792 cm^{-1} band, it can be concluded that both species interact with the silver particles *via* the deprotonated N3 site. Furthermore since the 792 cm^{-1} band is a conformational marker of the deoxyribose puckering, both 3'-imino[60]fulleryl-3'-deoxythymidine and 3'-azido-3'-deoxythymidine can be reported to adopt a C3'-endo conformation, sterically favoured in the case of the 3'-imino[60]fulleryl-3'-deoxythymidine by the C_{60}.

7.1.3. Conclusion

The ability of surface-enhanced Raman spectroscopy to provide detailed information on adsorption mechanisms, surface reactions, and the surface orientation of adsorbates motivated our investigation of the adsorption of 3'-imino[60]fulleryl-3'-deoxythymidine on silver colloids using SERS.

Provided that 3'-imino[60]fulleryl-3'-deoxythymidine does not degrade and thus that no deoxythymidine non-bounded to C_{60} is responsible for the signals measured in SERS, the following conclusions can be drawn. Similarly to thymidine and its analogs, 3'-imino[60]fulleryl-3'-deoxythymidine adsorbs on the colloidal silver surface via the lone pair electrons of the deprotonated N3 nitrogen atom. From the structural marker bands used to characterize the conformation of the thymidine, it was found that 3'-imino[60]fulleryl-3'-deoxythymidine behaves as 3'-azido-3'-

deoxythymidine and adopts a C3'-endo conformation. As for 3'-azido-3'-deoxythymidine, the C3'-endo conformation is sterically favoured by the C_{60}.

In order to try enhancing the signals in some of the spectral regions and to study the influence of the laser excitation frequency used, colloids with absorption maxima shifted to the longer wavelengths were synthesized. Gold nanorods with an absorption maximum at 760 nm were produced but due to a lack of time they were not tested within the time dedicated to this work.

7.2. Coordination of transition metals with C_{60}

Supramolecular assemblies of porphyrins and related tetraazamacrocyclic compounds with fullerenes have potential applications as photosynthetic systems, data storage media, and photovoltaic and electrochemical devices [49, 50, 51, 52, 53, 54, 55, 56]. In these porphyrin-fullerene systems, the porphyrins act as light receptors and electron donors. Upon photo-excitation, an excited state of the porphyrin relaxes by charge donation to the nearby fullerene acting as an electron acceptor. Besides its ability to undergo up to six reversible one-electron reductions [57], C_{60} in fullerene-porphyrin dyads was shown to cause an acceleration of the photoinduced charge separation and a retardation of the charge recombination compared to conventional acceptors such as quinones [58]; these properties are related to its exceptionally small reorganization energy when involved in electron-transfer reactions [59, 60, 61, 62].

Supramolecular architectures, in which photo-/electroactive donors and acceptors are organized intermolecularly *via* non-covalent linkages, are appealing since they might provide long-lived charge separated states [1, 2, 3, 63]. In non-covalent systems, a rapid photoinduced electron transfer should be followed by a splitting of the charge

separated components [64]. Therefore, the development of synthetic strategies aimed at associating a donor and an acceptor in a well-defined geometry through non-covalent linkages is of high interest. Besides, the weak molecular interactions offer an opportunity to control (i) the organization of photo- and redox active components and (ii) their mutual, electronic coupling [64]. In principle, a variety of non-covalent interactions, such as hydrogen-bond, donor-acceptor complexation, electrostatic interactions and π-π stacking, can be exploited for the design and synthesis of donor-acceptor systems with high directionality and selectivity for achieving predetermined architectures [64]. The approach considered here involves the interactions between metalloporphyrins and C_{60} to potentially engineer supramolecular assemblies with the potential for remarkable photophysical and magnetic properties [65, 66, 67, 68, 69].

Depending on their size, charge, and spin multiplicity, metal ions can fit into the central hole of the porphyrin ring, forming regular metalloporphyrins, or be located out of the ligand plane, resulting in sitting-on-top complexes. Porphyrin derivatives display intense electronic absorption bands in the 380-500-nm range (the so-called Soret or B bands) with molar extinction coefficients of 10^5 $M^{-1}cm^{-1}$ magnitude. At longer wavelengths, in the 500-750-nmrange, a set of weaker, but still considerably intense Q-bands, with molar extinction coefficients of 10^4 $M^{-1}cm^{-1}$ magnitude can be found. Thus due to significant overlap of their absorption bands with the emission spectrum of the solar radiation reaching the biosphere, porphyrins are efficient tools for conversion of radiation to chemical energy.

The present work was motivated by the theoretical work of Basiuk [70] on the complexation of C_{60} by metallo-porphines (P) and its effect on the interaction strength and electronic structure of these complexes. While the interaction of porphyrins (not

complexing metal cations) with C_{60} is extremely weak (the energy of complex formation is-0.3 kcal/mol), the calculated formation energies of the metal complexes vary from -27.3, -38.6 kcal/mol ($MnCl•C_{60}$ and $FeCl•C_{60}$) to -45.8, -43.8 kcal/mol ($Mn•C_{60}$ and $Fe•C_{60}$) [70]. In the present work we report, using mass spectrometry, on the formation and characterization of meso-Tetratolylporphyrins complexing manganese and iron cations with the C_{60} molecule since these complexes are reportedly the most stable.

7.2.1. Experimental

The meso-Tetratolylporphyrin-Fe(III) chloride (98%) and meso-Tetratolylporphyrin-Mn(III) chloride (98%) used in this study were purchased from Porphyrin-Systems (Lübeck, Germany). The [60]fullerene was purchased from MER Corporation at a purity of 99.9%. All samples and solvents were used without further purification. 10^{-3} M stock solutions of the porphyrins and C_{60} were prepared by dissolving them in toluene with the complex prepared from these stock solutions. The samples were mass analyzed on a Q-Tof Ultima Global mass spectrometer using a nanospray source and home pulled, gold coated borosilicate capillaries. 20% acetonitrile v:v was added to the toluene complex solutions to facilitate electronebulization.

All the electronebulized solutions were 5 10^{-5} M in porphyrin and/or C_{60}, and composed of toluene:acetonitrile 4:1 v:v. The complex formation was only detected upon the addition of lithium iodide or sodium iodide to the mixture of meso-tetratolylporphyrin-metal(III) and C_{60} (followed by vigorous agitation) prior to the addition of acetonitrile and mass analysis.

7.2.2. Results and Discussion

The first analysis of porphyrins using electrospray ionization was performed by Van Berkel *et al.* [71] while for fullerenes it was performed by Drewello and coworkers [72]. Porphyrins were shown to ionize via solution-phase protonation while metalloporphyrins (without counterion) ionize *via* either electrochemical oxidation or when chelating trivalent metals and associated with a negatively charged counterion, $[(metal^{3+})(porphyrin^{2-})]^{+}L^{-}$, by dissociation into $[(metal^{3+})(porphyrin^{2-})]^{+}$ [71]. C_{60}, on the other hand, is readily reduced but hard to oxidize. After unfructuous attemps in negative mode, characterization was performed exclusively in positive ion mode. In order to observe the $[(\text{meso-tetratolylporphyrin-metal(III)}):C_{60}]^{+}$ ions, and thus the complex formation, iodide salts (such as LiI and NaI) were added to the solution containing meso-tetratolylporphyrin-metal(III)] chloride and C_{60}. Other salts, e.g. chloride salts, heating, prolongated reaction did not lead to the complex observation.

Since the Fe isotope of mass 55.93 Da has the highest abundance (~92 %), in order to facilitate the discussion, all the isotopic distributions will be referenced according to their ^{56}Fe signal and not according to the first isotope of their distribution involving ^{54}Fe. See Fig. 7.2.1.-a' illustrates that meso-tetratolylporphyrin-Fe(III) chloride oxidation (759.21 m/z) is the dominant ionization process in absence of LiI added to the toluene:acetonitrile 4:1 solution. Upon LiI addition, the meso-tetratolylporphyrin-Fe(III) chloride dissociates and only the cation $[\text{meso-tetratolylporphyrin-Fe(III)}]^{+}$ (724.23 m/z) is detected (see Fig. 7.2.1.A). Another consequence of the addition of LiI in large excess is the apparition of the signal corresponding to the ion $[(\text{tetratolylporphyrin-Fe(III)})_2:I]^{+}$ at 1576.38 m/z (see Fig. 7.2.1.B). This observation suggests the substitution of the chloride by the iodide. When C_{60} is added to a tetratolylporphyrin-Fe(III) chloride solution containing LiI, a peak corresponding to

the [tetratolylporphyrin-Fe(III):C_{60}]$^+$ is detected at 1444.26 m/z (see Fig. 7.2.1.B). Its attribution is confirmed by its collision induced dissociation leading to the retrieval of Tetratolylporphyrin-Fe(III)$^+$ (724.25 m/z) and a neutral fragment of mass 720.01 Da (derived from the mass difference between the parent and fragment ions) corresponding within experimental error to the mass of C_{60} (see Fig. 7.2.1.C).

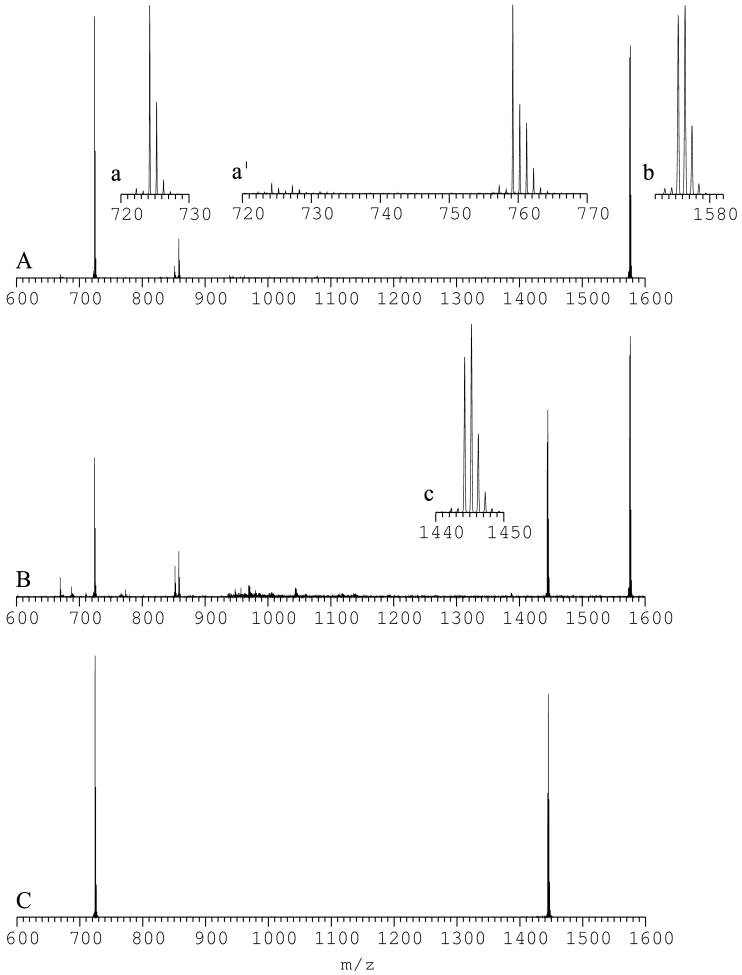

Fig. 7.2.1. Tetratolylporphyrin-Fe(III) : C_{60} complex cations. A. Positive ion mass spectrum of the tetratolylporphyrin-Fe(III) chloride (a') upon addition of LiI. The scale-ups (a) and (b) respectively correspond to the cations [tetratolylporphyrin-Fe(III)]$^+$ and [(tetratolylporphyrin-Fe(III))$_2$:I]$^+$. B. Positive ion mass spectrum of a mixture of tetratolylporphyrin-Fe(III) and C_{60} in presence of LiI. The scale-up (c) corresponds to the complex [tetratolylporphyrin-Fe(III):C_{60}]$^+$. C. Positive ion CID spectrum of the [tetratolylporphyrin-Fe(III):C_{60}]$^+$ ions. The signal at lower m/z corresponds to [tetratolylporphyrin-Fe(III)]$^+$.

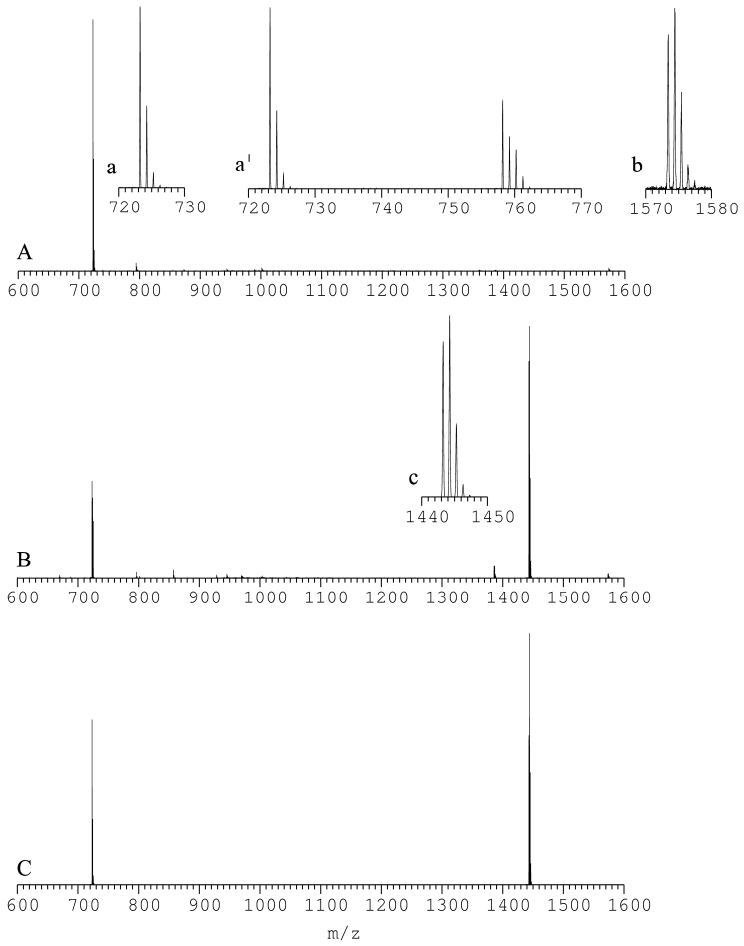

Fig. 7.2.2. Tetratolylporphyrin-Mn(III) : C_{60} complex cations. A. Positive ion mass spectrum of the tetratolylporphyrin-Mn(III) chloride (a') upon addition of LiI. The scale-ups (a) and (b) respectively correspond to the cations [tetratolylporphyrin-Mn(III)]$^+$ and [(tetratolylporphyrin-Mn(III))$_2$:I]$^+$. B. Positive ion mass spectrum of a mixture of tetratolylporphyrin-Mn(III) and C_{60} in presence of LiI. The scale-up (c) corresponds to the complex [tetratolylporphyrin-Mn(III):C_{60}]$^+$. C. CID spectrum of the [tetratolylporphyrin-Mn(III):C_{60}]$^+$ ions. The signal at lower m/z corresponds to [tetratolylporphyrin-Mn(III)]$^+$.

Essentially the same behaviour is observed for the tetratolylporphyrin-Mn(III) chloride. LiI accelerates but is not required for the formation of the cation Tetratolylporphyrin-Mn(III)$^+$ of 723.26 m/z (see Fig. 7.2.2.A). The complex [(Tetratolylporphyrin-Mn(III))$_2$:I]$^+$ (1573.45) is typically detected upon addition of LiI in large excess although slightly different conditions can lead to significant

fluctuations in its abundance. It also replaces the [(tetratolylporphyrin-Fe(III))$_2$:Cl]$^+$ (1481.47 m/z) cation observed in absence of LiI. Finally upon addition of C_{60} to a tetratolylporphyrin-Mn(III) chloride solution containing LiI, a peak corresponding to the [tetratolylporphyrin-Mn(III):C_{60}]$^+$ is detected at 1443.28 m/z (see Fig. 7.2.1.B). Its attribution is confirmed by its collision induced dissociation leading to the retrieval of Tetratolylporphyrin-Mn(III)$^+$ (723.26 m/z) and a neutral fragment of mass 720.02 m/z) corresponding within experimental error to the mass of C_{60} (see Fig. 7.2.1.C).

Raman measurements on dried droplet samples and UV-Visible measurements in solution (toluene) were also attempted in order to characterize the complex, however, without success regarding to the identification of a signal characteristic of the C_{60} complexes. All the changes observed, i.e. the apparition of a Raman band at 271 cm^{-1} and a shift in the UV-Vis Absorption of the prophyrins have been attributed as direct consequences of the addition of LiI. Further experimental work is required to ascertain the exact conditions of the complex formation and most specifically the addition of the polar co-solvent, acetonitrile [66].

7.2.3. Conclusion

The present results provide evidence, using mass spectrometry, of the formation of a complex between meso-tetratolylporphyrin-Fe(III) or meso-tetratolylporphyrin-Mn(III) and C_{60}. The existence of these complexes as gas phase ions produced by electrospray ionization is a further demonstration that there is no need to match the convex surface of the C_{60} with concave hosts such as cyclodextrins to form supramolecular assemblies. It also allows investigating these complexes using gas phase approaches. Although no direct evidence of the complexation in condensed phases was found using Raman spectroscopy, it is suggested that adequate preparation

conditions involving solvents more polar than toluene and the manipulation of the porphyrin substituents, should make it possible to construct such molecular assemblies for photophysical investigation [66]. ^{13}C-NMR will be used in order to confirm the present results.

References

[1] H. Anderson, C. Hunter, J. Sanders, *Journal of the Chemical Society, Chemical Communications* p. 226 (1989).

[2] M. D. Ward, *Chemical Society Reviews* **26**, 365 (1997).

[3] T. Hayashi, H. Ogoshi, *Chemical society Reviews* **26**, 355 (1997).

[4] J. F. Maguire, M. S. Amer, J. Busbee, *Applied Physics Letters* **82**, 2592 (2003).

[5] V. Schettino, M. Pagliai, L. Ciabini, G. Cardini, *Journal of Physical Chemistry A* **105**, 11192 (2005).

[6] Y. Fang, Q. J. Huang, P. Wang, X. Y. Li, N. T. Yu, *Chemical Physics Letters* **381**, 255 (2003).

[7] C. Otto, T. J. Van der Tweel, F. F. de Mul, J. Greve, *Journal of Raman Spectroscopy* **17**, 289 (1986).

[8] J. Suh, M. Moskovits, *Journal of the America Chemical Society* **108**, 4711 (1986).

[9] L. Rivas, S. Sanchez-Cortes, J. V. Garcia-Ramos, *Journal of Raman Spectroscopy* **33**, 6 (2001).

[10] L. Rivas, S. Sanchez-Cortes, J. V. García-Ramos, *Physical Chemistry Chemical Physics* **4**, 1943 (2002).

[11] A. Toyama, Y. Takino, H. Takeuchi, I. Harada, *Journal of the American Chemical Society* **115**, 11092 (1993).

[12] M. T. Cotton, *Advances in Spectroscopy* **16**, 91 (1988).

[13] R. L. Garrel, *Analytical Chemistry* **61**, 401A (1989).

[14] K. Kneipp, H. Kneipp, R. Itzkan, I. Dasari, M. S. Feld, *Chemical Reviews* **99**, 2957 (1999).

[15] K. Kneipp, *et al.*, *Physical Review Letters* **78**, 2444 (1996).

[16] K. Kneipp, *et al.*, *Physical Review Letters* **78**, 1667 (1997).

[17] M. Moskovits, *Review of Modern Physics* **57**, 783 (1985).

[18] M. Moskovits, *Journal of Chemical Physics* **77**, 4408 (1982).

[19] A. J. Haes, *et al.*, *Matrial Research Society Bulletin* **30**, 368 (2005).

[20] A. Zangwill, *Physics at surfaces* (Cambridge University Press, Cambridge, 1996).

[21] S. Zhang, L. Echegoyen, *Tetrahedron* **62**, 1947 (2006).

[22] N. Armaroli, *et al.*, *Chemistry a European Journal* **4**, 406 (1998).

[23] F. Diederich, J. F. Nierengarten, J. P. Sauvage, *Journal of the Chemical Society, Chemical Communications* p. 781 (1995).

[24] M. G. Albrecht, J. A. Creighton, *Journal of the American Chemical Society* **99**, 5215 (1977).

[25] J. A. Sanchez-Gil, J. V. Garcia-Ramos, *Journal of Chemical Physics* **108**, 317 (1998).

[26] P. C. Lee, D. Meisel, *Journal of Chemical Physics* **92**, 1709 (1982).

[27] G. Schmid, *Chemical Reviews* **92**, 1709 (1992).

[28] R. S. Sheng, L. Zhu, M. D. Morris, *Analytical Chemistry* **58**, 1116 (1986).

[29] L. Rivas, S. Sanchez-Cortes, J. V. García-Ramos, G. Morcillo, *Langmuir* **17**, 574 (2001).

[30] S. L. Zhang, M. K. H., G. R. Loppnow, *Journal of Chemical Physics* **102**, 461 (1998).

[31] M. Tsuboi, *et al.*, *Journal of the American Chemical Society* **119**, 2025 (1997).

[32] A. F. Bell, L. Hecht, L. D. Barron, *Journal of the Chemical Society, Faraday Transactions* **93**, 553 (1997).

[33] P. Escobar R. Carmona, M. Molina, *Analyst* **121**, 105 (1996).

[34] K. Ushizawa, T. Ueda, M. Tsuboi, *Journal of Molecular Structure* **412**, 169 (1997).

[35] C. H. Munro, W. E. Smith, M. Garner, J. Clarkson, P. C. White, *Langmuir* **11**, 3712 (1995).

[36] D. Fornasiero, F. Grieser, *Journal of Chemical Physics* **87**, 5 (1987).

[37] O. Siiman, L. A. Bumm, R. Callaghan, B. C. G., M. Kerker, *Journal of Physical Chemistry* **87**, 1014 (1983).

[38] M. Kerker, O. Siiman, D. S. Wang, *Journal of Physical Chemistry* **88**, 3168 (1984).

[39] K. Kneipp, *et al.*, *Physical Review E* **57**, R6281 (1998).

[40] J. A. Creighton, C. G. Blatchford, M. G. Albrecht, *Journal of the Chemical Society, Faraday Transactions 2* **75**, 545 (1979).

[41] M. Ostblom, B. Liedberg, L. M. Demers, C. A. Mirkin, *Journal of Physical Chemistry B* **109**, 15150 (2005).

[42] S. Dijkstra, J. M. Benevides, G. J. Thomas, *Journal of Molecular Structure* **242**, 283 (1991).

[43] J. M. Benevides, P. L. Stow, L. L. Ilag, N. L. Incardona, G. J. J. Thomas, *Biochemistry* **30**, 4855 (1991).

[44] M. Moskovits, D. P. DiLella, *Journal of Chemical Physics* **73**, 6068 (1980).

[45] M. Moskovits, J. S. Suh, *Journal of Physical Chemistry* **88**, 5526 (1984).

[46] V. M. Hallmark, A. Campion, *Journal of Chemical Physics* **84**, 2933 (1986).

[47] A. Campion, P. Kambhampati, *Chemical Society Reviews* **27**, 241 (1998).

[48] S. Y. Kim, T. H. Joo, S. W. Suh, M. Y. Kim, *Journal of Raman Spectroscopy* **17**, 381 (1986).

[49] D. V. Konarev, E. I. Yudanova, I. S. Neretin, Y. L. Slovokhotov, R. N. Lyubovskaya, *Synthetic metals* **121**, 1125 (2001).

[50] Y. Kubo, *et al.*, *Organic Letters* **4**, 925 (2002).

[51] D. V. Konarev, *et al.*, *Inorganic Chemistry* **41**, 3638 (2002).

[52] F. S. Sun, D. Tham, C. A. Reed, P. D. W. Boyd, *Proceedings of the National Academy of Sciences of the U.S.A.* **99**, 5088 (2002).

[53] T. Ishii, *et al.*, *Coordination Chemistry Reviews* **226**, 113 (2002).

[54] T. Hasobe, H. Imahori, S. Fukuzumi, P. V. Kamat, *Journal of Physical Chemistry B* **107**, 12105 (2003).

[55] T. Hasobe, *et al.*, *Journal of Physical Chemistry B* **108**, 12865 (2004).

[56] S. Yoshimoto, *et al.*, *Langmuir* **20**, 11046 (2004).

[57] Q. Xie, E. Perez-Cordero, L. Echegoyen, *Journal of the American Chemical Society* **114**, 3978 (1992).

[58] H. Imahori, *et al.*, *Journal of the American Chemical Society* **118**, 11771 (1996).

[59] H. Imahori, *et al.*, *Chemical Physics Letters* **263**, 545 (1996).

[60] D. M. Guldi, K. D. Asmus, *Journal of the American Chemical Society* **119**, 5744 (1997).

[61] D. Guldi, M. Prato, *Accounts of Chemical Research* **33**, 695 (2000).

[62] H. Imahori, *et al.*, *Journal of Physical Chemistry A* **105**, 325 (2001).

[63] F. D'Souza, *et al.*, *Journal of Physical Chemistry B* **108**, 11333 (2004).

[64] D. M. Guldi, T. Da Ros, P. Braiuca, M. Prato, E. Alessio, *Journal of Material Chemistry* **12**, 2001 (2002).

[65] D. R. Evans, *et al.*, *Journal of the American Chemical Society* **121**, 8466 (1999).

[66] P. D. W. Boyd, *et al.*, *Journal of the American Chemical Society* **121**, 10487 (1999).

[67] M. M. Olmstead, *et al.*, *Journal of the American Chemical Society* **121**, 709 (1999).

[68] T. Ishii, *et al.*, *Journal of the Chemical Society, Dalton Transactions* p. 4407 (2000).

[69] D. V. Konarev, *et al.*, *Chemistry, a European Journal* **7**, 2605 (2001).

[70] V. A. Basiuk, *Journal of Physical Chemistry A* **109**, 3704 (2005).

[71] G. J. Van Berkel, S. A. McLuckey, G. L. Glish, *Analytical Chemistry* **63**, 1098 (1991).

[72] M. P. Barrow, *et al.*, *Chemical Physics Letters* **330**, 267 (2000).

Chapter 8. General Conclusion

Whatever the scale and the application, development and engineering of devices imply the characterization of the properties of components involved. At the molecular and nanometric scales, access to these properties often requires the combination of multiple instrumental techniques and is complicated by the difficulty to assess the influence of the environment. The present work demonstrates the capabilities of mass spectrometry and related techniques, such as ion mobility and action spectroscopy, for the characterization of gas phase ions under minimal interference conditions from the environment. The results presented herein focus on the understanding of fullerenes, fullerene derivatives, and fullerene complexes with in mind the ulterior development of fullerene based devices for sensing applications and beyond.

Ion-molecule reactions were used to study both protonated 2'-deoxyguanosine to determine the hydrogen atoms involved in its fragmentation mechanism, and the reactivity of $C_{60}^{\bullet-}$ anions with methanol. The interest for 2'-deoxyguanosine, a component of deoxyribonucleic acids (DNA), was motivated by the recognition and structuring properties of their assemblies. Self-assembly of G-rich DNA strands leads to the formation of G-quadruplex structures with high potential applications as molecular wires and telomere related sensors. The present work provides information about the reactivity of 2'-deoxyguanosine hydrogen atoms via hydrogen/deuterium exchange and kinetic isotope effects. Understanding of these mechanisms should prove useful in the development of larger and more complex entities incorporating 2'-deoxyguanosine and fullerenes. The study of $C_{60}^{\bullet-}$ gas phase reactivity with methanol, on the other hand, was discovered during the structural analysis of its derivatives. Its further study was motivated by fullerene use as model structures for studying the

reversible hydrogenation of carbon materials such as fullerenes, nanotubes, peapods, etc. The present work demonstrates $C_{60}^{\bullet-}$ hydrogenation by reaction with methanol vapour in the gas phase at pressures in the microbar range and room temperature conditions. For the experimental condition used, a maximum of eleven hydrogen atoms were added successively to $C_{60}^{\bullet-}$ with reaction rates higher for radical than for closed-shell fullerene species. The C_{60} hydride ions and the oxygen containing species formed at longer reaction times were then reversibly reconverted into C_{60}^{-} ions by low-intensity infrared multiphoton activation using a continuous-wave CO_2 laser. The existence of a radical multistep mechanism for hydrogen loss was confirmed, in agreement with previously published theoretical results.

Covalent chemistry in solution was used to produce 3'-imino[60]fulleryl-3'-deoxythymidine to assess the interactions, the spontaneous or photoinduced electron transfer between a DNA strand and C_{60}, and to study the ability to immobilize C_{60} derivatives on metallic sufaces. Interaction between the C_{60} and the deoxythymidine was initially studied using collision induced dissociation (CID) in mass spectrometry. CID of the sodiated and reduced 3'-imino[60]fulleryl-3'-deoxythymidine yields fragment ions including the ionization site, respectively the thymine and the C_{60} subunits. Deprotonated 3'-imino[60]fulleryl-3'-deoxythymidine behaves differently. The observed fragments include the subunit of highest electron affinity, i.e. C_{60}, but not the deprotonation site located either on the thymine or deoxyribose units. This leads, using photoelectron detachment as probing technique and *ab initio* calculations, to the identification of the most likely deprotonation site as being O5' on the deoxyribose, in opposition to N3 previously reported for thymidine and 3'-azido-deoxythymidine and to the evidence of charge and hydrogen transfers to the C_{60}

involving the rearrangement of the deprotonated deoxyribose in agreement with the measured CID mass spectra. The present work suggests steric hindrance should help prevent charge migration following for instance rearrangement from deprotonated groups to the C_{60}.

The study of the complexation of C_{60} by water soluble γ-cyclodextrins was motivated by the increased solubility of the encapsulated [60]fullerene in polar solutions and by the steric barrier formed by cyclodextrins against reactions with dissolved species or involving rearrangements with atom transfers to the C_{60}. Using for the first time electrospray ionization, the following stability order was found upon collisional activation for the doubly deprotonated, protonated and sodiated $[C_{60}:(CyD)_2]$ ions: $[C_{60}:(\gamma\text{-cyclodextrin})_2 + 2H]^{2+} < [C_{60}:(\gamma\text{-cyclodextrin})_2 - 2H]^{2-} < [C_{60}:(\gamma\text{-cyclodextrin})_2 + 2Na]^{2+}$ with deprotonation inducing both electron and proton transfers from the γ-cyclodextrin to the C_{60}. Conformational/ 3D structure information on sodiated, $[C60:(\gamma\text{-CyD})_2 + 2.Na]^{2+}$, and deprotonated $[C60:(\gamma\text{-CyD})_2 - 2.H]^{2-}$ complex ions was further obtained using ion mobility measurements and molecular modeling calculations. Six distinct families of conformers mainly characterized by different orientations of the primary hydroxyl groups have been theoretically identified. These families can be subdivided into three groups, sphere-, cup-, and barrel-shaped with increasing cross-sections and relative energies/heats of formation. The sphere-shaped conformers are the lowest in energy, have the smallest cross-sections possible and are in excellent agreement with the experimentally inferred cross-section of the $[C60:(\gamma\text{-CyD})_2 + 2.Na]^{2+}$ ions. The $[C60:(\gamma\text{-CyD})_2 + 2.Na]^{2+}$ ions have their two γ-cyclodextrins involved in sixteen intermolecular hydrogen bonds and the C_{60} fully encapsulated with only two small polar caps accessible to solvent or reagents. The

experimentally inferred cross-sections of the $[C60:(\gamma\text{-}CyD)_2 - 2.H]^{2-}$ ions, on the other hand, are larger and thus related to less compact conformers, either cup-shaped conformers or with the complex partially opened up like a pearl oyster explaining the lower stability of the deprotonated complex.

Overall, useful information on the reactivity and physico-chemical properties of fullerene related systems has been obtained using mass spectrometry and related techniques, as well as theoretical approaches. Although the information obtained using mass spectrometry pertains to gas phase ions and is often of unknown transferability to solution species, the conclusion of the present work is that one should pay extensive care to the experimental conditions used to synthesize and study nanoscale and molecular devices when working on adsorbed or condensed phase materials. Some changes, only easily detected in the gas phase, can be misleading in their implications.

Appendix 1. Appendix to Chapter 6

Table 1: Energetics, conformational markers, and cross-sections obtained at the HF/sto-3g and PM6 levels of the two γ-cyclodextrins involved in different conformers of the [C60:(γ-CyD)2] complex. The conformers have been divided into three groups, sphere- (sph), cup- (cup) and barrel-shaped (bar). The lowest energy conformer of each group, at both levels of theory, has been underlined. The cyclodextrins with T2 conformation of the primary hydroxyl groups while stable at the HF/sto-3g level, collapse to lower energy T5 conformers at the PM6 level. Only one H3 conformer stable at the HF/sto-3g level collapses to an H5 conformer. At the PM6 level, the values of the collapsed T2 and H3 structures have been stroked.

Conf.	E_{tot} (h) (HF/sto3g)	$\Delta_f H$ (Kcal) (PM6)	θ_1	θ_2	ω	ϕ	ψ	φ	τ	σ (HF/sto3g)	σ (PM6)
sph T5H5T	-11836.5759359	-2900.50715	51.8 (0.3) 51.8 (0.3)	-66.1 (0.1) -66.1 (0.1)	123.4 (0.4) 123.4 (0.4)	98.6 (0.4) 98.6 (0.4)	126.7 (0.3) 126.7 (0.3)	114.9 (0.1) 114.9 (0.1)	114.2 (0.4) 114.2 (0.4)	364.3 (0.7)	368.7 (0.7)
			57.2 (0.5) 57.2 (0.5)	-65.2 (0.2) -65.2 (0.3)	115.6 (0.7) 115.6 (0.7)	100.9 (0.7) 100.8 (0.6)	130.3 (0.6) 130.3 (0.5)	115.7 (0.1) 115.7 (0.1)	114.5 (1.0) 114.5 (0.6)		
sph T5T5T	-11836.5733770	-2880.78742	54.1 (0.3) 54.1 (0.3)	-66.9 (0.1) -66.9 (0.1)	122.8 (0.4) 122.8 (0.4)	99.8 (0.4) 99.8 (0.4)	128.0 (0.3) 128.0 (0.3)	115.2 (0.1) 115.2 (0.1)	113.0 (0.5) 113.0 (0.5)	363.9 (0.6)	366.7 (0.6)
			57.3 (0.4) 57.3 (0.4)	-64.5 (0.3) -64.5 (0.3)	115.8 (0.7) 115.8 (0.7)	99.8 (0.5) 99.8 (0.5)	129.5 (0.5) 129.5 (0.5)	115.4 (0.1) 115.4 (0.1)	115.6 (0.7) 115.7 (0.6)		
sph H5H5T	-11836.5623659	-2894.06695	52.2 (0.3) 51.9 (0.3)	-66.3 (0.1) -66.0 (0.1)	107.7 (0.5) 123.0 (0.5)	97.4 (0.3) 98.1 (0.3)	127.7 (0.3) 127.0 (0.3)	114.9 (0.1) 114.9 (0.1)	115.4 (0.3) 114.7 (0.3)	364.1 (0.9)	368.5 (0.8)
			57.0 (0.5) 57.1 (0.5)	-65.3 (0.4) -65.2 (0.2)	108.3 (1.0) 115.6 (0.7)	100.8 (0.6) 100.8 (0.7)	130.0 (0.5) 130.2 (0.6)	115.5 (0.1) 115.6 (0.1)	114.8 (0.8) 114.6 (1.0)		
sph H5T5T	-11836.5592542	-2874.89422	54.6 (0.3) 54.1 (0.3)	-67.2 (0.1) -66.9 (0.1)	107.0 (0.4) 122.7 (0.4)	98.8 (0.4) 99.7 (0.4)	128.8 (0.3) 128.0 (0.3)	115.2 (0.1) 115.2 (0.1)	113.9 (0.4) 113.1 (0.4)	364.1 (0.8)	367.0 (0.8)
			57.0 (0.4) 56.9 (0.5)	-64.8 (0.3) -64.5 (0.3)	108.4 (0.6) 115.8 (0.7)	99.7 (0.4) 99.7 (0.5)	129.2 (0.4) 129.4 (0.5)	115.3 (0.1) 115.4 (0.1)	116.0 (0.5) 115.8 (0.6)		
sph	-11836.5493348	-2887.49879	52.3	-66.3	107.7	97.2	127.9	114.9	115.6	363.4	368.8

H5H5H			(0.3) 52.3 (0.2)	(0.1) -66.3 (0.1)	(0.5) 107.7 (0.5)	(0.3) 97.2 (0.3)	(0.3) 127.9 (0.3)	(0.1) 114.9 (0.1)	(0.3) 115.6 (0.3)	(0.6)	(0.5)
			56.9 (0.5) 56.9 (0.5)	-65.3 (0.4) -65.3 (0.4)	108.4 (1.1) 108.4 (1.1)	100.9 (0.6) 100.8 (0.6)	129.9 (0.5) 129.9 (0.6)	115.5 (0.1) 115.5 (0.1)	114.7 (0.9) 114.7 (0.9)		
sph H5T5H	-11836.5456068	-2868.91450	54.5 (0.3) 54.5 (0.3)	-67.1 (0.1) -67.1 (0.1)	106.9 (0.5) 106.9 (0.5)	98.4 (0.3) 98.4 (0.3)	129.1 (0.4) 129.1 (0.4)	115.1 (0.1) 115.2 (0.1)	114.4 (0.4) 114.4 (0.4)	364.1 (0.7)	366.5 (0.6)
			56.7 (0.5) 56.7 (0.4)	-64.7 (0.3) -64.7 (0.3)	108.5 (0.7) 108.5 (0.6)	99.9 (0.5) 99.9 (0.5)	128.9 (0.5) 128.9 (0.4)	115.3 (0.1) 115.3 (0.1)	115.8 (0.7) 115.9 (0.6)		
cup T1T5T	-11836.5570756	-2853.33827	47.4 (0.6) 54.9 (0.2)	-57.6 (0.3) -67.5 (0.1)	-54.1 (0.1) 123.2 (0.3)	113.1 (0.4) 99.2 (0.3)	119.7 (0.8) 128.4 (0.3)	115.4 (0.1) 115.1 (0.1)	101.0 (0.6) 113.3 (0.4)	395.0 (0.5)	390.1 (0.7)
			53.2 (0.4) 57.5 (0.4)	-58.1 (0.2) -64.6 (0.3)	-56.5 (0.2) 116.0 (0.3)	104.5 (0.5) 99.8 (0.2)	127.8 (0.5) 129.5 (0.2)	114.8 (0.1) 115.2 (0.1)	111.2 (0.6) 115.5 (0.3)		
cup T1H5T	-11836.5492428	-2872.01229	44.7 (0.4) 51.7 (0.2)	-57.3 (0.3) -66.6 (0.1)	-54.0 (0.1) 124.3 (0.3)	111.1 (0.4) 98.8 (0.3)	117.1 (0.7) 125.9 (0.2)	115.1 (0.1) 114.8 (0.1)	102.4 (0.5) 113.9 (0.4)	393.9 (0.7)	392.1 (0.8)
			55.6 (0.6) 57.1 (0.4)	-58.1 (0.1) -65.2 (0.3)	-58.6 (0.6) 115.5 (0.7)	105.2 (0.9) 100.5 (0.6)	130.4 (0.9) 130.5 (0.7)	115.0 (0.1) 115.5 (0.1)	109.6 (1.2) 115.0 (0.9)		
cup T2T5T	-11836.5441487	~~-2880.77623~~	46.6 (0.8) 54.9 (0.2)	-58.3 (0.3) -67.5 (0.1)	52.6 (0.2) 123.3 (0.3)	114.6 (0.4) 99.1 (0.3)	117.8 (0.9) 128.5 (0.3)	115.6 (0.1) 115.1 (0.1)	99.8 (0.5) 113.2 (0.4)	384.0 (0.4)	~~367.0~~ (0.9)

T**5**T5T	PM6-sph		57.3 (0.5) 57.2 (0.4)	-64.6 (0.3) -64.6 (0.3)	115.8 (0.6) 115.8 (0.7)	99.8 (0.6) 99.8 (0.4)	129.5 (0.5) 129.5 (0.4)	115.3 (0.1) 115.4 (0.1)	115.6 (0.7) 115.6 (0.5)		
cup T1T5H	-11836.5427538	-2865.24832	47.3 (0.7) 55.3 (0.2)	-57.6 (0.3) -67.7 (0.1)	-54.2 (0.1) 108.0 (0.3)	113.1 (0.4) 98.3 (0.3)	119.7 (0.8) 129.2 (0.3)	115.4 (0.1) 115.0 (0.1)	101.1 (0.6) 114.0 (0.4)	395.7 (0.7)	389.9 (0.8)
			55.4 (0.7) 57.1 (0.5)	-58.0 (0.1) -65.4 (1.0)	-58.8 (0.8) 108.8 (2.6)	105.2 (0.9) 100.4 (0.9)	130.3 (1.1) 130.2 (1.0)	115.0 (0.1) 115.4 (0.1)	109.5 (1.3) 115.3 (1.3)		
cup H4T5T	-11836.5406240	-2844.78458	50.1 (0.4) 54.7 (0.2)	-61.0 (0.2) -67.4 (0.1)	-91.9 (0.3) 123.1 (0.3)	108.0 (0.5) 99.2 (0.4)	122.2 (0.4) 128.4 (0.3)	115.5 (0.1) 115.1 (0.1)	105.5 (0.5) 113.3 (0.4)	381.8 (0.8)	385.0 (0.7)
			50.0 (0.3) 57.7 (0.4)	-58.7 (0.4) -64.8 (0.3)	-109.7 (1.1) 116.5 (0.5)	109.3 (0.5) 99.6 (0.3)	119.8 (0.6) 129.3 (0.3)	115.2 (0.1) 115.3 (0.1)	115.8 (0.6) 115.2 (0.5)		
cup H3T5T	-11836.5396452	-2844.19506	47.5 (0.8) 55.1 (0.2)	-54.5 (0.4) -67.5 (0.1)	164.7 (0.7) 123.9 (0.3)	112.9 (0.3) 99.1 (0.3)	119.8 (0.7) 128.6 (0.3)	115.7 (0.1) 115.1 (0.1)	99.6 (0.5) 113.3 (0.4)	378.7 (1.0)	379.8 (0.8)
			48.9 (0.6) 58.8 (0.3)	-55.8 (0.7) -65.0 (0.3)	161.0 (0.9) 116.5 (0.6)	112.2 (0.2) 99.6 (0.4)	118.9 (0.9) 129.8 (0.5)	115.7 (0.1) 115.3 (0.1)	102.5 (0.7) 102.5 (0.7)		
cup T2H5T	-11836.5371960	~~-2900.49481~~	44.2 (0.4) 51.7 (0.2)	-58.1 (0.2) -66.6 (0.1)	52.2 (0.2) 124.4 (0.3)	112.2 (0.4) 98.9 (0.3)	115.6 (0.6) 125.8 (0.2)	115.2 (0.1) 114.9 (0.4)	101.5 (0.5) 113.8 (0.4)	382.5 (0.9)	~~368.9~~ (0.5)
T**5**H5T	PM6-sph		57.0 (0.8) 57.2	-65.2 (0.2) -65.2	115.4 (0.8) 115.6	100.8 (0.7) 100.8	130.3 (0.5) 130.3	115.6 (0.1) 115.7	114.5 (1.0) 114.6		

			(0.5)	(0.2)	(0.6)	(0.5)	(0.5)	(0.1)	(0.8)		
cup H4H5T	-11836.5355830	-2861.96994	48.2 (0.3) 51.6 (0.2)	-60.4 (0.1) -66.4 (0.1)	-90.3 (0.3) 124.1 (0.3)	105.5 (0.5) 98.7 (0.3)	121.1 (0.5) 125.9 (0.3)	115.1 (0.1) 114.8 (0.1)	107.3 (0.5) 114.1 (0.4)	380.8 (0.6)	386.8 (0.7)
			50.9 (2.4) 56.5 (0.6)	-58.1 (2.29) -65.2 (0.4)	-114.1 (10.2) 115.6 (0.8)	110.4 (2.1) 100.5 (0.7)	120.4 (5.6) 130.1 (1.3)	115.4 (0.4) 115.7 (0.1)	103.7 (3.7) 115.1 (1.5)		
cup T1H5H	-11836.5350064	-2847.13931	44.7 (0.4) 52.1 (0.2)	-57.3 (0.3) -66.8 (0.1)	-54.0 (0.1) 109.2 (0.2)	111.0 (0.4) 98.0 (0.2)	117.2 (0.7) 126.6 (0.2)	115.1 (0.1) 114.7 (0.1)	102.6 (0.5) 114.7 (0.3)	394.0 (0.9)	391.6 (0.8)
			52.9 (0.4) 57.3 (0.4)	-58.0 (0.2) -64.8 (0.5)	-56.6 (0.2) 108.6 (0.7)	104.6 (0.5) 99.9 (0.2)	127.5 (0.5) 129.0 (0.3)	114.8 (0.1) 115.2 (0.1)	111.0 (0.6) 115.6 (0.4)		
cup T2T5H	-11836.5298679	~~-2874.89305~~	46.5 (0.7) 55.4 (0.2)	-58.2 (0.3) -67.7 (0.1)	52.6 (0.2) 108.0 (0.3)	114.5 (0.4) 98.3 (0.3)	117.8 (0.8) 129.2 (0.3)	115.6 (0.1) 115.0 (0.1)	99.9 (0.5) 114.0 (0.4)	384.1 (0.9)	~~366.3~~ (0.9)
T**5**T5H	PM6-sph		56.9 (0.5) 57.0 (0.5)	-64.5 (0.4) -64.7 (0.3)	115.8 (0.7) 108.4 (0.5)	99.7 (0.5) 99.7 (0.5)	129.4 (0.5) 129.2 (0.5)	115.4 (0.1) 115.2 (0.1)	115.8 (0.5) 116.0 (0.6)		
cup H3H5T	-11836.5295121	-2864.79749	44.6 (0.5) 51.7 (0.2)	-54.2 (0.4) -66.7 (0.1)	169.3 (0.6) 124.4 (0.3)	111.1 (0.2) 98.8 (0.3)	116.9 (0.6) 125.8 (0.2)	115.3 (0.1) 114.8 (0.1)	100.7 (0.4) 113.8 (0.4)	378.4 (0.7)	381.4 (0.8)
			54.4 (0.8) 56.3 (0.3)	-55.7 (1.0) -65.0 (0.3)	155.2 (1.9) 115.5 (0.5)	112.7 (0.9) 100.3 (0.5)	123.7 (2.0) 130.2 (0.7)	115.8 (0.2) 115.7 (0.1)	100.6 (1.4) 115.3 (0.8)		
cup H4T5H	-11836.5262517	-2838.63305	50.1 (0.4)	-61.0 (0.2)	-91.9 (0.4)	108.0 (0.5)	122.2 (0.4)	115.5 (0.1)	105.6 (0.5)	381.6 (0.5)	384.8 (0.9)

			55.1 (0.2)	-67.5 (0.1)	107.9 (0.3)	98.4 (0.3)	129.1 (0.3)	115.0 (0.1)	114.1 (0.4)		
			49.8 (0.3) 57.6 (0.4)	-58.5 (0.4) -65.0 (0.4)	-109.9 (1.2) 108.9 (0.8)	109.3 (0.5) 99.8 (0.3)	119.7 (0.6) 128.9 (0.5)	115.2 (0.1) 115.2 (0.1)	105.7 (0.6) 115.3 (0.6)		
cup H3T5H	-11836.5253947	-2838.38515	47.4 (0.8) 55.5 (0.2)	-54.5 (0.4) -67.7 (0.1)	164.7 (0.6) 108.0 (0.3)	112.9 (0.3) 98.2 (0.3)	119.8 (0.7) 129.3 (0.3)	115.7 (0.1) 115.0 (0.1)	99.7 (0.5) 114.0 (0.4)	378.8 (0.6)	379.7 (0.7)
			48.8 (0.6) 58.8 (0.2)	-55.9 (0.7) -65.2 (0.3)	161.2 (1.0) 108.8 (0.7)	112.2 (0.2) 99.6 (0.4)	118.9 (1.0) 129.5 (0.6)	115.7 (0.1) 115.2 (0.1)	102.6 (0.8) 115.0 (0.7)		
cup T2H5H	-11836.5229796	~~-2894.05014~~	44.3 (0.4) 52.1 (0.2)	-58.1 (0.3) -66.9 (0.1)	52.2 (0.2) 109.2 (0.2)	112.0 (0.4) 98.1 (0.2)	115.8 (0.6) 126.5 (0.2)	115.3 (0.1) 114.7 (0.1)	101.7 (0.5) 114.6 (0.3)	382.8 (1.0)	~~369.1~~ (0.6)
T**5**H5H	PM6-sph		57.0 (0.7) 57.0 (0.7)	-65.2 (0.3) -65.3 (0.3)	115.6 (0.7) 108.3 (1.0)	100.8 (0.6) 100.8 (0.7)	130.2 (0.5) 129.9 (0.6)	115.7 (0.1) 115.5 (0.1)	114.6 (0.8) 114.7 (1.0)		
cup H4H5H	-11836.5213544	-2855.49717	48.2 (0.3) 52.0 (0.2)	-60.4 (0.1) -66.7 (0.1)	-90.3 (0.3) 109.1 (0.2)	105.4 (0.5) 97.9 (0.3)	121.2 (0.5) 126.7 (0.2)	115.1 (0.1) 114.7 (0.1)	107.4 (0.5) 114.9 (0.3)	381.6 (0.6)	386.4 (0.7)
			50.0 (2.8) 56.5 (0.7)	-57.9 (2.5) -65.4 (0.9)	-113.2 (11.7) 108.6 (2.2)	110.6 (2.2) 100.5 (1.0)	119.8 (5.4) 129.9 (1.4)	115.4 (0.3) 115.6 (0.1)	103.5 (3.8) 115.2 (1.8)		
cup H3H5H	-11836.5153084	-2858.31998	44.6 (0.5) 52.1 (0.2)	-54.2 (0.3) -66.9 (0.1)	169.2 (0.5) 109.2 (0.2)	110.9 (0.2) 98.0 (0.2)	117.0 (0.6) 126.5 (0.2)	115.3 (0.1) 114.7 (0.1)	100.8 (0.4) 114.5 (0.3)	378.3 (0.8)	381.8 (0.8)
			53.9	-55.8	155.6	112.5	123.4	115.9	100.9		

			(1.2) 56.4 (0.5)	(1.3) -65.2 (0.5)	(2.8) 108.3 (1.3)	(1.1) 100.3 (0.7)	(3.1) 130.0 (1.1)	(0.2) 115.6 (0.1)	(2.2) 115.4 (1.3)		
bar T1T1T	-11836.5367889	-2824.47558	48.2 (0.8) 48.2 (0.6)	-57.8 (0.5) -57.7 (0.5)	-54.5 (0.1) -54.5 (0.1)	113.6 (0.3) 113.6 (0.3)	119.7 (0.7) 119.7 (0.7)	115.3 (0.1) 115.3 (0.1)	100.3 (0.5) 100.3 (0.5)	428.1 (0.9)	412.4 (1.0)
			53.3 (0.7) 53.4 (0.6)	-58.2 (0.2) -58.2 (0.2)	-56.6 (0.2) -56.6 (0.2)	104.6 (0.2) 104.6 (0.3)	127.5 (0.3) 127.6 (0.4)	114.8 (0.1) 114.8 (0.1)	111.0 (0.2) 111.0 (0.3)		
bar T1H1T	-11836.5262290	-2841.85933	43.7 (0.5) 43.6 (0.5)	-57.3 (0.5) -57.3 (0.5)	-54.2 (0.1) -54.2 (0.1)	114.2 (0.2) 114.2 (0.2)	113.8 (0.9) 113.8 (0.9)	114.9 (0.1) 114.9 (0.1)	99.5 (0.7) 99.5 (0.7)	428.9 (0.9)	415.4 (0.6)
			54.5 (3.1) 54.9 (1.7)	-58.0 (0.6) -58.0 (0.6)	-58.7 (1.5) -58.9 (2.0)	104.9 (1.0) 105.2 (1.3)	129.9 (2.7) 129.9 (3.4)	115.0 (0.3) 115.0 (0.3)	109.9 (1.7) 109.6 (2.0)		
bar T1T2T	-11836.5239824	~~-2853.33981~~	48.3 (0.7) 47.5 (1.1)	-57.8 (0.4) -58.5 (0.5)	-54.4 (0.1) 53.2 (0.2)	113.5 (0.3) 115.1 (0.4)	119.7 (0.7) 117.9 (1.0)	115.3 (0.1) 115.5 (0.1)	100.3 (0.5) 99.1 (0.5)	416.8 (0.9)	~~389.7~~ (0.6)
T1T**5**T	PM6-cup		53.3 (0.4) 57.5 (0.4)	-58.1 (0.2) -64.6 (0.3)	-56.5 (0.3) 116.0 (0.3)	104.5 (0.5) 99.8 (0.2)	127.8 (0.5) 129.5 (0.2)	114.8 (0.2) 115.3 (0.1)	111.2 (0.6) 115.5 (0.3)		
bar T1T4H	-11836.5196543	-2816.15040	48.0 (0.7) 51.0 (0.4)	-57.7 (0.4) -61.3 (0.2)	-54.6 (0.1) -91.3 (0.4)	113.5 (0.3) 108.1 (0.4)	119.7 (0.8) 122.4 (0.3)	115.3 (0.1) 115.4 (0.1)	100.5 (0.5) 105.1 (0.4)	414.4 (0.9)	409.6 (1.0)
			52.9 (0.5) 49.1 (1.0)	-58.3 (0.2) -58.2 (1.0)	-56.7 (0.2) -111.7 (2.8)	105.4 (0.6) 110.4 (0.6)	126.5 (0.5) 118.6 (0.9)	114.9 (0.1) 115.2 (0.1)	109.9 (0.5) 104.7 (0.9)		

bar T1T3H	-11836.5192461	-2816.45690	48.7 (0.6) 48.4 (0.7)	-57.8 (0.4) -54.8 (0.5)	-54.5 (0.1) 164.7 (0.5)	113.5 (0.4) 113.4 (0.2)	120.2 (0.6) 119.9 (0.6)	115.3 (0.1) 115.5 (0.1)	100.3 (0.5) 98.9 (0.4)	411.7 (0.9)	403.5 (0.7)
			55.5 (0.3) 48.3 (0.9)	-58.5 (0.2) -56.0 (0.9)	-56.7 (0.4) 161.7 (1.0)	104.2 (0.6) 113.1 (0.2)	128.4 (0.9) 117.9 (1.1)	114.9 (0.1) 115.7 (0.1)	110.6 (0.7) 101.7 (0.9)		
bar T1H2T	-11836.5150822	~~-2872.01310~~	43.8 (0.5) 43.3 (0.5)	-57.3 (0.5) -58.0 (0.5)	-54.2 (0.1) 53.3 (0.2)	114.2 (0.2) 115.1 (0.2)	113.8 (0.9) 112.5 (0.8)	114.9 (0.1) 115.0 (0.1)	99.3 (0.8) 98.7 (0.6)	417.4 (0.8)	~~392.6~~ (0.7)
T1H**5**T	PM6-cup		55.6 (0.6) 57.1 (0.4)	-58.1 0.1 -65.2 (0.3)	-58.6 (0.7) 115.5 (0.8)	105.2 (0.8) 100.5 (0.6)	130.4 (0.9) 130.4 (0.6)	115.3 (0.1) 115.6 (0.1)	109.6 (1.2) 115.0 (0.9)		
bar T2T2T	-11836.5108645	~~-2880.77485~~	47.5 (1.2) 47.5 (1.2)	-58.5 (0.4) -58.5 (0.4)	53.1 (0.2) 53.1 (0.2)	115.0 (0.5) 115.1 (0.4)	117.9 (0.9) 117.9 (0.9)	115.5 (0.1) 115.5 (0.1)	99.1 (0.4) 99.1 (0.4)	406.1 (0.7)	~~367.2~~ (0.9)
T**5**T**5**T	PM6-sph		57.2 (0.5) 57.2 (0.4)	-64.6 (0.3) -64.6 (0.3)	115.8 (0.7) 115.8 (0.6)	99.8 (0.6) 99.8 (0.5)	129.5 (0.5) 129.5 (0.4)	115.4 (0.1) 115.4 (0.1)	115.6 (0.7) 115.6 (0.5)		
bar T1H4H	-11836.5092191	-2832.20732	43.6 (0.5) 47.8 (0.3)	-57.3 (0.5) -60.4 (0.2)	-54.4 (0.1) -91.3 (0.3)	113.2 (0.2) 107.3 (0.3)	114.5 (0.6) 119.3 (0.4)	114.9 (0.1) 115.0 (0.1)	100.4 (0.5) 105.5 (0.4)	414.2 (0.9)	410.1 (0.9)
			55.0 (0.6) 48.8 (2.9)	-58.2 (0.2) -57.8 (2.8)	-58.6 (2.2) -115.3 (11.8)	104.6 (1.5) 111.1 (2.3)	130.3 (2.5) 118.8 (6.7)	115.1 (0.1) 115.4 (0.4)	110.3 (2.4) 103.2 (4.5)		
bar T1H3H	-11836.5073719	-2836.34196	43.6 (0.5) 44.2	-57.3 (0.5) -54.7	-54.2 (0.2) 170.4	114.4 (0.2) 113.0	113.6 (0.9) 114.7	114.9 (0.1) 115.1	99.3 (0.7) 98.9	411.9 (1.1)	402.1 (1.1)

			(0.5)	(0.5)	(0.7)	(0.2)	(0.8)	(0.1)	(0.6)		
			54.7 (0.8) 52.5 (2.2)	-58.1 (0.3) -57.7 (5.3)	-58.6 (2.6) 149.4 (3.3)	104.0 (2.0) 111.8 (2.9)	130.5 (3.6) 122.5 (9.9)	115.1 (0.1) 115.9 (0.3)	110.9 (3.4) 103.1 (6.9)		
bar T2T4H	-11836.5071077	~~-2844.78078~~	47.2 (1.0) 51.0 (0.4)	-58.4 (0.4) -61.4 (0.2)	53.3 (0.2) -91.2 (0.4)	114.8 (0.4) 108.1 (0.4)	118.0 (0.9) 122.4 (0.3)	115.5 (0.1) 115.4 (0.1)	99.4 (0.4) 105.1 (0.4)	403.4 (0.7)	~~385.0~~ (1.1)
T**5**T4H	PM6-cup		57.8 (0.2) 49.9 (0.6)	-64.8 (0.3) -58.6 (0.4)	116.5 (0.5) -109.8 (1.0)	99.6 (0.2) 109.3 (0.4)	129.3 (0.4) 119.8 (0.6)	115.3 (0.1) 115.2 (0.1)	115.2 (0.4) 105.8 (0.5)		
bar T2T3H	-11836.5059114	~~-2844.18123~~	48.0 (1.0) 48.4 (0.9)	-58.5 (0.4) -54.8 (0.5)	53.2 (0.1) 164.9 (0.5)	114.8 (0.4) 113.3 (0.3)	118.5 (0.7) 119.8 (0.5)	115.5 (0.1) 115.5 (0.1)	99.2 (0.4) 98.9 (0.4)	400.9 (0.5)	~~379.7~~ (0.8)
T**5**T3H	PM6-cup		58.8 (0.3) 49.0 (0.6)	-64.9 (0.2) -55.8 (0.7)	116.5 (0.5) 161.0 (0.7)	99.6 (0.4) 112.2 (0.3)	129.8 (0.4) 119.0 (0.8)	115.3 (0.1) 115.7 (0.1)	114.8 (0.7) 102.5 (0.7)		
bar T2H2T	-11836.5037052	~~-2900.51060~~	43.4 (0.5) 43.4 (0.5)	-58.1 (0.5) -58.1 (0.6)	53.2 (0.2) 53.2 (0.2)	115.2 (0.2) 115.2 (0.2)	112.4 (0.8) 112.5 (0.8)	115.1 (0.1) 115.1 (0.1)	98.6 (0.6) 98.6 (0.6)	406.6 (0.6)	~~368.8~~ (0.7)
T**5**H**5**T	PM6-sph		57.2 (0.5) 57.2 (0.5)	-65.2 (0.2) -65.2 (0.3)	115.6 (0.7) 115.6 (0.7)	100.9 (0.7) 100.8 (0.6)	130.3 (0.6) 130.2 (0.6)	115.7 (0.1) 115.7 (0.1)	114.5 (1.0) 114.6 (0.9)		
bar H3T4H	-11836.5023650	-2809.04034	48.1 (0.8) 51.3 (0.4)	-54.8 (0.4) -61.4 (0.3)	164.8 (0.6) -91.1 (0.4)	113.2 (0.2) 108.0 (0.4)	119.8 (0.7) 122.6 (0.3)	115.6 (0.1) 115.4 (0.1)	99.1 (0.4) 105.1 (0.4)	397.8 (1.2)	399.3 (0.8)
			48.0 (0.6)	-56.4 (1.0)	164.0 1.1	113.5 (0.2)	116.8 (1.3)	115.8 (0.1)	101.2 (1.2)		

			49.3 (0.7)	-58.3 (1.1)	-113.5 (2.8)	111.6 (0.5)	117.9 (1.3)	115.4 (0.1)	103.2 (1.3)		
bar H4T4H	-11836.5022273	-2809.47556	50.7 (0.4) 50.7 (0.4)	-61.2 (0.2) -61.2 (0.2)	-91.4 (0.4) -91.3 (0.4)	108.0 (0.4) 108.0 (0.4)	122.3 (0.3) 122.3 (0.3)	115.4 (0.1) 115.4 (0.1)	105.2 (0.4) 105.2 (0.4)	401.1 (0.7)	405.0 (1.0)
			48.7 (0.6) 48.7 (0.5)	-58.1 (1.0) -58.1 (0.9)	-113.4 (2.3) -113.5 (2.3)	110.2 (3.8) 111.5 (0.4)	117.5 (1.0) 117.6 (1.0)	115.3 (0.1) 115.3 (0.1)	103.3 (1.0) 104.1 (2.4)		
bar H3T3H	-11836.5010426	-2807.90905	48.9 (0.6) 48.9 (0.6)	-54.8 (0.4) -54.9 (0.4)	164.5 (0.5) 164.5 (0.5)	113.3 (0.3) 113.3 (0.2)	120.3 (0.5) 120.3 (0.5)	115.5 (0.1) 115.5 (0.1)	98.8 (0.4) 98.4 (0.4)	395.2 (0.8)	394.1 (0.8)
			49.4 (3.2) 49.5 (3.3)	-56.5 (1.8) -56.5 (1.8)	162.1 (3.1) 162.0 (3.0)	113.8 (0.9) 113.7 (0.9)	117.8 (4.8) 117.9 (4.8)	115.9 (0.3) 115.9 (0.3)	100.8 (3.0) 100.9 (3.0)		
bar T2H4H	-11836.4982069	~~-2862.00446~~	43.3 (0.5) 47.9 (0.3)	-58.0 (0.4) -60.4 (0.2)	53.2 (0.2) -91.3 (0.3)	114.1 (0.2) 107.3 (0.3)	113.3 (0.5) 119.2 (0.4)	115.1 (0.1) 115.0 (0.1)	99.6 (0.4) 105.4 (0.4)	402.2 (0.7)	~~386.9~~ (0.6)
T**5**H4H	PM6-cup		56.6 (0.5) 50.8 (3.4)	-65.2 (0.5) -58.0 (3.0)	115.6 (0.8) -114.3 (12.9)	100.4 (0.6) 110.3 (2.9)	130.2 (1.2) 120.6 (6.4)	115.7 (0.1) 115.4 (0.4)	115.1 (1.3) 103.9 (4.3)		
bar T2H3H	-11836.4959166	~~-2864.79613~~	43.2 (0.5) 44.3 (0.5)	-58.0 (0.5) -54.7 (0.5)	53.3 (0.2) 170.5 (0.7)	115.3 (0.2) 113.0 (0.2)	112.3 (0.7) 114.8 (0.7)	115.1 (0.1) 115.1 (0.1)	98.5 (0.6) 98.8 (0.6)	401.2 (0.7)	~~382.6~~ (0.7)
T**5**H3H	PM6-cup		56.2 (0.4) 54.4 (1.1)	-65.0 (0.3) -55.7 (1.0)	115.4 (0.6) 155.4 (1.4)	100.2 (0.5) 112.8 (1.1)	130.2 (0.6) 123.6 (2.0)	115.7 (0.1) 115.9 (0.2)	115.3 (0.8) 100.6 (1.4)		
bar	-11836.4928028	-2821.44117	47.6	-60.4	-90.8	106.6	119.6	115.0	106.1	400.0	406.1

H4H4H			(0.3) 47.6 (0.3)	(0.2) -60.3 (0.2)	(0.3) -90.8 (0.3)	(0.4) 106.7 (0.4)	(0.4) 119.6 (0.4)	(0.1) 115.0 (0.1)	(0.3) 106.1 (0.3)	(0.8)	(1.0)
			50.2 (3.5) 50.1 (2.8)	-57.9 (3.5) -57.8 (3.5)	-115.1 (13.7) -114.8 (9.9)	110.5 (2.5) 110.9 (2.1)	120.4 (7.7) 120.1 (5.7)	115.5 (0.4) 115.5 (0.3)	103.7 (4.9) 103.3 (3.7)		
bar H3H4H	-11836.4903966	~~-2855.54311~~	44.0 (0.5) 47.8 (0.3)	-54.6 (0.4) -60.4 (0.2)	170.5 (0.6) -91.3 (0.4)	112.4 (0.1) 107.3 (0.3)	115.1 (0.5) 119.2 (0.4)	115.1 (0.1) 115.0 (0.1)	99.5 (0.4) 105.4 (0.4)	397.4 (0.8)	~~386.5~~ (0.6)
H**5**H4H	PM6-cup		56.5 (0.9) 50.9 (3.0)	-65.3 (0.9) -57.8 (3.4)	108.6 (2.0) -115.5 (15.4)	100.5 (1.1) 110.4 (3.0)	129.9 (2.0) 120.8 (7.8)	115.6 (0.2) 115.4 (0.4)	115.2 (2.3) 103.8 (5.6)		
bar H3H3H	-11836.4879129	-2827.05301	44.1 (0.6) 44.2 (0.5)	-54.8 (0.5) -54.7 (0.5)	170.5 (0.7) 170.5 (0.7)	113.1 (0.1) 113.1 (0.2)	114.6 (0.8) 114.5 (0.8)	115.1 (0.1) 115.1 (0.1)	98.8 (0.6) 98.8 (0.6)	394.7 (1.1)	393.2 (0.8)
			51.6 (2.9) 52.7 (2.9)	-56.8 (4.5) -56.6 (4.5)	153.5 (3.6) 152.8 (2.7)	111.9 (1.4) 112.2 (1.1)	122.1 (8.2) 122.9 (8.0)	116.0 (0.4) 116.0 (0.4)	102.5 (5.8) 101.5 (6.7)		

With C_{60} characterized by a cross section of 127.0 (0.1) $Å^2$.

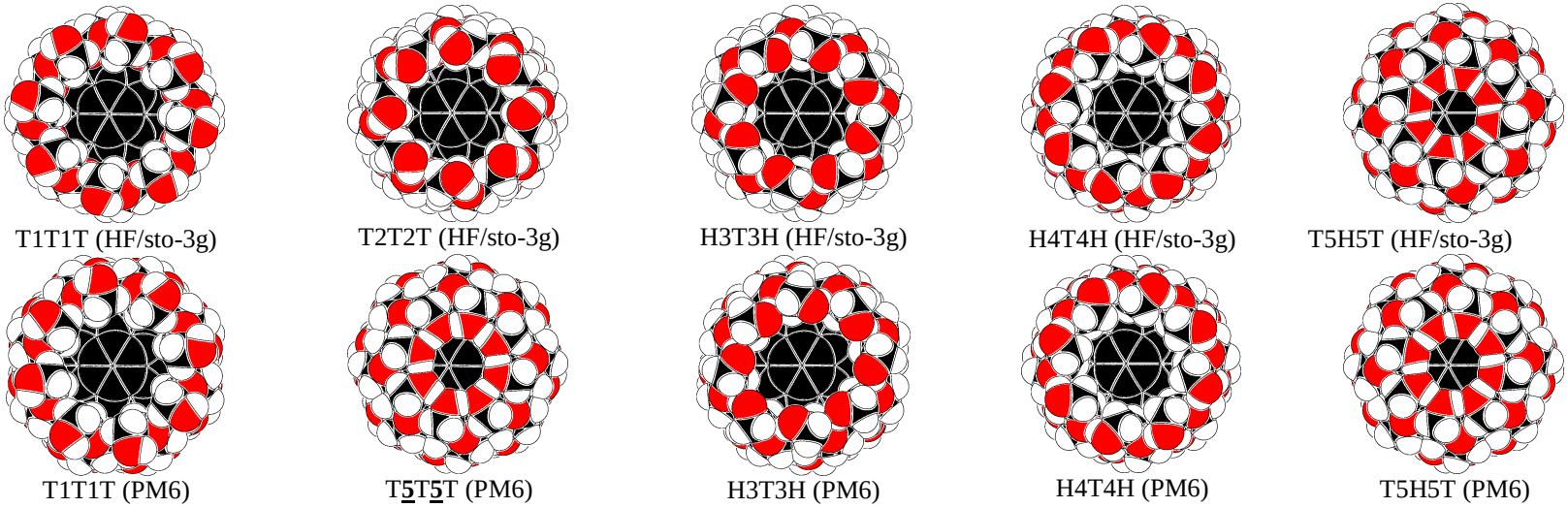

Figure 1: Top view of five of the six families of [C_{60}:(γ-CyD)$_2$] conformers. The T5H5T and H5H5H (not shown) families are largely similar.

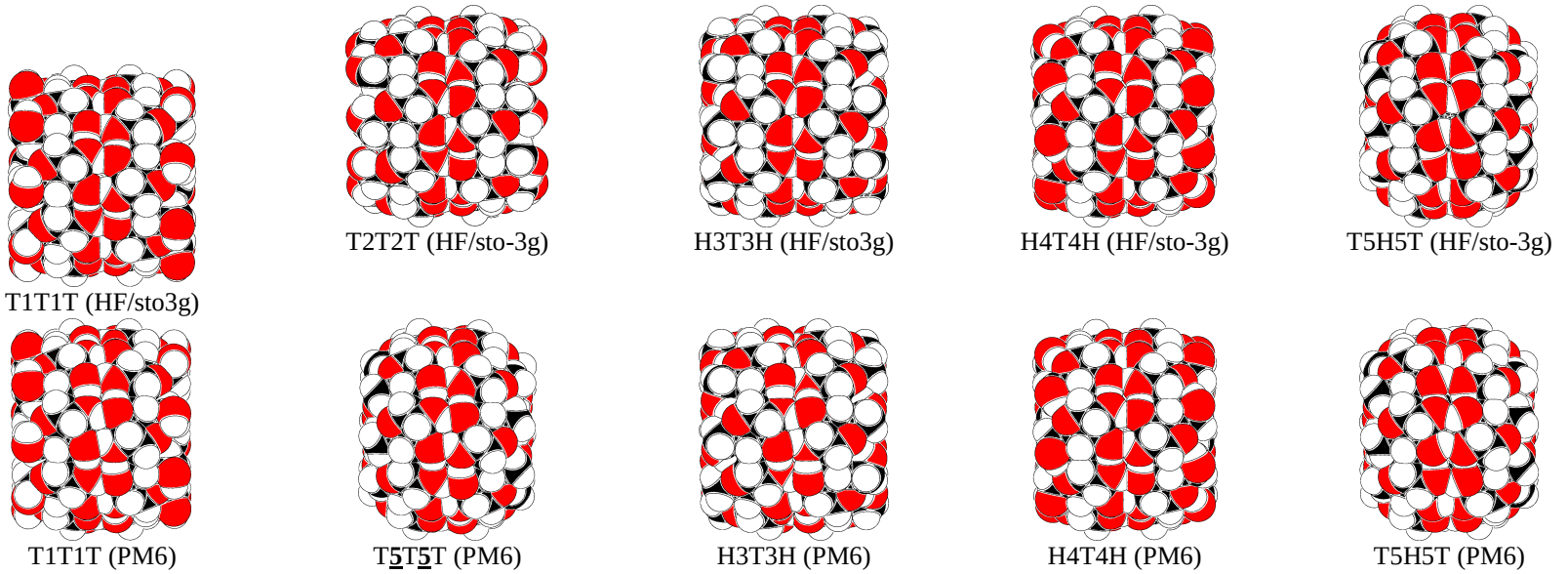

Figure 2: Side view of five of the six families of symmetric [C_{60}:(γ-CyD)$_2$] conformers. The T5H5T and H5H5H (not shown) families are largely similar.

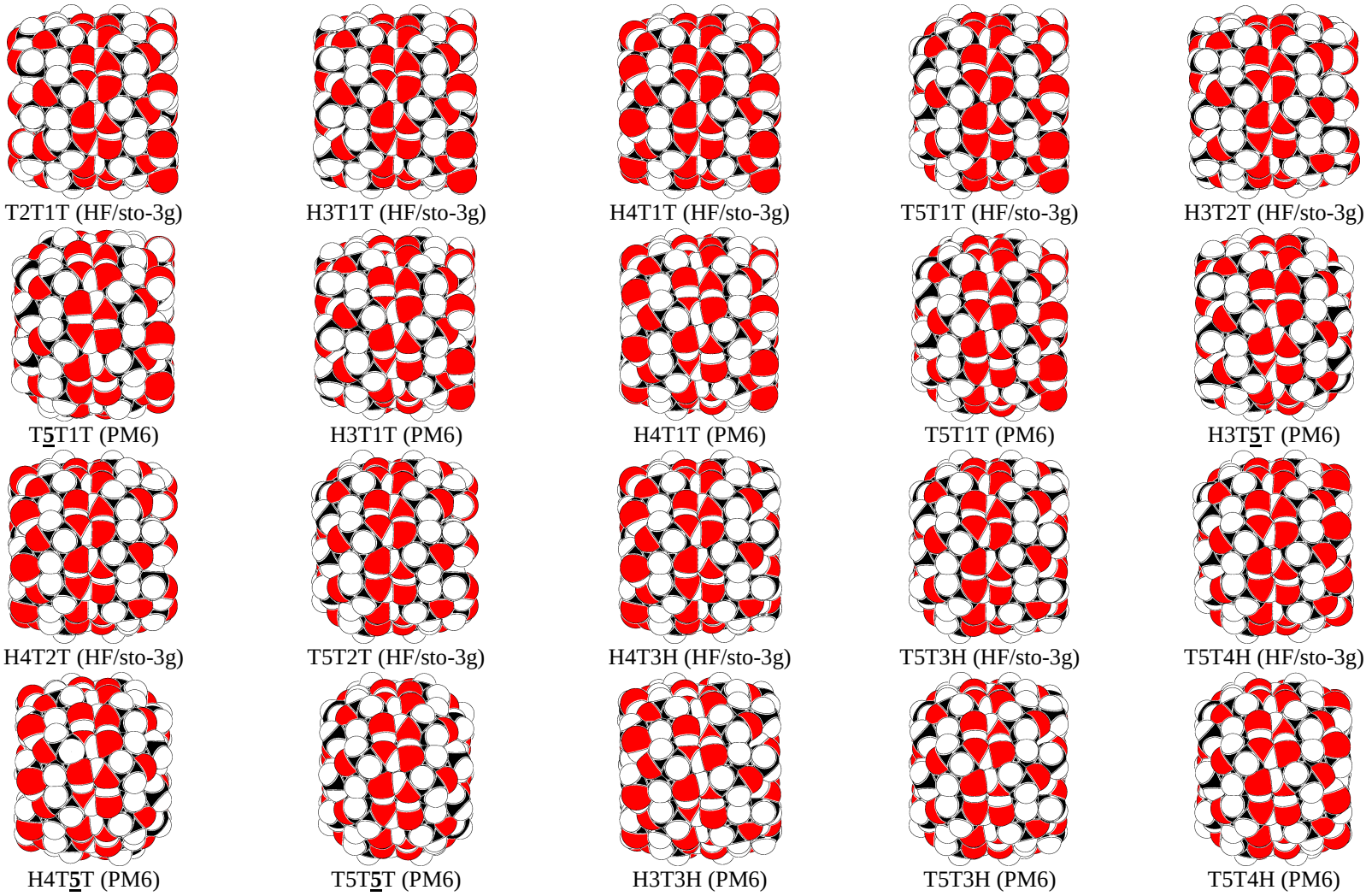

Figure 3: Side view of five of the six families of asymmetric [C_{60}:(γ-CyD)$_2$] conformers. The T5H5T and H5H5H (not shown) families are largely similar.